A Mathematical Modelling Study of Fluid Flow and Mixing in Gas Stirred Ladles

by

Schalk Willem Petrus Cloete

Thesis submitted in partial fulfilment of the requirements for the degree of

MASTER OF SCIENCE IN ENGINEERING
(EXTRACTIVE METALLURGICAL ENGINEERING)
in the Department of Process Engineering at Stellenbosch University

Supervised by
Professor Jacques J. Eksteen
Professor Steven M. Bradshaw

December 2008

Declaration

By submitting this thesis electronically, I declare that the entirety of the work contained therein is my own, original work, that I am the owner of the copyright thereof (unless to the extent explicitly otherwise stated) and that I have not previously in its entirety or in part submitted it for obtaining any qualification.

Date: 15 December 2008

ABSTRACT

A full scale, three dimensional, transient, mathematical model was developed to simulate fluid flow and mixing in gas stirred ladles. The volume of fluid (VOF) and discrete phase (DPM) models were used in combination to account for multiphase aspects, and a slightly modified version of the standard k-ε model was employed for turbulence modelling. The model was validated to compare well against published physical modelling results.

Model results were interpreted from the fundamental grounds of kinetic energy transport within the ladle. This approach led to the specification of three key measures of mixing efficiency: The rate and efficiency of kinetic energy transfer from the buoyant gas to the bulk steel as well as the total kinetic energy holding capacity of the ladle. These measures describe the quantity of mixing in any specific ladle setup, whereas the traditional measure of mixing time reflects mixing quality, i.e. the degree of kinetic energy distribution through the entire ladle.

The model was implemented in designed experiments to assess various operating and design variables pertaining to mixing quantity and quality. Considerable time was invested in finding the correct balance between numerical accuracy and computational time so that the model could be used to generate the required data within the given time frame.

Experiments on the operating variables drew an important distinction between factors influencing the shape and the strength of gas induced flow patterns. Flow pattern strengthening variables, such as gas purge rate, significantly affected the quantity of mixing, but had a limited effect on mixing quality. Variables such as mass loading that influence the shape of the flow patterns had much larger potential to influence both the quantity and quality of mixing.

Minimization of turbulence losses in the region of the plume eye was identified as the primary outcome of ladle design. It was shown that a taller vessel allowed more distance over which the plume could disperse, thereby reducing velocity gradients and subsequent turbulence generation at the free surface. Multiple tuyere systems yielded similar improvements by dividing the gas flow into several weakened plumes.

Surface wave formation was investigated as an added mixing mechanism and demonstrated to be impractical for application in full scale gas stirred ladles. The conditions for resonance between the surface wave and the bubble plume were met only in vessels with a very low aspect ratio. Performance improvements offered by swirl in these ladles could easily be replicated in more practical ways.

This study demonstrated the potential of mathematical modelling as a tool for in-depth investigation into fluid flow and mixing in the hostile environment of a full scale gas stirred ladle. Scaled-down cold models are the only alternative and can offer no more than a reasonably reliable predictive framework. The ease of flow data extraction from the numerical model also proved invaluable in facilitating a fundamental understanding of the effects of various important independent variables on ladle hydrodynamics.

At this stage of development, however, the model is recommended for use on a comparative basis only. Two important developments are required for complete quantitative agreement: The inclusion of turbulence modulation by the bubbles and the increased turbulence kinetic energy dissipation rate in the vicinity of the free surface. A general strategy was developed to account for these effects and it compared favourably with published cold model results. Further research is required to generalize this approach for application in full scale gas stirred ladles.

OPSOMMING

‘n Volskaalse, drie dimensionele, tydsafhanklike, wiskundige model is ontwikkel om die vloei en mengvermoeë van industriële gasaangedrewe smeltpotte te simuleer. Die ‘volume of fluid’ (VOF) en ‘discrete phase’ (DPM) modelle is in kombinasie gebruik om multifase aspekte in ag te neem, en ‘n effens gemodifiseerde weergawe van die ‘standard k-ε model’ is gebruik vir turbulensie modellering. Die model is suksesvol geyk teen gepubliseerde koue model resultate.

Die fundamentele gronde van kinetiese energiebehoud is as basis gebruik vir die interpretasie van resultate. Hierdie benadering het gelei tot die identifikasie van drie maatstawwe vir mengvermoë: die tempo en effektiwiteit van kinetiese energie oordrag van die drywende gas na die staal asook die kinetiese energie stoorvermoë van die smeltpot. Hierdie maatstawwe beskryf die kwantiteit van vermenging in die spesifieke smeltpot opstelling, terwyl die tradisionele maatstaf van vermengingstyd die kwaliteit van vermenging reflekteer, i.e. die effektiwiteit waarmee die kinetiese energie reg deur die smeltpot versprei word.

Die model is gebruik in ontwerpte eksperimente om die effekte van verskeie bedryfs- en ontwerpsveranderlikes op mengvermoë te ondersoek. ‘n Groot hoeveelheid tyd is bestee om die regte balans tussen numeriese akkuraatheid en rekenaartyd te vind sodat die model gebruik kon word om die nodige hoeveelheid data binne die gegewe tydsbeperking te genereer.

Eksperimente op die bedryfsveranderlikes het ‘n belangrike onderskeid getref tussen faktore wat die vorm en die sterkte van vloeipatrone beïnvloed. Vloeipatroon versterkende veranderlikes, soos die gasvloeitempo, het ‘n betekenisvolle invloed op die kwantiteit van vermenging, maar ‘n kleiner effek op die vermengingskwaliteit gehad. Veranderlikes soos die massalading wat die vorm van vloeipatrone beïnvloed het ‘n veel groter potensiële impak op beide die kwantiteit en kwaliteit van vermenging.

Die hoofdoel van smeltpotontwerp is geïdentifiseer as die minimisering van turbulensie aan die bokant van die borrelkolom. ‘n Hoër smeltpot het meer afstand toegelaat waaroor die borrelkolom kon uitsprei, en het daardeur die snelheidsgradiënte en daaropvolgende turbulensie generasie by die oppervlakte verminder. ‘n Hoër aantal spuitproppe het dieselfde verbeterings aangebring deurdat dit die gasvloei verdeel in verskeie swakker borrelkolomme.

‘n Ondersoek is geloods na die gebruik van golwe op die oppervlak van die staal as ‘n bykomende vermengingsmeganisme, maar is onprakties bevind in volskaalse gasaangedrewe smeltpotte. Die kondisies waaronder die borrelkolom die oppervlakte golf onderhou deur resonansie vind slegs plaas in smeltpotte met ‘n baie lae hoogte tot deursnit verhouding. Verbeterings in vermenging in hierdie tipe smeltpotte kan maklik oortref word op meer praktiese maniere.

Hierdie studie het die potensiaal van wiskundige modellering vir gebruik in ondersoeke na vloei en vermenging in die gevaarlike omgewing van volskaalse gasaangedrewe smeltpotte bewys. Afgeskaalde koue modelle is die enigste alternatief en kan slegs redelike akkurate voorspellings maak. Die gemak waarmee vloeidata uit die numeriese model ontgin kon word het ook bygedra tot

die identifikasie van sekere fundamentele beginsels agter die effekte van belangrike onafhanklike veranderlikes op smeltpot hidrodinamika.

Die model word tans slegs aanbeveel vir vergelykende studies. Twee belangrike ontwikkelings is nodig vir volledige akkuraatheid: Die insluiting van turbulensie modulering deur borrels en die verhoogde energie verkwisting weens turbulensie reg onder die oppervlakte. ‘n Algemene strategie is ontwikkel om hierdie faktore in ag te neem en dit het goed vergelyk met gepubliseerde koue model resultate. Verdere ondersoek is nodig om hierdie benadering te veralgemeen vir gebruik in volskaalse gasaangedrewe smeltpotte.

ACKNOWLEDGEMENTS

Firstly, thanks to my mom, Alta, for providing me with the researcher's heaven – a place where you can just eat, sleep and do research. You have helped more than you can ever know. Thank you also for refraining to no more than one recital per week of the phrase, "You are becoming more of a workaholic than you father."

A big thank you goes to my dad, Schalk, for shifting my definition of 'normal' standards and 'normal' production outputs. I now finally understand the reason for your insane working hours. Productive research is like a drug – the more you learn, the more you want to learn.

Thank you to my brother, Henri, for constantly reminding me that I am becoming a true engineering freak. (This is while he tops his first year engineering class, of course.) Thank you also for your willingness to either join me with your guitar to give my right brain some much needed stimulation, or to take another table-tennis defeat to re-inflate my ego every time my simulations refuse to work.

To the guys in the Penthouse – Johan, Gearmo and Danie in particular – thank you for constantly providing the alternative of some mindless conversation when the most productive thing my brain would do is estimate the number of left clicks employed in the creation of my thesis to date.

Special thanks go to my supervisor, Professor Jacques Eksteen, for so rudely interrupting my serene 3rd year December holiday with an introductory CFD workshop. Quite simply put; that workshop changed my life.

On the more technical side, thanks must go to my co-supervisor, Professor Steven Bradshaw, for putting me on the trail of designed experiments. Without that input this thesis would have taken twice as long to tell the same story in a much more confusing way.

I am also very grateful towards Leon du Preez from Mittal Steel: Saldanha for showing me around their ladle and giving me some valuable insights into practical limitations regarding ladle operation. The photos in this thesis come courtesy of his skill with the camera.

Finally, thanks to the Heavenly Father for making this world just so darn interesting and giving me all the tools necessary to fully enjoy it. As Edwin Hubble said: "With his five senses, man explores the universe around him and calls the adventure Science."

TABLE OF CONTENTS

CHAPTER I:
INTRODUCTION

The steelmaking industry is among the largest in the world, producing about 1.35 billion metric tonnes of steel annually. Currently, China is the leading producer of steel, followed by the European Union and Japan. It is the United States, however, that is credited for fathering industrial steelmaking as we know it today, thereby starting the second industrial revolution and changing the world forever.

Mass manufacturing of steel was the first of its kind and laid the foundation for similar developments in the chemical industries, petroleum refining, electrical and automotive industries. At the spearhead of this world-altering movement was a Scottish immigrant to the United States by the name of Andrew Carnegie. Carnegie, often called the Steel King, started his illustrious career in the cotton mills of Pennsylvania, working 12 hours per day for $1.20 per week. From these humble beginnings he rose to be the second richest man the world has ever seen, trumped only John D. Rockefeller who made his fortune from oil.

Thanks to the fortune he made in steelmaking industry, Carnegie evolved into arguably the greatest philanthropist the world has ever known. His efforts were mostly directed at aiding the worldwide sharing of knowledge by erecting a multitude of public libraries in English speaking countries worldwide. He also funded several universities and research institutions, facilitating an exponential increase in worldwide research efforts.

Interestingly, Carnegie also initiated the concept of personal development by commissioning Napoleon Hill to study the wealth building strategies of a number of the most successful people of his time. Findings of this study were published in a book entitled 'Think and Grow Rich' which sold a record-breaking 30 million copies worldwide. Hill's book has not been out of print since its release in 1937, constantly spreading the recipes of success and creating a large share of the self-made millionaires shaping the world today.

This brief trip through history clearly illustrates the profound influence that the steelmaking industry has had, and continues to have, on global development and progress. Carnegie's actions have taught the world mass-production, enabled countless researchers to follow in Isaac Newton's footsteps and 'stand on the shoulders of giants', and inspired the greatest of modern businessmen to manifest their ideas into reality.

This thesis is written to add another drop in the vast and well matured pool of steelmaking development by utilizing the modern tool of computer aided mathematical modelling. These two distinctly different fields of study combine in a fitting marriage that can and should lead to mutual benefit. The pages that follow describe how the steelmaking ladle, normally untouchable due to high temperatures and opaque process nature, can be broken down and investigated from every conceivable angle by means of mathematical modelling. Considerable focus also falls on improvements necessary to further the mathematical modelling of buoyancy driven flows, holding

the promise of rapid and meaningful development in a whole range of processes utilizing gas injection.

This then is the specific purpose statement of the present study: To investigate the functionality of a gas stirred steelmaking ladle by means of mathematical modelling over a range and depth that has not been possible up to date. Designed experiments are employed to estimate the effects of the entire range of factors having an influence on mixing, while the post-processing capabilities of mathematical modelling present these effects in a very eloquent manner. Through the use of these tools, the study aims to make meaningful conclusions and offer clear direction for future work in both the fields of secondary steelmaking and mathematical modelling of buoyancy driven flows. These two concepts are reviewed separately in Chapters II & III to follow.

The remainder of the document is arranged as follows: Chapters IV & V describe the numerical model development process by first presenting two preparatory models and then implementing results from these models in the development of the primary model. This is followed by Chapter VI discussing all the assumptions incorporated in the study. Chapter VII implements the model in a number of validation experiments against published physical modelling results.

The presentation and discussion of results commences in Chapter VIII where the kinetic energy transport considerations in gas stirred ladles are outlined. Important modelling improvements required to accurately describe the various energy exchanges in the ladle are identified and investigated in Chapter IX. The primary mathematical model is finally implemented in designed experiments in Chapters X, XI & XII, disclosing the effects of various operating- and design variables as well as the formation of surface waves on mixing efficiency. General conclusions are drawn in Chapter XIII.

Appendices are added in Chapters XIV through XVIII. These contain the nomenclature of symbols and various acronyms used throughout the text, source code of user defined functions employed, further detail on the design of the various experiments, ANOVA tables generated by all experimental runs and the references consulted.

CHAPTER II:
GAS STIRRED LADLES

Persistence is to the character of man as carbon is to steel.
- Napoleon Hill

1. Introduction to Secondary Steelmaking

Secondary steelmaking operations employ gas stirred ladles primarily for purposes of degassing and decarburization. Dissolved carbon, nitrogen and hydrogen are the primary components that need to be removed in the production process of high quality, reliable steel (1):

$$[C]+[O]=CO(g)$$ Reaction 1

$$[H]=\frac{1}{2}H_2(g)$$ Reaction 2

$$[N]=\frac{1}{2}N_2(g)$$ Reaction 3

In some processes such as vacuum oxygen decarburization (VOD), a vacuum of as low as 1 mbar is drawn at the top of the vessel to decrease the partial pressure of the dissolved elements, shifting the equilibrium to the right in the above reactions. Argon purging through plugs located at the bottom of the vessel serves to decrease the partial pressure even further.

The argon injections also provide the sole source of mixing in the vessel. This mixing is essential for bringing reactants together and removing products from reaction sites, thereby driving the decarburization and degassing reactions once the initial vacuum has been drawn. Various impurities are also removed to the slag layer resting on top of the purified steel. A schematic of the process is presented in Figure 1:

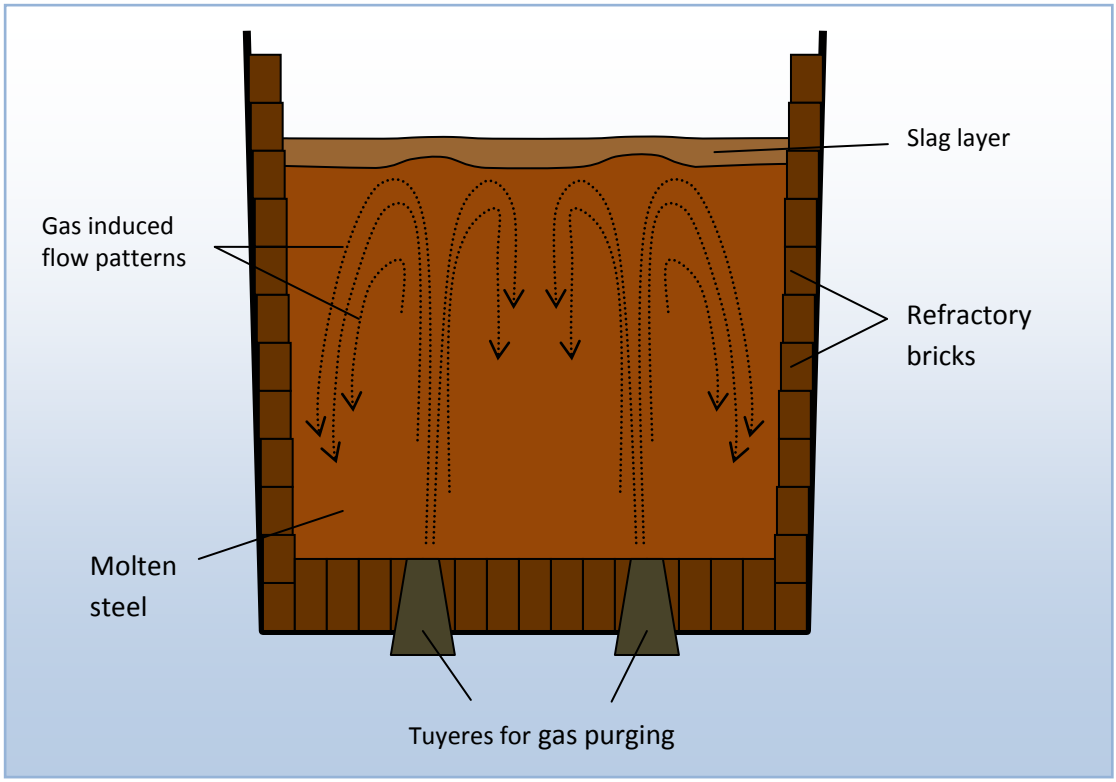

Figure 1: A typical gas stirred ladle.

2. Reaction Stages

Reactions occur at a number of zones during the different stages of the process. Primarily, reactions take place at the metal/gas and metal/slag interfaces (2), but liquid-solid interactions also take place between the steel and refractory lining and possible solid flux additions (1).

2.1. Oxygen Blowing/Addition Stage

The oxygen blowing stage adds dissolved oxygen to the metal phase. This can be accomplished by pure oxygen blowing through a top lance, adding oxygen as a fraction of the stirring gas purged through the bottom tuyeres or by adding fluxes like FeO to the melt. For gaseous oxygen injections:

$$O_2(g) = 2[O]$$ Reaction 4

This allows for decarburization (Reaction 1) as well as the removal of various other impurities to the slag. The removal of silicon is shown as an example:

$$\frac{1}{2}[Si] + [O] = \frac{1}{2}SiO_2$$ Reaction 5

Metal/slag reactions are strongly dependent on the impurities present in the system. Ding et al. (2) identify the following reactions as the most important in their specific system:

$$Cr_2O_3 + 3[C] = 2[Cr] + 3CO$$ Reaction 6

$$2Cr_2O_3 + 3[Si] = 4[Cr] + 3SiO_2$$ Reaction 7

$$3FeO + 2[Cr] = 3Fe + Cr_2O_3$$ Reaction 8

$$MnO + [C] = [Mn] + CO$$ Reaction 9

From these reactions it can clearly be seen that the metal/slag reactions play an important role in the liberation of carbon as carbon monoxide as well as the removal of inclusions such as silicon. Slag/metal reactions are often promoted by using strong gas purging to provide increased contact between metal and slag.

2.2. Vacuum Degassing Stage

During this stage, a vacuum is drawn at the top of the vessel, reducing the partial pressure of all dissolved gasses still in solution. Degassing and decarburization reactions are strongly pressure dependent and proceed more readily when a vacuum is drawn. Ghosh (1) calculates the equilibrium concentration of nitrogen in steel at 10, 100 and 400 Pa as 4.3, 14 and 28 ppm respectively, demonstrating the effect that a strong vacuum has on degassing.

Vacuum treatment is essential for the dehydrogenization since the hydrogen concentration in the liquid steel has to be reduced below 0.8 ppm to avoid flaking (3). Such low pressures are not required for the removal of carbon and nitrogen where concentrations of 30 ppm are generally acceptable (3). The required treatment time of these operations can be significantly shortened under a vacuum though.

Gas stirring under a vacuum has to be very gentle since the low surface pressures cause rapid expansion of gas in the upper regions of the melt. The rapid increase in gas volume can lead to severe melt splashing and possible spillage.

2.3. Reduction Stage

If needed, a reducing agent can be added in a separate stage to recover any oxidized chromium. Additional fluxes can also be added to control slag composition and fluidity, while alloys can be added to adhere to the specified steel composition and grade.

3. Rate Control

The steelmaking ladle as a whole presents a complex modelling challenge, containing elements of reaction, thermal and complex turbulent multiphase flow phenomena. Studies have been completed on all of these aspects. The true practical value of these studies, however, depends mainly on the identification of the limiting step of the process. Improvements made in areas that are not rate limiting will offer very little benefit on overall process performance. Accordingly, the first step in any investigation regarding gas stirred ladles should be the identification of the rate controlling step.

3.1. Identification of the Limiting Step

Ghosh (1) presents a well researched investigation into this important topic. The first step is to break the general decarburization or degassing reaction into the following steps:

1. Transfer of the gas forming elements H, N, C and O from the bulk metal to the metal/gas interface
2. Chemical reactions (Reaction 1 to Reaction 3) at the interface
3. Transfer of gaseous species H_2, N_2 and CO from the interface to the bulk gas
4. Nucleation, growth, and escape of gas bubbles
5. Mixing in the bulk metal
6. Mixing in the bulk gas

Common sense suggests that steps 3 and 6 will not be controlling. The high temperatures, low viscosity and constant motion of the gas phase are all conducive to very fast mass transfer and mixing. As for step 4, various cold model studies have shown that the nucleation of gas bubbles is not a problem either (1). Furthermore, the rate of nitrogen desorption is the only case partially controlled by chemical reaction at the gas/metal interface (1), warranting the exclusion of step 2.

This leaves steps 1 and 5: mass transfer in the metal and bulk mixing. Ghosh (1) presents some studies comparing the time it takes to reach 95% refining through mass transfer and the time it takes to achieve 95% mixing. These two measures were defined as follows:

For mass transfer:

$$\ln\left[\frac{C_i}{C_i^0}\right] = 1 - X = k_m \frac{A}{V} t = k_m a t \qquad \text{Equation 1}$$

Using Equation 1 and $k_m a$ parameters from the literature, Ghosh (1) calculated the time required for 95% conversion in a number of steelmaking reactions ranging from 40 to 260 seconds.

The degree of bulk mixing is often quantified by tracking the concentration of an inert tracer (C_i) at various points within the melt.

$$X = \frac{C_{i,\min}}{C_{i,ave}}$$ Equation 2

The vessel can be seen as well mixed when the minimum tracer concentration in the ladle is 95% of the average tracer concentration. Ghosh (1) found from the literature that these 95% bulk mixing times range from 50 to 500 seconds.

It can already be seen that the mixing times are generally longer than mass transfer times, but Ghosh (1) goes even further to confirm this notion. The literature contains some experimentally determined rate constants for the removal of carbon and hydrogen. According to these sources, these two rate constants are relatively similar. Theoretically however, the ratio between mass transfer coefficients is dependent only of the respective diffusivities:

$$\frac{k_{H,emp}}{k_{C,emp}} = \frac{D_H}{D_C} = \frac{10^{-7}}{7.2\times10^{-9}} = 3.73$$

Since this ratio is far from unity (as suggested by the experimental measurements), mass transfer rate is not controlling. Mixing control, on the other hand, would result in identical rate constants for all reactions since all reactants and products are transported to and from reaction sites at equal rates. It can thus be concluded that reactions taking place within a gas stirred ladle are controlled by the quality of mixing in the bulk metal phase.

3.2. Implications

Since system performance is completely mixing controlled, the opportunity is presented for significant simplification. All chemical reactions, thermodynamics, species transfer and -diffusion can be completely ignored on the assumption that any improvement in mixing will result in a parallel improvement in overall system performance. Accordingly, the remainder of this chapter can focus solely on mixing in gas stirred ladles.

4. Mixing in Gas Stirred Ladles

In addition to being rate controlling, a high degree of mixing is essential for temperature and concentration homogenization as well as inclusion removal. Recognizing its effect on the success of steelmaking processes, mixing in gas stirred ladles has been the focal point of numerous research efforts. Many correlations have been proposed in an attempt to predict the effects of various parameters on the efficiency of mixing. Earlier studies focussed on the gas purging rate as the primary control variable, but later studies recognized other contributing factors as well.

It is now common practice to correlate mixing to the rate of buoyant energy input per mass of liquid to be mixed (W/kg). The following correlation derived by Ghosh (1) is adapted for use in molten steel systems:

$$\varepsilon_b = \frac{336 Q_{V,N} T_l}{M_l} \ln\left(1 + 0.681 \frac{H}{P_0}\right)$$ Equation 3

Equation 3 is theoretically derived and provides a valuable understanding of the influence that different operating variables have on the mixing energy provided by gas injection. Note that Equation 3 is altered slightly from the original source to apply to the current metal density of 6942.9 kg/m^3 and also to correct for a typing error in the bracketed term (the 1 and the 0.681 were incorrectly bracketed together). The surface pressure is given in bar.

Apart from the factors influencing the buoyant energy input, the gas stirred ladle contains a substantial number of process variables that could have an influence on mixing efficiency. A summary of the all applicable variables (operating- and design-) is given below:

- Operating variables
    - Gas purging
        - Total gas purge rate
        - Distribution of gas purge rate between multiple tuyeres
    - The mass loading (depth of molten steel)
    - Liquid temperature
    - Operating pressure
    - Slag layer
        - Thickness
        - Composition
- Design variables
    - Tuyere setup
        - Number of tuyeres
        - Positioning of tuyeres on the ladle floor
    - Injection philosophy
    - Material processed
    - Flow pattern manipulation
    - Ladle geometry
        - Ladle shape
        - Ladle aspect ratio
        - Ladle size

Another promising phenomenon sometimes present in gas stirred ladles is the onset of a sloshing or swirling motion of the free surface. This surface wave form presents an additional mixing mechanism and can lead to significant increases in mixing efficiency.

Each of these variables influences the quality of mixing, and therefore the efficiency of the process, to some degree. The extent of this influence is as of yet unknown, and additional information is required to ensure that research effort is directed appropriately. Accordingly, a thorough review and analysis of each variable follows below.

4.1. Operating Variables

An investigation into the effects of operating variables on mixing is of special importance since improvements can be implemented in any existing steelmaking ladle. Any meaningful discoveries in this category will offer immediate value to the industry.

4.1.1. Gas Purging

A. Total Gas Purging Rate

The gas purging rate is regarded as the most influential mixing parameter, simply because it is the sole driving force for mixing. It has therefore been the focal point of a large number of research studies. Initially, all of these studies focussed on cold modelling, but later studies introduced the promising field of mathematical modelling often accompanied by cold model verification.

Some of the foremost authorities in the field of buoyancy driven flow have proposed correlations expressing mixing time in terms of gas flow rate and ladle geometry measurements. Initial research was focussed on centric gas injection, but later expanded to the industrially more popular twin tuyere setup.

i. Single Tuyere

One of the first fundamentally derived expressions for the mixing time in a centred tuyere system was formulated by Mazumdar and Guthrie (4):

$$\tau_{95\%} = 5.04 \frac{D^{7/3}}{Q_V^{1/3} H}$$ Equation 4

Several other water model studies (reviewed in (5) & (6)) have yielded similar equations. Iguchi *et al.* (7) developed such an equation featuring the kinematic viscosity (ν_l) of the liquid as well.

$$\tau_{95\%} = 1200 \frac{D^{1.97} \nu_l^{0.47}}{Q_V^{0.47} H}$$ Equation 5

Equation 5 was compared against experimental results from several sources and was found to be superior to Equation 4. Mazumdar and Guthrie (8) responded to this claim by critically analyzing Equation 5 and questioning its validity in high Reynolds number flows typical in gas stirred ladles.

Mazumdar and Guthrie (9) also reviewed a large number of published mixing time correlations (shown in Figure 2) and reproduced their original equation (Equation 4) through dimensional analysis.

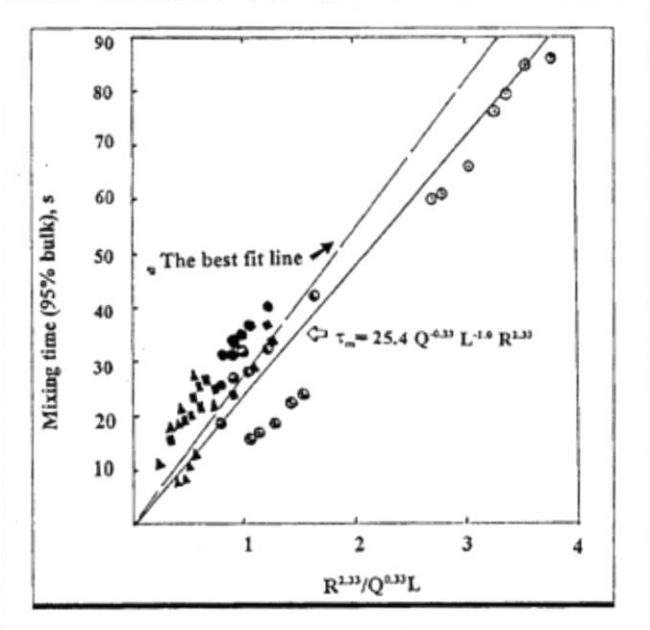

Figure 2: Scatter of 95% bulk mixing times calculated by various studies (9).

Significant variance is present in Figure 2, suggesting that the estimation of the effect of gas purge rate on mixing time cannot be accurately determined through purely empirical measures. The good fit of Mazumdar and Guthrie's fundamentally derived equation (Equation 4) does increase the confidence in its accuracy though.

Ghosh (1) also compared the mixing time predictions of a number of different equations (Figure 3) as applied to a standard water model and scaled for application to a 150 ton steel ladle.

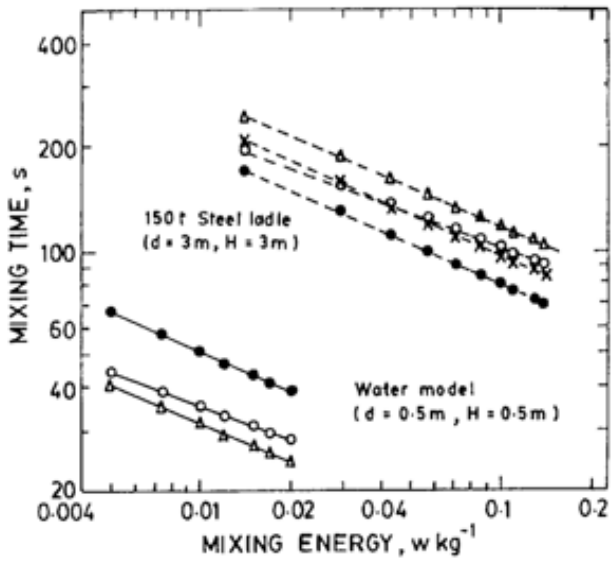

Figure 3: Comparison of different mixing time predictions compiled by Ghosh (1).

The issue of scale-up is also raised. Ghosh (1) reports that some authors claim their equations to be valid even for liquid iron, while others suggest a scaling factor of 1.9. In general, it was concluded from the literature that model equations somewhat under-predict mixing times in real industrial vessels.

For the purposes of this study, however, it is interesting to note that Equation 4 (o- - o - - o in Figure 3) is again positioned favourably even when scaled-up to a full 150 ton steel ladle. This shows that Mazumdar and Guthrie's relationship of $\tau_{95\%} \propto Q^{-0.33}$ is fundamentally sound.

Mazumdar and Guthrie (4) also identified two distinct regions in the relationship between mixing time and purge rate:

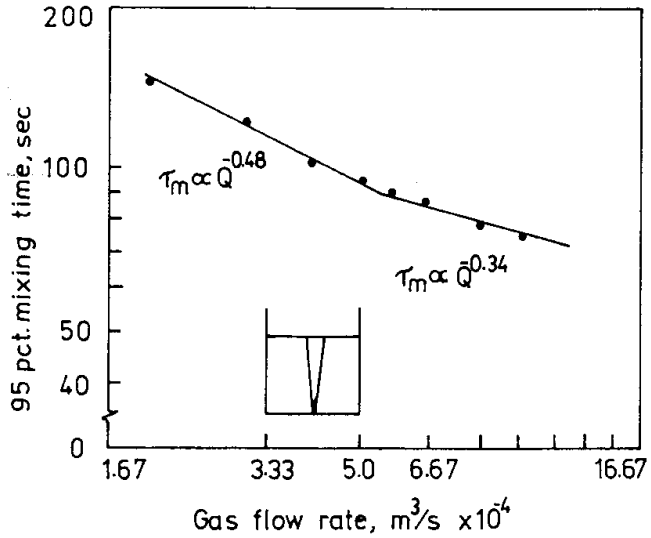

Figure 4: Variation of mixing time with gas purge rate for a single centred tuyere setup (4).

Figure 4 shows that mixing time decreases fairly rapidly ($\tau_{95\%} \propto Q^{-0.46}$) with increasing purge rate, up to a certain point where the relationship changes to $\tau_{95\%} \propto Q^{-0.34}$. The latter relationship is in good agreement with Equation 4, while the prior agrees with Equation 5 derived by Iguchi *et al.* (7). This strengthens the claim by Mazumdar and Guthrie (8) that Equation 5 is valid only for low Reynolds number (i.e. low purging rate) flows.

ii. Twin Tuyeres

A later study (10), co-authored by Mazumdar, revealed a similar pattern for dual purge plugs (Figure 5). Here an initial relationship of $\tau_{95\%} \propto Q^{-0.58}$ was followed by a relationship described by $\tau_{95\%} \propto Q^{-0.35}$.

The transition between the two power relationships was found to occur when the prevailing flow pattern in the vessel ceased to change with time. Initial increases in gas flow rate caused the gas induced flows to spread through the vessel, steadily eliminating any dead zones and therefore causing large reductions in mixing time ($\tau_{95\%} \propto Q^{-0.58}$). Once all the dead zones were eliminated, however, the flow pattern became invariant. Further increases in gas flow rate after this point could only increase the strength of this steady flow pattern and yielded smaller improvements in mixing time ($\tau_{95\%} \propto Q^{-0.35}$).

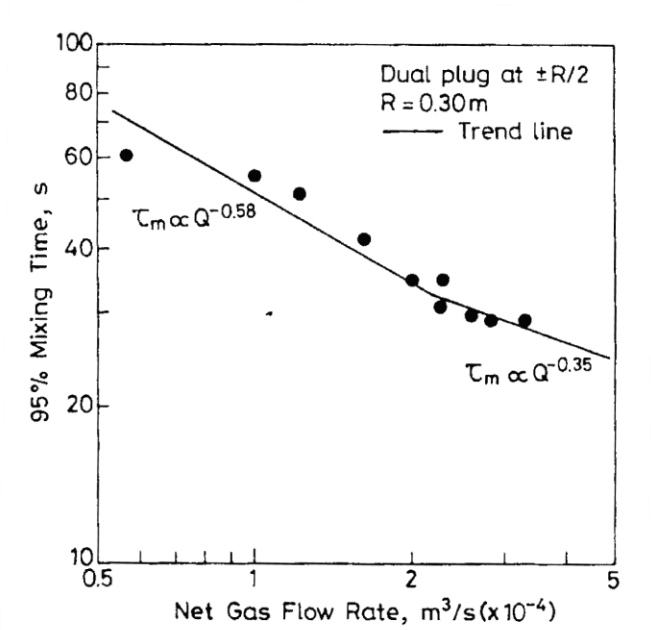

Figure 5: Variation of mixing time with gas purge rate for a twin tuyere setup (10).

Concurrently with this study, Mazumdar co-authored an empirical study (11) yielding the following relationship:

$$\tau_{95\%} = 3.75 \frac{D^{2.0}}{Q_V^{0.38} H^{0.56}} \qquad \text{Equation 6}$$

The smaller empirical constant (3.75 as opposed to 5.04 in Equation 4) suggests that twin tuyere setups provide a substantially better return in mixing efficiency when compared to single tuyere setups. The coefficient of Q (0.38 as opposed to 0.33) also suggests a greater return in mixing efficiency with increased gas purging rates.

iii. Alternative Mixing Models

Two papers co-authored by Oeters (12) & (13) discuss some alternative mixing models. Particular attention was paid to a model featuring a number of ideally mixed tanks in series connected with a dead volume and recirculation. This model was shown to be very effective in predicting tracer concentrations at specified measuring points in the vessel and was even validated against tracer concentration measurements taken in a 40 ton industrial ladle.

The model is somewhat complex, however, and requires knowledge of parameters such as the recirculating volume flow, the volume of dead zones and the volume flow in and out of dead zones. Accordingly, the simple relationships presented in the preceding sections will be preferred as a basis for comparison.

B. Distribution of Gas Purge Rate between Multiple Tuyeres

No literature could be found on this subject, but it is known that industrial ladle operators sometimes employ other than equally distributed purging philosophies. They have learned through experience that such alterations provide good process performance and it is therefore well worth investigating.

4.1.2. The Mass and Depth of the Melt

When handled as an operating variable in an existing vessel, changes in the mass of molten steel and its depth in the vessel are synonymous. Therefore, when looking at Equation 4 and Equation 6, it would seem favourable to fill the vessel to maximum capacity. It is interesting to note that both equations show the depth of liquid to have a much larger effect on the mixing time than the gas purging rate.

The buoyant energy input per unit mass (Equation 3) decreases in an inversely proportional manner with the mass of liquid in the vessel, but increases logarithmically with the height of the liquid. It stands to reason that there will be a certain range where the positive effect of the liquid depth is larger than the negative effect of the total mass and vice versa.

Numerous studies have shown, however, that taller vessels tend to leave large dead zones in the bottom regions even when higher gas flow rates are used (6; 13; 14; 15; 16). These dead zones will compromise process performance regardless of the amount of mixing present in other regions of the vessel.

To add further complexity, it has been demonstrated that a swirling or sloshing motion tends to develop in baths with an aspect ratio of lower than 1 or higher than 2 (17). This sloshing motion has a significant influence on mixing (see Section 4.3 of this chapter).

4.1.3. Liquid Temperature

According to the ideal gas law, an increase in temperature would have the same effect on buoyant energy input as a proportional increase in gas flow rate. Equation 3 supports this by showing that melt temperature and gas flow rate are both directly proportional to buoyant energy input.

Practically speaking though, the operating conditions in a fully functional steel mill do not allow for large alterations in the melt temperature. When evaluating parameters for increasing buoyant energy input, the gas flow rate has a much larger scope for experimentation.

Gas stirred mixing vessels in general are employed over a large spectrum of processes (and temperature ranges) labelling the effect of temperature more profound as a design variable than an operating variable. Nonetheless, it will be worthwhile to investigate the influence of liquid temperature on mixing time, even if only to confirm a parallel effect to that of gas flow rate.

4.1.4. Operating Pressure

Similarly to melt temperature, the melt surface pressure will also influence the bubble volume in the melt through the ideal gas relationship. Vacuum systems employed in industrial steelmaking can affect surface pressures as low as 10 mbar, yielding a 100 time gas volume increase just below the surface of the melt.

The buoyant energy input equation (Equation 3) also shows a reduction in pressure to increase the buoyant driving force. Tatsuoka *et al.* (18) conducted cold model experiments to prove that reductions in operating pressure shorten mixing time. Pressure reductions below 6.66 kPa, however, did not have any effect on mixing time. The conclusion was drawn that most of the bubble expansion energy was dissipated near the surface at these very low pressures.

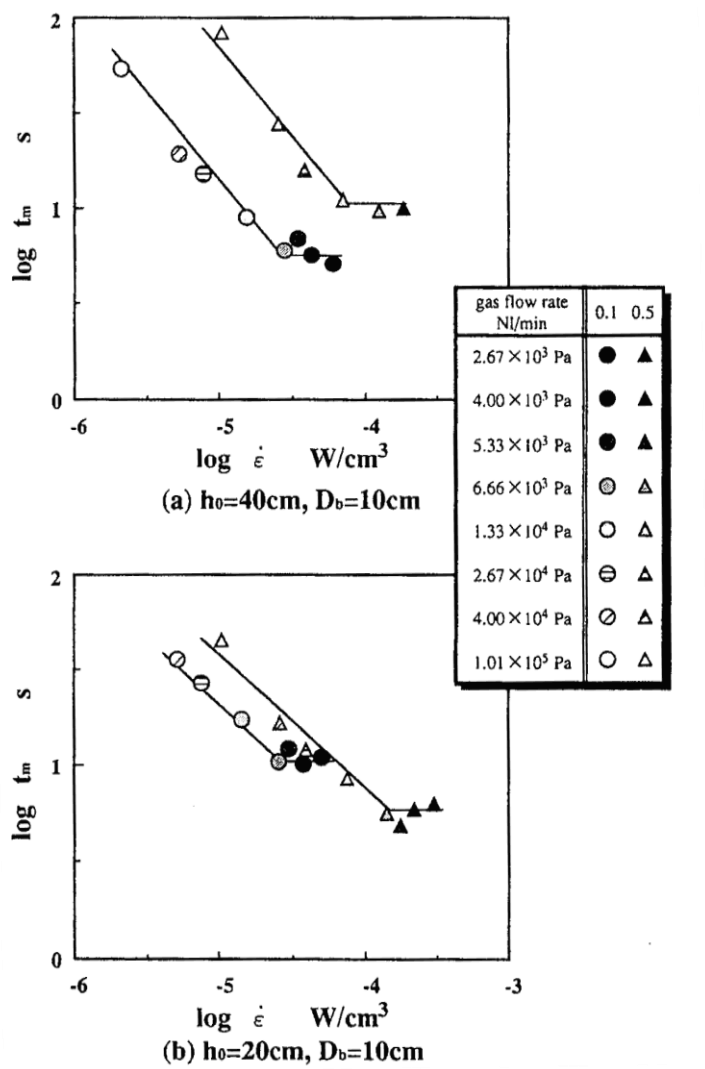

Figure 6: Variations of mixing time with operating pressure in a silicon oil bath (18).

The large degree of improvement displayed in Figure 6 is also worth mentioning. It is shown that pressure reductions from atmospheric to a vacuum of 6.66 kPa shortened mixing times eight-fold (from 50 to 6 seconds).

4.1.5. The Slag Layer

The thickness, composition and physical properties of the slag layer are strongly dependent on the system under consideration. In some systems slag is present as an unwanted carry-over from previous process steps, but the majority of secondary steelmaking operations purposefully employ a slag layer as an important role-player in melt reactions and inclusion removal (see Chapter II:2.1). Various steps can also be taken by plant operators to influence the physical properties of the slag layer. Therefore, a slag layer of varying thickness and physical characteristics will be present in the majority of steelmaking ladles.

Mazumdar (19) concluded from cold modelling that the presence of a top layer dissipates some of the buoyant energy provided by gas bubbling. Experimentation revealed recirculating and fluctuating velocities to be substantially lower in systems with a top layer than in systems without. Three mechanisms were presented to explain this dissipation of buoyant energy:

- Formation of multiple slag droplets
- Potential energy required to keep these droplets in suspension in the metal phase
- Potential energy required to maintain the deformed interface between the phases

Further analysis showed the energy dissipated to deform the free surface to have the largest impact. The remaining two dissipation mechanisms could be seen as insignificant.

At a later stage Iguchi *et al.* (20) came to a similar conclusion stating that the central bubble region is narrowed and the mean flow and turbulence outside of the plume is suppressed in the presence of a top layer. In a subsequent study, co-authored by Iguchi (21), a mathematical model was employed to investigate the effect of slag density. In addition to the above mentioned findings, it was also concluded that flow and turbulence characteristics are suppressed even further in systems with a smaller density ratio between phases. This reduction in mixing efficiency was attributed solely to slag entrainment. The density ratio at which slag entrainment became the dominant force was very close to 1, however. Such situations are not known to occur in steelmaking ladles.

Yamashita and Iguchi (22) conducted an interesting investigation into the possibility of controlling top-layer emulsification and mixing time by immersing a circular plate directly on top of the rising bubble plume, thus altering the flow patterns. The conclusion was drawn that reverse emulsification can be controlled and mixing time significantly shortened when a plate with diameter greater than that of the bubble plume was used. The depth of insertion also played a significant role in the degree of improvement.

Even though the majority of studies agree that the presence of a slag layer decreases mixing efficiency, it has been found to be beneficial to mixing as well (23). The slag layer in this study was modelled with small plastic balls and was therefore not truly fluid. This modelling assumption might explain the improvement in mixing time offered by the slag layer.

4.2. Design Variables

By definition, any alteration in design variables will require a totally new ladle design, thereby demanding large investments of time and capital. Design variables do offer a much larger scope for improvement though, and many exciting and imaginative innovations can be made in this category.

4.2.1. Tuyere Setup

Initially, studies on buoyancy driven flows focussed solely on injection through a single tuyere, positioned axis-symmetrically at the centre of the vessel. It was not long, however, before more attention was given to the possibilities of eccentric and multiple tuyere setups.

The reason for this interest in alternative tuyere setups is clearly articulated in an article by Mietz and Oeters (14): “The intensity of the flow is determined by the gas flow rate, its pattern is given by the position of the nozzle.” In other words, if a specific tuyere setup creates dead zones, little can be gained by simply increasing the gas flow rate. Flows in the well mixed regions will increase, but the dead zones will remain. The only real solution is an alteration in the tuyere setup.

A. Tuyere Positioning

Mietz and Oeters (14) completed experiments in an air-water system showing that eccentric gas stirring through a single tuyere can completely eliminate the dead zones left in a similar system employing centric stirring. It was observed that the eccentric setup resulted in one great flow loop filling the entire vessel, while the centric setup creates a toroid in the upper- and a dead zone in the lower regions of the vessel. This was later confirmed in a nitrogen-Wood’s metal system (16).

In an extensive review on flow and mixing in secondary metallurgy, Oeters *et al.* (13) concluded that mixing will continue to improve as the tuyere is moved closer to the side of the vessel. Figure 7 illustrates:

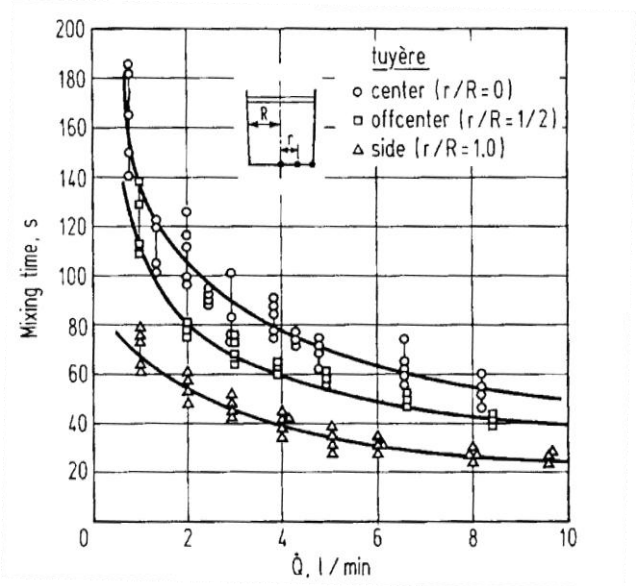

Figure 7: The effect of single tuyere positioning on mixing time (13).

Contrary to the conclusions of Oeters et al. (13), Joo and Guthrie (24) found that a mid-radius placement of the off-centre tuyere resulted in minimum mixing times. Any tuyere placements closer to the wall would distort the plume towards the wall, increasing mixing time and refractory wear.

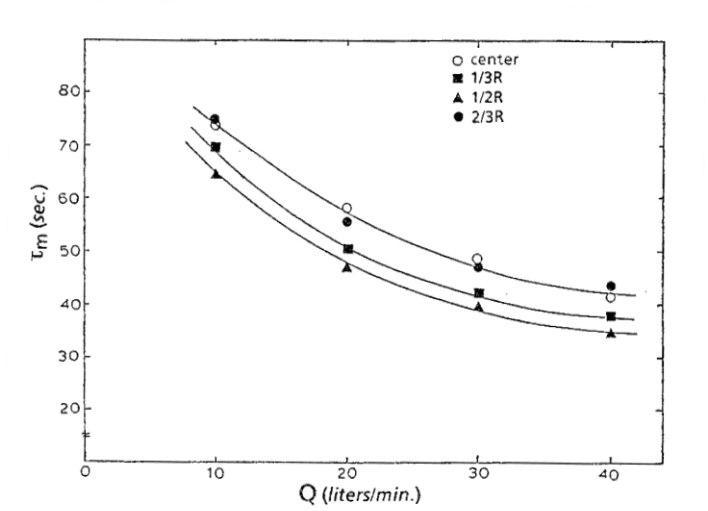

Figure 8: The effect of single tuyere positioning on mixing time (24).

Studies therefore agree that eccentric tuyere setups provide superior mixing capability. The best position for the eccentric tuyere, however, seems to differ from system to system. Further research is indicated.

B. Number of Tuyeres

The study of Joo and Guthrie (24) referenced in the previous section was expanded further to investigate the effect of utilizing two tuyeres instead of one. It was found that, by placing two tuyeres at mid-radius and diametrically opposite each other, the mixing time could be reduced even further. The positioning of these twin tuyeres also played a key role in determining the resulting flow patterns as illustrated in Figure 9.

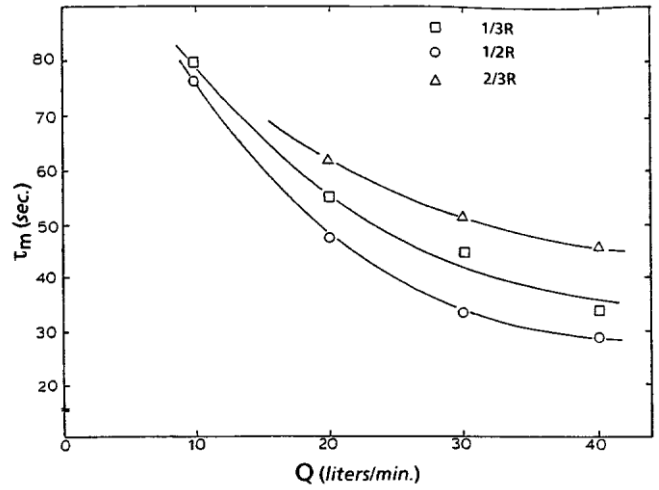

Figure 9: The effect of twin tuyere positioning on mixing time (24).

A recent study by Mandal *et al.* (11) established that there exists a critical gas flow rate for any given vessel beyond which mixing times in dual plug configurations become shorter than their axis-symmetric counterparts. This relationship is illustrated in Figure 10.

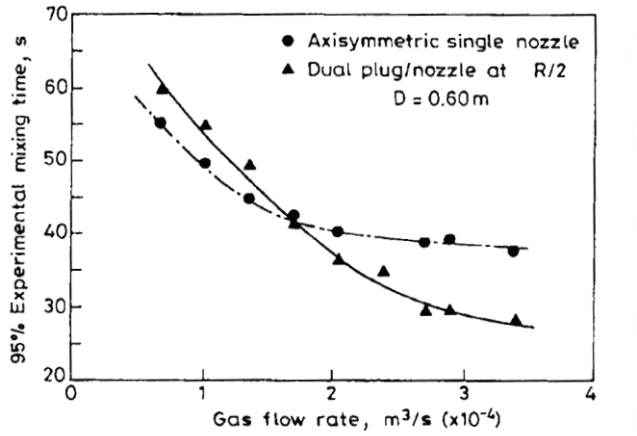

Figure 10: Variation in mixing times for the axis-symmetrical and the mid-radius dual plug setup (11).

This would suggest that the twin tuyere setup is suited for applications involving larger gas purging rates, while single tuyere setups should be preferred in applications requiring weaker flow. The exact location of the transfer point between these two situations in full scale ladles is well worth investigating. When considering Equation 4 and Equation 6, however, it is likely that the transfer point will be at very low gas flow rates, uncharacteristic to gas stirred ladles.

A study by Roth *et al.* (23) presents flow and mixing results in a water model designed with a large number of alternative tuyere setups. Optimum mixing was attained by an eccentric triangular tuyere arrangement. It was also found that mixing increased with an increase in the number of tuyeres and with greater spacing between tuyeres.

4.2.2. Injection Philosophy

A variety of purging plugs are available for purposes of bottom blowing in steel ladles, with the major distinction made between slotted and porous plugs (25). Various combinations of these are available as well, altering the shape of the slotted region and combing slotted and porous regions.

For the purposes of the current study, however, this information is of little interest. It is indicated in reviews by authorities in the field of buoyancy driven flows (1) & (6) that a stable, spherical capped bubble region occupies the vast majority of the vessel regardless of the injection method employed. This region is responsible for the majority of buoyant energy transfer, causing mixing patterns to vary only marginally between different tuyere setups. The influence of nozzle diameter on flow and mixing is also regarded to be insignificant (15).

Accordingly, the effects of different injection philosophies will not be investigated.

4.2.3. Material Processed

Physical properties of the materials being mixed will have an influence on the mixing time. Of primary importance here is the density and viscosity of the specific material.

The scaling issues involved in applying results from water modelling studies to industrial ladles has resulted in a good understanding of the impact that material properties have on flow (the physical properties of water are evidently quite different from that of molten steel). It is generally agreed that the degree of mixing is dependent on the inertial, gravitational and viscous forces acting on the fluid. The importance of gravitational forces is hardly a matter for debate, but a substantial review by Mazumdar and Evans (5) did establish that the effect of viscous forces is many times smaller than that of inertial forces. This implies that the density of the liquid is of much greater importance than the viscosity when studying mixing phenomena.

Researchers (7) have attempted to correlate mixing time to the kinematic viscosity of the fluid involved (see Equation 5), but it has been argued (8) that this correlation is applicable only in low Reynolds number regions (i.e. regions where the inertial/viscous force ratio is small) which fall outside the range common to most steelmaking processes.

When dealing with full scale gas stirred ladles though, the differences in viscosity and especially density of molten steels are often insignificant. The properties of the slag, as discussed in Section 4.1.5, are highly process dependent and known to vary from an almost solid crust to a free flowing melt. Therefore, only changes in slag parameters will be investigated as operating variables (reviewed in Section 4.1.5).

4.2.4. Flow Pattern Manipulation

The logic behind flow pattern manipulation is to modify flow direction in such a way that minimal energy dissipation occurs in forms such as slag entrapment and surface deformation. As described in Section 4.1.5, the effects of these energy dissipations can lengthen mixing times quite significantly.

A surprisingly small amount of research has been done in this promising field. Iguchi *et al.* (26) investigated the possibility of controlling the mixing time by bringing a flat circular disc or a circular cylinder into contact with the surface of the liquid at the point where the bubble plume exits. It was found that the presence of the cylinder caused drastic reductions in the flow while the flat disc resulted in mixing times similar to those achieved with the aid of a strong swirling motion (see Section 4.3).

In 2003, Iguchi co-authored another article (22) on flow control. Here, the flow patterns were altered by submerging a circular disk on top of the rising bubble plume in a system containing a buoyant upper phase. It was concluded that the mixing time can be altered substantially by changing the vertical position of the plate. The results emerging from this study are shown in Figure 11.

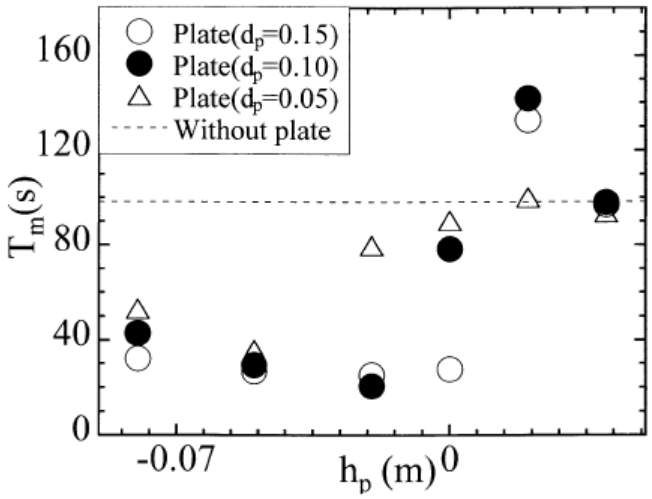

Figure 11: Variation in mixing times with different plate depths and sizes (22).

The difference in mixing times attained with the disk positioned above and below the simulated slag/metal interface $(h_p = 0)$ is certainly significant. The experiment was carried out in a system with a density ratio of close to 1 between the phases, thereby augmenting the retarding effect of slag entrainment. The improvement offered by this type of flow control in actual ladles will therefore not be as drastic.

4.2.5. Ladle Geometry

A. Ladle Shape

Mazumdar (27) investigated the influence of ladle bottom design on mixing time. It was concluded that the shape of the ladle bottom played only a minor role in determining the mixing time, and that a standard flat bottomed vessel still produced the best flow results.

The bottom regions of a gas stirred ladle usually contain low flow velocities and will not benefit greatly from flow pattern manipulation. Flow altering designs in the fast flowing upper regions of the vessel (as discussed in the previous section) have a much stronger potential for mixing time reduction.

B. Ladle Aspect Ratio

Many authors have acknowledged the influence of vessel dimensions on mixing efficiency. Most of the resulting correlations have already been provided in Section 4.1.1. The most prominent of these is repeated below (4).

$$\tau_{95\%} = 5.04 \frac{D^{7/3}}{Q_v^{1/3} H}$$ Equation 7

Equation 7 clearly shows that ladle height and diameter have a much stronger influence on the mixing time than gas flow rate. A high aspect ratio definitely seems to be beneficial, simply because the high velocity gas plume will take up a higher percentage of the vessel volume, thereby increasing the buoyant energy input (Equation 3).

It has been shown in Section 4.1.2, however, that taller vessels often result in dead zone formation, seriously compromising process performance. Vessel dimensions should therefore be chosen to facilitate the development of good circulatory flow patterns rather than high buoyant energy input.

C. Ladle Size

Larger vessels will always be beneficial to speed up the overall process, reduce the required number of heats, improve product consistency and minimize heat losses. It will certainly be beneficial to see if a fully developed circulatory flow pattern will hold if the entire system is simply scaled up.

4.3. Sloshing and Swirling

Under certain conditions, a self-sustaining sloshing or swirling motion can originate in a bath stirred with gas injection. The development of sloshing is normally avoided in existing ladles for fear of melt spillage and vessel vibration, but could lead to significant improvements in mixing efficiency if fully understood and handled correctly.

Several studies confirm that swirling does increase mixing (26; 28; 29; 30). The study completed by Iguchi *et al.* (28) states that mixing times in ladles with a swirling motion present are generally about one third of those obtained in the same vessel without swirling. This is certainly a noteworthy improvement, especially since the sloshing motion is self-sustaining, thus delivering an additional mixing mechanism at no extra buoyant energy input.

CHAPTER III:
MATHEMATICAL MODELLING THEORY

> *Programming today is a race between software engineers striving to build bigger and better idiot-proof programs, and the Universe trying to produce bigger and better idiots. So far, the Universe is winning.*
>
> ***Anonymous***

Computational fluid dynamics, or CFD for short, is the science of solving the set of governing equations numerically to predict the fluid flow, mass and heat transfer, chemical reactions, and other related phenomena. Applying the above mentioned quote to commercial CFD packages available today, it certainly is true that software engineers have made this once exclusive science of CFD available to some of the Universe's best works.

To understand the true essence of CFD engineering, consider the following anecdote: A consulting engineer was once called in to deal with the poor performance of a specific chemical plant. After spending a day or two mulling over P&ID's and wandering about the plant, he took a ladder and a piece of white chalk, climbed up to a certain valve and made a single cross above it. Sure enough, when the valve was fixed the plant returned to full capacity. A week later, the bill arrived for R1 million. The plant manager was a bit perplexed by this unreasonable price and asked for a breakdown of the costs involved. The consulting engineer replied with these famous words: "One chalk mark – R1. Knowing where to put it – R999,999."

Any institution can afford a CFD licence (especially the academic one) and a computer on which to run the package. Knowing which boxes to tick, however, is a completely different story. There are good reasons why CFD results are still perceived with a degree of distrust by the general engineering community. If it is handled irresponsibly or even worse, naively, the results obtained can be completely misleading. If these wrong results are then practically implemented, a whole range of catastrophes can arise.

The commercial CFD package, ANSYS FLUENT 6.3 (31), offers a multitude of numerical models, applicable to different flow situations. In order to make the correct choices, however, the theoretical implications behind every tic-box must be understood. Therefore, this chapter deals with science of 'tic-box selection' by taking an informed look at the mathematics happening behind the scenes.

1. MERIT OF THE CFD APPROACH

Two methods exist for the simulation of any process (32): Experimental investigation (physical modelling) and theoretical calculation (mathematical modelling). Experimental investigations are standard and have been performed for centuries, but are usually slow, expensive, tedious and quite often difficult (or even impossible) to perform. Theoretical calculations, on the other hand, alleviate

all of the difficulties and expenses required to build, operate and collect data from an experimental investigation.

In the realm of mathematical modelling, two forms exist (33): analytical and numerical. Analytical methods yield closed-form solutions which give complete information about the process at hand, while numerical methods yield discrete solutions at various points in space and time.

Obviously analytical solutions would be the preferred choice, but due to sheer complexity of these methods, analytical methods are not viable for most practical engineering applications. By using numerical methods, however, it is possible (in principle at least) to simulate any conceivable process. And, by increasing the number of solution points, the numerical solution can be made to be virtually identical to its analytical counterpart. CFD is a numerical method for solving flow phenomena and, if implemented correctly, can give highly accurate results to any possible flow problem.

Due to the high temperatures and opaque nature of any secondary steelmaking application, process simulation of gas stirred ladles by experimental investigation is extremely difficult if not impossible. Scaled-down physical modelling and mathematical modelling are therefore left as the only viable options.

Many cold model studies have been documented and, as a result of substantial research effort, they have grown to be quite sophisticated. A recent review by Mazumdar and Evans (5) on the subject of macro-modelling concluded the following: “Macroscopic models, despite being simplistic, have a sound basis and therefore can form a reasonably reliable predictive framework, particularly in the absence of any elaborate computer solutions, for first hand analysis of rate processes in gas stirred ladles.”

The facts are, however, that downscaled physical models (scaled both for size and process materials) will never form more than a reasonably reliable predictive framework. Therefore, the development of the ‘elaborate computer solutions’ alluded to by Mazumdar and Evans (5) are the only option for establishing sufficiently accurate correlations between the multitude of applicable process variables and mixing time. A commercial CFD package such as FLUENT 6.3 provides the tools with which to meet this challenge.

2. CFD AT A GLANCE

2.1. BASIC ELEMENTS

Any CFD code consists of three basic elements (34): the pre-processor, the solver and the postprocessor.

The pre-processor provides the means to define the specific system under investigation. FLUENT 6.3 uses the pre-processor GAMBIT 2.3 to construct and mesh the desired geometry. Boundary- and continuum types are also assigned in GAMBIT.

The geometry created in the pre-processor is then read into the solver (FLUENT) where the required models are selected and tuned to fit the current situation. The set of governing equations can now be solved to yield a converged set of discrete solutions throughout the flow domain.

These discrete solutions must now be presented in a conceivable manner by means of a postprocessor. The postprocessor provides the user interface for the interpretation of the solution, usually in the form of graphical displays.

2.2. Basic Method

The CFD process starts with a mathematical model comprising of the governing equations together with the appropriate boundary- and initial conditions (33). To enable a numerical solution, the governing equations are then discretized, expressing them as a set of algebraic equations. These equations are then used to calculate discrete values of the dependent variables (such as flow velocity, pressure, temperature and the like) at a specified set of independent variables (discrete points in space and time).

The locations of these discrete points in the space of the flow domain are specified by a numerical grid, or mesh, as defined in the pre-processor. For transient simulations a time step is specified to define the location of these points in time.

A solution method must then be applied to solve this set of algebraic equations. For nonlinear cases, which are the norm, an iterative solution method is necessary. A form of convergence criteria is then required to decide when to stop the simulation.

3. Governing Equations

Physical phenomena in a closed system are governed by three equations: the conservation of mass, momentum and energy. When more than one chemical species are present, the species conservation equation is solved as well.

3.1. Conservation of Mass

The mass conservation or continuity equation is given below (31):

$$\frac{\partial \rho}{\partial t} + \nabla \cdot (\rho \vec{v}) = S_m$$ Equation 8

The operator (∇) represents the partial derivative of a quantity with respect to all directions in the chosen coordinate system. In the current 3-D problem it would be in the *i, j* and *k* directions, i.e. $\left(\mathrm{i}\frac{\partial}{\partial x} + \mathrm{j}\frac{\partial}{\partial y} + \mathrm{k}\frac{\partial}{\partial z}\right)$. The left hand side of Equation 8 contains the transient term and the convection term, while the right hand side contains any mass source term that might be specified.

3.2. Conservation of Momentum

Equations for the conservation of momentum in all three Cartesian directions are given below (33):

$$\frac{\partial}{\partial t}(\rho u)+\nabla\cdot(\rho\vec{v}u)=-\frac{\partial p}{\partial x}+\nabla\cdot(\mu\nabla u)+S_u$$ Equation 9

$$\frac{\partial}{\partial t}(\rho v)+\nabla\cdot(\rho\vec{v}v)=-\frac{\partial p}{\partial y}+\nabla\cdot(\mu\nabla v)+S_v$$ Equation 10

$$\frac{\partial}{\partial t}(\rho w)+\nabla\cdot(\rho\vec{v}w)=-\frac{\partial p}{\partial z}+\nabla\cdot(\mu\nabla w)+S_w$$ Equation 11

In sequence from left to right, the terms in the above equations can be identified as the transient term, the convection term, the pressure source term, the diffusion term and the source term. Source terms play an especially important role in the present study, since the momentum sources from the discrete phase model provide the sole drive for mixing in the system (see Section 4.2.2).

FLUENT implements the momentum equation in the following form (31).

$$\frac{\partial}{\partial t}(\rho\vec{v})+\nabla\cdot(\rho\vec{v}\vec{v})=-\nabla p+\nabla\cdot(\bar{\bar{\tau}})+\rho g+\vec{F}$$ Equation 12

Together with the mass conservation equation (Equation 8) this set of equations are collectively known as the Navier-Stokes equations.

3.3. Conservation of Energy

The energy equation is solved in the following form (31):

$$\frac{\partial}{\partial t}(\rho E)+\nabla\cdot(\vec{v}(\rho E+p))=\nabla\cdot\left(k_{eff}\nabla T-\sum_j h_j\vec{J}_j+(\bar{\bar{\tau}}_{eff}\cdot\vec{v})\right)+S_E$$ Equation 13

Similarly to the momentum equation, the terms from left to right also represent the transient, convection, diffusion and source terms. The diffusion term (bracketed on the right hand side of Equation 13) represent energy diffusion by conduction, species transfer and viscous dissipation respectively. The energy term, E is described as follows:

$$E=h+\frac{p}{\rho}+\frac{v^2}{2}$$ Equation 14

3.4. Conservation of Species

When a mixture of different species is specified, FLUENT adapts the mass conservation equation for the mass fraction of each species (Y_i). For the *i*'th species (31):

$$\frac{\partial}{\partial t}(\rho Y_i) + \nabla \cdot (\rho \vec{v} Y_i) = -\nabla \cdot \vec{J}_i + R_i + S_i \qquad \text{Equation 15}$$

Equation 15 has two terms in addition to those contained in the conservation equation (Equation 8). These are the diffusive flux term ($\vec{J}_i$) and the reaction source term (R_i). As mentioned in Chapter II:3.2, no reacting species will be modelled. The species equation will only be used to track the spread of a tracer through the domain for determining the mixing time.

3.4.1. The Diffusive Flux

When the flow is turbulent, FLUENT 6.3 solves the diffusive flux ($\vec{J}_i$) in the following form:

$$\vec{J}_i = -\left(\rho D_{i,m} + \frac{\mu_t}{Sc_t} \right) \nabla Y_i \qquad \text{Equation 16}$$

Here, the first term in brackets represents molecular species diffusion and the second term represents turbulent diffusion. Turbulent diffusion is typically several orders of magnitude greater than laminar diffusion in turbulent flows.

The turbulent Schmidt number (Sc_t) represents the ratio of turbulent kinematic viscosity to turbulent diffusivity and is approximated by default as 0.7 in FLUENT 6.3. Since molecular diffusion is normally negligibly small the diffusive flux can be seen as being inversely proportional to the constant value specified for the turbulent Schmidt number. This very direct influence of the turbulent Schmidt number on the magnitude of the turbulent flux makes the specification thereof very important.

It has been shown, however, that the turbulent Schmidt number is not constant. Koeltzsch (35) reviewed a number of studies on the variability of the turbulent Schmidt number, quoting findings of Schmidt numbers anywhere between 0.4 and 0.9 depending on the flow situation. Ghosh (1), on the other hand, states that a turbulent Schmidt number of 1 is a good approximation in modelling the spread of a tracer through the melt. This approximation was also made by Joo and Guthrie (24).

For the moment, however, the default value of 0.7 falls on the average of the recommendations given in the literature and will be assumed accurate until proven otherwise.

3.4.2. Mathematical Modelling of Mixing Time

Mixing time is the most popular way in which mixing efficiency is quantified in the literature. Since bulk mixing is the limiting step in the performance of the process, as shown in Chapter II:3, mixing time is also the primary performance variable of the overall process. Even though the measurement of mixing time is standard practice in cold modelling experiments, only two mathematical modelling experiments could be located where mixing time was determined (10; 24).

Mathematical modelling does present the opportunity to ensure high accuracy in mixing time computations. In physical experiments, mixing time is highly dependent on the location and method of tracer addition as well as the location of tracer concentration measurement (6). It is often difficult to keep the tracer addition point constant with respect to the bubble plume, especially when more complex tuyere arrangements are considered. The location of minimum tracer concentration also varies depending on the flow situation in the vessel. Mathematical modelling presents the opportunity to monitor the minimum tracer concentration, regardless of its location in the vessel. Any human errors associated with tracer addition are also eliminated.

4. Additional Models

CFD simulation of a gas stirred ladle requires two additional physical models: a turbulence model to account for the basic turbulent nature of the process and a multiphase model to separate the different phases of metal, slag and gas.

4.1. Turbulence

When the Reynolds number becomes sufficiently large, flow instabilities become large enough to cause a flow field. These new vortices and other flow structures occur over a large range of length and time scales, are three dimensional, unsteady, and effectively stochastic even at the smallest scales (36).

Classification of turbulence modelling schemes generally depends on the number of turbulence structures that are resolved directly. Techniques exist where all, some or none of the turbulent eddies are resolved. As a general rule, accuracy is traded for computational time as less turbulent eddies are solved directly.

This gives rise to two main schools of approach in turbulence modelling: Reynolds-averaged formulations (no structures are resolved directly) and eddy-resolved formulations (some or all of the structures are resolved directly). Qualitatively, Figure 12 provides a clear view of the error involved in the Reynolds-averaged school of turbulence modelling. The stochastic nature of turbulence captured by eddy resolved formulations is certainly far removed from the smooth Reynolds-averaged boundary layer.

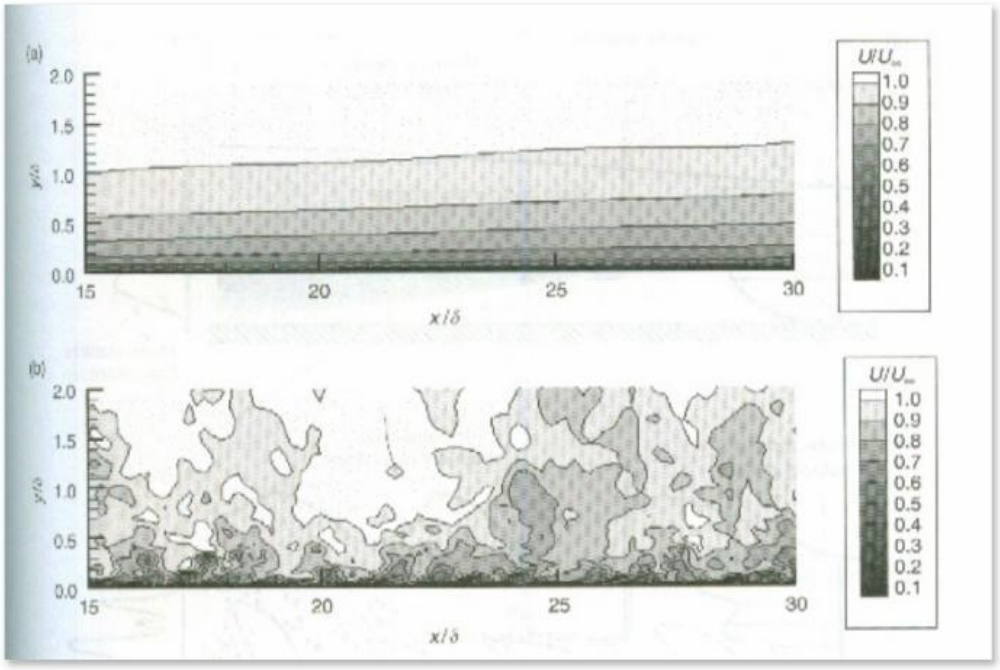

Figure 12: The difference between a turbulent boundary layer as simulated with a time averaged scheme (top) and a combined eddy-resolved/Reynolds-averaged scheme (bottom) (36).

The large length scales involved in practical engineering problems favour some form of averaging. Eddy-resolved formulations are not yet practical in large scale applications and, when determining bulk flow, they would offer very little improvement on their Reynolds-averaged counterparts. Accordingly, continuous development has given rise to a number of Reynolds-averaged formulations providing satisfactory predictions of turbulent effects in a wide variety of applications.

Despite the qualitative error, the difficulty in choosing the correct model and the complexity of these models, the choice of Reynolds-averaged over eddy-resolved formulations is well justified when looking at Figure 13.

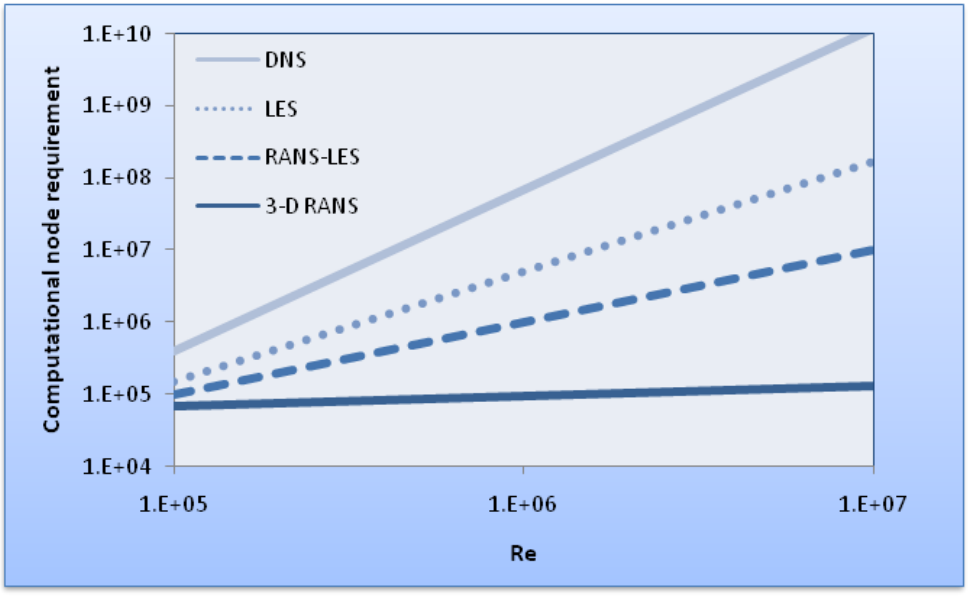

Figure 13: Approximation of the computational node requirements for different approaches to turbulence modelling (36).

Figure 13 displays the substantial differences in computational requirements between the RANS (Reynolds-Averaged Navier-Stokes) Reynolds-averaged approach and the DNS (Direct Numerical Simulation) eddy-resolved approach. For turbulent Reynolds numbers of 10^7 it can be seen that complete eddy-resolved methods are in the order of 10^5 times more computer resource intensive than their Reynolds-averaged counterparts.

There are a number of methods that offer a combination of Reynolds-averaged and eddy-resolved formulations (the LES and RANS-LES methods in Figure 13) for special situations where pure Reynolds-averaged formulations are not sufficient. In the current application, however, little can be gained by using the LES method and Reynolds-averaging will suffice.

4.1.1. Reynolds-Averaging

In Reynolds-averaged formulations, all the high-frequency unsteadiness which characterizes a turbulent process is averaged out. This averaging process gives rise to various terms that cannot be determined from first principles and must be modelled. It is through this modelling step that a wide variety of approaches have been adopted to cater for different flow situations – hence the wide range of turbulence models we have at our disposal today.

The principle behind Reynolds-averaging is to divide any flow variable (ϕ) into its mean and fluctuating components (33). For a statistically steady process:

$$\phi(x,y,z,t) = \bar{\phi}(x,y,z) + \phi'(x,y,z,t) \qquad \text{Equation 17}$$

where

$$\bar{\phi}(x,y,z) = \lim_{\Delta t \to \infty} \frac{1}{\Delta t} \int_0^{\Delta t} \phi(x,y,z,t)\,dt \qquad \text{Equation 18}$$

In statistically steady processes the flow variable statistics (such as the mean) do not vary over time and time-averaging (Equation 18) can be employed to obtain the mean value. When dealing with statistically unsteady processes (variable statistics vary over time), ensemble-averaging (Equation 19) has to be used:

$$\bar{\phi}(x,y,z,t) = \lim_{N \to \infty} \frac{1}{N} \int_0^{\Delta t} \phi(x,y,z,t)\,dt \qquad \text{Equation 19}$$

Here N represents the number of members of the ensemble (a set of flows in which all controllable variables are identical). N must be sufficiently large to eliminate the effects of the fluctuations.

The term Reynolds-averaging refers to both these averaging methods. Applying this analogy to the Navier-Stokes equations (Equation 8 to Equation 11) yields the well known RANS (Reynolds-Averaged Navier-Stokes) equations.

To attain the RANS equations, the standard velocities are substituted with values separated into a Reynolds-averaged part and a fluctuating component part. In the x-direction:

$$u = \bar{u} + u' \qquad \text{Equation 20}$$

Making this substitution into the Navier-Stokes equations yields the following (33):

$$\frac{\partial \rho}{\partial t} + \nabla \cdot \left(\rho \vec{\upsilon} \right) = S_m \qquad \text{Equation 21}$$

$$\frac{\partial}{\partial t}\left(\rho \bar{u}\right) + \nabla \cdot \left(\rho \vec{\upsilon} \bar{u} \right) = -\frac{\partial \bar{p}}{\partial x} + \nabla \cdot \left(\mu \nabla \bar{u} \right) + \bar{S}_u + \left(\frac{\partial}{\partial x}\left(-\rho \overline{u'u'} \right) + \frac{\partial}{\partial y}\left(-\rho \overline{u'v'} \right) + \frac{\partial}{\partial z}\left(-\rho \overline{u'w'} \right) \right) \qquad \text{Equation 22}$$

$$\frac{\partial}{\partial t}\left(\rho \bar{v}\right) + \nabla \cdot \left(\rho \vec{\upsilon} \bar{v} \right) = -\frac{\partial \bar{p}}{\partial y} + \nabla \cdot \left(\mu \nabla \bar{v} \right) + \bar{S}_v + \left(\frac{\partial}{\partial x}\left(-\rho \overline{v'u'} \right) + \frac{\partial}{\partial y}\left(-\rho \overline{v'v'} \right) + \frac{\partial}{\partial z}\left(-\rho \overline{v'w'} \right) \right) \qquad \text{Equation 23}$$

$$\frac{\partial}{\partial t}\left(\rho \bar{w}\right) + \nabla \cdot \left(\rho \vec{\upsilon} \bar{w} \right) = -\frac{\partial \bar{p}}{\partial z} + \nabla \cdot \left(\mu \nabla \bar{w} \right) + \bar{S}_w + \left(\frac{\partial}{\partial x}\left(-\rho \overline{w'u'} \right) + \frac{\partial}{\partial y}\left(-\rho \overline{w'v'} \right) + \frac{\partial}{\partial z}\left(-\rho \overline{w'w'} \right) \right) \qquad \text{Equation 24}$$

And for any other scalar quantity, ϕ:

$$\frac{\partial}{\partial t}\left(\rho \bar{\phi}\right) + \nabla \cdot \left(\rho \vec{\upsilon} \bar{\phi} \right) = \nabla \cdot \left(\Gamma^{\phi} \nabla \bar{\phi} \right) + \bar{S}_{\phi} + \left(\frac{\partial}{\partial x}\left(-\rho \overline{u'\phi'} \right) + \frac{\partial}{\partial y}\left(-\rho \overline{v'\phi'} \right) + \frac{\partial}{\partial z}\left(-\rho \overline{w'\phi'} \right) \right) \qquad \text{Equation 25}$$

This averaging process has now introduced some additional terms such as $-\rho\overline{u'v'}$ and $-\rho\overline{w'u'}$ which are known as Reynolds stresses, and $-\rho\overline{u'\phi'}$, known as a turbulent scalar flux. The introduction of these additional terms into the governing equations means that these equations are no longer 'closed' (i.e. they contain more variables than there are equations). Closure requires some additional equations to describe these Reynolds stress terms, and this is where the turbulence models come in.

4.1.2. Reynolds-Averaged Turbulence Models

The majority of turbulence models are based on the introduction of a so-called turbulent viscosity, μ_t. The underlying assumption is that the turbulence effects can be represented as an increased viscosity in the RANS equations. FLUENT employs the Boussinesq hypothesis (37) to relate the Reynolds stresses $(\bar{R}_{ij})$ to the mean velocity gradients using the turbulent viscosity.

$$\bar{R}_{ij} = -\rho\overline{u_i' u_j'} = \mu_t\left(\frac{\partial \bar{u}_i}{\partial x_j} + \frac{\partial \bar{u}_j}{\partial x_i}\right) - \frac{2}{3}\left(\mu_t \frac{\partial \bar{u}_k}{\partial x_k} + \rho k\right)\delta_{ij} \qquad \text{Equation 26}$$

Equation 26 indicates velocity and Cartesian directions as u and x with directional subscripts.

Turbulence models employing this approach are collectively known as eddy viscosity models. FLUENT offers three different schools of eddy viscosity models: the Spalart-Allmaras model, the k-ε models, and the k-ω models.

- The single equation Spalart-Allmaras model solves directly for a modified turbulent viscosity. It is very economical on computing power, but performs poorly in 3-D flows.
- k-ε models are the most commonly used eddy viscosity models. These models solve two separate partial differential equations for turbulence kinetic energy (k) and its dissipation rate (ε). A number of improvements have been made on the standard k-ε model to make it applicable over a wider array of problems. FLUENT offers three k-ε models, covering a wide range of flow applications.
- Lastly, the k-ω models incorporate modifications for low-Reynolds-number effects, compressibility, and shear flow spreading. They are very well applicable to wall bounded flows and free shear flows. FLUENT offers two models of the k-ω family.

Of these three, the k-ε model would be most suited to the current application, which is why the majority of published mathematical studies on gas stirred ladles employ some variant of the k-ε family. It was concluded in an extensive review (6), however, that the standard k-ε model fails to give a realistic account of turbulence phenomena in most gas stirred systems. This conclusion was drawn from various studies comparing physical turbulence measurements to calculated ones.

The major disadvantage of eddy viscosity models (such as the k-ε model) is that the turbulent viscosity is treated as an isotropic scalar quantity (its effects are similar in all directions), which is rarely true. This shortcoming is emphasized when modelling complex flows involving streamline curvature, swirl, rotation, and rapid changes in strain rate. Two studies in particular state that the turbulence inside the vessel indeed qualifies as anisotropic. Sheng and Irons (38) concluded that turbulence is greater in the axial direction inside the two phase plume, while Johanssen *et al*. (39) found the radial turbulence to be dominant near the free surface.

Ilegbusi *et al.* (21) also arrived at the conclusion that the k-ε model is inadequate as a result of the anisotropy of the system and recommends the use of an alternative RANS model: the Reynolds stress model (RSM). The RSM abandons the eddy viscosity hypothesis and closes the RANS equations

by solving separate transport equations for the Reynolds stresses in every direction, together with an equation for the dissipation rate. This approach allows the RSM to account for anisotropy in the Reynolds stresses, but is much more costly on computational resources. Where the k-ε models solves only two equations, the RSM solves seven when modelling 3D flows.

All the evidence does suggest, however, that this sacrifice in computational time is indeed necessary. Accordingly, a short review of the RSM is presented below.

4.1.3. The Reynolds Stress Model

The general model equation for the Reynolds stresses, $-\rho\overline{u_i u_j}$, is given below (31) – more to illustrate the sheer complexity of the model than to serve as a guide to complete comprehension.

$$\begin{aligned}\frac{\partial}{\partial t}\left(\rho\overline{u_i'u_j'}\right)+\frac{\partial}{\partial x_k}\left(\rho u_k\overline{u_i'u_j'}\right) &= -\frac{\partial}{\partial x_k}\left(\rho\overline{u_i'u_j'u_k'}+\overline{p\left(\delta_{kj}u_i'+\delta_{ik}u_j'\right)}\right)\\ &+\frac{\partial}{\partial x_k}\left(\mu\frac{\partial}{\partial x_k}\left(\overline{u_i'u_j'}\right)\right)-\rho\left(\overline{u_i'u_j'}\frac{\partial u_j}{\partial x_k}+\overline{u_i'u_j'}\frac{\partial u_i}{\partial x_k}\right)\\ &-\rho\beta\left(g_i\overline{u_j'\theta}+g_j\overline{u_i'\theta}\right)+\overline{p\left(\frac{\partial u_i'}{\partial x_j}+\frac{\partial u_j'}{\partial x_i}\right)}-2\mu\overline{\frac{\partial u_i'}{\partial x_k}\frac{\partial u_j'}{\partial x_k}}\\ &-2\rho\Omega_k\left(\overline{u_j'u_m'}\varepsilon_{ikm}+\overline{u_i'u_m'}\varepsilon_{jkm}\right)+S\end{aligned}$$

Equation 27

From left to right the terms represent: the local time derivative, convection, turbulent diffusion, molecular diffusion, stress production, buoyancy production, pressure strain, dissipation, production by system rotation and a user defined source term. It can plainly be seen that the Reynolds stresses are handled in a much more complex way by the RSM than the various eddy viscosity models using the Boussinesq hypothesis (Equation 26).

Out of these terms, the turbulent diffusion, buoyancy production, pressure strain and dissipation all require further modelling in order to close the equations. Some of these terms are extremely difficult to model and require various assumptions often considered to compromise the fidelity of the RSM.

Failures by the RSM are not readily recorded in formal literature, but it is known from experience and informal academic discussion that the RSM sometimes results in completely unrealistic solutions. It is said that the necessity for the RSM to have additional models within the model itself makes it lose much of its generality, i.e. it may only be applicable to a very limited range of modelling setups. For this reason, the k-ε family will also be presented as a tried and tested alternative for turbulence modelling.

4.1.4. THE k-ε FAMILY

Models in the k-ε family solve only two transport equations: the turbulence kinetic energy (k) and its dissipation rate (ε). The model transport equation for turbulence kinetic energy is mathematically derived, but the equation for ε is obtained in an empirical fashion from physical reasoning.

In addition to the assumption of isotropic turbulence, the k-ε approach adds two more assumptions: The flow is fully turbulent and the effects of molecular viscosity are negligible (31).

A. THE STANDARD k-ε MODEL

The SKE model is the most robust and widely used in industrial applications since it was first proposed by Launder and Spalding (40). It is easy to converge, light on computational resources and reasonably accurate over a wide array of larger scale flow applications.

The transport equations solved for k and ε are given below, indicating velocity and Cartesian directions as u and x with directional subscripts:

$$\frac{\partial}{\partial t}(\rho k)+\frac{\partial}{\partial x_i}(\rho k u_i)=\frac{\partial}{\partial x_j}\left[\left(\mu+\frac{\mu_t}{\sigma_k}\right)\frac{\partial k}{\partial x_j}\right]+G_k+G_b-\rho\varepsilon-Y_M+S_k \qquad \text{Equation 28}$$

$$\frac{\partial}{\partial t}(\rho \varepsilon)+\frac{\partial}{\partial x_i}(\rho \varepsilon u_i)=\frac{\partial}{\partial x_j}\left[\left(\mu+\frac{\mu_t}{\sigma_\varepsilon}\right)\frac{\partial \varepsilon}{\partial x_j}\right]+ C_{1\varepsilon}\frac{\varepsilon}{k}\left(G_k+C_{3\varepsilon}G_b\right)-\rho C_{2\varepsilon}\frac{\varepsilon^2}{k}+S_\varepsilon \qquad \text{Equation 29}$$

Turbulence generation due to buoyancy (G_b) is only included when gravity and a temperature gradient is present simultaneously. G_k represents the generation of turbulence kinetic energy due to mean velocity gradients and is calculated as follows:

$$G_k=-\rho\overline{u'_i\,u'_j}\frac{\partial u_j}{\partial x_i} \qquad \text{Equation 30}$$

The turbulent viscosity can now be calculated for use in the Boussinesq hypothesis (Equation 26).

$$\mu_t=\rho C_\mu\frac{k^2}{\varepsilon} \qquad \text{Equation 31}$$

Model constants were derived from water-air experiments and are accepted as standard over a wide range of wall bounded and free shear flows (40).

$$C_{1\varepsilon} = 1.44,\ C_{1\varepsilon} = 1.92,\ C_{\mu} = 0.09,\ \sigma_k = 1.0,\ \sigma_{\varepsilon} = 1.3$$

B. RNG k-ε MODEL

The RNG k-ε model is based on a statistical technique called renormalization group theory proposed by Yakhot and Orszag (41). The statistical derivation was made from the instantaneous, rather than the Reynolds averaged, Navier-Stokes equations.

The transport equation solved for k is identical that of the SKE model, but the ε equation includes an additional term (R_{ε}) offering significant improvements when modelling highly strained flows.

$$\frac{\partial}{\partial t}(\rho\varepsilon) + \frac{\partial}{\partial x_i}(\rho\varepsilon u_i) = \frac{\partial}{\partial x_j}\left[\left(\mu + \frac{\mu_t}{\sigma_{\varepsilon}}\right)\frac{\partial \varepsilon}{\partial x_j}\right] + C_{1\varepsilon}\frac{\varepsilon}{k}\left(G_k + C_{3\varepsilon}G_b\right) - \rho C_{2\varepsilon}\frac{\varepsilon^2}{k} - R_{\varepsilon} + S_{\varepsilon}$$

Equation 32

Another improvement over the SKE model is the option of swirl modification. When significant rotation or swirl is present in the system, the RNG k-ε model can modify the turbulent viscosity appropriately. This modification is reflected in a function involving two swirl terms as shown below:

$$\mu_t = \mu_{t0}\, f\left(\alpha_s, \Omega, \frac{k}{\varepsilon}\right)$$

Equation 33

The default model constants are as follows (31):

$$C_{1\varepsilon} = 1.42,\ C_{1\varepsilon} = 1.68$$

C. REALIZABLE k-ε MODEL

The RKE model is a relatively recent development by Shih *et al.* (42) and offers improvements in flows involving rotation, boundary layers under strong adverse pressure gradients, separation, and recirculation (31). It is also differs from other k-ε models by the manner in which ε is modelled.

$$\frac{\partial}{\partial t}(\rho\varepsilon) + \frac{\partial}{\partial x_i}(\rho\varepsilon u_i) = \frac{\partial}{\partial x_j}\left[\left(\mu + \frac{\mu_t}{\sigma_{\varepsilon}}\right)\frac{\partial k}{\partial x_j}\right] + \rho C_1 S\varepsilon - \rho C_2\frac{\varepsilon^2}{k + \sqrt{\nu\varepsilon}} + C_{1\varepsilon}\frac{\varepsilon}{k}C_{3\varepsilon}G_b + S_{\varepsilon}$$

Equation 34

The primary improvement offered by Equation 34 is that the production term (second term on the right) does not include the production of k (Equation 30). It is believed that this modification results in improved modelling of the overall energy transfer.

Another distinctive feature of the RKE model is that the C_μ term (used in Equation 31) is no longer constant, but a function of the mean strain rate and the turbulence fields (k and ε). It is this feature that makes the model 'realizable' by adhering to certain mathematical constraints on the Reynolds stresses.

The default model constants are (31):

$$C_{1\varepsilon} = 1.44,\ C_{1\varepsilon} = 1.9,\ \sigma_k = 1.0,\ \sigma_\varepsilon = 1.2$$

4.1.5. Near Wall Regions

Turbulent flows are significantly affected by the presence of walls. Accordingly, the shear stress at the walls and possible flow altering obstructions inside a gas stirred ladle has a significant influence on the turbulent flow patterns inside, and must be accounted for.

When the flow is laminar, the near wall region consists of a uniform boundary layer and the shear is dependent only on the velocity gradient at the wall. In turbulent flows, however, the near wall region can be subdivided into three dominant regions, each with unique characteristics (31). Figure 14 illustrates these divisions.

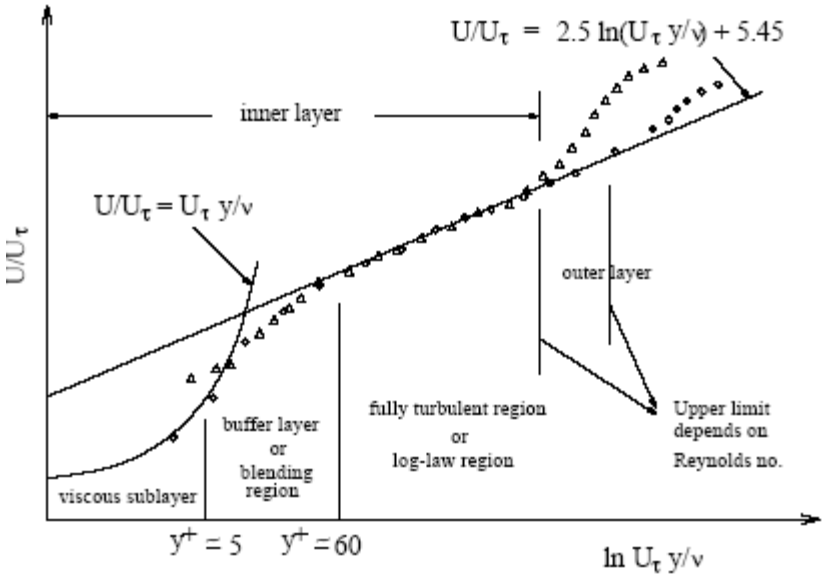

Figure 14: Boundary layer regions in the near wall turbulent flows (31).

The innermost layer is called the viscous sub-layer and is almost laminar. Here the molecular viscosity plays a major role in the momentum transfer. In the outer, fully turbulent layer, turbulence (modelled as turbulent viscosity) is the major role player. The area between these two layers,

however, displays characteristics of both the viscous sub-layer and the fully turbulent layer. Here the effects of viscosity and turbulence are equally important.

FLUENT provides two options for near wall modelling: wall functions and modified turbulence models. Turbulence models such as the k-ε group, RSM and LES are primarily valid for core flows (i.e. flows far from walls) and therefore require additional wall functions to make them suitable to wall bounded flows. The Spalart-Allmaras and k-ω turbulence models were designed specifically to be applied throughout the boundary layer and require no additional wall functions.

In the current application, however, the wall function method is the preferred choice for two reasons:

- For high Reynolds numbers, the wall function method is recommended. This method can be implemented on a relatively course near wall mesh, in contrast to the fine boundary layer mesh required by the modified turbulence models.
- Wall functions are economical, robust, and reasonably accurate. In the current application little can be gained from resolving the viscous sub-layer using modified turbulence models. The large volume to surface area ratio of the modelled geometry makes the choice of core turbulence model much more important.

A. Wall functions

Wall functions are semi-empirical formulas that link the flow variables in near-wall cells to their corresponding quantities at the wall. Two variations are possible: standard wall functions and non-equilibrium wall functions.

Standard wall functions are the default and most widely used option. Non-equilibrium wall functions, however, are recommended for use in complex flows involving separation, reattachment, and impingement where the mean flow and turbulence are subjected to severe pressure gradients and change rapidly. This is not the case in the current application and standard wall functions can be used with good accuracy.

The wall functions comprise of two parts: Laws-of-the-wall for mean velocity close to the wall and some additional formulas for near-wall turbulent quantities.

The law-of-the-wall for velocity is given below (31):

$$U^* = \frac{1}{\kappa}\ln\left(C_{emp}y^*\right)$$ Equation 35

where

$$U^* = \frac{U_p C_\mu^{1/4} k_p^{1/2}}{\tau_w / \rho}$$ Equation 36

and

$$y^* = \frac{\rho C_\mu^{1/4} k_p^{1/2} y_p}{\mu}$$ Equation 37

These equations apply to a point, *P*, a certain distance from the wall. The subscript *p* indicates quantities at that point.

The turbulence kinetic energy is calculated with Equation 28 throughout the domain. The production of turbulence kinetic energy (G_k) and its dissipation rate (ε), however, are calculated from the local equilibrium hypothesis which assumes G_k and ε to be equal in the wall-adjacent cells.

The production of turbulence kinetic energy is calculated according to Equation 38:

$$G_k = \tau_\omega \frac{\tau_\omega}{\kappa \rho C_\mu^{1/4} k_P^{1/2} y_P}$$ Equation 38

The turbulence dissipation rate at point *P* is computed from Equation 39:

$$\varepsilon = \frac{C_\mu^{3/4} k_P^{3/2}}{\kappa y_P}$$ Equation 39

The normal equation for ε is not used in the wall-adjacent cells. Instead, Equation 39 is used to calculate the turbulence kinetic energy dissipation rate.

4.2. MULTIPHASE

Multiphase flow problems can be classified as either dense or disperse depending on the concentration of the dispersed phase in the continuous phase. This classification determines the coupling mechanism to be employed between the phases. For highly dispersed flows one way coupling, where the continuous phase influences the motion of the dispersed phase and not vice versa, is sufficient. When the dispersed phase becomes denser though, its influence on the flow of the continuous phase cannot be ignored and two way coupling has to be employed.

An additional distinction is made when looking at the numerical treatment of the dispersed phase: the Eulerian-Eulerian (Eulerian for short) and the Eulerian-Lagrangian (normally just called Lagrangian) approach. In the Eulerian reference frame, the different phases are treated as interpenetrating continua (31), implying that characteristics of the dispersed phase (e.g. velocity or temperature) can be described as a continuum. This approach allows the dispersed phase to be treated with the same discretization and numerical techniques as the continuous phase, automatically ensuring two way coupling.

The Lagrangian approach, on the other hand, treats the dispersed phase as a set of discrete particles and is quite fittingly known as the discrete method in some circles. Each one of these discrete particles is represented as an individual identity, freely moving through the continuum and carrying

all relevant information with it. In comparison, the Eulerian approach would pass this information from cell to cell as the dispersed phase moves along.

4.2.1. Multiphase Modelling in Gas Stirred Ladles

The literature is divided into three schools of modelling flows in the gas stirred ladle: quasi-single phase, Lagrangian and Eulerian. In terms computational time, these are arranged from least costly to most costly, but each decrease in computational power comes at the cost of some simplifying assumption, slightly undermining the accuracy of the solution. Accordingly, the choice of multiphase model involves another balancing act between computational time and accuracy.

A. Quasi-Single Phase

In the nineties, computing power was limited and the quasi-single phase model was developed for simulating fluid flow in gas stirred ladles (24; 43; 44; 45). This model requires no multiphase modelling and simulates gas bubbles by specifying the shape, size and strength of the plume *a priori*. A schematic diagram is shown in Figure 15.

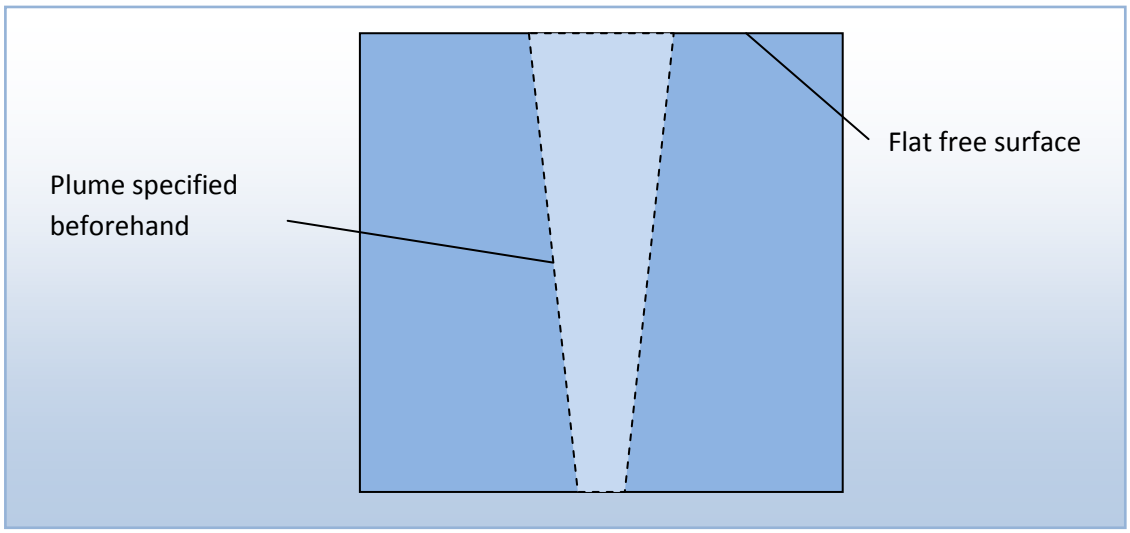

Figure 15: Simple diagram of the quasi-single phase calculation procedure.

The quasi-single phase method requires numerous parameters to be specified beforehand which can result in significant error. Of these, the plume shape, bubble slip velocity and void fraction are the most prominent (6). In reality, the plume shape is quite dynamic and rarely resembles the perfect cone used in the model, especially in systems employing eccentric stirring. The plume also contains significant spatial void fraction variation. Additionally, a flat and frictionless free surface is employed, completely neglecting plume eye formation and natural wavelike motion on the surface.

B. Lagrangian

The Lagrangian method presents a more fundamentally correct alternative (10; 46; 47). In the Lagrangian reference frame, the bubbles are simulated as discrete particles, each subject to a force balance as shown in Figure 16. Momentum, mass and energy can be exchanged between the particles and the continuum.

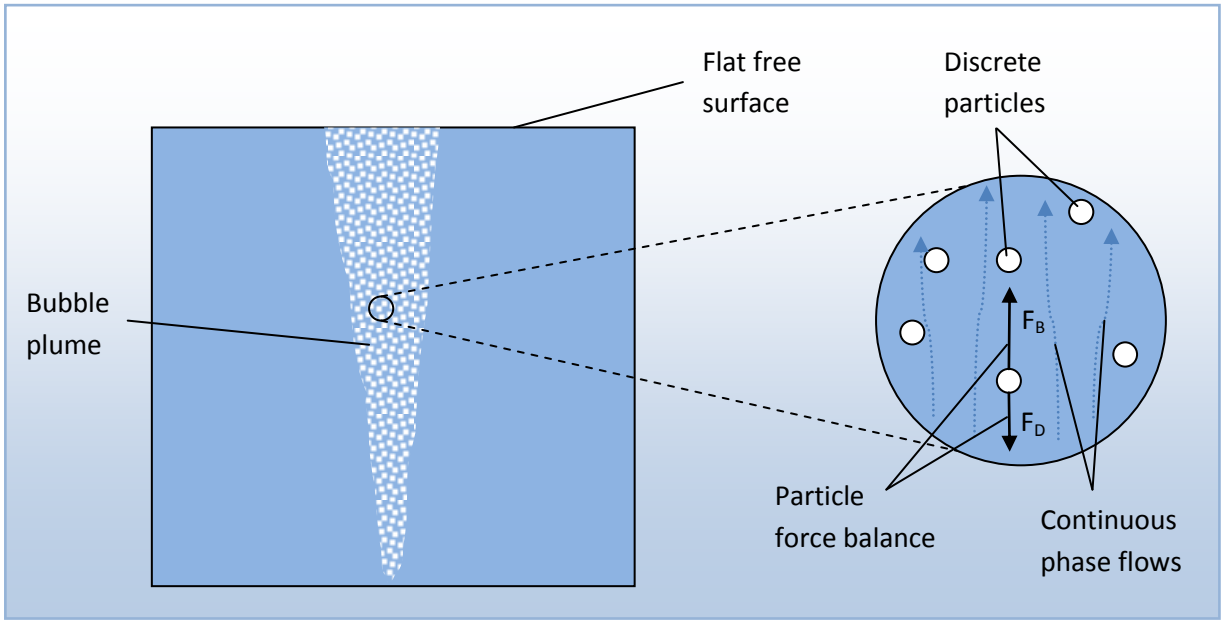

Figure 16: Simple diagram of the Lagrangian calculation procedure.

Although the plume is now represented much more realistically, a large number of models and approximations are necessary to ensure sufficient accuracy. A drag law for the spherical capped bubbles, a turbulent dispersion model, a particle growth and breakup algorithm and a pre-defined size distribution are required. In addition, the surface is once again assumed to be flat and frictionless.

C. Eulerian

In this approach the governing equations are solved separately for each phase and the interfaces between phases are tracked exactly (Figure 17). In its purest sense, the Eulerian approach requires no additional models, approaching every aspect of multiphase flow from fundamental principles.

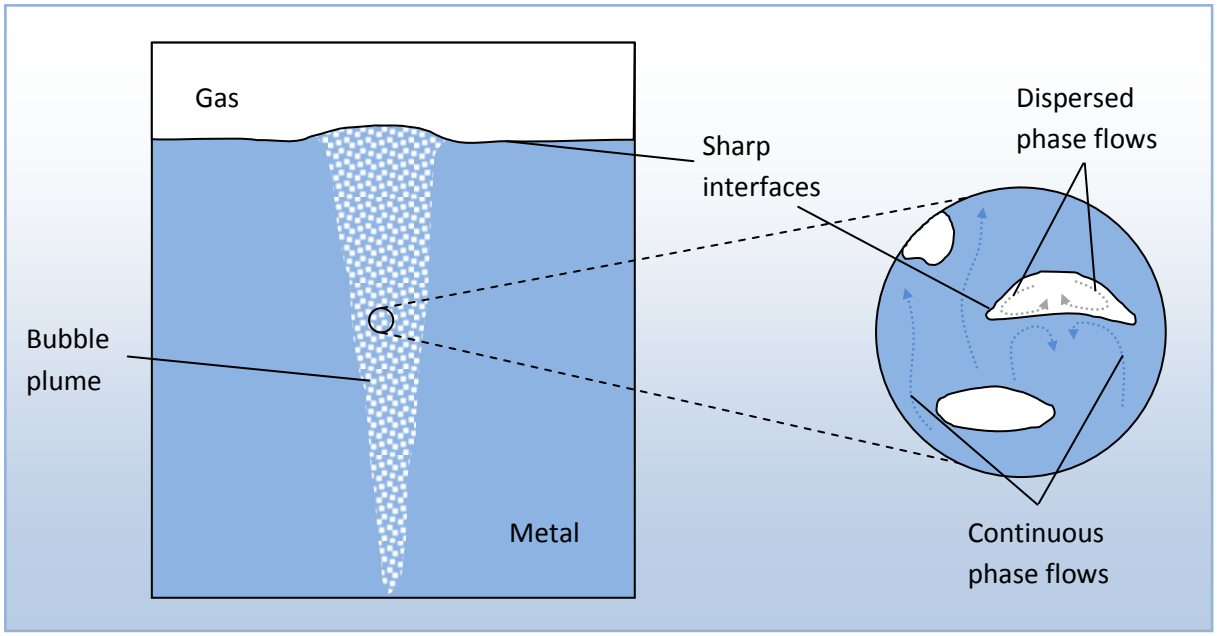

Figure 17: Simple diagram of the Eulerian calculation procedure.

The grid resolution required for accurate modelling of a full sized three dimensional gas stirred vessel renders this approach impractical, however. Modified, volume-averaged Eulerian multiphase models allowing for coarser grid resolutions are available and have been used in the modelling of gas stirred ladles (48; 49; 50). These averaged approaches require additional models governing inter-phase transport properties. Interface tracking, which is essential for a true representation of the free surface, is also compromised by the averaging procedure.

D. A Suitable Combination

The challenge now exists to compile a suitable model with which to simulate a full-sized 3D gas-stirred vessel with a realistically represented plume region and a well defined free surface. A specialized interface tracking version of the Eulerian model can provide the free surface, but is far too computationally expensive when tracking the surface and internal flows of every single bubble rising through the melt. The Lagrangian method can model the rising bubbles very economically and very accurately (51), but cannot provide the free surface.

The logical next step is the development of an Eulerian-Lagrangian combination. The Eulerian method can simulate the large free surface while the Lagrangian particle tracking deals with the rising bubbles. This approach has been used in the simulation of an oil-water model of a gas stirred ladle (52) although it was only applied to track the interface between metal and slag leaving the top gas interface flat and immobile. This approach is shown in Figure 18.

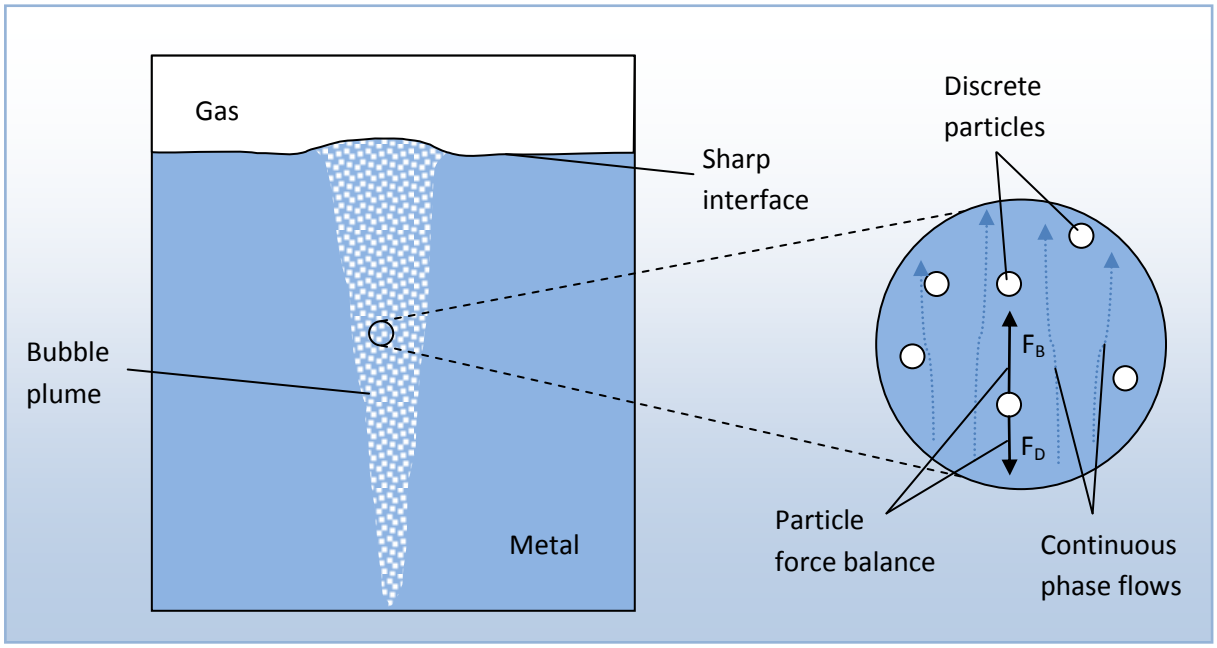

Figure 18: Simple diagram of the combined Eulerian-Lagrangian approach.

In FLUENT the Eulerian method is best represented by the volume of fluid (VOF) model. This is one of several Eulerian models available and is especially formulated to accurately track any interface between two or more immiscible phases. FLUENT presents the Lagrangian approach as the discrete phase model (DPM). These two multiphase models will now be discussed in more detail.

4.2.2. Lagrangian Approach

Lagrangian methods are further subdivided into point-force and resolved-surface treatments (36). The resolved surface method handles the particle-fluid interaction from first principles, i.e. the flow solution is numerically integrated around the particle surface to obtain the net momentum interaction of the fluid on the particle and vice versa. This allows for complex particle shapes, particle rotation and a solution without any additional empirical models, but for practical application with a great many of these particles the resolved surface approach would not be practical.

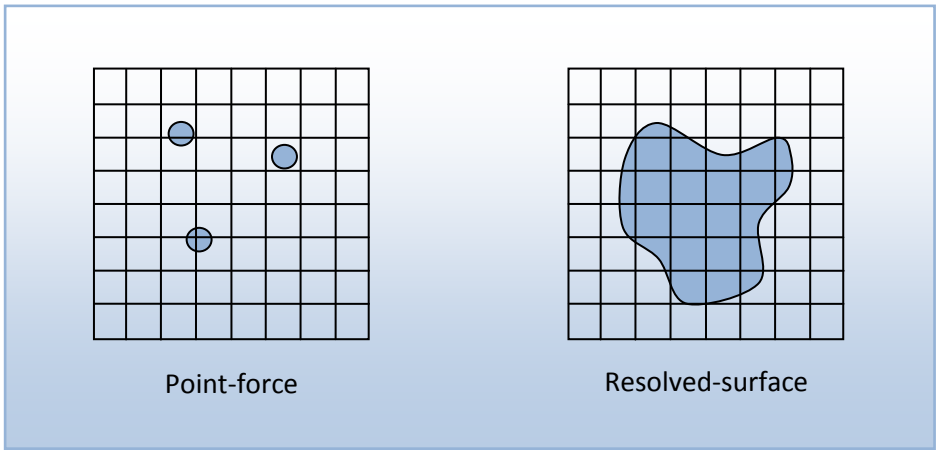

Figure 19: A comparison between the point-force and resolved-surface Lagrangian methods.

A more realistic approach to the current problem lies with the point-force approach. Particles are described as point sources occupying no volume in the continuum. Hence the surface of such a particle has no effect on the flow of the continuous phase and a separate specification of the force balance is required to describe the motion of the particle and its effect on the continuous phase. These additional models allow the particle trajectory to be calculated with ordinary differential equations, as opposed to the PDEs required by other multiphase approaches, resulting in a highly computationally efficient process.

FLUENT'S discrete phase model (DPM) utilises the point-force Lagrangian approach and is well suited to the current application.

A. The Discrete Phase Model

FLUENT'S discrete phase model injects a stream of particles into the continuous phase and then tracks them through the domain. Using two-way coupling, the buoyant potential energy contained in the gas bubbles (simulated as discrete particles) can be transferred to the continuous phase as a momentum source term.

Because the discrete phase particles occupy no volume, the model is limited in terms of the dispersed phase volume fraction that can be accounted for. A value of 10-12% is recommended as the maximum dispersed phase volume fraction will provide a reliable simulation of actual multiphase flows (31).

i. Steady or Unsteady Formulation

The first distinction to be made when DPM particle tracking is employed is between the formulations of steady and unsteady particle tracking. The choice between these formulations is not limited by the solver specification, i.e. unsteady particle tracking can be used in a steady state model and steady particle tracking can be employed in a transient simulation.

The steady state formulation, true to its name, tracks particle streams spatially only, independent of time. With every DPM iteration, these particle streams are tracked from the DPM inlet to a certain termination condition. In FLUENT 6.3 this condition can either be impact with a boundary specified to let the particles escape or the exhaustion of the permitted number of steps. The particle stream length is always limited to a certain number of steps so as to prevent particle streams being tracked infinitely through recirculating flow zones.

The strength of each particle stream (the number of particles flowing along it per second) is calculated according to the specified mass flow rate, particle density and diameter and the number of streams. A sample output of steady particle streams is presented below:

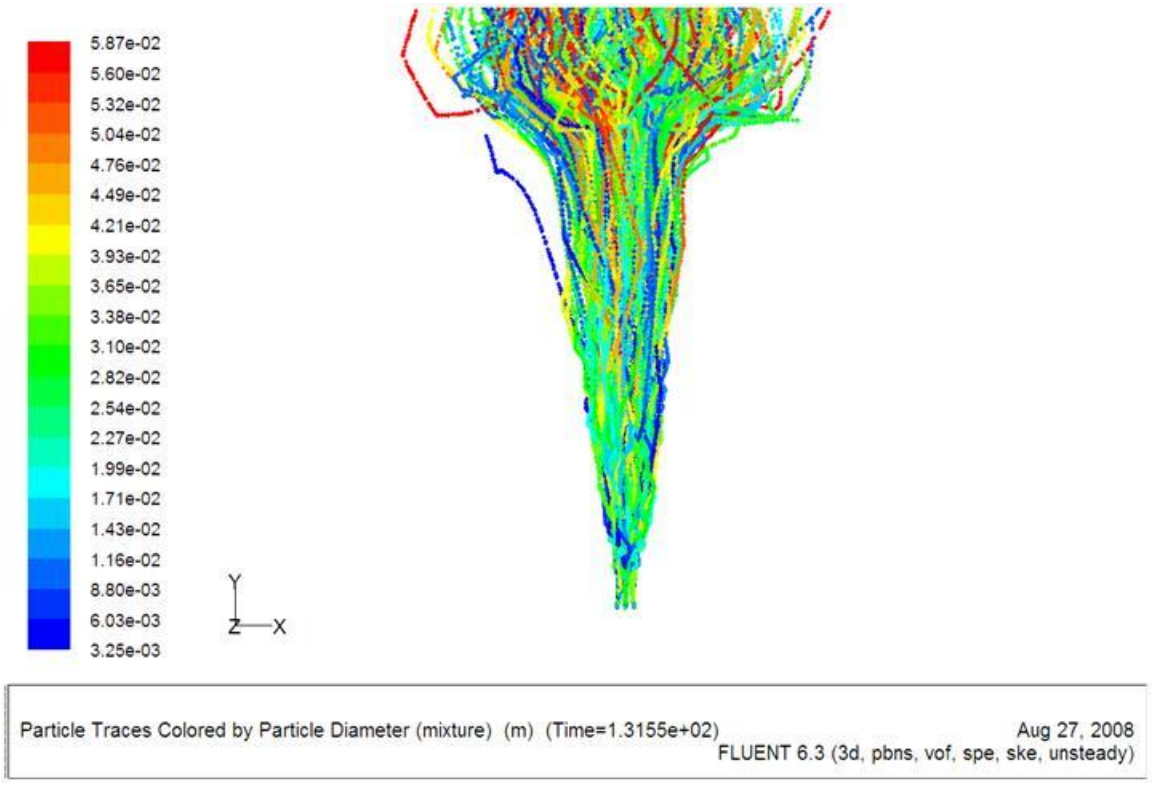

Figure 20: Particles streams as tracked with the steady DPM formulation.

When unsteady particle tracking is required, particles are tracked through space and time. This requires the particles to be treated as separate entities to be translated a certain distance at every time step. FLUENT 6.3 accomplishes this by tracking parcels of particles through the domain, updating their positions every time step according to the time step size and local flow conditions.

The number of parcels can be controlled directly by setting the amount of DPM sources and the time between injections. The number of particles in each parcel is then calculated according to the

specified mass flow rate and particle diameter. A sample output of parcels tracked in an unsteady fashion is presented below:

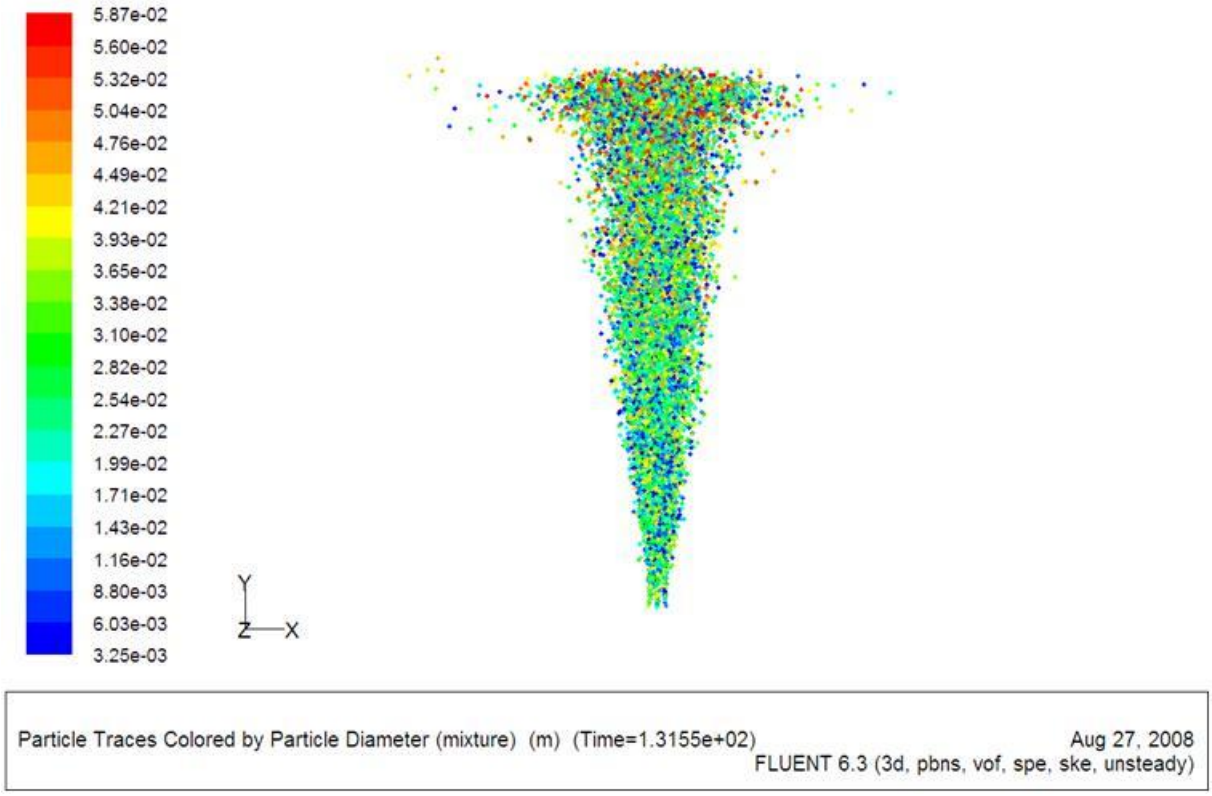

Figure 21: Particles parcels as tracked with the unsteady DPM formulation.

The steady state formulation is computationally more efficient because the number of particle streams required for accurate flow simulation is much lower than the required amount of unsteady particle parcels. When the intermediate transient behaviour is important, however, use of the unsteady particle tracking formulation is mandatory for accurate flow representations.

ii. Particle Equations of motion

The trajectory of every individual particle (stream or parcel) is calculated by integrating a force balance over it. This force balance equates the particle inertia to the forces acting on it and can be written as follows (for the x direction) (31):

$$\frac{du_p}{dt} = F_D\left(u - u_p\right) + \frac{g_x\left(\rho_p - \rho\right)}{\rho_p} + F_x \qquad \text{Equation 40}$$

From right to left, the terms represent an additional acceleration (force/unit particle mass) term, the contribution of gravity (the forces of weight and buoyancy) and the effects of drag on the particle motion. The drag force term (F_D) is calculated from the drag coefficient (C_D) which, in turn, is a function of particle shape.

The largest portion of bubbles rising through a general gas stirred system normally assumes a spherical capped shape with a constant drag coefficient of $8/3$ (53). It is well known, however, that the size of the bubble plays the dominant role in determining its shape, and bubble sizes vary quite significantly in the general gas stirred system. To this end, Xia *et al.* (50) adapted an earlier equation by Harmathy (54) to account for 'distorted bubbles' of different shapes.

$$C_D = \frac{2}{3}\left(\frac{E_0}{3}\right)^{0.5}$$ Equation 41

The Eotvos number (E_0) characterises the shape of the bubble and is expressed as follows:

$$E_0 = \frac{g\ \ \rho_l - \rho_g\ \ d_B^2}{\sigma}$$ Equation 42

The variables of density difference and surface tension can be assumed constant for most systems, but the bubble size is an important variable and is shown to have a second order influence on the bubble shape.

iii. Turbulent Dispersion of Particles

Turbulence plays a major role in the current application and the correct prediction of turbulent dispersion of discrete phase particles is essential to ensure an accurate representation of the plume. FLUENT achieves this by using stochastic tracking (random walk) models (31).

Without stochastic tracking enabled, FLUENT will predict particle trajectories using the mean fluid velocity $(\bar{u})$ in Equation 40. By enabling stochastic tracking, however, these calculations are carried out using the instantaneous velocities of the turbulent flow:

$$u = \bar{u} + u'$$ Equation 43

The discrete random walk model must now be employed to calculate the velocity fluctuation term, u'. The velocity fluctuation that prevails during the lifetime of the eddy is calculated by assuming that a Gaussian probability distribution is followed:

$$u' = \zeta\sqrt{\overline{u'^2}}$$ Equation 44

Here, ζ is a normally distributed random number, while the remainder of the right hand side represents the root mean square (RMS) value of the local velocity fluctuations. When using eddy viscosity turbulence models (under the assumption of isotropy) this RMS value can be presented in terms of the known calculated value of turbulence kinetic energy:

$$\sqrt{\overline{u'^2}} = \sqrt{2k/3}$$ Equation 45

The Reynolds stress model does not employ the assumption of isotropy and models each of the Reynolds stresses separately in Equation 27. Thus:

$$u' = \zeta\sqrt{\overline{u'^2}}$$
$$v' = \zeta\sqrt{\overline{v'^2}}$$
$$w' = \zeta\sqrt{\overline{w'^2}}$$ Equation 46

Once the instantaneous velocity is known, a measure is required for the time spent by the particle within the turbulent eddy. This is accomplished by using an integral time scale. For small tracer particles used in the DPM, the integral time becomes known as the Lagrangian integral time and can be approximated by Equation 47 for the k-ε models and Equation 48 when the RSM is used.

$$T_L = 0.15\frac{k}{\varepsilon}$$ Equation 47

$$T_L = 0.3\frac{k}{\varepsilon}$$ Equation 48

This time scale constant (estimated as 0.15 in Equation 47) has a significant impact on the spread of particles and finally on the bulk flow solution and is conceded as being 'not well known' (31). Accordingly, this constant might require some tailoring to fit the current application.

The characteristic eddy lifetime is determined directly from the Lagrangian integral time (Equation 47),

$$\tau_e = 2T_L$$ Equation 49

while the particle-eddy crossing time is defined as follows:

$$t_{cross} = -\tau\ln\left[1-\left(\frac{L_e}{\tau|u-u_p|}\right)\right]$$ Equation 50

The interaction between the particle and the fluid phase eddy is now assumed to last for the smaller of the eddy lifetime and the particle-eddy crossing time, after which a new value of the instantaneous fluid velocity is obtained by applying a new value of ζ in Equation 46.

4.2.3. Eulerian Approach

Eulerian methods can be further subdivided into mixed-fluid and separated-fluid formulations (36). The mixed-fluid approach assumes the continuous and dispersed phases to be in kinetic and thermal equilibrium, implying that velocity and temperature differences between phases are negligible compared to variations in the overall flow field.

The mixed-fluid approach does have some significant advantages though. It allows the use of a single set of momentum conservation equations for the entire mixture (as opposed to separate sets for each phase) making it numerically much simpler and easily applicable over a wide range of multiphase problems. FLUENT's mixture model employs a special slip velocity option to account for multiphase flow applications where the difference in velocity between the dispersed and continuous phases is significant (such as the current application). Unfortunately, the mixture model cannot accurately track the free surfaces featured in the current application.

The volume of fluid (VOF) model also shares a single set of governing equations between phases, but its treatment of the interface is distinctly different from that of the mixture model. The emphasis of the VOF model falls on tracking the interface between phases exactly. This feature makes it the ideal choice for tracking the large metal/slag/gas interfaces.

On a much smaller scale, the VOF model can also be used to simulate the behaviour of a single bubble to further understanding of bubble behaviour inside the melt. For bubble plume tracking in engineering scale simulations, however, the VOF model will be impractically expensive on computational resources.

A. The VOF Model

The position of the surface between two immiscible fluids is the primary focus of the VOF model. Volume fractions of the different phases are tracked throughout the domain and a continuous interface is created in cells containing more than one phase. FLUENT's VOF model is recommended especially for the motion of large bubbles in a liquid and free surface flows (31) and will be employed as such.

i. The Volume Fraction Equation

FLUENT tracks the interface between phases by solving a continuity equation for a single phase *q*:

$$\frac{\partial}{\partial t}\left(\alpha_q \rho_q\right) + \nabla\left(\alpha_q \rho_q \vec{v}_q\right) = S_{\alpha_q} + \sum_{P=1}^{n}\left(m_{pq} - m_{qp}\right) \qquad \text{Equation 51}$$

Equation 51 differs from the general continuity equation (Equation 8) only by a volume fraction term $\left(\alpha_q\right)$ and a term for mass transfer between phases (rightmost term).

Equation 51 will only be solved for the secondary phases, with the primary phase volume fraction adhering to the simple constraint:

$$\sum_{q=1}^{n} \alpha_q = 1$$ Equation 52

When a cell contains more than one phase, an interface must be interpolated through it to separate the different phases. Numerous interface interpolation schemes are available in FLUENT, but the geometric reconstruct theme is known to be the most accurate and best suited to time dependent solutions.

The geometric reconstruction scheme represents the interface between the two phases using a piecewise linear approach as illustrated in Figure 22:

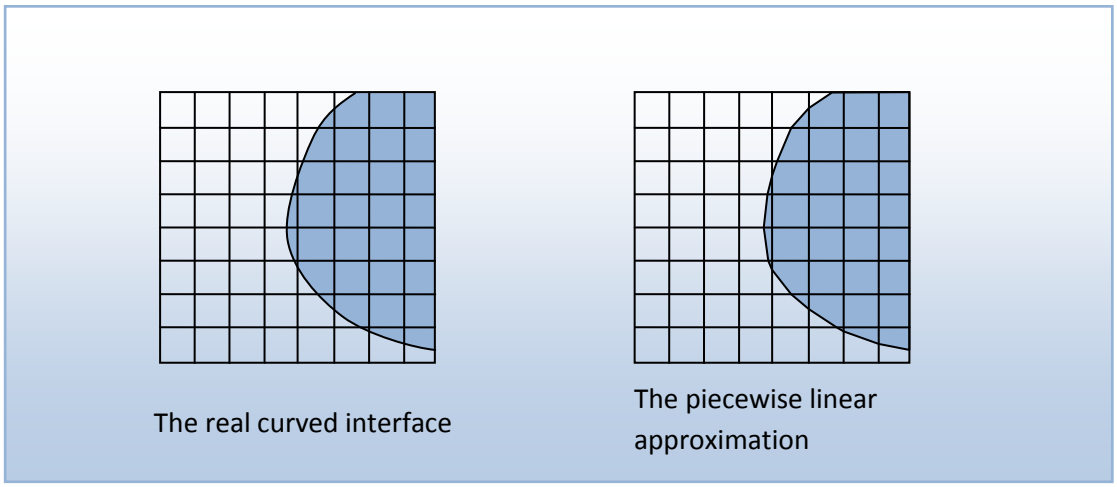

Figure 22: A comparison between the real interface (left) and the interface calculated using the geometric reconstruction model (right).

Figure 22 shows the linear interfaces created in every cell containing two different phases. The position of this interface is determined from the volume fractions and the positions of interfaces in neighbouring cells.

ii. Momentum and Turbulence

As a mixed fluid approach, the VOF model shares a single set of momentum and turbulence equations between phases.

5. Advanced Modelling

The commercial CFD code, FLUENT 6.3, provides a large selection of mathematical modelling tools, covering a wide range of flow situations. To achieve optimal accuracy when modelling flows in a gas stirred ladle, however, a number of additional models also need to be implemented. These models are not included in commercial CFD codes and will be discussed in the following subsections.

It is interesting to note that these models are mostly neglected in more recent studies employing commercial CFD codes. The reason for this is that implementation of such models is somewhat easier when a mathematical model is designed from the ground up to cater especially for a gas

stirred vessel. It is therefore understandable that the four articles most referred to in this section are quite old by mathematical modelling standards: Johansen and Boysan (46) published in 1988, Mazumdar and Guthrie (47) published in 1994 and Sheng and Irons (55; 56) published in 1992 and 1995.

5.1. Computational Bubble Dynamics

CFD modelling of bubble driven flows is used over a wide array of industrial processes and has become known as computational bubble dynamics (CBD). When studying CBD, the treatments of the dispersed bubbly phase can be categorized into 4 separate approaches: Averaging methods, bubble tracking methods, interface tracking methods and microscopic methods (57).

- Averaging methods treat the dispersed phase in the Eulerian sense, creating two separate fluids. The dispersed phase is then transformed to a mathematically continuous phase by means of volume averaging. Due to this averaging procedure, the interface is not resolved and the transfer terms between phases need to be modelled to close the equations.
- Bubble tracking methods utilize the Lagrangian approach, tracking bubbles as mass points through the continuum. The coupling between the phases can be one-way, two-way or four-way. In four-way coupling, not only the influence of the continuous phase and the dispersed phase on each other is modelled, but also the hydrodynamic interactions and collisions between bubbles.
- Interface tracking methods resolve the interface between the dispersed and continuous phase exactly, thereby requiring no further modelling to account for drag and other applicable forces.
- Microscopic methods focus on the translation and collision of pseudo molecules. These methods can reproduce micro-scale phenomena such as interfacial tension which normally require further modelling.

As far as practicality is concerned, the only methods viable for engineering scale simulations are the averaging or bubble tracking approaches. These methods rely on various constitutive models in order to close the equations, and their performance is primarily determined by the quality of those models.

The Interface tracking and microscopic methods are more fundamentally based, but cannot be implemented on a large scale. These models are implemented as fundamental tools for the development and improvement of constituent models used in the averaging and bubble tracking methods.

The model developed in the present work utilizes the bubble tracking approach by employing the discrete phase model in FLUENT 6.3, thus requiring additional models to close the conservation equations. A number of the factors that require further modelling are not available in the commercial code and need to be manually implemented.

5.2. Forces Acting on a Bubble

Laux *et al.* (57) lists the most important forces acting on a bubble as the drag force, transversal lift force, added mass force, hydrodynamic forces due to bubble-bubble interactions, force due to fluid pressure gradient and body force due to gravity.

All of these, except for the latter two, require further modelling. The transversal lift force, added mass force and hydrodynamic forces make only minor contributions to the overall force balance and are very hard to model. Sheng and Irons (56) modelled the transversal lift force and found that it caused smaller bubbles to move to the outside and larger bubbles to the inside of the plume. The effect of this phenomenon on overall momentum transfer is unclear though. In general, these models are not included in engineering scale simulations.

The drag force is of primary importance and requires further modelling. The most widely quoted drag law used for describing bubbly flows is one by Harmathy (54):

$$C_D = \frac{2}{3}\left(E_0\right)^{0.5} \qquad \text{Equation 53}$$

Xia et al. (50) tested the performance of this drag law among others against experimental results obtained in a Wood's metal bath. It was found that a slight modification in the drag law resulted in improved prediction of flow parameters.

$$C_D = \frac{2}{3}\left(\frac{E_0}{3}\right)^{0.5} \qquad \text{Equation 54}$$

The improved results offered by the slightly reduced drag coefficient can be explained by the interaction of bubbles moving in a group. The wake effects tend to reduce the drag on subsequent bubbles. Johansen and Boysan (46) implemented a modification to the drag coefficient of a single bubble to account for this reduction in drag. Prior knowledge of the distance between bubbles (y_B) is required.

$$C_{D,\mathrm{mod}} = C_D\left(1-\left[\frac{d_B}{y_B}\right]^2\right) \qquad \text{Equation 55}$$

Since Equation 54 was derived from a situation involving a bubble plume, the assumption can be made that it represents a modification of Equation 53 with an expression similar to Equation 55. The coefficient given in Equation 54 is therefore selected as the best available option for modelling drag in bubble plumes.

5.3. Size Distribution

The majority of mathematical studies of gas stirred ladles have considered only a single averaged bubble size. A number of models maintaining the correct size distribution through the processes of breakup, coalescence and gas compressibility are available in the Eulerian framework. These include the classes method (58) and the Multiple-Size-Group-Method (59).

In the Lagrangian framework, however, no comprehensive model for maintaining size distributions in bubbly flows is available. FLUENT 6.3 does supply models for breakup and coalescence in liquid sprays, but these cannot be applied to bubbly flows. Accordingly, any models for breakup, coalescence and growth will have to be implemented manually.

Bubble growth can simply be assumed to follow the ideal gas relationship along the pressure gradient of the vessel. The high temperatures involved in steelmaking operations ensure validity of the ideal gas law.

Breakup and coalescence, however, are much harder to model. A fairly recent development for predicting bubble size distribution in the Lagrangian framework is presented by Alexiadis *et al.* (60) utilizing the concept of spot turbulence. This phenomenon only becomes prominent at high gas flow rates, however, while the ladle setups under consideration function at relatively gentle stirring. Additionally, the spot turbulence concept has only been tested in air water models and has not been implemented in any subsequent study to validate its applicability to multiple flow situations.

Sheng and Irons (56) fitted a breakup model to data obtained from a water model. The model realistically simulates the breakup of a mother bubble into one larger bubble and several smaller ones. The breakup probability of the bubble is calculated from the measured breakup heights recorded in the water model. The authors (56) recommend, however, that the model first be tested in metal baths such as mercury or Wood's metal before any attempts can be made to implement it in full scale ladle situations.

Accordingly, some simplified in-house model for breakup due to bubble growth will have to suffice in the current modelling setup. The starting size distribution can be estimated with an equation developed by Davidson and Schuler (61):

$$d_B = 0.35\left(\frac{Q^2}{g}\right)^{0.2} \qquad \text{Equation 56}$$

Equation 56 estimates the maximum bubble size formed at the nozzle tip. The average bubble size can then be assumed to be 25% of this maximum value (46). FLUENT 6.3 offers some models for injecting a pre-determined size distribution of particles into the melt. Equation 56 can therefore be used to correctly parameterize such a model.

5.4. Turbulence Modulation by Bubbles

The two phase plume region presents a highly complex turbulence modelling situation. The interactions of the bubbles among themselves and with the metal phase are dependent on many factors and not completely understood at present. Turbulence modulation brought about by dispersed particles present one particular gray area. The most recent edition of the Multiphase Flow Handbook (36) states that "…the available theories often cannot predict the level or even sign of the change in turbulence kinetic energy."

As a result, the bubbles' contribution to turbulence is mostly ignored in engineering scale mathematical modelling studies (57), leading to over-predictions of flow velocity and under-predictions of the turbulence kinetic energy within the plume. This is an indication that too little of the kinetic energy induced by the buoyant energy input is realized as turbulence kinetic energy. An example of such a situation is presented below:

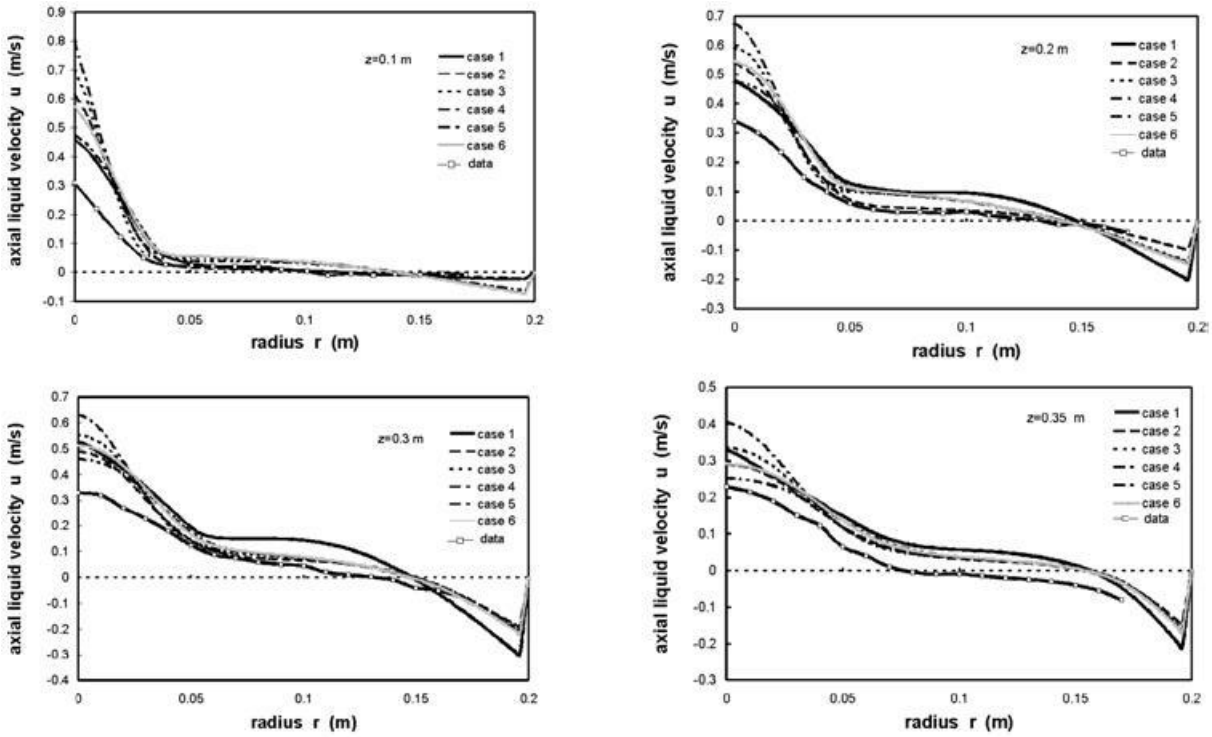

Figure 23: Over-predicted flow velocities in the plume region attained by several modelling approaches (50) (cases 1-6) compared to experimental data.

Some efforts have been made to account for the additional turbulence provided by the bubbles by adding source terms to the turbulence model. Sheng and Irons (55; 56) employed one such approach by adding the following source terms to the turbulence transport equations of the SKE model:

$$S_k = P_k - C_D \rho \varepsilon + C_{k1} \alpha (1-\alpha) P_k + C_{k2} C_f \alpha \rho_l k$$ Equation 57

$$S_\varepsilon = \frac{C_1 \varepsilon P_k}{k} - \frac{C_2 \rho \varepsilon^2}{k} + C_{\varepsilon 1} \alpha (1-\alpha) P_k \frac{\varepsilon}{k} + C_{\varepsilon 2} C_f \alpha \rho_l \varepsilon$$ Equation 58

This modification yielded the following velocity measurements in the plume:

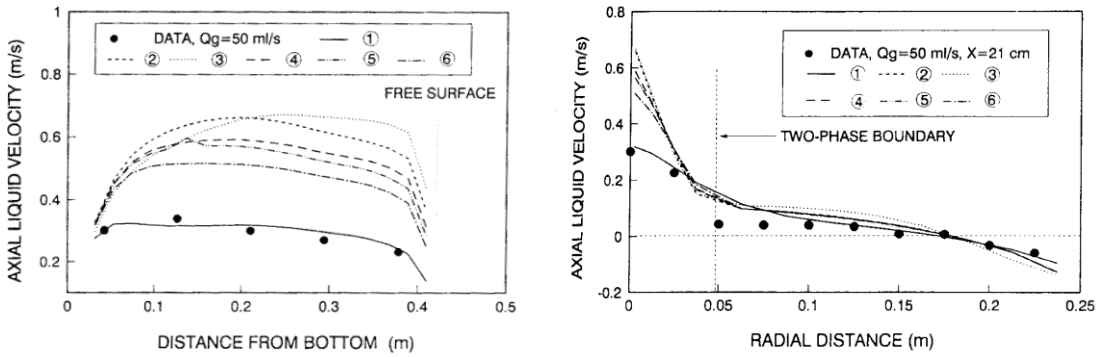

Figure 24: The improvement in plume prediction attained by Sheng and Irons (55) (case 1) compared to other modelling approaches (cases 2-6).

The line identified as case 1 represents the performance of the turbulence model modified for bubble turbulence production, while the other cases form a control group of other approaches. It can plainly be seen that the modification for bubble induced turbulence successfully eliminated the over-prediction of flow velocity.

An approach for turbulence modulation in the Lagrangian reference frame is used by Johansen Boysan (46). This approach introduces a turbulence production source term together with the momentum source term already transferred by the discrete particles to the continuous phase. It is shown that the total additional turbulence production per unit volume is:

$$P_B = \frac{Q}{N\Delta V} C_B \sum_{m=1}^{n} \int_0^{t_{R,m}} \frac{4}{3} \frac{\mu_l}{d_B^2} C_D \,\mathrm{Re}_B \left(U_{B,i} - U_i\right)^2 dt \qquad \text{Equation 59}$$

This relationship shows that the turbulence contribution of the bubbles is dependent on the liquid viscosity, bubble diameter, Reynolds number and bubble slip velocity. It can provide an excellent starting point in developing a similar model for bubble turbulence production in steel ladles. Results achieved with this approach are presented below:

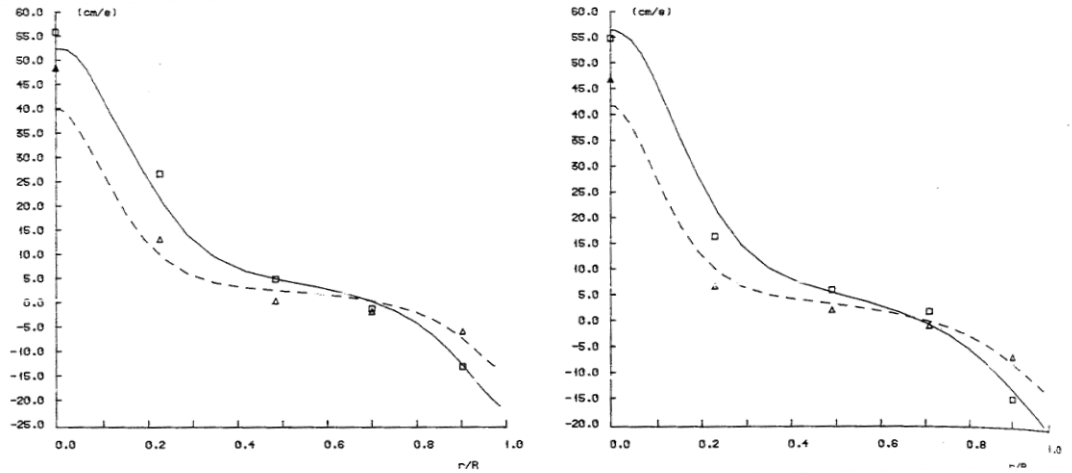

Figure 25: The improvement in plume velocity prediction attained by Johansen and Boysan (46).

Figure 25 shows an even better prediction of plume flow velocity than that achieved by Sheng and Irons (55).

On the subject of predicting plume turbulence, Sheng and Irons (55) published an excellent visual representation by plotting contours of turbulent kinetic energy for both experimental and modelled results. These contours are repeated below:

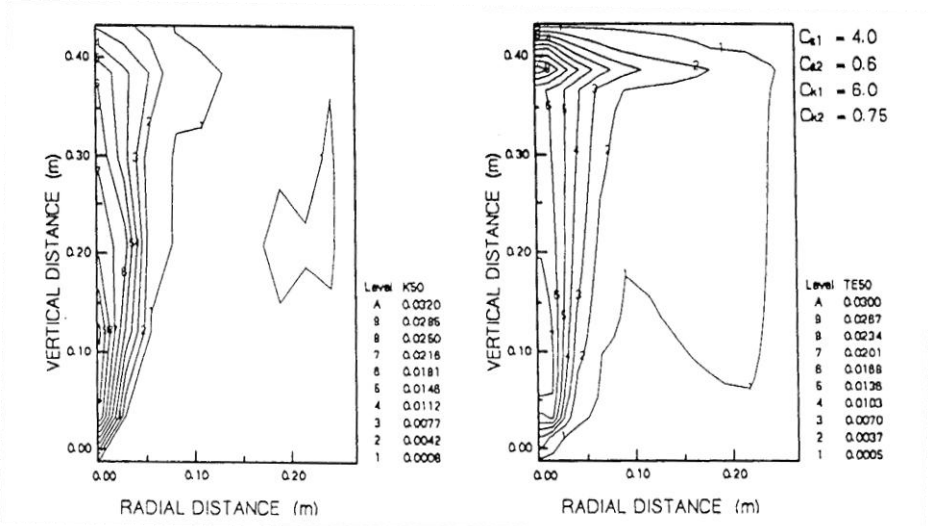

Figure 26: Measured and computed turbulence contours (55).

Figure 26 shows a reasonable agreement between experimental and model outputs, but also identifies another problem: the incorrect modelling of a large amount of turbulence just below the free surface of the melt.

This phenomenon has mostly been ignored by mathematical modelling studies to date. The only solution to this problem that could be located in the literature is employed by Johansen and Boysan (46). A boundary condition is employed at the top of the plume causing a redistribution of turbulent energy in different directions, in turn leading to increased dissipation rates. The argument behind this boundary condition is that the turbulence is damped when turbulent eddies approach and locally lift the free surface. This modification succeeded in removing the access turbulence just below the free surface, but still deviated significantly from experimental data.

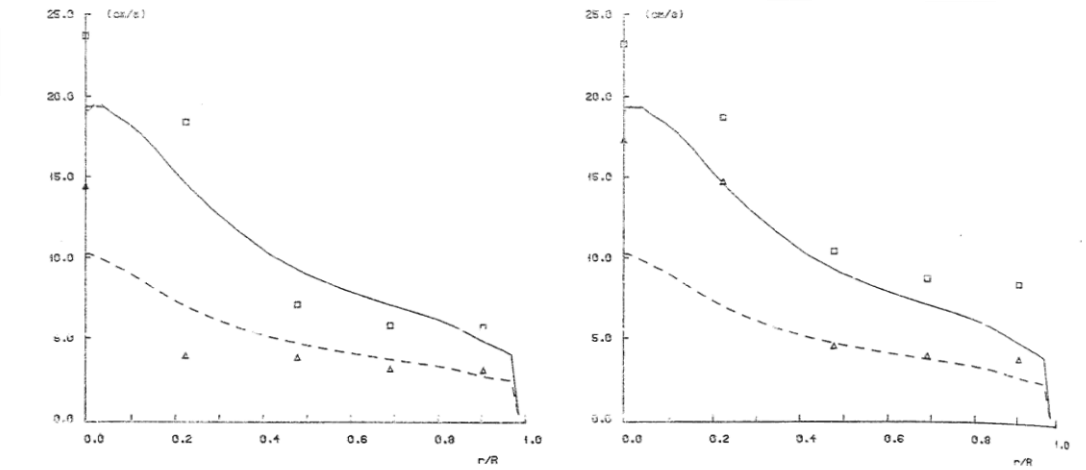

Figure 27: Measured and computed isotropic turbulent velocities just below the free surface (46).

The improvement shown by Figure 27 was achieved by modifying the relationship between the only non-zero off-diagonal component of the Reynolds stress tensor and the mean strain rate as follows:

$$\left\langle u_1' u_2' \right\rangle = -\frac{\mu_t}{\rho_l}\left(\frac{C_1'}{C_1' + \frac{3}{2}C_3'}\right)\left(\frac{C_1'}{C_1' + 2C_3'}\right)\left(\frac{\partial u_1}{\partial x_2} + \frac{\partial u_2}{\partial x_1}\right) \qquad \text{Equation 60}$$

This mechanism is fairly complex and cannot be conveniently included in the commercial CFD code by means of user defined functions. A simpler option that can be investigated is simply increasing the turbulence dissipation rate in the vicinity of the free surface.

5.5. Void Fraction

Since the Lagrangian discrete phase particles occupy no volume in the domain, the effects of void fraction on the flow scenario in completely ignored. The present study will investigate relatively low gas purging rates and therefore relatively low void fractions, limiting the error induced. When higher flow rates are considered, however, certain adaptations need to be made from a modelling point of view.

The effect of void fraction is mostly accounted for by modelling the void fraction that would be occupied by the gas phase as shown in Equation 61.

$$\alpha_g = \frac{Q}{N\Delta V}\sum_{m=1}^{n} t_{R,m} \qquad \text{Equation 61}$$

The liquid volume fraction is simply computed from the knowledge that the volume fractions must sum to one. The liquid volume fraction is then used to alter the density employed in the liquid phase conservation equations as follows:

$$\rho_{l,\text{mod}} = \alpha_l \rho_l \qquad \text{Equation 62}$$

CHAPTER IV:
NUMERICAL MODEL SETUP PART 1: PREPARATORY MODELS

Hope for the best, but prepare for the worst...
- English proverb

1. Experimental Objectives and Motives

The experimental model was developed for the purpose of producing mixing times and a number of other flow-related outputs for different flow setups as accurately as possible, while still remaining economical on computational resources.

The size of the domain, the complexity of the flow conditions to be simulated and the transient simulation setup combine to give this study the potential to be computationally very expensive. Additionally, a large number of experimental runs will be necessary to statistically describe the effects of numerous operating and design parameters on mixing.

Numerical studies reported in the literature have never investigated the mixing effects of more than three factors. The majority of these studies also incorporate the assumption of a flat free surface that can completely alter flow pattern development (see Chapter VI:2) so as to save computational time.

Accordingly, three areas are identified into which meaningful research can be directed:

- Attainment of sufficiently accurate solutions of flow and mixing in full scale gas stirred ladles
- Investigation into methods for saving computational time without undermining the fidelity of the solution
- A holistic statistical modelling exercise pinpointing the effects of all applicable parameters on mixing efficiency

An accurate and well researched numerical modelling setup is essential to ensure the fulfilment of the above mentioned criteria. The following two chapters detail the development of such a model.

2. Three Sets of Simulations

The development of the three sets of simulations completed in this study is presented over two chapters. The subsequent chapter deals with the development of the primary model used for investigating flow and mixing in gas stirred ladles. Certain crucial aspects of this model are not well known, however, and two additional models had to be completed in advance to attain closure in the final model development. This chapter deals with these two additional models.

Firstly, the ideal balance between numerical accuracy and computational time had to be found. To this end, a steady state simplification of the primary model was implemented to carry out an extensive grid independence study. In this model, multiphase effects were described by the DPM only and the SKE model was used to account for turbulence effects.

Secondly, a small scale, three dimensional, transient, mathematical model was developed to investigate the growth, shape and breakup characteristics of a single bubble as it rises through the melt. Information obtained from this simulation was essential for ensuring accurate representation of the rising bubbles as discrete phase momentum sources employed by the DPM. This simulation utilized the VOF multiphase model and the SKE turbulence model.

The model development philosophy as well as the relevant locations in the text is given below:

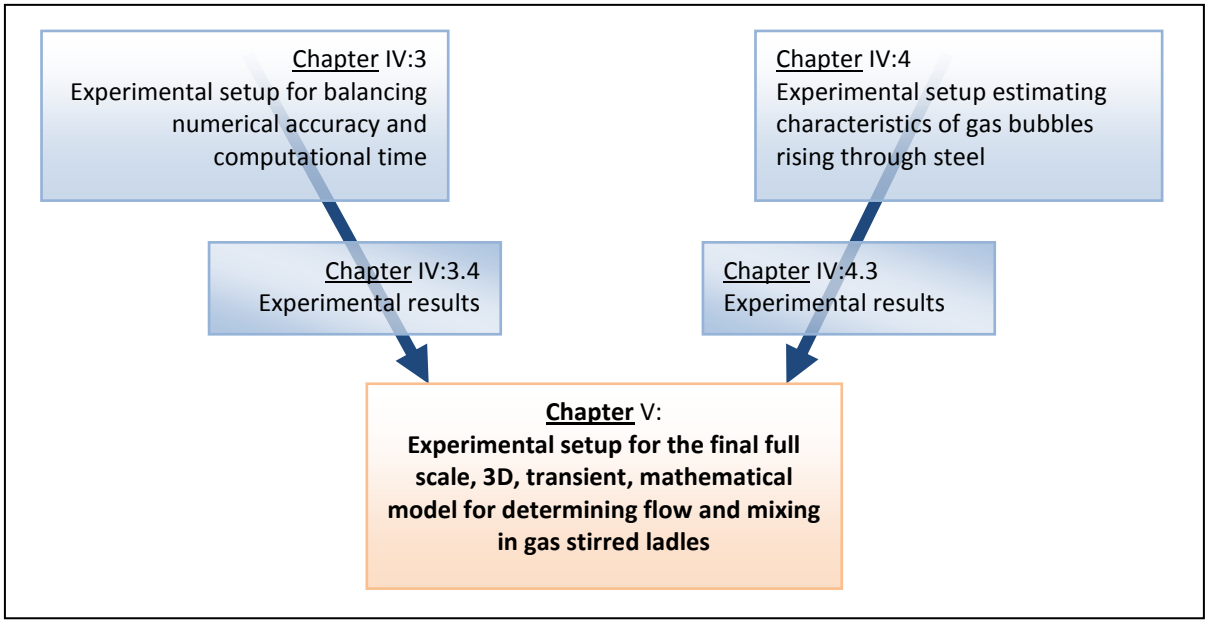

Figure 28: Outline of the information given in the following two chapters.

3. Numerical Accuracy vs. Computational Time

3.1. Background

It has already been established that careless model development could result in a computationally expensive model that cannot generate the required results within the given time frame. Various steps can be taken to reduce the amount of computational time required, but this can easily be done at the expense of numerical accuracy. Hence, a delicate balancing act between numerical accuracy and computational time is required.

A number of factors influence numerical accuracy in CFD. The four most important ones are discussed below.

3.1.1. Grid Size

Grid independence is the primary measure of numerical accuracy in any numerical simulation. The grid should be sufficiently fine so that subsequent refinements of the grid do not offer significant improvements in the solution. In a three dimensional domain, however, a finer grid will cause a substantial increase in the number of cells and therefore, the computational cost.

Literature sources assumed grid independence at cell sizes varying from 0.8 to 10cm (10; 24; 43; 44; 46; 49; 52) but the majority of studies used grid sizes in the vicinity of 4cm. The grids in question were mostly axis-symmetric 2D setups, which only allow the simulation of a single tuyere positioned at the centre of the vessel floor. Three dimensional setups were also completed in cylindrical coordinates (10; 24) creating a wide range of cell sizes (cells expand towards the outside of the vessel). No studies could be found which utilize the uniform 3D hexahedral grid setup used in the present study.

Mazumdar (47) did a simple grid independence study on a 2D axis-symmetric grid and found 4.5 by 2cm cells to be sufficiently fine. Accordingly, a cell size of 4cm will be a good starting point in the investigation.

Grid size will simply be referred to as '$Grid$' in the remainder of this chapter.

3.1.2. Location Specific Grid Refinement

FLUENT 6.3 offers the capability of refining the grid only in areas with significant quantities of turbulence, flow velocity, streamline curvature and other important flow parameters. For 3D hexahedral cells this is accomplished by dividing the mother cell into eight daughter cells by bisecting it once in each of the Cartesian directions. This method can facilitate a significant reduction in the number of computational cells by allowing a coarse grid in areas of low flow intensity, while still ensuring numerical accuracy in the domain as a whole.

The location specific refinement process must be done with caution so as to ensure sufficient refinement in areas of high flow intensity and prevent excessive coarsening in areas of low flow rates. If done carelessly, this process can undermine the fidelity of the solution.

No examples of this type of refinement could be found in literature pertaining to gas stirred baths. Some attempts have been made to refine the 2D grid in the radial direction in regions of intense flows (43), resulting in tall narrow cells in the region of the plume. When considering that the flow velocity inside the plume is typically an order of magnitude greater than flows outside of the plume though, location specific refinement should be a factor of primary importance. The grid adaption process is described in more detail in Section 3.2.3 of this chapter.

The location specific grid refinement will henceforth be shortened to '$Refine$'.

3.1.3. Discretization Scheme

The partial differential equations used in CFD need to be discretized into discrete algebraic equations for each cell in order to make numerical solution of the domain possible. A number of schemes are available with which to accomplish this.

These schemes are distinguished by the order of accuracy achieved. First order schemes simply assign cell face values as equal to values at the cell centroid, while higher order schemes employ a flow variable gradient through the cell to compute different cell face and centroid values.

As a rule, higher order schemes offer improved accuracy, but tend to decrease stability of the solver. This requires stronger under-relaxation, thereby increasing the number of iterations to convergence. Accordingly, the discretization scheme should be chosen to ensure maximum solution accuracy, but also to maintain solver stability and ensure fast convergence.

Literature sources use a number of different discretization schemes; mostly improvements on the first order scheme such as the power law scheme (44) and hybrid scheme (24). The third order QUICK scheme is also used (49). Other papers are very vague about the discretization scheme used and no reasons are provided for any specific decision regarding. Thus, the actual effect of changes in the discretization scheme still remains to be determined.

The factor of discretization scheme will be referred to as '$Discrete$' from this point forward.

3.1.4. Discrete Phase Number of Tries

The Discrete Phase Model (DPM) offered in FLUENT 6.3 is used to track the bubbles through the domain. The DPM employs a random walk approach on every particle stream for a certain 'number of tries' to account for the turbulent dispersion of bubbles. Numerical accuracy can be improved by increasing the number of tries, but this also causes an increase in computational time.

Due to the computational efficiency of the DPM, changes in computational time brought about by altering the number of tries are likely to be insignificant when compared to the other factors. It will, however, still be meaningful to investigate the effect that changes in the number of tries have on the solution outputs. No literature sources could be found on this topic.

This factor will be abbreviated as 'NOT' for the remainder of the chapter.

3.2. Model Description

Steady state, three dimensional flow computations were carried out using the discrete phase model for tracking the bubble plume and the standard k-ε model to account for turbulence. The free surface of the melt was assumed to be flat and frictionless.

This steady state modelling procedure entails several assumptions (Chapter VI:2) that decrease its fidelity. It must be stressed that this model will only be used to investigate the effects of the different factors on both numerical accuracy and computational time on a comparative basis. Individual quantitative flow results should not be taken as accurate.

3.2.1. Geometry

The numerical geometry was modelled on a 250 ton vacuum oxygen decarburization vessel. A simple cylinder, 3.4 m in diameter and 4 m in height, was meshed with uniform hexahedral cells using the Cooper scheme. Cell size was specified according to the specific experimental run.

3.2.2. Physical Properties and Boundary Conditions

A. Continuous Phase

Metal density and viscosity was specified as 6942.9 kg/m^3 and 0.00503 Pa.s respectively (62).

The bottom and side boundaries of the vessel were specified as walls with no-slip boundary conditions imposed on them. The top boundary was defined as a frictionless wall in an attempt to simulate the free interface between the metal and the top gasses.

B. Discrete Phase

Mono-sized spherical bubbles (2 cm in diameter) were released from four equally spaced point sources located on a radius of 0.05 m around a point positioned concentrically on the vessel floor.

Bubbles were released at a relatively high flow rate of 0.015 kg/s, corresponding to a volumetric flow rate of 562.5 litres/min at STP. This high flow rate was selected on the assumption that grid independence achieved in rapid flows will automatically hold in gentler flow situations. The bubble density was specified as a constant value calculated at a depth of 2 m (half way) using the ideal gas law. The effects of this assumption are discussed in Chapter VI:2.2.1 and is avoided in the primary model setup (Chapter V:2.5.2.B).

$$\rho_g = \frac{(P_0 + \rho_l g H) M_r}{RT}$$ Equation 63

For argon gas injected into a melt of molten iron at 1908K with atmospheric surface pressure, the calculated density at a depth of 2 m is 0.6 kg/m^3.

The bottom and side walls were designated to reflect any particles that come into contact with them, while the top wall was set to let particles escape.

3.2.3. Grid Refinement

The dynamic gradient adaption option in FLUENT 6.3 was utilized to refine cells according to the velocity in that cell. In this way, a certain value of velocity was specified (according to the experimental run) and the solver was set to refine any cells with velocities above and coarsen any cells with velocities below that specified value. This refinement and coarsening process was repeated automatically every 50 iterations to ensure that the correct refinement is maintained as the solution is improved.

Refinement was specified to occur over two levels, meaning that cells containing high velocities were refined twice. The result is that every mother cell located in a region of high velocity (the rising gas/liquid plume) is split into 64 daughter cells, thereby significantly improving the accuracy of the solution in this very important region. This strong refinement is certainly merited when the velocity profiles inside the vessel are observed.

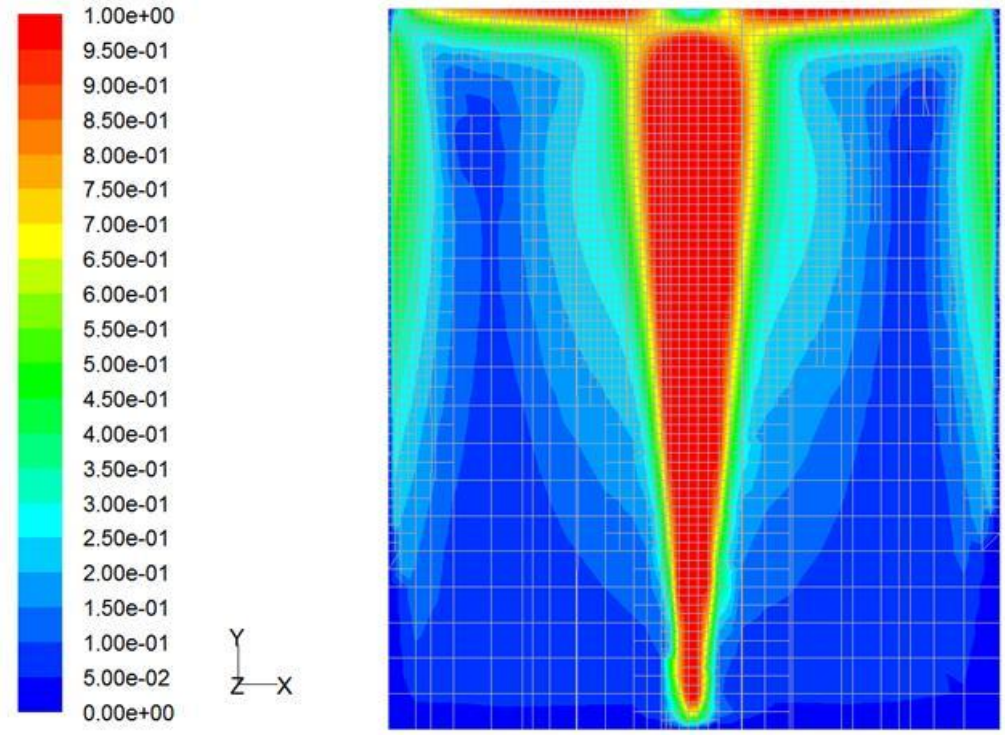

Figure 29: Example of the grid refined at velocity measures larger than 0.2 m/s.

From Figure 29 it can clearly be seen that the average velocity within the plume is larger than 1 m/s while the average velocity in the bulk of the vessel is generally smaller than 0.1 m/s. The distinct difference in flow intensity between these two regions merits the strong 2-level refinement.

3.3. METHODS

The domain was initialized with zero-values for all the flow variables and some constant values for turbulence ($k = 0.02$ m^2/s^2, $\varepsilon = 0.002$ m^2/s^3). No location specific refinement was present initially since no velocity profiles were available against which to specify the refinement. The iteration procedure was then started. The first refinement was done automatically at 50 iterations after a quick initial solution was attained on the coarse grid. Following the first double refinement, the iteration process was much slower, but ensured an accurate solution.

Convergence was judged by observing the volume-weighted averages of velocity and turbulence kinetic energy.

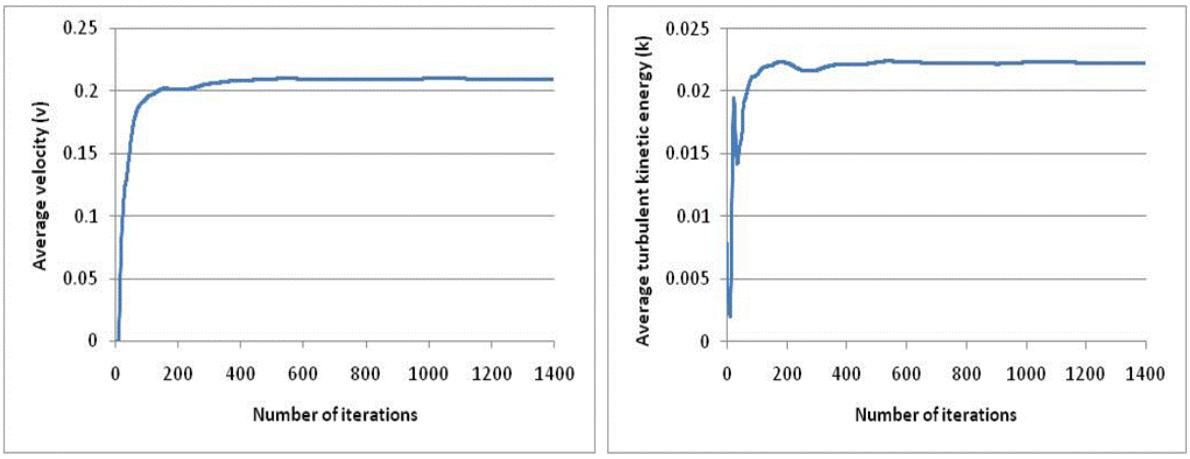

Figure 30: Plots of average velocity and turbulence kinetic energy against the number of iterations.

The solution was seen as converged when both of these average values flatten out. These graphs were then used to extract the four dependent variables used in the study:

- The average velocity (v_{ave}). This value was simply read from the velocity plot once convergence was attained.
- The average turbulence kinetic energy (k_{ave}) was read from the turbulence plot in a similar fashion.
- The time taken for the solution to converge (t_c) was obtained by physically timing the solution process, recording a few points and establishing a linear relationship between iterations and time. The number of iterations to convergence was then read from Figure 30 and the gradient of the linear relationship (seconds/iteration) was used to calculate the time to convergence.
- Solution instability (SI). Once the volume-weighted average plots flattened out, a certain amount of oscillation around the final value was observed. The amplitude of these instabilities was expressed as a percentage of the average value around which the oscillations occur.

3.4. Results and Discussion

Three sets of statistical experiments were designed and completed: two 2^3 full factorial designs and one three-factor rotatable central composite design. The factorials were used to investigate the effect of changing the discretization scheme $(Discrete)$, while the central composite design analyzed the influence of grid size $(Grid)$, location specific refinement $(Refine)$ and discrete phase number of tries (NOT). For more detailed accounts of the design of these experiments, see Chapter XVI:1.

3.4.1. Factorial Designs

Results from the two factorial designs are presented in Table 1.

Table 1: Results from the two 2^3 full factorial designs.

Run	*Grid* [level]	*Refine* [level]	*Discrete* [order]	v_{ave} [m/s]	k_{ave} [m^2/s^2]
1	Low	Low	First	0.189	0.0147
2	High	Low	First	0.188	0.0146
3	Low	High	First	0.192	0.0162
4	High	High	First	0.191	0.0161
5 / 1	Low	Low	Second	0.217	0.0235
6 / 2	High	Low	Second	0.208	0.0220
7 / 3	Low	High	Second	0.217	0.0234
8 / 4	High	High	Second	0.213	0.0225
5	Low	Low	Third	0.221	0.0233
6	High	Low	Third	0.211	0.0220
7	Low	High	Third	0.223	0.0240
8	High	High	Third	0.215	0.0226

The first factorial design was completed to investigate the effect of changing *Discrete* from first to second order. Sums of squares resulting from this analysis are reported in Table 2. The assumption was made that the numerically generated results include no error variance.

Table 2: Sums of squares and percentage variance explained by *Grid*, *Refine* and *Discrete* (1st & 2nd order).

Factor	Velocity		Turbulence kinetic energy	
	SS	SS [%]	SS	SS [%]
(1) *Grid*	2.813E-05	2.358	8.450E-07	0.736
(2) *Refine*	1.513E-05	1.268	1.445E-06	1.258
(3) *Discrete*	1.128E-03	94.572	1.110E-04	96.665
1 by 2	3.125E-06	0.262	4.500E-08	0.039
1 by 3	1.512E-05	1.268	6.050E-07	0.527
2 by 3	1.250E-07	0.010	8.450E-07	0.736
1 by 2 by 3	3.125E-06	0.262	4.500E-08	0.039
Total	**1.193E-03**	**100.000**	**1.148E-04**	**100.000**

Table 2 clearly shows that *Discrete* explains virtually all of the variance present in the model. By calculating the means, it was found that the average velocity increased by 13.2% and the average turbulence kinetic energy by 48.4% when second order discretization was implemented. This confirms that first order accuracy is not sufficient for the present study and that higher order discretization will have to be employed.

The second full factorial investigated the effect of changing *Discrete* from second to third order. Sums of squares are reported in Table 3.

Table 3: Sums of squares and percentage variance explained by $Grid$, $Refine$ and $Discrete$ (2nd & 3rd order).

Factor	Velocity		Turbulence kinetic energy	
	SS	SS [%]	SS	SS [%]
(1) $Grid$	1.125E-04	65.407	3.251E-06	84.475
(2) $Refine$	1.800E-05	10.465	3.612E-07	9.386
(3) $Discrete$	3.200E-05	18.605	3.125E-08	0.812
1 by 2	4.500E-06	2.616	3.125E-08	0.812
1 by 3	4.500E-06	2.616	1.125E-08	0.292
2 by 3	0.000E+00	0.000	1.012E-07	2.631
1 by 2 by 3	5.000E-07	0.291	6.125E-08	1.591
Total	1.720E-04	100.000	3.849E-06	100.000

It is evident that the effect of changing $Discrete$ from second to third order is much smaller than a similar change from first to second order. When all interaction effects were pooled with the error, this effect was found to be moderately significant $(p = 0.021)$ in the average flow velocity and insignificant in the average turbulence kinetic energy. A marginal means plot showed that a change in $Discrete$ from second to third order only caused a 1.9% increase in average flow velocity. Accordingly, second order discretization is deemed sufficiently accurate for the current application.

3.4.2. Central Composite Design

The central composite design was used to determine the response of dependent variables to changes in $Grid$, $Refine$ and NOT. Results from the CCD are reported in Table 4. Refer to Chapter XVI:1.2 for the specification of coded variables.

Table 4: Results from the three factor rotatable central composite design.

Run	$Grid$ [coded]	$Refine$ [coded]	NOT [coded]	t_c [s]	v_{ave} [m/s]	k_{ave} [m²/s²]	SI [%]
1	0.000	-1.682	0.000	1194	0.213	0.0217	0.51
2	0.000	1.682	0.000	7207	0.212	0.0224	0.23
3	1.000	-1.000	1.000	3114	0.208	0.0219	0.21
4	0.000	0.000	-1.682	2225	0.209	0.0224	1.01
5	0.000	0.000	0.000	1661	0.210	0.0223	0.43
6	1.000	-1.000	-1.000	3130	0.207	0.0220	0.28
7	0.000	0.000	1.682	1761	0.210	0.0223	0.34
8	1.000	1.000	-1.000	13274	0.209	0.0223	0.23
9	-1.000	1.000	-1.000	2905	0.222	0.0240	0.25
10	-1.000	1.000	1.000	2757	0.220	0.0238	0.28
11	-1.000	-1.000	1.000	843	0.211	0.0231	0.59
12	-1.682	0.000	0.000	415	0.221	0.0239	1.00
13	-1.000	-1.000	-1.000	628	0.211	0.0231	1.13
14	1.000	1.000	1.000	12958	0.207	0.0222	0.11
15	0.000	0.000	0.000	1515	0.209	0.0223	0.36
16	1.682	0.000	0.000	6777	0.205	0.0223	0.15

ANOVA results are given below. The bracketed L and Q denote the linear and quadratic effects respectively.

Table 5: Percentage of variance explained by $Grid$, $Refine$ and NOT.

Factor	t_c	v_{ave}	k_{ave}	SI
(1) $Grid$ (L)	38.01	66.70	63.47	37.64
(1) $Grid$ (Q)	4.31	3.71	14.30	0.38
(2) $Refine$ (L)	34.41	6.94	10.53	15.20
(2) $Refine$ (Q)	6.19	2.74	0.05	1.30
(3) NOT (L)	0.03	0.03	0.30	15.47
(3) NOT (Q)	0.97	0.00	0.84	2.17
1L by 2L	12.47	11.45	1.58	8.56
1L by 3L	0.01	0.03	0.00	0.81
2L by 3L	0.02	0.79	0.06	2.14
Error	7.39	8.06	5.69	13.89
Total	100.00	100.00	100.00	100.00

$Grid$ is the most influential factor in the design and is significant $(p < 0.01)$ in each of the dependent variables. The effect of $Refine$ is also at least marginally significant $(p < 0.05)$ in all of the dependent variables save for the average velocity. NOT, on the other hand, seems only to have a borderline significant $(p = 0.042)$ influence on the amplitude of oscillations. The interaction effect between $Grid$ and $Refine$ is marginally significant in the simulation time $(p = 0.019)$ and the average velocity $(p = 0.027)$.

Moderate error terms are also present in all of the dependent variables. For the dependent variables of time and amplitude, this is largely because of the human error involved in the graphical collection of data. The error in the velocity and turbulence is due to the expected shape of the response, i.e. a flattening out towards higher factor levels as grid independence is achieved. This response cannot be fully described by a second order polynomial.

A. The Amplitude of Oscillation

A strict measure of solution instability was imposed by setting the maximum allowable amplitude of oscillation to be 1% of the steady state value. Figure 31 shows the amplitude of oscillation plotted on a scatter plot against NOT.

It is clear from Figure 31 that three of the data points are responsible for most of the linear effect of NOT on amplitude. These three points can be identified as the star points of the central composite design where NOT and $Refine$ are set to their lowest levels, as well as the cube point where all three factors are set to their low levels. Thus, it can be concluded that solution instability measured by the amplitude of oscillations is only significant at the lowest (least accurate) levels investigated. It is also clear that, at higher levels of $Grid$ and $Refine$, NOT has no effect save for the lowest star point. Accordingly, the discrete phase number of tries can safely be set to any level of low and above, i.e. a value resulting in 168 or more particle tracks.

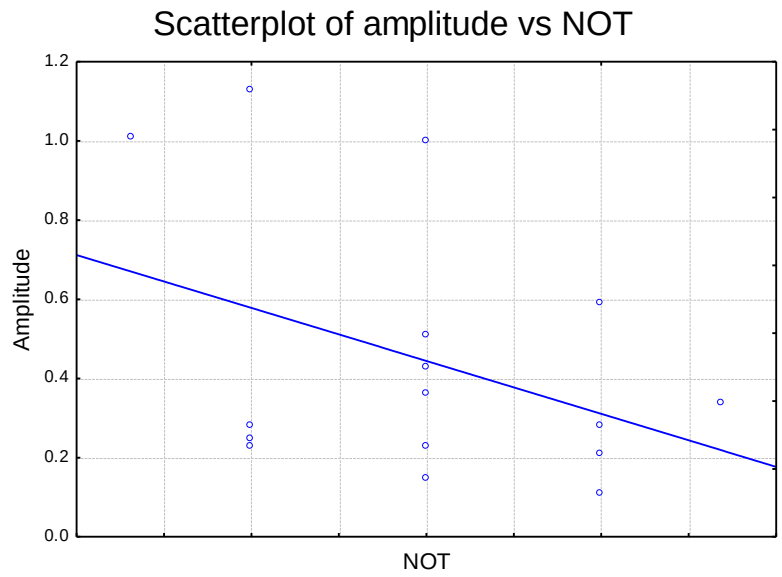

Figure 31: Scatter plot of amplitude vs. NOT.

B. Surface Responses

The remaining dependent variables (time, velocity and turbulence kinetic energy) are influenced only by $Grid$ and $Refine$. These influences can be visualized by surface plots generated by smoothing splines:

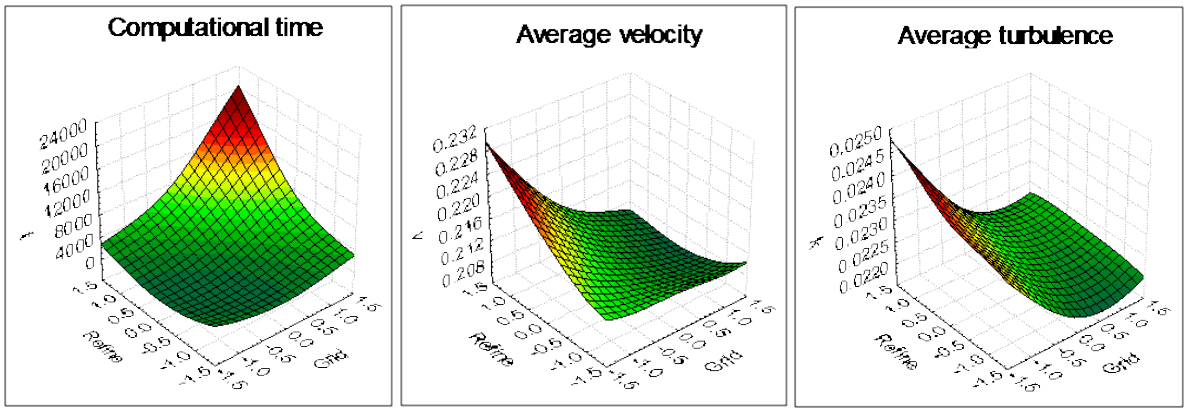

Figure 32: Spline surface responses of dependent variables to changes in $Grid$ and $Refine$.

Figure 32 clearly shows the strong exponential growth in time required to reach steady state as both $Grid$ and $Refine$ are increased. The responses of average velocity and turbulence kinetic energy, on the other hand, flatten out towards higher levels as grid independence is achieved.

The response surfaces also show that higher levels of $Grid$ and $Refine$ offer only marginal improvements in numerical accuracy at substantial computational costs, while some significant inaccuracies do exist at lower levels. These findings emphasize the need to find the delicate balance between computational power and numerical accuracy.

It is also interesting to observe the trend in the dependent variables of average velocity and turbulence kinetic energy at lower levels of $Grid$. In this region an increase in the level of $Refine$

seems only to worsen the solution instead of making it more accurate. The reason for this trend is that the effects of $Grid$ and $Refine$ on are in opposite directions. Table 6 illustrates:

Table 6: Linear effect coefficients of the 2nd order polynomials fitted to velocity and turbulence kinetic energy.

Dependent variable	v_{ave}	k_{ave}
$Grid$ effect coefficient	-0.00439	-0.000607
$Refine$ effect coefficient	0.00142	0.000247

From the coefficients of the fitted response, it can be seen that a decrease in $Grid$ would result in an increase in velocity and turbulent kinetic energy, while a decrease in $Refine$ would decrease those same variables. Accordingly, when the levels of $Grid$ and $Refine$ are decreased simultaneously, their effects cancel each other out to a certain extent as illustrated in Figure 32.

C. Balancing Numerical Accuracy and Computational Time

The contour plots of the surfaces displayed in Figure 32 are shown below:

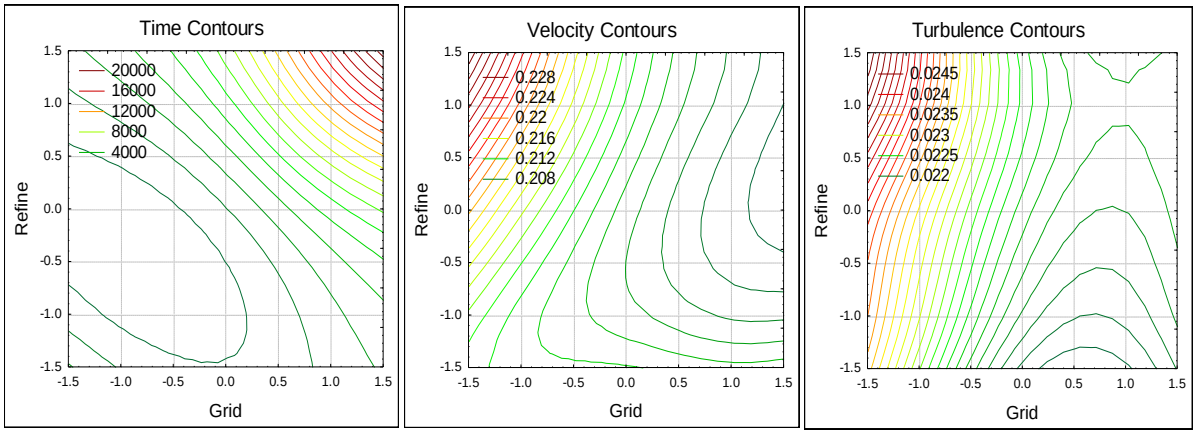

Figure 33: Contour plots of dependent variable responses to changes in $Grid$ and $Refine$.

It is accepted that areas towards the top right corner of the contour plots in Figure 33 represent regions of greater accuracy and higher computational cost, while areas at the bottom left are of lower accuracy, but much more economical on computational time. A fixed criterion is thus required to decide on a point, as far as possible towards the bottom left of the graphs, where the numerical accuracy is still acceptable.

A graphical measurement criterion was developed as follows: Rectangles were drawn from the top right corner of the contour plots of velocity and turbulent kinetic energy. The lack of grid independence at the bottom left corner of the rectangle was then quantified by the amount of variance present within the rectangle.

The maximum allowable variance within the rectangle was set to be 2% of the value at the top right corner of the contour plot. This is a very strict criterion and will ensure grid independent results. The graphical calculations are shown in Figure 34.

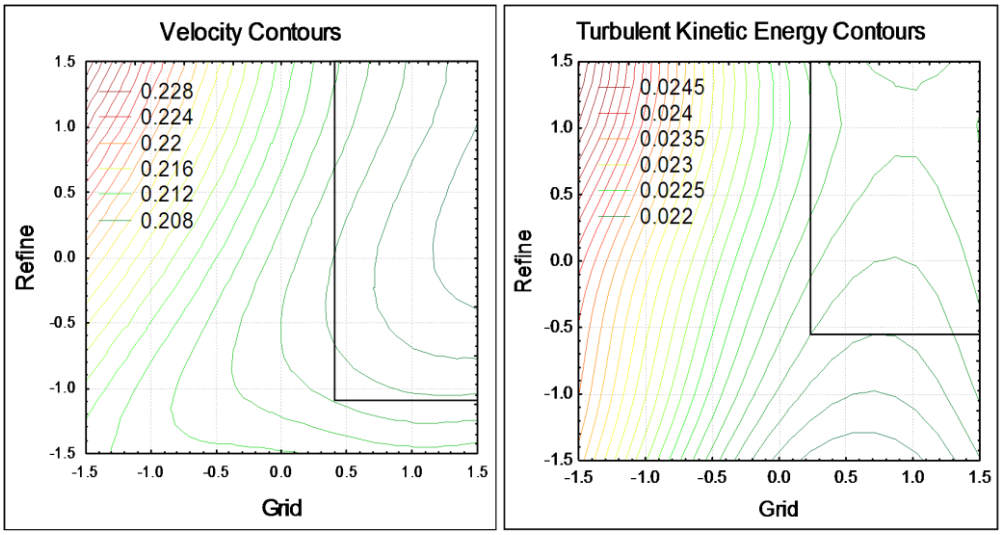

Figure 34: Graphical calculations on the contours of velocity and turbulent kinetic energy.

Under this criterion, the velocity contour plot specifies the minimum allowable values of $Grid$ and $Refine$ as 0.42 and -0.35 respectively (Figure 34). The contours of turbulent kinetic energy allow minimum values of 0.25 for $Grid$ and -0.52 for $Refine$. The combination of these two designates the point where $Grid$ is 0.42 and $Refine$ is -0.52 as grid independent under the criterion of 2% allowable variance.

This point can now be tracked on the contour plot of time to see whether the computational power requirements are still acceptable.

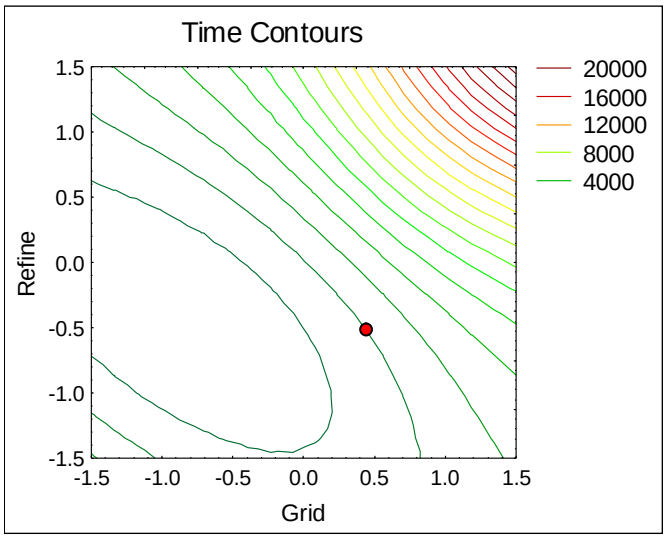

Figure 35: The time requirements for the point adhering to the 2% variance grid independence criterion.

Figure 35 shows that the designated point falls safely before the strong exponential rising stage toward the top right of the graph. This confirms that good grid independence (2% variance) can be achieved at acceptable computational costs.

3.5. Implications on the Primary Model

It was statistically proven that important parameters should be set in the following manner to ensure sufficient numerical accuracy at acceptable computational costs:

- Second order discretization is mandatory for accurate solutions.
- The discrete phase number of tries can safely be set to result in a conservatively high value of 400 particle tracks without significant computational costs.
- An initial grid size of 14.52 cm should be implemented to result in a refined grid size of 3.63 cm.
- A double grid refinement should be employed in the gas/liquid plume region on cells having a velocity larger than 0.35 m/s.

4. Bubble Characteristics

4.1. Background

When the DPM is used to track the bubble plume, special care must be taken to implement the correct force balance over each particle. Additional information on the characteristics of argon bubbles rising in molten steel is therefore required.

An extensive literature survey could not turn up any conclusive information on bubble characteristics, warranting a separate investigation on the subject. Accordingly, a small scale simulation of a single bubble rising through the melt was completed to acquire the necessary information.

4.2. Model Description

A small scale, 3D, transient model was developed implementing the standard k-ε model to model turbulence and the VOF multiphase model to track the interface between metal and gas.

4.2.1. Geometry

A small cylinder, 50 cm in diameter and 20 cm height was meshed with uniform hexahedral cells of size 1.25 cm up to an inner diameter of 30 cm. This inner region was refined once to a grid size of 6.25 mm. Larger cells were used on the outside of this region to ensure that the walls of the cylinder were sufficiently far removed to have no impact on flow phenomena near the centre of the cylinder. Figure 36 displays the meshed geometry.

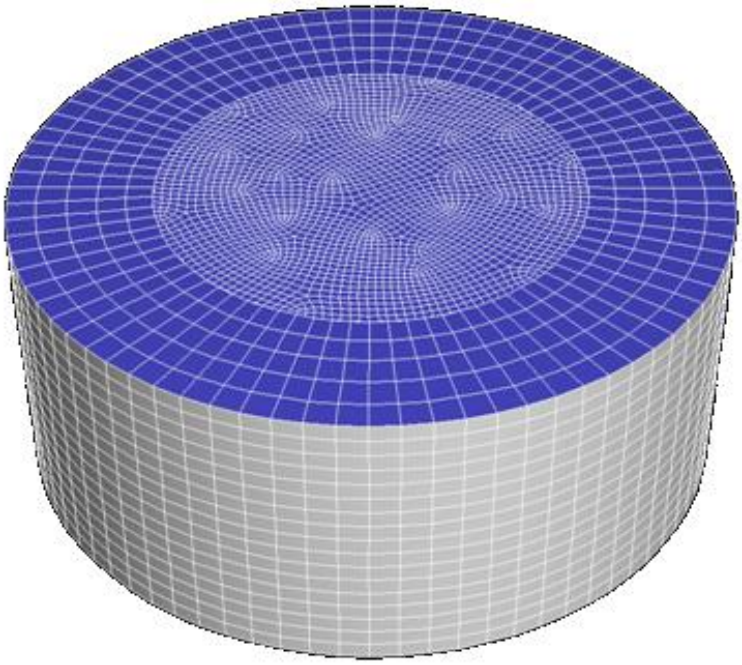

Figure 36: The meshed geometry used in the small scale simulation.

4.2.2. Boundary Conditions

A downwards flow of steel was induced in the cylinder to keep the rising bubble near the centre of the geometry. Through trial and error, the terminal velocity of the bubble was determined to be 0.35 m/s. This downwards flow condition was imposed at the mass flow inlet boundary defined at the top of the cylinder. The bottom of the cylinder was defined as a pressure-outlet.

Due to the strong hydrostatic pressure gradient present in the vessel, the bubble experiences a reduction in pressure as it rises through the melt. Hence, the pressure specified at the top and bottom boundaries were modified to change with time by using user defined functions (Chapter XV:1).

From previous simulations it was known that a bubble requires approximately 2.5 seconds to traverse the length of a 4 m steel vessel, giving it a rise velocity of 1.6 m/s. It is also known that 1 meter of steel equals a pressure difference of 68,11 kPa. Accordingly, the rate of pressure change on the bubble was calculated as 108.98 kPa/s.

A boundary condition of frictionless wall was imposed on the sides of the cylinder to ensure that the walls have no influence on the flow.

4.2.3. Material Properties

The gas was specified as a compressible ideal gas. This formulation required the energy equation (Equation 13) to be activated as well. Table 7 gives the physical properties employed.

Table 7: Material properties used in the small scale simulation.

Material	Steel (62)	Argon
Density (kg/m^3)	6942.9	Ideal Gas
Viscosity (Pa.s)	0.00503	8.9E-5 (63)
Thermal conductivity (W/(m.K))	35.24	0.071 (64)
Heat capacity (J/(kg.K))	795	520 (65)
Interfacial tension (N/m)	1.823	

4.2.4. Methods

The solution was initialized to consist only of molten steel flowing downward at the terminal rising velocity of the bubble. Subsequently, a stationary spherical gas bubble was patched in and the iteration process was started.

Two seconds of simulation time were run at constant pressure to allow the spherical bubble to attain the correct spherical capped shape. The pressure reduction UDF's were then activated to simulate the rise of the spherical capped bubble through the hydrostatic pressure gradient.

Animation files of an iso-surface created at a steel volume fraction of 0.5 were saved at every time step to qualitatively observe the behaviour of the rising bubble.

4.3. Results and Discussion

The bubble experienced some pronounced changes as it rose through the melt. Figure 37 shows the bubble as it was patched in and again as it has evolved after 3.9 seconds of evaluation.

Figure 37: The bubble at t = 0 s (left) and t = 3.9 s (right).

Four distinct characteristics can be observed in a qualitative evaluation of Figure 37:

- Larger bubbles adopt the characteristic spherical capped shape
- Significant growth results from the decrease in pressure around the bubble
- Bubbles break up once a critical size is reached
- A number of smaller bubbles travel in the wake of the larger bubbles

4.4. Implications on the Primary Model

In order to ensure an accurate force balance over the discrete particles tracked by the DPM, the following modifications are required:

- A custom drag law to account for the bubble shape
- A decrease in bubble density and a consequent increase in volume and diameter as a result of decreasing pressure
- A law governing bubble breakup
- A modified size distribution at the discrete phase inlet

CHAPTER V:
NUMERICAL MODEL SETUP PART 2: PRIMARY MODEL

> *Always design a thing by considering it in its next larger context –*
> *a chair in a room, a room in a house, a house in an environment,*
> *an environment in a city plan.*
> ***- Aliel Saarinen***

Following the advice provided above, the model was designed not only for believable results, but also for computational efficiency, simplicity of use and easy generalization. This model would now have the ability to generate flow and mixing results of sufficient accuracy at reasonable computational costs for a large number of distinctly different ladle setups.

1. Initial Decisions

The first decision to be made in geometry creation is the distinction between 2D and 3D and the possibility of using symmetry planes. The majority of mathematical modelling studies presented in the literature employ a two dimensional axis-symmetrical approach with a plane of symmetry on the centreline (43; 44; 52; 49; 46).

The most obvious drawback of this setup is the restriction to a single tuyere positioned axis-symmetrically on the centre floor. Studies also indicate that conditions inside the turbulent bubble plume are not well represented by 2D models (10) & (66), mostly due to the inherent 3D nature of turbulence. It was also argued that the rising bubble plume is asymmetric by nature and swirls around with time, thus requiring a full 3D continuum for accurate simulation.

Once the 3D decision has been made, the meshing philosophy must be established. The limited number of 3D studies located in the literature utilizes a grid built on cylindrical coordinates (10; 24). The drawback of this setup lies in the wide range of cell sizes created, ranging from very small at the centre to very large at the perimeter. If tuyere setups other than axis-symmetrical are investigated, the high velocity plumes will fall in this region of coarse cells and result in serious grid independence problems.

For improved model accuracy and versatility it is required that the cylindrical model be filled with grid cells of constant size. No 3D models utilizing this setup could be located in the literature, but it is definitely the preferred option.

The next decision is to distinguish between a steady state and a transient solution. The vast majority of literature studies have been completed at steady state, simply because it is much more economical on computational resources. There are substantial drawbacks in calculating a steady state solution, however. No transient phenomena (such as surface wave formation) can be

simulated and the primary performance measure of mixing – the mixing time – cannot be determined. Additionally, the geo-reconstruction scheme used to capture the interfaces in the VOF model only functions with the transient solver. A very limited amount of information can be extracted from a simulation burdened with these drawbacks, and a transient simulation therefore is the only option.

2. Model Description

A fully transient 3D numerical computation of flow and mixing was carried out using a combination of the discrete phase and volume of fluid multiphase models. Turbulence was modelled using the standard k-ε model with a slightly reduced ε generation constant. The commercial CFD package, FLUENT 6.3 was employed as outlined below.

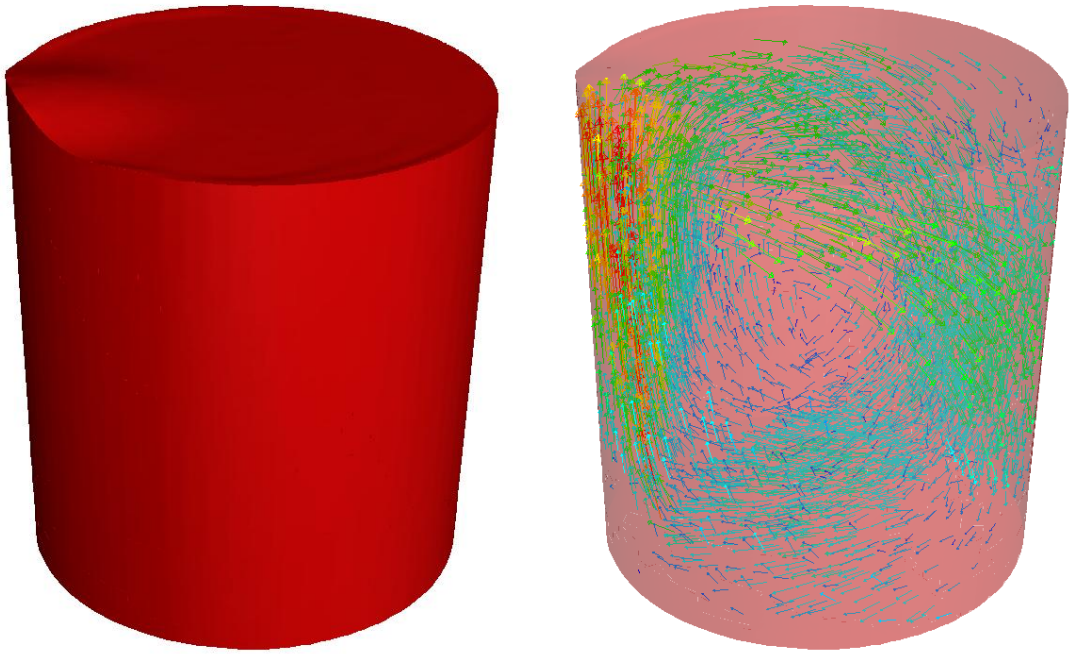

Figure 38: The simulated melt (left) with the flow patterns inside (right).

2.1. Geometry Creation

FLUENT's standard pre-processor, GAMBIT 2.3, was used to create and mesh the geometries. The 3D cylindrical volumes were created with dimensions required by the specific experimental run for which they were intended.

Each volume was meshed with uniform 14.52 cm hexahedral cells as determined in the grid independence study (Chapter IV:3) using the Cooper scheme available in GAMBIT 2.3. Due to the simplicity of the geometry, the mesh generated was of very high quality and the worst element typically had a skewness of 0.4.

2.2. Dynamic Grid Adaption

Macros were implemented to maintain the double refinement in regions with a flow velocity higher than 0.35 m/s as recommended in Chapter IV:3.5. Additionally, the double refinement was also maintained at the interfaces between metal, slag and gas. Further tests also revealed that solution accuracy could be improved by another 4% when a single level of refinement was implemented at flow rates above 0.1 m/s. Refinement masks were implemented to ensure that these refinements did not occur in the top gas phase.

These criteria typically resulted in 3.63 cm cells in the plume and at the interfaces, 7.26 cm cells in the upper recirculating regions and 14.52 cm cells in the lower bulk of the ladle as illustrated in Figure 39.

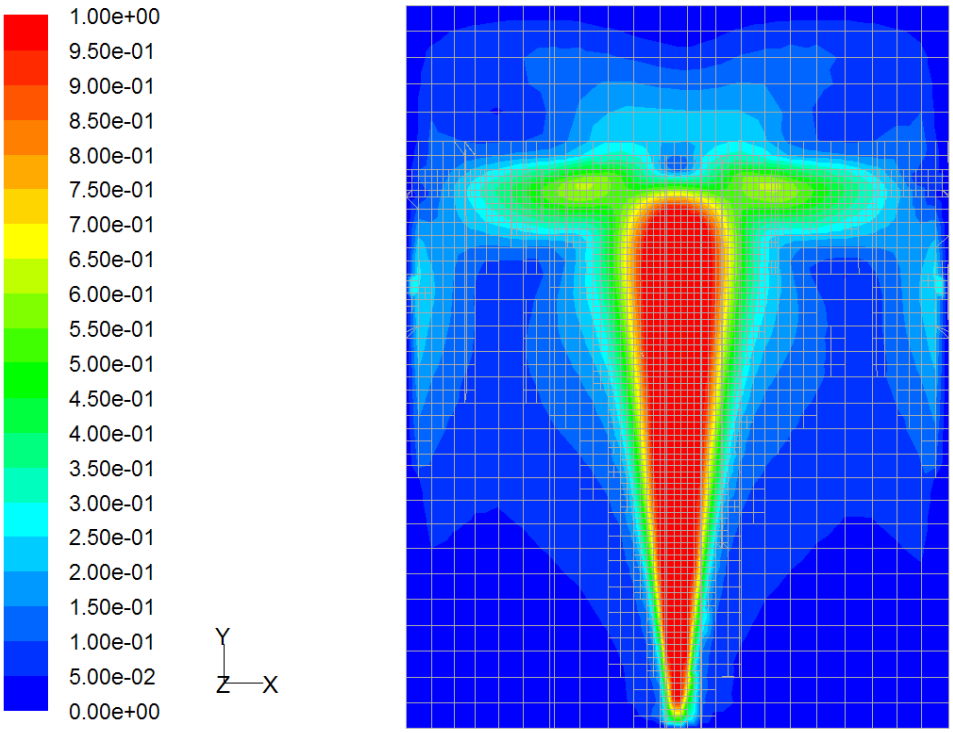

Figure 39: Grid refinement implemented in the full scale simulation exercise.

The stability of the model could also be improved by refining for the turbulence kinetic energy dissipation rate, especially in ladle setups where the plume approached the wall and wall functions were used under strong turbulence. Therefore, a double refinement was implemented when $\varepsilon > 0.05$ m^2/s^3. This criterion typically increased the refinement in the plume eye region where the plume impinges on the free surface.

2.3. Governing Equations

The standard conservation equations for mass (Equation 64), momentum (Equation 65) and species (Equation 66) were used as implemented in FLUENT 6.3 For a more comprehensive description, see Chapter III:3.

$$\frac{\partial \rho}{\partial t} + \nabla \cdot \left(\rho \vec{v} \right) = S_m$$ Equation 64

$$\frac{\partial}{\partial t}\left(\rho \vec{v} \right) + \nabla \cdot \left(\rho \vec{v} \vec{v} \right) = -\nabla p + \nabla \cdot \left(\bar{\bar{\tau}} \right) + \rho g + \vec{F}$$ Equation 65

$$\frac{\partial}{\partial t}\left(\rho Y_i \right) + \nabla \cdot \left(\rho \vec{v} Y_i \right) = -\nabla \cdot \mathbf{J_i} + R_i + S_i$$ Equation 66

Species conservation was completed only to track the inert tracer through the domain, neglecting all chemical reactions. Additionally, no energy transport was modelled. See Chapter VI:1.1 & 1.2 for a discussion of these assumptions.

2.4. Turbulence Modelling

The standard k-ε model was implemented to model turbulence inside the ladle. A modification was made to the model by reducing the ε generation constant from the default value of 1.44 to 1.38. This modification was needed to correctly predict the turbulent dispersion within the plume in the absence of a generalized model for turbulence modulation by the rising bubbles. Clarification of this decision is given in Chapter IX:4.

The Reynolds stress model was tested and found to give unrealistic flow results (Chapter VI:1.4.1).

2.5. Multiphase Modelling

Multiphase characterises were treated with a combination of the volume of fluid and discrete phase models. To review the logic behind this decision, see Chapter III:4.2.1.

2.5.1. Volume of Fluid Model

The VOF model adapts the continuity equation with a volume fraction term, α_q (Equation 51). If a cell is found to consist of two or more phases, an interface must be interpolated through it. The geometric reconstruction scheme was selected as the interface interpolation method to ensure maximum accuracy in interface tracking.

The explicit VOF formulation was selected so that the accurate interface tracking capability of the geometric reconstruct scheme could be utilized. The explicit formulation is also necessary to study transient solution behaviour such as surface waves. The implicit body force formulation was selected to improve model stability in the presence of large body forces.

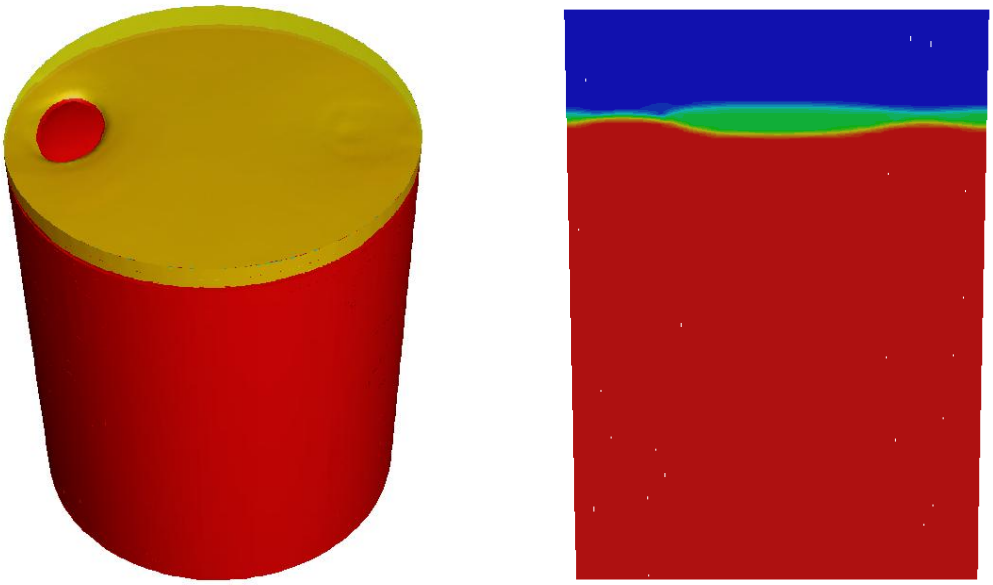

Figure 40: Three- and two dimensional representations of the two free surfaces tracked by the VOF model when a slag layer is included.

2.5.2. Discrete Phase Model

In the Lagrangian framework of the DPM, the trajectory of every individual particle is calculated by integrating a force balance over it. The accuracy of this force balance is of cardinal importance, since it is the sole medium through which the buoyant energy is transferred to the continuous phase.

To increase the accuracy of this force balance, a number of mandatory alterations to the standard DPM formulation were identified in Chapter IV:4.4. These, along with a few others, were implemented in the primary model as described under the sub-headings that follow.

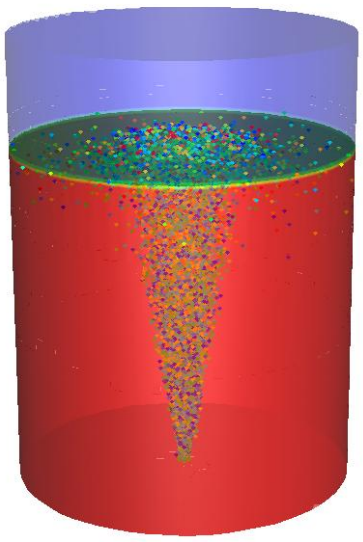

Figure 41: Discrete phase particles rising through the melt.

A. Bubble Shape

Due to the characteristic spherical capped shape assumed by the majority of the rising bubbles, a custom drag law had to be implemented. A suitable drag law was proposed by Xia *et al.* (50) which accurately accounts for the way a bubble changes shape as it grows. This drag law is given in Equation 67.

$$C_D = \frac{2}{3}\left(\frac{E_0}{3}\right)^{0.5}$$ Equation 67

The Eotvos number (E_0) is a dimensionless number describing the shape of the bubble and is expressed as follows:

$$E_0 = \frac{g\left(\rho_l - \rho_g\right)d_B^2}{\sigma}$$ Equation 68

The custom drag law was implemented by means of a user defined function (UDF) as given in Chapter XV:2.

B. Bubble Growth

Particle growth was linked to the absolute pressure experienced by the particle in any given computational cell. Subsequently, the ideal gas relationship was used to alter the density of the particle as it rose through the melt.

$$\rho_B = \frac{M_r P}{RT}$$ Equation 69

From the density, the volume was calculated as follows:

$$V = \frac{M_B}{\rho_B}$$ Equation 70

And the diameter:

$$d_B = 1.6\left(\frac{6V_B}{\pi}\right)^{\frac{1}{3}}$$ Equation 71

The small scale VOF simulation revealed that the diameter of the average spherical capped bubble was 1.6 times that of a spherical bubble of equal volume – thus the factor of 1.6 in Equation 71.

C. Bubble Breakup

From qualitative observation of the small scale VOF simulation it was observed that the bubble breaks up into two daughter bubbles of roughly equal size once it reaches a diameter of 4 cm. Accordingly, this breakup characteristic was built into the model as well. Bubble growth and breakup was implemented in a single UDF as displayed in Chapter XV:3.

D. Turbulent Dispersion

Turbulent dispersion of the bubbles is implemented using a stochastic tracking approach as provided in FLUENT 6.3. In this approach, the trajectory of the particle is influenced by the instantaneous velocity $(\bar{u} + u')$ and not solely by the Reynolds averaged velocity $(\bar{u})$. For more detailed information, refer to Chapter III:4.2.2.A.iii.

A constant of 0.16 was specified in calculating the Lagrangian time (Equation 47) according to the experimental measurements of Xie and Oeters (15). The discrete phase number of tries was set to result in 400 particle tracks.

E. Phase Coupling

Two-way coupling was implemented between the discrete and continuous phases. Discrete particles can therefore transfer momentum to the continuous phase to facilitate flow and mixing.

F. Steady or Unsteady Particle Tracking

The steady state DPM formulation was employed in the majority of the experiments where the focus was on the attainment of a flow steady state solution in the shortest amount of time possible. Shorter solution times could be attained with the steady state formulation because it tracks particle streams, and transfers momentum, through the entire length of the melt from the very start of the simulation. Additionally, the steady state formulation is more computationally efficient (review Chapter III:4.2.2.A.i for more detail).

When inherently transient phenomena are investigated, however, unsteady particle tracking is required. These situations include the investigation of surface wave formation and accurate representation of process start-up and shut-down.

The breakup model described in Subsection C above can only function when steady state particle tracking is employed. This model functions by simply halving the particle volume while the mass flow of the stream remains constant, thereby automatically doubling the amount of particles in the stream. When this model is implemented with the parcel formulation of unsteady particle tracking, particle volume is simply halved and no extra particles are created.

Ignoring bubble breakup when unsteady particle tracking is used has been investigated and was found to have a negligible influence when atmospheric pressure is employed at the surface (Chapter VI:1.3.3). It is only under reduced pressure, when the bubbles experience substantial growth in the upper regions of the vessel, that bubble breakup has a significant impact on the overall momentum transfer.

2.6. Physical Properties and Boundary Conditions

2.6.1. Continuous Phase

The bottom, side and top boundaries of the vessel were taken as walls with no-slip boundary conditions imposed on them.

Properties of the metal, slag and top gasses were specified as follows:

Table 8: Material properties of the three phases.

Material	Density (kg/m^3)	Viscosity (Pa.s)
Metal (62)	6942.9	0.00503
Slag (67)	2860	0.04
Top gasses	0.5	8.9E-5 (63)

The density of the top gas phase was chosen to be slightly higher than that of the discrete phase particles exiting through the free surface so that they can continue to rise upwards. This slightly increased density will not influence the solution since the gas phase is simply too light to have any impact on the flow in the steel phase.

Interfacial tension between the phases can be included when the VOF multiphase model is used and was specified as follows:

Table 9: Surface and interfacial tensions between the three phases.

Interface	Interfacial tension (N/m)
Metal/Gas (62)	1.823
Metal/Slag (67)	1.15
Slag/Gas (67)	0.58

2.6.2. Dispersed Phase

Side and bottom walls of the vessel were designated to reflect particles that come into contact with them, while the top wall was set to let the particles escape.

Every tuyere was represented by means of 16 point sources situated within a radius of 0.05 m, specified with the solid-cone DPM-injection option in FLUENT 6.3. Any number of these simulated tuyeres could be set to originate anywhere in the ladle.

The starting particle size distribution was built on an equation reported in the literature (61) as well as on knowledge obtained from the small scale VOF simulation. The Rosin-Rammler size distribution available in FLUENT 6.3 was implemented to release particles around an average diameter of 0.02 m. The Rosin-Rammler approach calculates the fraction of particles smaller than a given diameter (d) as follows:

$$Y_d = e^{-(d/\bar{d})^n}$$ Equation 72

The spread parameter (*n*) was defined as 2.5 and the distribution was constrained between maximum and minimum values of 0.002m and 0.025m respectively.

It is important to understand, however, that the injection parameters only play a minor role in determining bulk flow characteristics within the vessel. It is concluded in an extensive review (6) that bulk flow characteristics are determined by the bubble characteristics in the fully developed plume region and conditions at the injection tip are negligible. The custom drag, growth, breakup and bubble shape models discussed earlier ensure that momentum transfer inside this fully developed plume region is modelled accurately.

3. Solution Procedure

3.1. Numerical Model Start-Up Procedure

The vessel was initialized with zero values for all variables except for the turbulent quantities k and ε. These quantities were set to values 0.01 m^2/s^2 and 0.001 m^2/s^3 respectively, primarily to facilitate turbulent dispersion of the bubble plume from the start of the simulation. The top gas and slag regions were then patched in.

The transient simulation was allowed to run until flow steady state conditions were reached. Such a condition was identified by monitoring the average flow velocity and turbulent kinetic energy inside the vessel. Once these monitored flow variables settled at a constant value, a cylinder, 0.4 m in height and diameter, of tracer element was patched in on the floor of the vessel directly over the discrete phase source. This tracer element was specified as a separate species with identical physical properties to that of the steel.

The flow time was reset to zero, the solvers for momentum and turbulence were turned off and the spread of tracer was solved on the frozen steady state flow pattern. The validity of this simplification is discussed in Chapter VI:1.6 where it is shown that this strategy effectively halves simulation times at negligible costs in accuracy.

3.2. Solution Controls

Pressure discretization was done using the PRESTO! scheme, which is recommended for situations involving swirl and strong streamline curvature.

Discretization of the continuity, momentum and turbulence equations was done using the second order upwind scheme as recommended in Chapter IV:3.

The power law was used for species discretization. The second order upwind scheme would be preferable, but allowed for some diffusion of the tracer element through the free surface and into the top gas phase. The reason for this error is not well understood at present.

For pressure-velocity coupling, the PISO scheme is used. This scheme is part of the SIMPLE family of algorithms, but completes additional iterations for skewness and neighbour corrections. These

additional corrections counteract the biggest problem encountered by the SIMPLE algorithm – the fact that new computed velocities often do not satisfy the momentum equation after the pressure equation has been solved. By immediately correcting these discrepancies, the PISO scheme achieves faster convergence and also allows the use of significantly higher under-relaxation for both pressure and momentum, resulting in a substantial reduction in the number of iterations required for convergence.

3.3. Convergence Criteria

Convergence was judged by means of scaled residuals of flow variables. The scaled residual of continuity appeared unrealistically large due to the model having no in- or outflows. This overestimation of the continuity residual is known to occur when a good initial estimate is provided. It was found that a convergence criterion of scaled residuals < 10^{-3} for all the remaining variables was sufficiently accurate.

This criterion could be met within five iterations at time steps varying between 0.01 and 0.1 seconds depending on the ladle setup under consideration.

4. Materials and Methods

4.1. Hardware and Software

Six simulations were run simultaneously on six processing cores, with clock speeds of around 3 GHz. The 32-bit Windows version of FLUENT 6.3.26 was used as the solver and post-processor, while the pre-processor GAMBIT 2.3.16 was used to create and mesh the geometry.

4.2. Methods

The average flow velocity and turbulent kinetic energy was monitored at every time step throughout the transient simulation. These values indicate the incidence of flow steady state and give a general idea of the flow characteristics in the vessel at any given time.

The quality of mixing was assessed by determining 95% bulk mixing times, defined as the time it takes for the minimum tracer concentration to reach a value of 95% that of the average tracer concentration in the domain. This was accomplished by monitoring and recording the average and minimum tracer concentrations within the metal zone. 95 % bulk mixing time was recorded when the minimum tracer concentration reached a value 95% that of the average tracer concentration.

CHAPTER VI:
DISCUSSION OF ASSUMPTIONS

By ignorance is pride increased
Those most assume who know the least
- John Gay

The mathematical modelling tools provided by commercial CFD packages make it very easy to design a model without fully understanding (or even being oblivious to) a large number of simplifying assumptions. Such uninformed assumptions will always lead to anomalous results which are almost impossible to interpret correctly.

The facts are however, that detailed mathematical simulation of the full array of physical phenomena present in gas stirred ladles is not feasible at present, and will remain out of reach for many years to come. Therefore, a number of simplifying assumptions are necessary to make a numerical solution possible.

The choices regarding these assumptions are arguably the most important modelling decisions facing the CFD engineer. For this reason, an entire chapter is dedicated to the detailed evaluation of every assumption incorporated into the current model. The chapter will also take a look at some questionable assumptions regularly used in the literature and discuss how and why they have been avoided in the present model.

1. Assumptions Incorporated

1.1. No Chemical Reaction or Species Transport

The baseline assumption in the current study is that mixing rate is controlling and that any modification resulting in shorter mixing times would automatically result in improved overall process performance. This assumption is thoroughly discussed in Chapter II:3, and the substantial amount of literature evaluating mixing in gas stirred ladles only serves to further strengthen the case for its validity. Therefore, chemical reaction, thermodynamics and reacting species transport could be safely ignored.

1.2. No Energy Transport

If steel is held inside a ladle for with no stirring, thermal stratification takes place as a result of natural convection (44) and can adversely affect the quality of steel produced. Twenty minutes of standing time can result in substantial temperature differences of up to 31°C (49). When gas stirring is present though, it has been shown that even gentle mixing can reduce thermal stratification to 2-

3°C (43; 48). For the purposes of the current study, this implies that the entire melt can be assumed to be at one constant temperature.

Industrial experience has shown that the melt loses heat at a rate of 3°C/min for heavy stirring and less than 1°C/min for light to normal stirring. Reported mixing times are rarely above 3 minutes, implying a maximum heat loss of 9°C, which, seen against the operating temperature of 1635°C, is negligible.

Accordingly, energy conservation (Equation 13) does not need to be employed to account for any temperature gradients or losses. Temperature dependent physical properties can be taken as constant over space and time.

1.3. The Bubble Plume

The use of the DPM for tracking the bubble plume automatically incorporates a number of important assumptions into the model. These are discussed as follows:

1.3.1. Bubbles Occupy No Volume

The volumeless particles tracked by the DPM makes it applicable only to disperse flows (void fraction smaller than 10-12%) where the volume contribution of the particles is negligible. The gas-stirring rates under consideration in the present model are relatively low, violating the criterion of 12% volume fractions only in the bottom regions of the plume. In these regions, the gas density is typically around 0.8 kg/m^3, implying that the 12% void fraction criterion will be met at particle mass concentrations less than 0.1 kg/m^3. Figure 42 illustrates regions violating this criterion at the maximum single plug flow rate (0.01 kg/s) that will be examined in the current study.

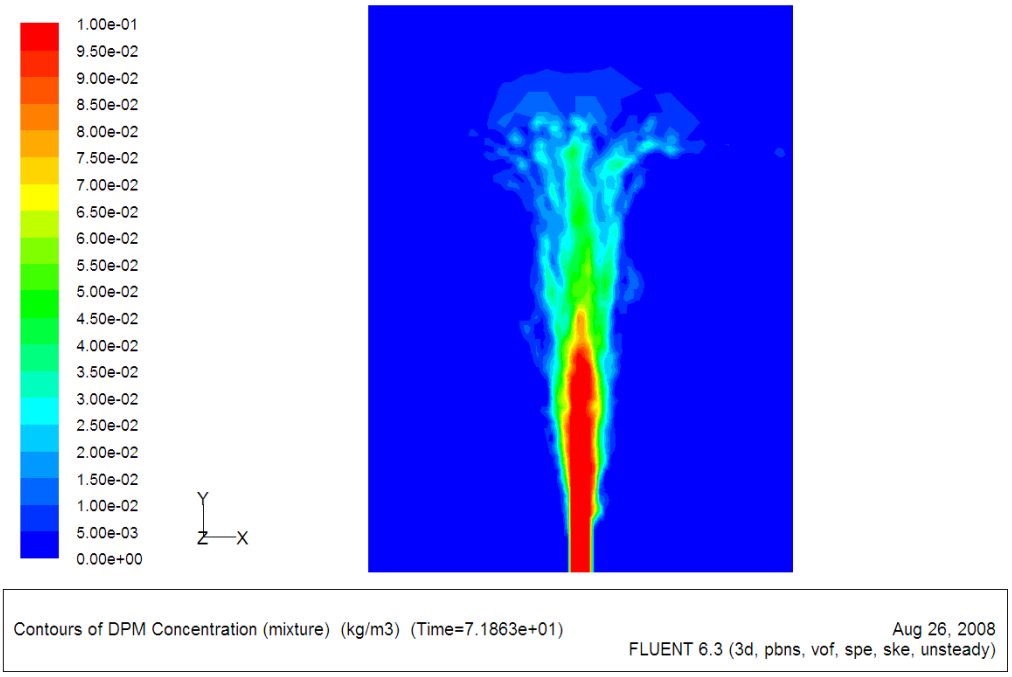

Figure 42: DPM concentration in full scale ladle purged at 0.01 kg/s.

The red region violating the 12% criterion seems quite large, but can be estimated to comprise only $0.023/0.786 \times 100\% = 2.9\%$ of the plume volume. In this calculation, the plume volume was calculated as a cone ($H = 3\ \mathrm{m}\ \&\ D = 1\ \mathrm{m}$) and the dense particle region as a cylinder ($H = 1.5\ \mathrm{m}\ \&\ D = 0.14\ \mathrm{m}$). No experiment was done at discrete phase concentrations larger than that shown in Figure 42.

These denser DPM concentrations at the base of the plume might cause slight over-predictions of momentum transfer in these regions. The bulk of momentum transfer takes place in the fully developed plume region, however, and small errors at the plume base will be negligible.

1.3.2. No Bubble-Bubble Interaction

In reality, bubbles rising in a concentrated plume interact through coalescence and breakup, vortex shedding and various other wake effects. The DPM particles, however, can only transfer momentum as a source term to the continuous phase and leave no vortex structures in their wakes. Additionally, DPM particles occupy no volume, meaning that two particles would simply pass straight through each other if they were to cross.

The cycle of breakup and coalescence is shown to be a steady state process, constantly maintaining a fixed size distribution (Chapter IX:1.2). A model for these effects is therefore redundant if the correct size distribution is specified initially.

Particle wake effects have been shown to reduce the drag coefficients on bubbles travelling in a swarm (Chapter III:5.2). The drag coefficient employed in the current simulation has been modified to account for these effects.

Any additional bubble-bubble interaction effects will only become important in dense bubble flows. Accordingly, the assumption of no bubble-bubble interaction would hold for flows below the recommended void fraction of 12%.

1.3.3. Models for Drag, Growth, Breakup and Size Distribution

It was concluded in an extensive review (6) that bulk flow characteristics are determined by the bubble characteristics in the fully developed plume region and conditions at the injection tip are negligible. Accordingly, it is very important to ensure accurate momentum transfer in all areas of this fully developed plume.

The artificial manner in which bubble characteristics are updated within the DPM bubble plume naturally comes with a number of assumptions: an empirical drag law, the ideal gas assumption for growth, breakup into two equally sized daughter bubbles and a roughly approximated size distribution. Additionally, the small scale VOF simulation (Chapter IV:4) which aided in the development of these approximated models, only represented a single bubble rising through the melt, completely neglecting any bubble-bubble interaction effects. These approximations are justified as follows:

Firstly, it is essential that the correct volume of gas be available for buoyant energy transfer in the entire length of the plume. For this reason the ideal gas law was implemented to account for gas

expansion due to the hydrostatic pressure gradient within the vessel. Under the high temperatures in steelmaking processes, the ideal gas law will hold.

The volume of gas must now be broken down into correctly sized parcels. This is the area in which the largest qualitative error will occur, simply because bubble size distributions, breakup and coalescence fall in a relatively poorly understood field of study. Quantitatively, however, it turns out that the bubble size distribution has a surprisingly small influence on bulk flow within the vessel.

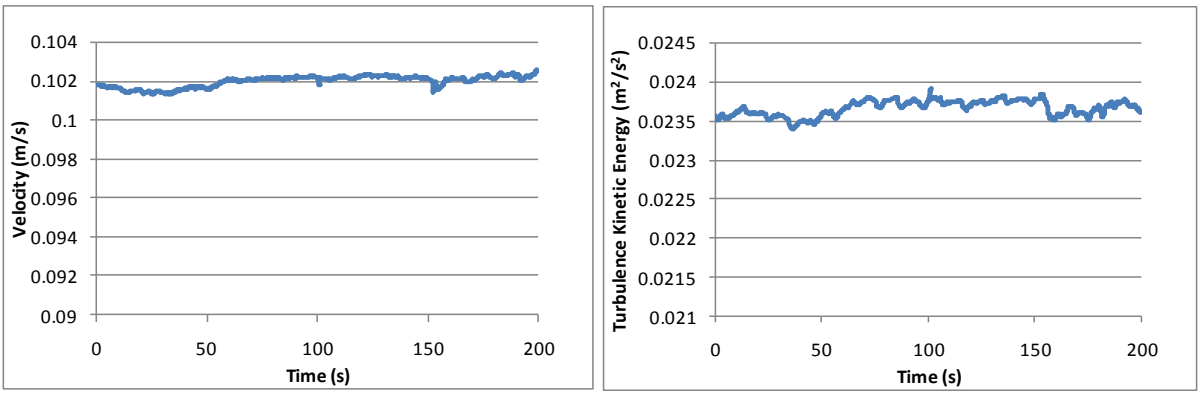

Figure 43: Response of the average flow and turbulence quantities within the vessel to changes in size distribution.

In Figure 43, the solution time on a steady state flow solution was reset to zero and the iteration process was started once more. At $t = 20$ s, the average diameter specification in the Rosin-Rammler size distribution was changed from 0.02 m to 0.01 m (see Chapter V:2.6.2). The injected particles were then specified be of constant size (0.02 m) at $t = 50$ s.

It was discussed in Chapter V:2.5.2.F that the breakup model cannot be implemented when unsteady particle tracking is used. To test the effect of this omission, the breakup model was disabled at $t = 100$ s and the switch to unsteady particle tracking made at $t = 150$ s.

From the evidence presented above, it is clear that even large errors in the specification of bubble size distribution will only cause a small error in the computation of overall flow fields. Accordingly, the margin for error is quite large and bubble size distributions derived from the small scale VOF simulation will ensure accurate buoyant energy transfer.

Lastly, the parcels of gas created should transfer the correct amount of momentum to the continuous phase. The drag law used for this purpose (50) is derived from a well established drag law for spherical capped and deformed bubbles and adapted especially to the case of a rising bubble plume. As a final test, this drag law was also compared against FLUENT's non-spherical drag law.

In Figure 44, the same process was followed as described above, this time only changing the drag law from the custom law (Equation 67) to FLUENT's non-spherical drag law (68) with a shape factor of 0.7 at $t = 20$ s.

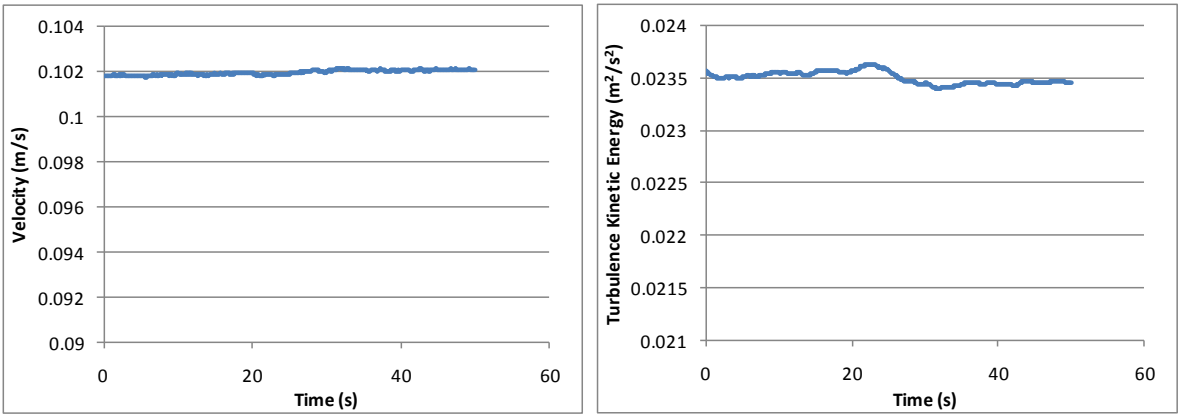

Figure 44: Effect of drag law on average flow and turbulence quantities inside the ladle.

Once again it can be seen that the effect of changing drag laws is negligible. This can either mean that the two drag laws, with distinctly different formulations, have exactly the same effect, or that the overall momentum transfer is not as sensitive to drag law as one might expect. Either way, Figure 44 installs confidence in the ability of the custom drag law to simulate accurate momentum transfer from the discrete to the continuous phase.

1.3.4. No Turbulence Modulation

The most important effect often neglected in the simulation of buoyancy driven flows is the contribution of bubbles to turbulence. This effect is thoroughly analysed and shown to be very important in Chapter IX:1.4, but is ignored in the full scale simulation exercise for lack of a generalized model.

1.4. Turbulence Modelling

1.4.1. Reynolds Stress Model vs. the k-ε Family

Theoretically speaking, the RSM is the best option for modelling turbulence in full scale gas stirred ladles. Validation experiments have shown, however, that results obtained with the RSM are completely unrealistic.

Figure 45 reveals that the flow pattern predicted by the RSM is distinctly different from the characteristic flows described frequently in the literature (see Chapter VII:1). The buoyant plume region is also predicted to be much narrower and more concentrated than recommended in literature sources (Chapter VII:2).

The reason for these discrepancies could lie anywhere in the complex formulation of the RSM, be the result of inappropriate model constants or possibly tie in with the multiphase approach used. It is known that the RSM has some generalization issues, and the current application clearly falls outside its range of valid applications.

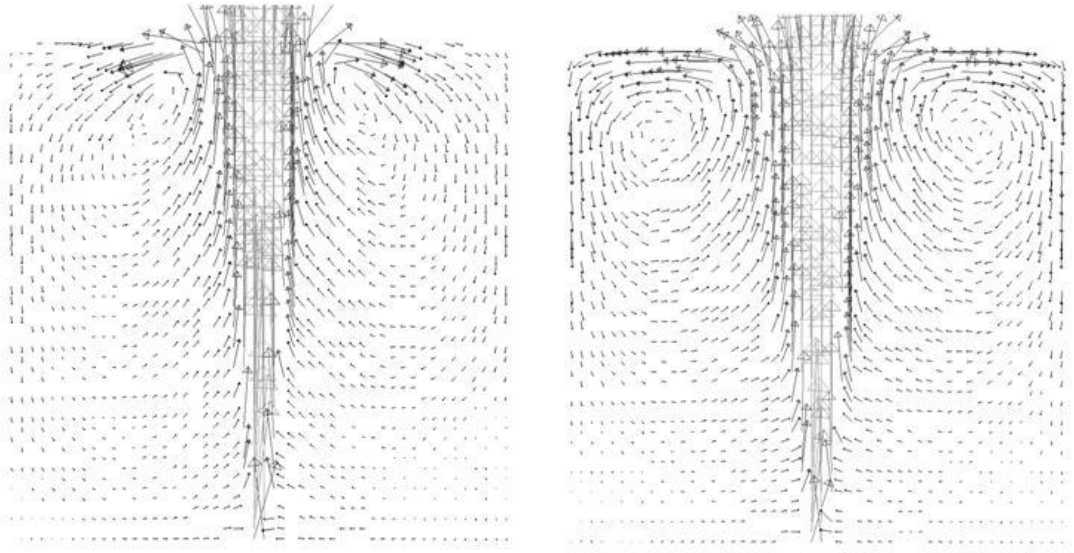

Figure 45: Flow patterns obtained with the RSM (left) compared to characteristic flows in centrically stirred ladles (right).

In the absence of the RSM, the k-ε models are the only alternative. A detailed study of these models has shown that the standard k-ε model is the only viable option when no turbulence modulation by bubbles is included in the model (Chapter IX:4.2).

1.4.2. Assumptions of the Standard k-e Model

Aside from the assumption of isotropic turbulence discussed in Chapter III:4.1.2, the SKE model also assumes that the flow is fully turbulent and that the effects of molecular viscosity are negligible.

Some studies have argued that the assumption of isotropic turbulence is incorrect (see Chapter III:4.1.2). This assumption is incorporated in the majority of mathematical modelling studies available in the literature though. Anisotropic turbulence is only present in the plume and its effect on the bulk flows outside the plume should be negligible. The exact impact of this assumption, however, cannot be determined at present.

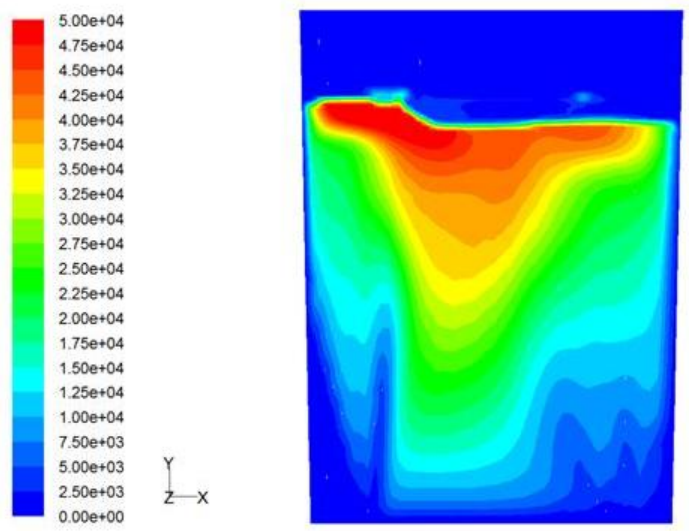

Figure 46: Contour plot of the turbulent viscosity ratio (μ_t/μ_m) from the experimental design in Chapter X:3.1.

When looking at the contours of the turbulent viscosity ratio (μ_t/μ_m) displayed in Figure 46, the remaining assumptions made by the SKE model are justified. It is clear that the majority of the vessel has a turbulent viscosity ratio greater than 10^3, implying that the diffusive influence of turbulence is more than 1000 times larger than that of molecular viscosity. It is therefore safe to assume that the flow is fully turbulent and the effects of molecular viscosity are negligible.

1.5. The Free Surface

The free surface and especially the plume eye, as tracked by the VOF model, contribute two more assumptions to the model.

The first lies in the formulation of the VOF model as a mixed fluid approach (see Chapter III:4.2.3) thereby sharing a single set of conservation equations between phases. The interface will influence the convective momentum transport, in this case forcing the flow to turn at the free surface under the force of gravity. Momentum will cross the free surface by diffusive transport, however, since the single momentum conservation equation does not recognize the interface and still diffuses momentum in all directions.

This modelling assumption will be of no significance when no slag layer is present. The density (and thus the momentum contribution) of the top gaseous phase is insignificantly small in comparison to the metal phase and will have no influence on bulk flows in the melt. Inclusion of a much more dense slag layer, however, could have an unwanted effect on flows in the steel phase. Momentum in the turbulent plume eye will cross from the steel to the slag layer by means of turbulent diffusion.

The second assumption lies in the representation of the plume eye:

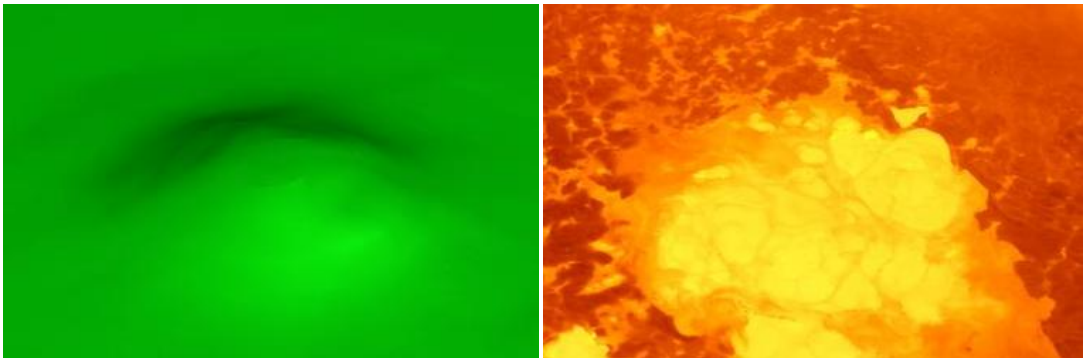

Figure 47: The plume eye as tracked by the VOF model compared to the actual process.

Figure 47 shows the modelled plume eye as a smooth bump at the top of the bubble plume. In reality though, the plume eye region is characterised by numerous smaller spouts resulting from the irregular arrival of bubbles to the free surface. The reason for the smooth appearance of the modelled plume eye resides in the large number of discrete phase particle tracks employed.

A large 'number of tries' of the stochastic particle tracking described in Chapter III:4.2.2.A.iii will create a stable, averaged representation of the plume and the plume eye. In reality though, the plume and the plume eye are meta-stable, constantly changing from one moment to the next. The averaged representation is simply preferred from a modelling point of view because it will give a stable flow steady state from which flow data can be extracted.

1.6. Mixing Time Computation

It was assumed that the mixing time could be determined accurately by solving the spread of tracer through the volume on the fixed flow patterns of an adjudged flow steady state. This was done by turning off the solvers for flow, turbulence and volume fraction, and solving only for species conservation. This assumption cut simulation time by about one day per experiment, literally saving weeks of computational time when summing over all the experiments completed.

The validity of this assumption was tested by comparing the tracer concentrations calculated when all solvers were activated to calculations completed using only the species solver.

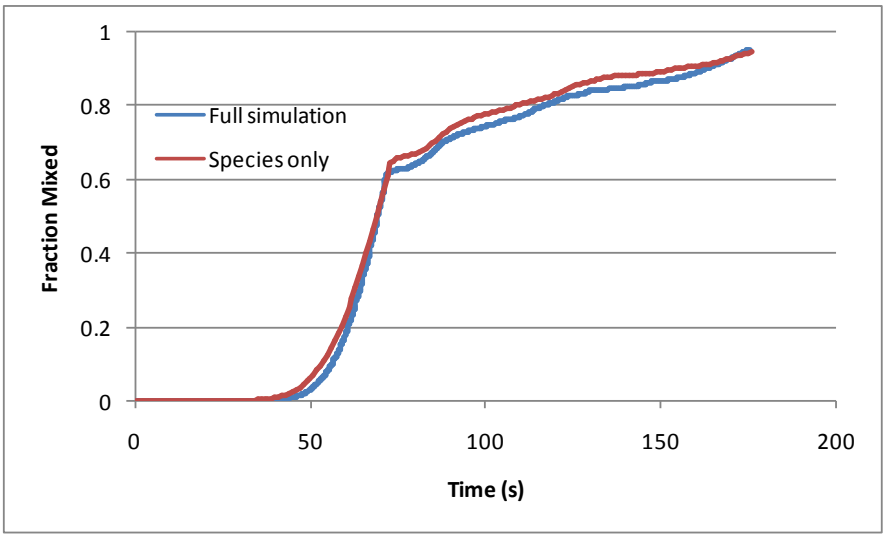

Figure 48: Comparison of the mixing time assumption to the real situation.

As displayed in Figure 48, the assumption holds true. Some minor discrepancies are observed over the course of the mixing as the result of some small flow pattern fluctuations still present in the vessel, but ends up in an almost identical final 95% bulk mixing time result.

2. Assumptions Avoided

A number of questionable assumptions were used in the majority of previous modelling attempts on flow in gas stirred ladles. Reasons for their avoidance are given in the following sections.

2.1. The Flat Free Surface

The flow problem is significantly simplified if the free surface separating the melt from the top gasses is simply approximated with a flat and frictionless wall. The error in this assumption is quite substantial, however, as displayed comparatively in Figure 49 and Figure 50.

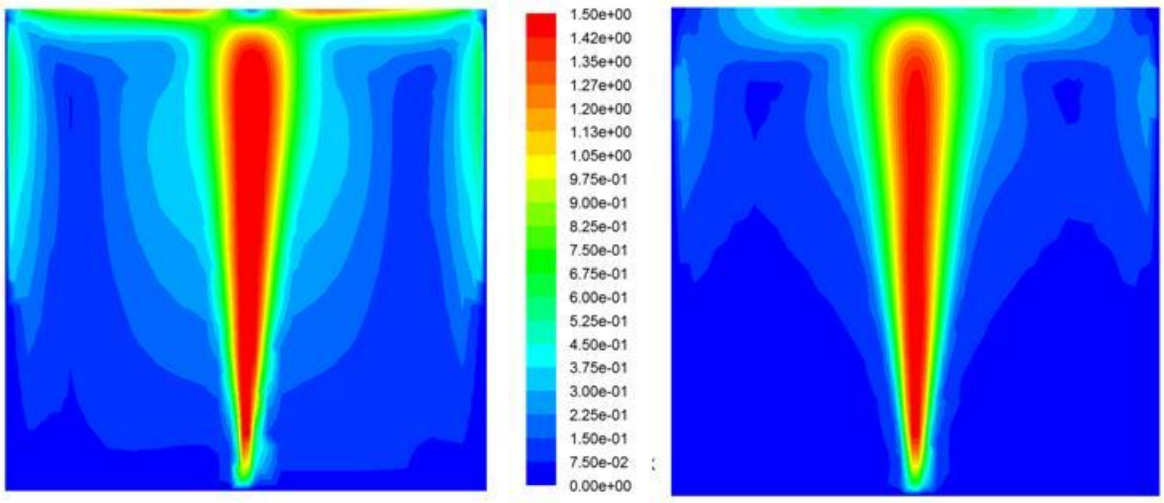

Figure 49: Comparison of flow velocities created by a flat free surface (left) and a mobile free surface (right).

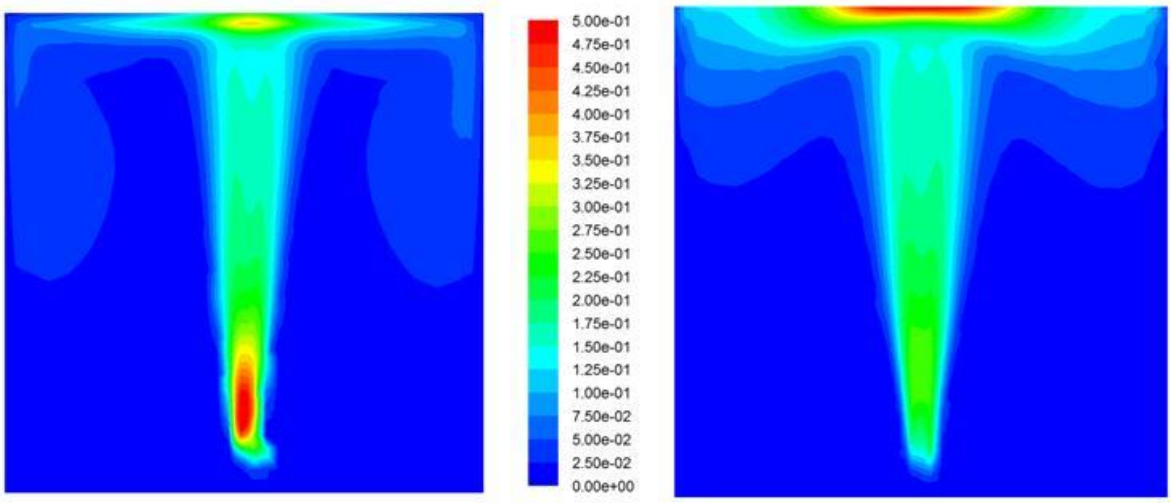

Figure 50: Comparison of flow turbulence kinetic energy distributions created by a flat free surface (left) and a mobile free surface (right).

Figure 49 indicates substantially stronger flow in the ladle with the assumption of a flat free surface. When quantified, this assumption results in errors of 81% for average flow velocity and 20% for average turbulence kinetic energy. The reason for this discrepancy lies just beneath the free surface of the plume, in the region known as the plume eye.

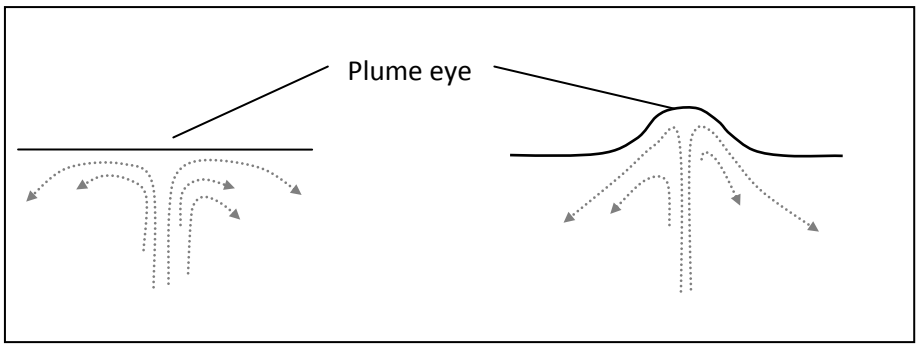

Figure 51: Flow patterns in the plume eye.

Figure 51 shows the difference in flow pattern development between simulations with a flat and a mobile free surface. When the surface is deformed, the flow is forced to go up into the plume, make a very sharp turn and then come back down again. The flat free surface allows flow patterns to turn much easier.

The biggest repercussion of this error in flow pattern development is the turbulence generation in the region of the plume eye. When a flat free surface is modelled, the velocity gradients are substantially under-predicted due to the smooth turns made by the flow patterns. The result is an equal under-prediction of turbulence generation due to mean velocity gradients (Equation 30). Turbulence kinetic energy dissipation is the primary kinetic energy sink in the ladle and an under-prediction of turbulence would result in an over-prediction of the overall kinetic energy in the ladle.

The error induced by this assumption becomes even more prominent when more complex tuyere setups are investigated. When more than one tuyere is involved, the incorrectly strong flow patterns resulting from one bubble plume can completely shift the direction of other plumes, creating very large discrepancies.

2.2. Bubble Size Distribution

The description of the size distribution in the bubble plume has often been approximated as spherical bubbles of constant size and constant gas density. Even though it has been proven that the flow problem is quite forgiving when it comes to the bubble size distribution (see Section 1.3.3), significant errors can arise through careless or uninformed modelling.

2.2.1. Constant Sized bubbles

The distribution of the bubble plume has often been approximated having a single, averaged size everywhere in the plume. The error induced by this assumption is shown in Figure 52.

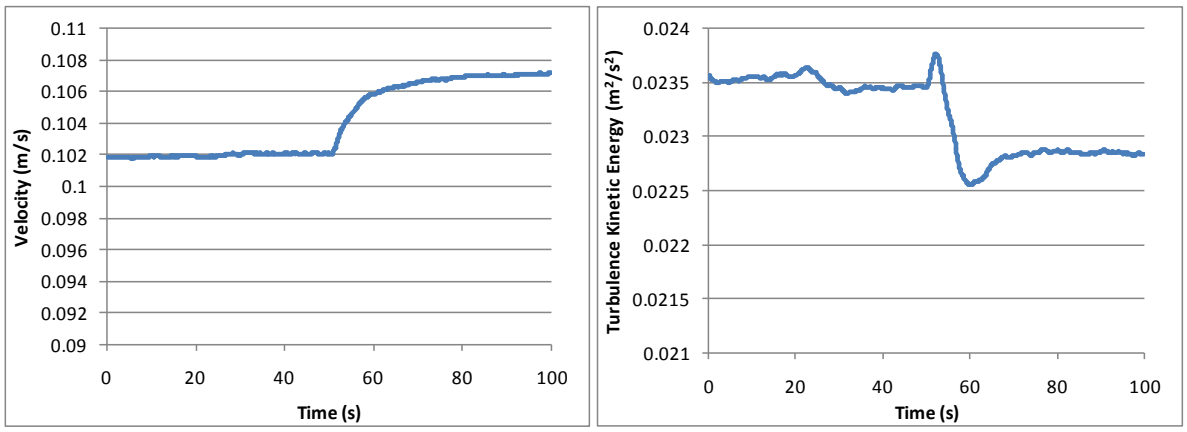

Figure 52: Response of averaged flow quantities to a change ($t = 50$ s) from growing to constant sized bubbles.

Figure 52 shows that the quantitative flow error (about 5%) induced by this assumption is not as great as might be expected. Still, the assumption of non-growing bubbles under the strong hydrostatic pressure gradient within the vessel redistributes the momentum input further towards

the bottom of the ladle. This results in weaker flows in the plume eye, where the majority of the turbulence is generated. Figure 53 illustrates:

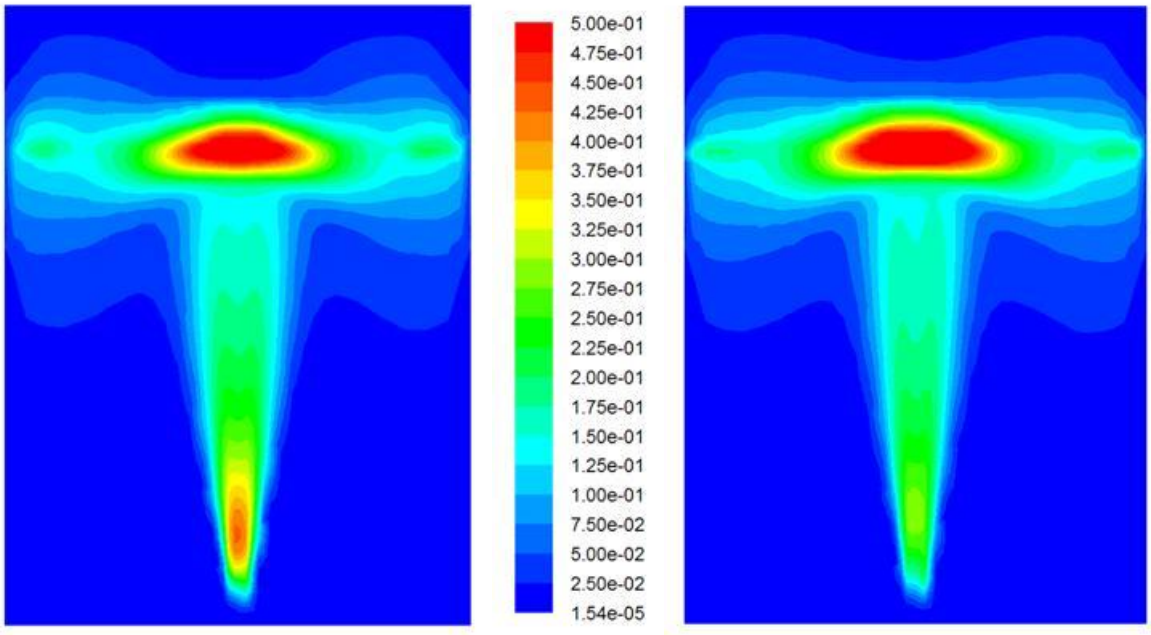

Figure 53: Turbulence profiles in the ladle with constant sized (left) and growing (right) bubbles.

Again the error is subtle, but the over-prediction of turbulence in the bottom regions and the under-prediction thereof in the plume eye region is clearly visible. When considering the ease of implementing a bubble growth law with the discrete phase model, this error should definitely be avoided.

2.2.2. Spherical Drag Law

It is well established that the majority of bubbles in the plume assume the spherical capped shape. Looking at the values of drag coefficients, a spherical bubble would have $C_D = 0.44$ and a 3.2 cm spherical capped bubble (calculated with Equation 67) would have $C_D = 2.38$. The impact of this discrepancy is shown below.

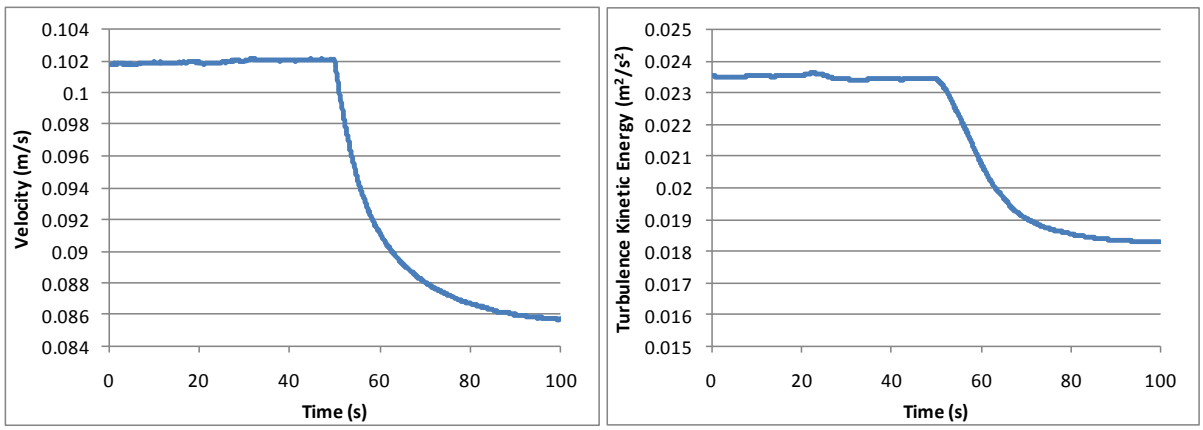

Figure 54: Response of averaged flow variables to a change ($t = 50$ s) from a non-spherical to a spherical drag law.

The error of this assumption is shown to be quite severe in Figure 54. The almost 20% decrease in both flow variables show a distinct decrease in the efficiency with which energy is being transferred from the rising bubbles to the metal. The assumption of spherical particles should therefore most certainly be avoided.

It is also interesting to note that a gross underestimation of drag coefficient (more than 5 times) incorporates an error of less than 20%. This strengthens the notion in Section 1.3.3 above that the solution is not very sensitive to the drag law implemented.

CHAPTER VII:
VALIDATION

> *All technology should be assumed guilty until proven innocent.*
> ***- David Brower***

Being a relatively new technology, computer aided mathematical modelling is certainly prone to the generalization mentioned above. Reality, known for often being stranger than fiction, can sometimes even be stranger than informed CFD.

To the author's knowledge, no flow probe has ever been designed and implemented to determine the exact flow field inside a gas stirred ladle. Exact mixing times in actual ladles have likewise never been determined. Accordingly, the only basis for comparison resides in the data provided by scaled cold model experiments.

A number of valuable validation experiments can be based on these small scale models though. A large body of flow pattern and mixing time data collected from water models is available, together with some scaled up mixing times which should provide a good comparative basis. Equations for plume parameters such as plume width and velocity have also been derived and scaled to application in actual steel ladles.

The remainder of this chapter will employ these resources to build a case for the validity of the present model.

1. Flow Field

The bulk flow field inside a gas stirred ladle is the primary influence on mixing, and therefore the most important subject for verification. High quality experimental data was acquired from the literature in a study by Xie and Oeters (15) measuring flow properties in a Wood's Metal bath (40 cm in diameter and 37 cm in height). Wood's metal is a low melting point alloy offering physical properties in the same range as those of the molten steel used in industrial ladles (Table 10).

Table 10: Physical properties of molten steel, Wood's metal and water.

Fluid	Density [kg/m^3]	Viscosity [Pa.s]	Surface tension [N/m]
Steel (1908K)	6943	0.00503	1.823
Wood's Metal (373K)	9400	0.0042	0.460
Water (298K)	998	0.001	0.073

An exact numerical replication of the experimental setup implemented by Xie and Oeters (15) was carried out using the primary model setup outlined in Chapter V. Unfortunately, the flow rates employed in this experimental study were very high relative to the small volume of the down-scaled

bath. These high gas purge rates caused particle void fractions inside the plume to be substantially higher than the recommended range of 10-12% (Figure 55). Some discrepancies can therefore be expected in the lower regions of the plume.

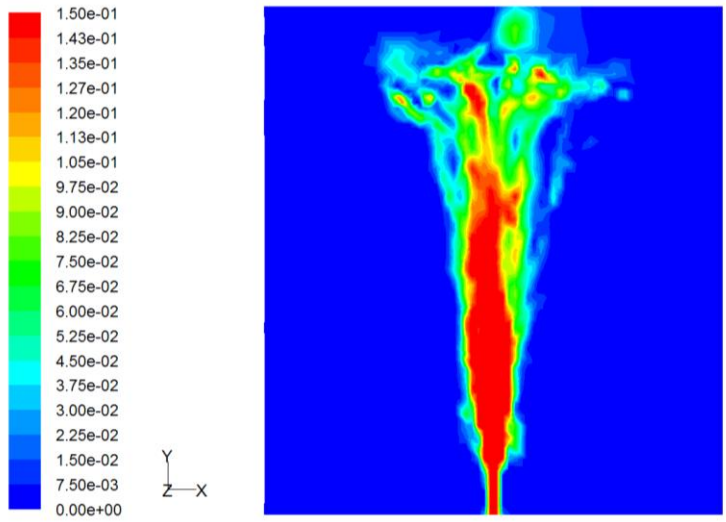

Figure 55: Contours of DPM particle concentration (kg/m^3).

Figure 55 shows regions of DPM volume fractions exceeding the recommended maximum of 12% as a large red zone in the centre of the plume. Experiments on the full scale ladle employ a smaller relative gas purging rate, working largely within the allowable range of the DPM (see Chapter VI:1.3.1). Nonetheless, the experimental data collected by Xie and Oeters (15) should provide a good basis for comparison of bulk flow fields on a qualitative basis.

1.1. Qualitative Comparison

The overall flow field inside the ladle as calculated with the model is shown below:

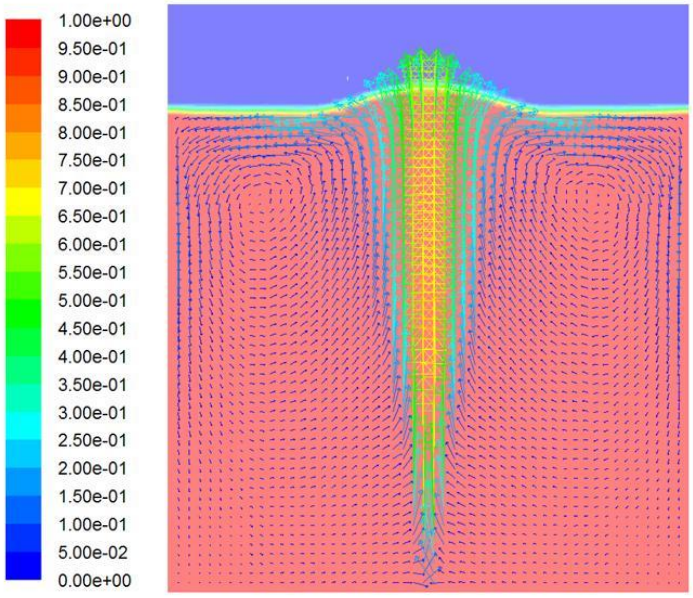

Figure 56: Flow velocity profile as calculated with the model.

Already, the characteristic dead zones at the bottom of the ladle and the torus on either side of the plume can clearly be distinguished. For better qualitative comparison, the flow fields as measured by Xie and Oeters (15) are given together with similar flow fields predicted by the model in Figure 57. Over-predicted plume velocities due to the omission of bubble induced turbulence (Chapter III:5.4) have been removed so as to not distract from the comparison.

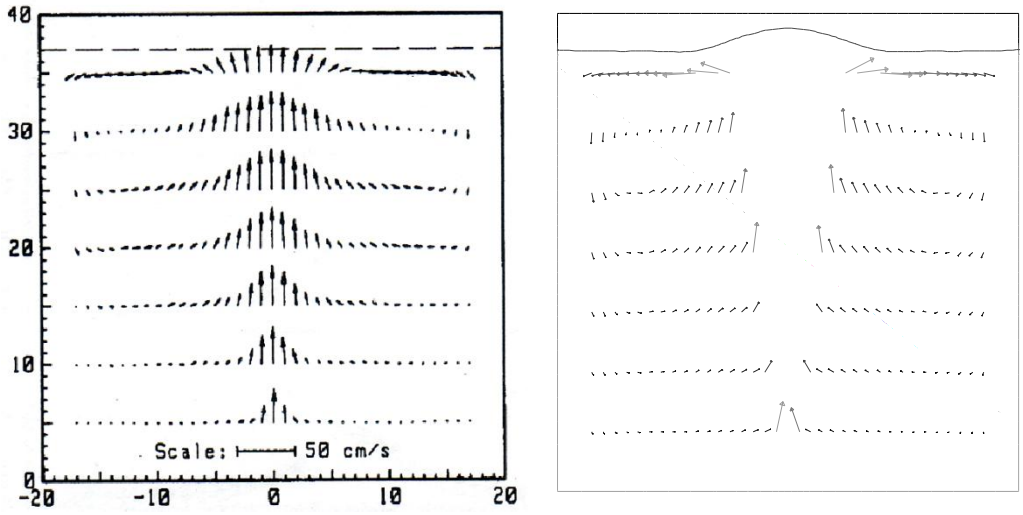

Figure 57: Side by side comparison of measured and predicted flow fields.

Close scrutiny yields an almost exact comparison between experimental measurements and model predictions.

1.2. Quantitative Comparison

Xie and Oeters also measured quantitatively the flow velocities on specific horizontal cuts through the model. These measured results along with model predictions are given below. The vertical axis displays axial velocity (cm/s) and the horizontal axis gives the radial coordinate (cm).

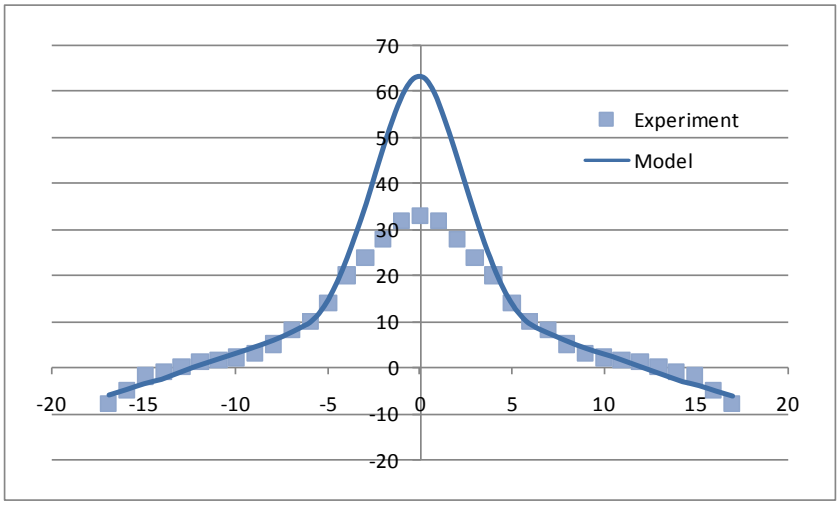

Figure 58: Graphical comparisons of axial flow velocities measured and predicted on a horizontal cut at 30 cm.

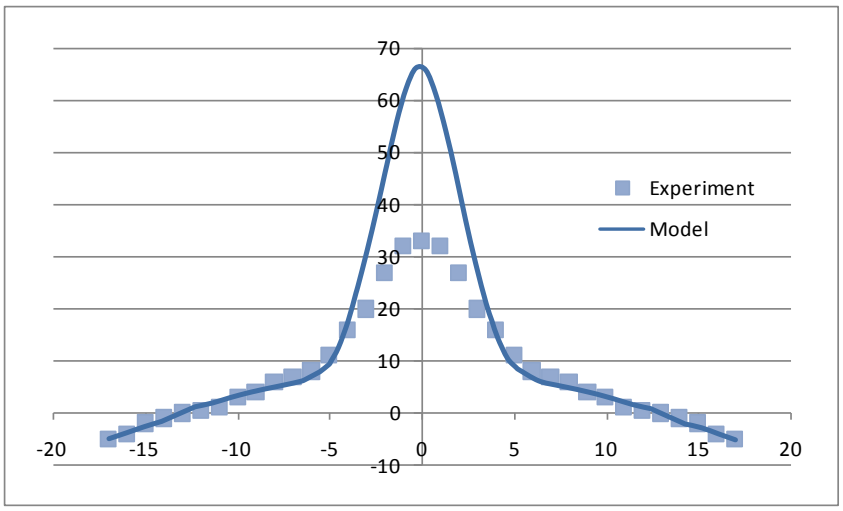

Figure 59: Graphical comparisons of axial flow velocities measured and predicted on a horizontal cut at 25 cm.

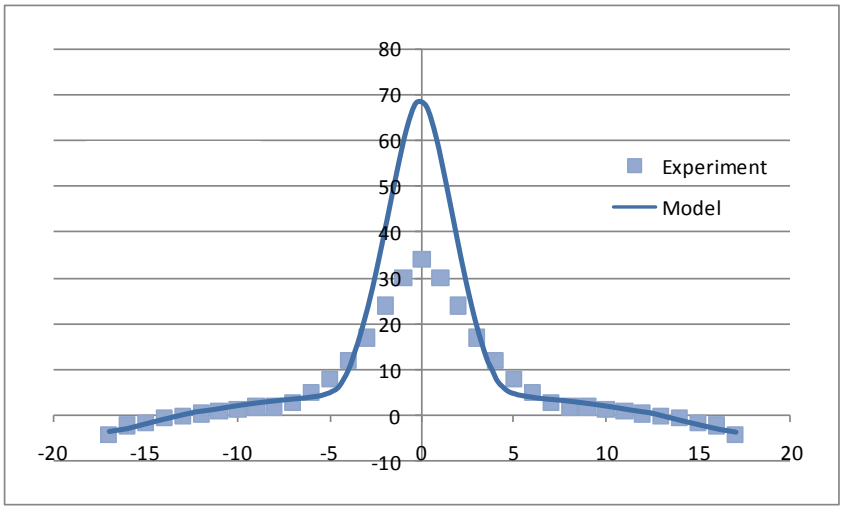

Figure 60: Graphical comparisons of axial flow velocities measured and predicted on a horizontal cut at 20 cm.

The graphs show very good quantitative agreement in all areas outside the plume. This is very encouraging since the flow patterns outside the plume are the primary influence on mixing. Accurate representation of these circulating flows thus ensures accurate prediction of the degree of mixing.

Inside the plume, however, large over-predictions of velocity resulting from the omission of bubble induced turbulence can clearly be seen. These large over-predictions are unavoidable at present for lack of a generalized model for bubble turbulence contribution (detailed discussion in Chapter IX:4.1), but seem not to have a negative effect on the prediction of flow patterns outside the plume.

2. Plume Characteristics

A review by Oeters *et al.* (13) provides some empirical equations for the centreline velocity and diameter of the plume. Plume velocities will be substantially over-predicted due to the omission of turbulence source terms from the bubbles (outlined in Chapter IX:1.4). The plume diameter, however, should provide a good platform for validation.

The following equation is recommended for estimating the plume radius (13):

$$r_P = 0.38 \cdot Q_1^{0.15} \cdot y_{P1}^{0.62}$$ Equation 73

where

$$Q_1 = \frac{Q}{\rho_N} \cdot \frac{T}{T_N} \cdot \left(\frac{1.43}{1.43 + H} \right)$$ Equation 74

$$y_{P1} = (1.43 + H) \ln\left(\left(1 - \frac{y_P}{1.43 + H} \right)^{-1} \right)$$ Equation 75

These equations were used to create a graphical representation of plume radius (r_P) as a function of plume height (y_P). The resulting graph was superimposed on a display of the bubble plume as tracked by the discrete phase model.

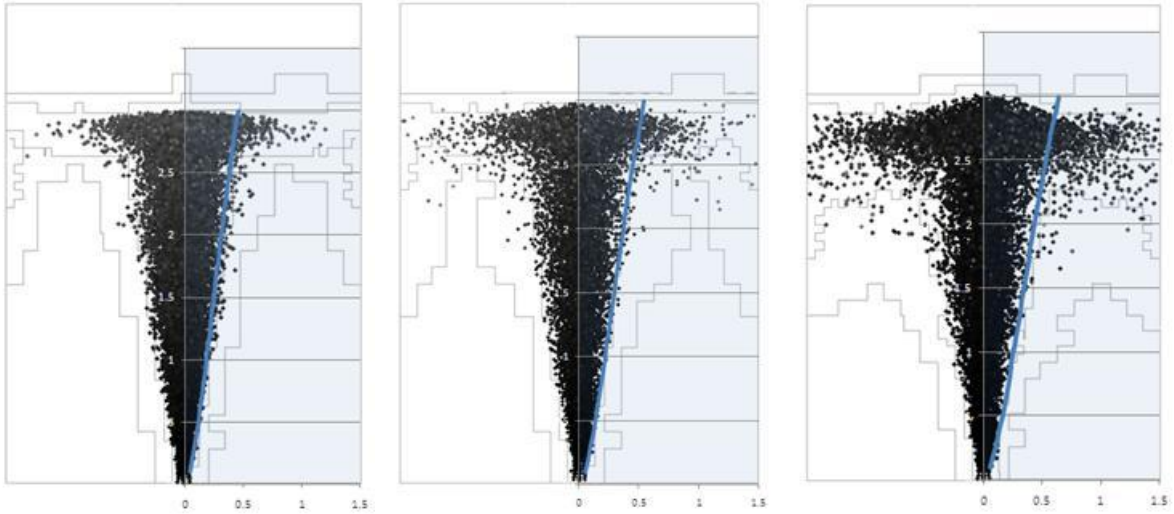

Figure 61: Plume representations ($Q = 0.003, 0.01$ and 0.03 kg/s) by the model compared to predictions by Oeters *et al.* (13).

Figure 61 shows a good agreement between the model predictions and Equation 73. The model does not seem to accurately predict the widening of the plume with increases in flow rate though. The three plumes shown in Figure 61 all maintain approximately the same diameter. This discrepancy is probably rooted in the omission of turbulence source terms.

Most importantly though, the plume diameters in the range over which the majority of experimentation will take place (0.003 to 0.01 kg/s) is predicted satisfactorily. This will help to ensure accurate momentum transfer from the discrete phase particles to the continuous phase.

3. Mixing Time

Traditionally, the mixing time is the primary measure of mixing efficiency gas stirred ladles. It is therefore essential that the model provides quantitative 95% bulk mixing times which are in good agreement with those given in literature.

Ghosh (1) has compiled mixing time results from a number of reliable sources which have been scaled up for application in a 150 t industrial ladle, 3 m in height and diameter. The designed experiment reported in Chapter X:1 employs this exact ladle setup and results from that experiment could therefore be used for purposes of validation.

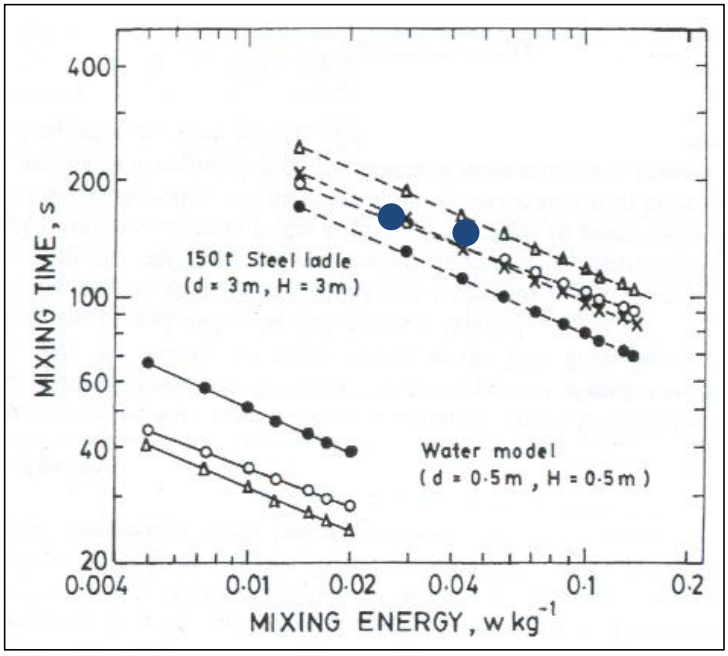

Figure 62: Comparison of mixing times computed in Chapter X:1 (blue circles) to experimental data assimilated by Ghosh (1).

Results from the numerical experiment (average of runs 2, 3 & 5 and also run 8 in Table 16, Chapter X:1) compare well to the scaled water model results, confirming that the model provides a good account mixing in gas stirred ladles.

4. Plume Eyes

Plume eye measurements are arguably the easiest information to extract from real steelmaking operations and can therefore provide a good basis for model verification. No scaling is required and a direct comparison can be drawn between model predictions and the actual industrial process.

The ladle implemented at Mittal Steel: Saldanha produces plume eyes at a flow rate of 100 l/min (0.00267 kg/s) per plug as displayed in Figure 63.

Figure 63: Plume eye formation in the actual ladle at 0.00267 kg/s/plug.

Figure 63 shows the small amount of metal (two white-hot spots) protruding above the slag at this relatively gentle purge rate. The bottom left hand plume eye was slightly elongated at the moment that the picture was taken, but the top right eye takes on a circular appearance. The measured diameter of this plume eye is 0.7 m.

The model representation is given below for comparison.

Figure 64: Plume eye formation predicted by the model at 0.0267 kg/s/plug.

It was discussed in Chapter VI:1.5 that the model gives an averaged representation of the plume and the plume eye. From Figure 64 it seems that this averaged plume eye is somewhat oval in shape. It can be seen, however, that the two plume eyes in Figure 63 both have distinctly different shapes due to the irregular arrival of gas bubbles to the melt surface. A thorough validation exercise would

therefore require a large number of the photographs shown in Figure 63 to calculate the average shape and size of the actual plume eye.

Such a detailed evaluation is not the aim of the current study and Figure 63 presents sufficient evidence that the model provides an acceptable representation of plume eye formation. The oval shaped plume eyes created by the model are 0.675 m in length, meaning that the size of the plume eye might be slightly under-predicted. This error is not great, however, and indicates a strong likeness between the model and the actual process.

5. Sloshing and Swirling

The phenomenon of sloshing has been studied in water models and various correlations have been developed to describe the characteristics of the surface wave. Hiratsuka *et al.* (30) proposed the following equation for determining the period of the swirl motion:

$$\frac{(D/g)^{0.5}}{T_s} = \frac{0.918}{2\pi}\left(\frac{D}{D_{app}}\right)^{0.5} \times \left(3.68 \tanh\left(3.68 \frac{H}{D}\frac{D}{D_{app}}\right)\right)^{0.5}$$ Equation 76

where

$$\frac{D}{D_{app}} = 1.25 - 0.25\frac{H}{D}$$ Equation 77

The swirl period attained in a vessel, 2.1 m in height and 3.54 m in diameter, is presented below. According to Equation 76, the swirl period in this vessel should be 2.06 s. The predicted swirling motion has a period of almost exactly 2 s as displayed in Figure 65 on the following page, showing excellent agreement with Equation 76.

Additionally, the fact that the model can in fact predict the surface wave formation raises confidence in its validity. The phenomenon of swirling has never been simulated before and the model seems to give a good account of the physics involved.

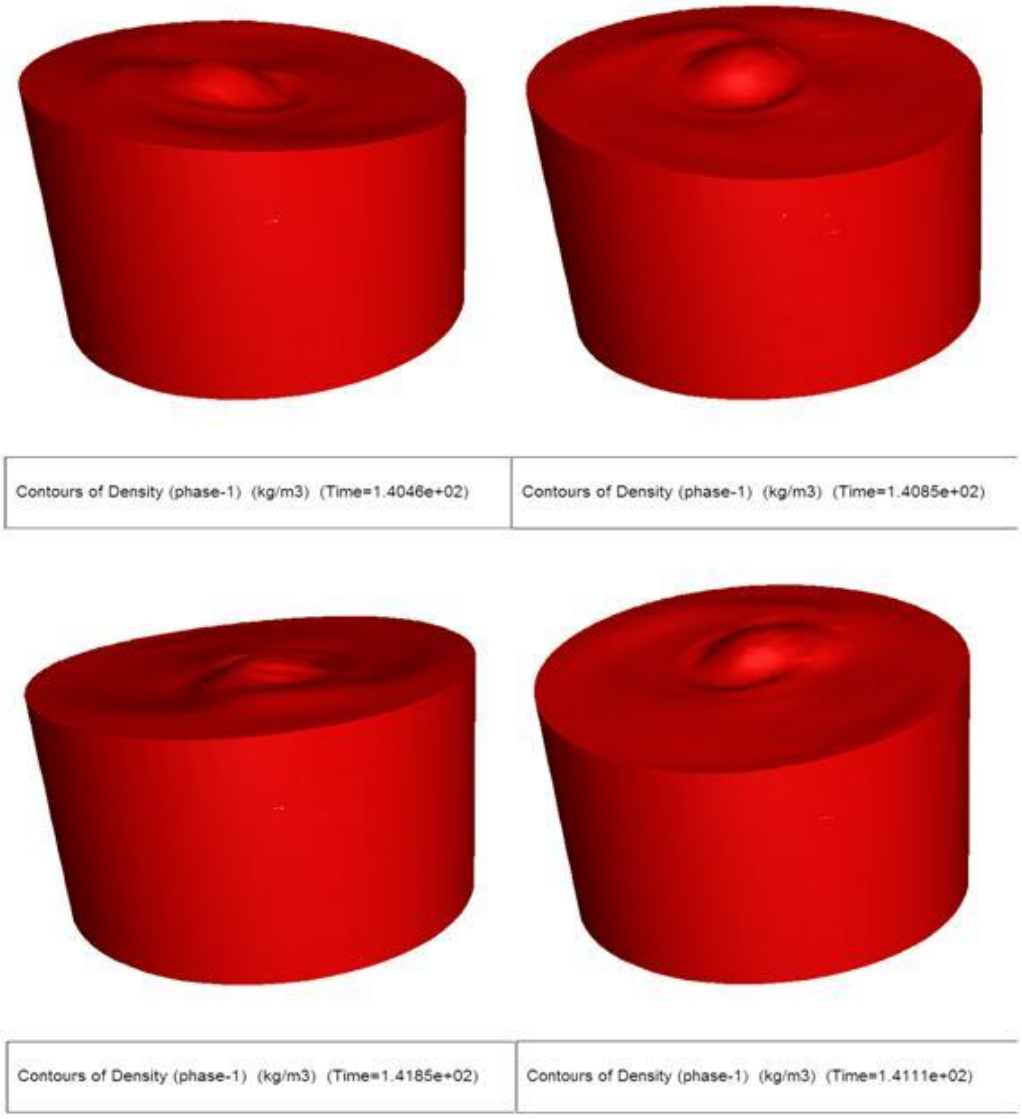

Figure 65: Four snapshots taken of the swirl motion within one period (sequenced in a clockwise fashion).

CHAPTER VIII:
RESULTS AND DISCUSSION PART 1: THE LADLE ENERGY BUDGET

There is a fact, or if you wish, a law, governing natural phenomena that are known to date. There is no known exception to this law — it is exact so far we know. The law is called conservation of energy; it states that there is a certain quantity, which we call energy that does not change in manifold changes which nature undergoes. That is a most abstract idea, because it is a mathematical principle; it says that there is a numerical quantity, which does not change when something happens. It is not a description of a mechanism, or anything concrete; it is just a strange fact that we can calculate some number, and when we finish watching nature go through her tricks and calculate the number again, it is the same.

- Richard Feynman

The ultimate purpose of gas stirred ladle design is to extract the maximum amount of kinetic energy from the buoyant gas and redirect it as efficiently as possible to affect motion in all areas of the melt. Similarly, the entire process of mathematical model design is focussed on ensuring the correct modelling of kinetic energy input, transfer and ultimate dissipation. Mathematical modelling and Mother Nature often have distinctly different views on the law of energy conservation.

The information contained in this chapter provides the theoretical basis for the interpretation of results in subsequent chapters. It is therefore recommended that this chapter be read with special care so that maximum value can be drawn from the large quantity of results that follow.

Note also that this chapter contains a number of results obtained from model setups defined elsewhere in the document. References are provided to the appropriate sections, but are meant only to assure the reader that results are believable. These results are presented for explanatory purposes only and the knowledge of explicit experimental parameters is not required for complete comprehension.

1. Role-Players in the Kinetic Energy Balance

The response of ladle hydrodynamics to various changes in operation and design is much easier to comprehend from the viewpoint of kinetic energy conservation. Figure 66 displays the primary sources of kinetic energy in and outflows present in the system.

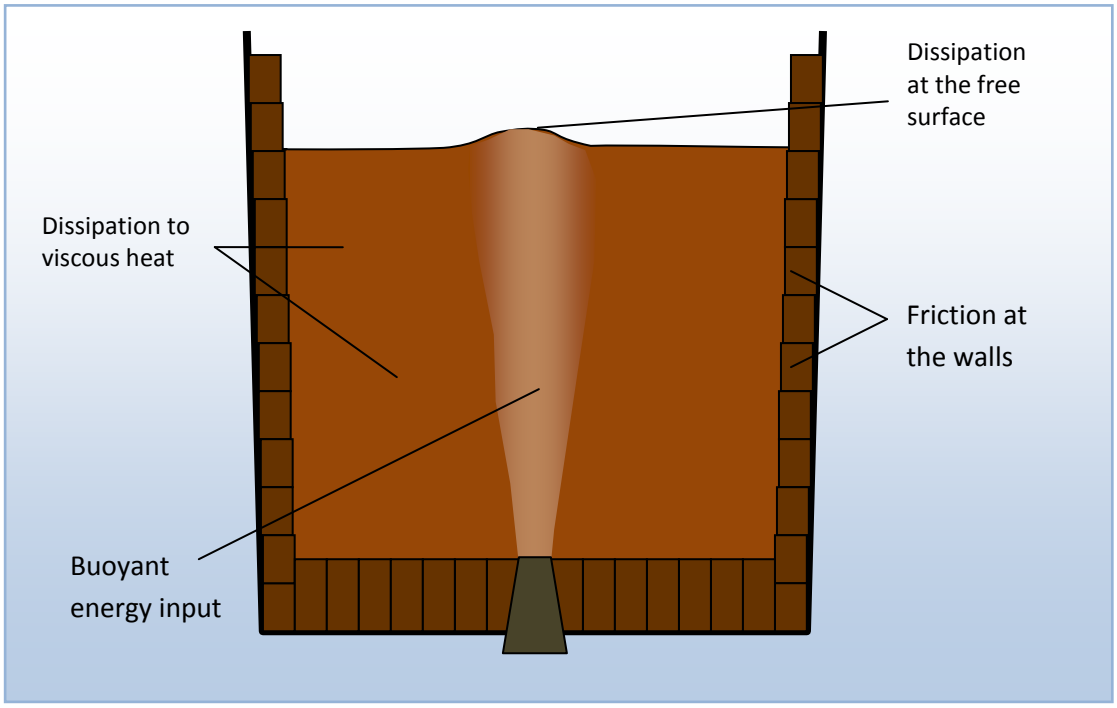

Figure 66: Major locations of kinetic energy input and dissipation in gas stirred ladles.

According to Figure 66, the buoyant energy input must equal the sum of the viscous dissipation, free surface dissipation and wall damping effects. Each of these factors plays an important role in the process of energy transfer within the vessel and will be discussed separately below.

1.1. Buoyant Energy Input

Ghosh (1) breaks the rate of energy input to the ladle into three parts:

$$e_{in} = e_b + e_k + e_{exp}$$ Equation 78

The three terms on the right of Equation 78 represent the buoyant, kinetic and bubble expansion energy input contributions. Of these, the kinetic and bubble expansion energies have been shown to be insignificant when compared with the magnitude of the buoyant potential energy (also called pressure energy) of a bubble entering at the bottom of the ladle (1). The total energy input can therefore be assumed to be equal to the buoyant potential energy of the rising bubble, hence the term buoyant energy input.

1.2. Turbulence Kinetic Energy Dissipation

The primary mechanism for kinetic energy loss is the viscous dissipation of turbulence kinetic energy to heat. To understand this phenomenon, one must follow the evolution of kinetic energy within the fluid. For the mean kinetic energy (69):

$$\frac{D}{Dt}\left(\frac{1}{2}\overline{u_i}^2\right)=\frac{\partial}{\partial x_j}\left(\frac{-\overline{pu_j}}{\rho}+2\nu\overline{u}_i S_{ij}-\overline{u_i u_j}u_i\right)-2\nu S_{ij}S_{ij}+\overline{u_i u_j}\frac{\partial\overline{u}_i}{\partial x_j}$$ Equation 79

From left to right the terms represent the total change in mean kinetic energy, the transport term, the viscous dissipation term and the loss to turbulence. Viscous energy dissipation from the mean flow is typically negligibly small. The loss to turbulence, however, is the dominant term on the right hand side of the equation, meaning that the mean flow continuously feeds energy to the large scale turbulent eddies.

It is interesting to note that the losses to turbulence term in Equation 79 is analogous to the turbulence generation term used in the transport equations of the k-ε turbulence models. This term represents the generation of turbulence due to mean velocity gradients and is the primary source of turbulence kinetic energy in free flowing fluids.

Once the mean kinetic energy is converted to turbulence kinetic energy, the evolution of kinetic energy can be tracked further (69):

$$\frac{D}{Dt}\left(\frac{1}{2}\overline{u_i'^2}\right)=\frac{\partial}{\partial x_j}\left(\frac{-\overline{p'u_j'}}{\rho}+2\nu\overline{u_i s_{ij}}-\overline{u_i'^2 u_j}\right)-2\nu s_{ij}s_{ij}+\overline{u_i'u_j'}\frac{\partial\overline{u}_i}{\partial x_j}$$ Equation 80

From left to right the terms represent the total change in turbulence kinetic energy, the transport term, the viscous dissipation term and the shear production term. In this case, the viscous dissipation term is far from negligible and represents the characteristic turbulence dissipation rate (ε) modelled by the k-ε turbulence models.

Through the evolution equations shown above, the kinetic energy is drawn from the mean flow to the large scale turbulent eddies. Once in turbulent motion, it is passed down to smaller and smaller eddies until it is finally dissipated as heat at the smallest turbulent length scale (also known as the Kolmogorov microscale) to become part of the internal energy of the fluid (69).

1.3. Dissipation at the Surface

Another very important energy dissipation mechanism occurs at the melt free surface. Kinetic energy is lost from the melt in four ways:

- Deformation of the free surface against gravity
- Additional turbulent dissipation to viscous heat
- Bubbles rupturing at the free surface
- Surface wave formation

When a slag layer is present, three additional mechanisms become possible:

- The formation of slag droplets
- The potential energy required to keep these droplets in suspension

- Deformation of the slag layer

Mazumdar *et al.* (19) investigated the effects of a slag layer on the total kinetic energy present in the melt to conclude that the formation and entrainment of slag droplets make negligible subtractions from total melt kinetic energy. The fluid work required to deform the free surface and displace the slag layer was the dominant mechanism for the dissipation of kinetic energy.

Johansen and Boysan (46) are the only authors to have modelled the additional turbulence dissipation at the free surface. The reason for increased dissipation rates is said to result from eddies approaching and locally lifting the free surface.

Dissipation rates due to bubble rupture at the ladle free surface have never been studied. Biological applications have found that the collapsing of bubbles at a free surface dissipates sufficient energy to explain animal cell damage in sparged suspended animal cell cultures (70). The scale of this energy dissipation mechanism compared to the others is not known, however.

Some kinetic energy is also lost to facilitate wave formation on the free surface on the regions outside the plume. Kishimoto *et al.* (71) have shown this mechanism to constitute less than 1% of the total kinetic energy losses from the melt.

1.4. Friction at the Walls

The final dissipation mechanism is through shear at the ladle walls. The low velocity (< 0.3 m/s) of typical recirculating flows on the outside of the vessel should minimize these energy losses though. When wider tuyere setups are investigated, however, the high velocity plume region (> 1.5 m/s) can approach the wall and cause more substantial wall shear energy losses.

2. Mathematical Modelling of Energy Exchanges

Each of the four primary regions of mechanical energy exchange described above holds a varying degree of difficulty for accurate mathematical modelling. Since the accurate modelling of these exchanges is paramount to the development of an accurate mathematical model, an investigation into the capabilities of current modelling techniques is well warranted.

2.1. Buoyant Energy Input

2.1.1. Energy Input Through Momentum Sources

The Lagrangian framework of discrete particle sources lends itself very well to the specification of accurate mechanical energy input. Chapter VI:1.3.3 has shown that this energy exchange site is very forgiving when it comes to the specification of bubble size distribution and even particle drag law.

These findings suggest that the accurate modelling of momentum input from buoyant sources is relatively easy. The specification of the correct bubble size distribution (the most challenging

modelling aspect) is shown to have a negligible impact on energy transfer, and the drag law (moderately challenging modelling aspect) is shown to be quite forgiving as well. Bubble growth is also easily modelled with the ideal gas law.

To understand why the simulation is so lenient when it comes to the specification of bubble size and drag, the buoyant energy transfer from bubble to continuous phase must be analyzed in a fundamental manner. An energy conservation analysis was therefore completed as reported below.

A. Energy Transfer from Rising Bubbles

A rising gas bubble contains energy in three forms: pressure energy from the buoyant force, potential energy and kinetic energy. Due to the low density of the gas bubble compared to the medium in which it rises, the potential and kinetic energies can be seen as negligible in comparison with the pressure energy. Therefore a bubble of volume (V_B) at a depth (y) in the vessel contains the following amount of energy:

$$E = \left(\rho_l g y\right) \cdot V_B \qquad \text{Equation 81}$$

Equation 81 represents the pressure energy as pressure times volume. An alternative representation is in terms of buoyant potential energy; the buoyant force times the potential distance over which the buoyant force can do work:

$$E = \left(\rho_l g V_B\right) \cdot y \qquad \text{Equation 82}$$

It is clear that Equation 82 is identical to Equation 81 and that any of these can be safely employed to quantify the energy input to the system. The pressure energy analogy (Equation 81) will be used in the remaining chapters.

For ease of discussion, the buoyant force $(F_b = \rho_l g V_B)$ exerted by the bubble will be treated as constant along its rise, implying that V_B also remains constant. In reality, however, V_B increases as the bubble expands along the hydrostatic pressure gradient of the ladle. The bubble volume in this context represents a suitably averaged value so that $\int_0^H (\rho_l g V_B) dy = \left(\rho_l g V_{B,ave}\right) H$. The term V_B will therefore indicate an averaged bubble volume for the remainder of this chapter.

When V_B is constant, the bubble loses pressure energy on its rise through the melt at a rate depending only on its rise velocity.

$$\begin{aligned} e &= \left(\rho_l g \frac{dy}{dt}\right) \cdot V_B \\ &= \left(\rho_l g \upsilon_B\right) \cdot V_B \end{aligned} \qquad \text{Equation 83}$$

In a rising plume, the bubble rise velocity (υ_B) is the sum of the bubble slip velocity (υ_s) and the local continuous phase flows (υ_c). Therefore,

$$e = \left(\rho_l g \left(\upsilon_s + \upsilon_c\right)\right) \cdot V_B \qquad \text{Equation 84}$$

The question that must now be answered is what happens to the pressure energy once it is lost by the bubble. Joshi (72) provides the following answer:

When a bubble rises in creeping flow it does not transfer any momentum to the liquid phase. The energy lost by the bubble is immediately dissipated in a viscous manner, thereby becoming part of the internal energy of the fluid. Naturally, the rate of this transfer process is governed by the buoyant force multiplied by the rise velocity. In a stationary fluid, the rise velocity and the bubble slip velocity are synonymous. Hence, the rate of energy dissipation is expressed according to Equation 85:

$$e_d = \left(\rho_l g \upsilon_s\right) \cdot V_B \qquad \text{Equation 85}$$

When the flow is turbulent, however, the frictional energy losses resulting from slip are first transferred to the continuous phase turbulence to be subsequently dissipated to the internal energy of the fluid (72) (see Section 1.2 above).

In a turbulent rising bubble plume, the total rate of pressure energy lost by the bubble is described by Equation 84 and the fraction of that energy lost to turbulence by Equation 85. To ensure energy conservation, the balance must be lost to the kinetic energy of the continuous phase. Therefore, the rate of kinetic energy input from the bubble to the continuous phase is described as follows:

$$e_k = \left(\rho_l g \upsilon_c\right) \cdot V_B \qquad \text{Equation 86}$$

Note that if υ_c is negative, i.e. the bubble is travelling against the continuous phase flow, the kinetic energy contribution by the bubble would also be negative. In such a case, the kinetic energy of the fluid would be transferred to pressure energy in the bubble, which is subsequently lost through viscous dissipation (Equation 85).

B. Impact of Size Distribution

When summed over all the bubbles in the plume (total gas volume = V_{tot}) the total transfer rate of kinetic energy to the continuous phase can be estimated from the average plume velocity $\left(\upsilon_p\right)$:

$$e_{k,tot} = \left(\rho_l g \upsilon_p\right) \cdot V_{tot} \qquad \text{Equation 87}$$

The reason for the small impact of bubble size distribution on buoyant energy transfer becomes clear from Equation 87. The rate of energy transfer is dependent only on the total gas volume and not on the size of the parcels into which this total volume is divided.

C. Impact of the Drag Law

The impact of drag is explained by the pressure energy dissipated by the bubble slip. Higher drag coefficients would result in smaller slip velocities since the drag force must always equal the buoyant force in a bubble rising at constant velocity:

$$F_b = F_D$$
$$\rho_l g V_B = \frac{1}{2} C_D A_B \rho_l \upsilon_s^2$$

Equation 88

Since the buoyant force is constant, an increase in drag coefficient (C_D) would require a decrease in slip velocity (υ_s) to maintain the force balance. A smaller slip velocity would mean that less of the pressure energy contained in the bubble is dissipated to turbulence (Equation 85) leaving a larger percentage to add to the kinetic energy of the continuous phase (Equation 86).

Chapter VI:2.2.2 showed that a large error in drag coefficient (0.44 as opposed to 2.34) resulted in a relatively small overall flow error (<20%), implying that the spherical bubbles ($C_D = 0.44$) did not lose as much of their pressure energy to viscous heat as one might expect. The fraction of buoyant energy lost to viscous dissipation is simply the ratio of the distance covered by slip to the total distance covered by the bubble under the constant force of buoyancy. Therefore, the fraction of pressure energy lost can be expressed as the ratio of the bubble slip velocity to the overall bubble rise velocity (υ_s/υ_B).

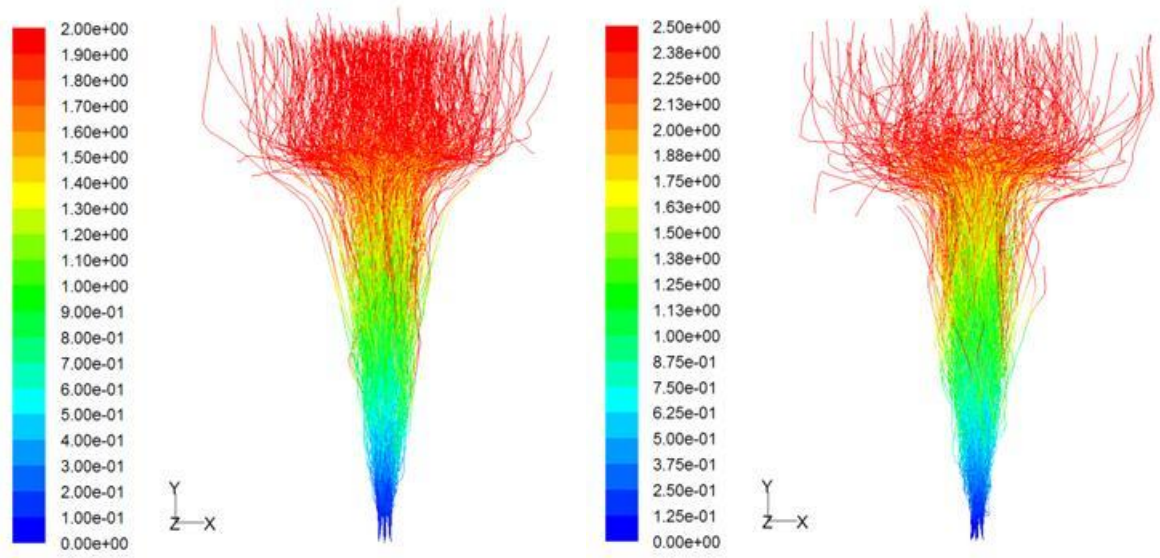

Figure 67: Particle residence times for a spherical drag law (left) and the custom drag law (right).

Figure 67 shows that the spherical capped bubbles ($C_D = 2.34$) needed about 2.5 s to traverse the 3 m height of the ladle, while the spherical bubbles ($C_D = 0.44$) needed only 2 s. Therefore the

spherical capped bubbles have a velocity $v_B = 3/2.5 = 1.2$ m/s and the spherical bubbles have $v_B = 3/2 = 1.5$ m/s. The fraction of energy lost by the spherical capped bubbles can thus be estimated as $v_s/v_B = 0.23/1.2 = 0.183$, while the spherical bubbles lost a fraction of $0.7/1.5 = 0.467$. Bubble slip velocities were calculated from the force balance in Equation 88. By this estimation, the spherical bubbles would lose $46.7 - 18.3 = 28.4\%$ more of their pressure energy to viscous dissipation than the spherical capped bubbles.

It will be shown in Section 3 of this chapter that the integral of the turbulence kinetic energy dissipation rate over the entire mass of steel in the ladle is a good indication of the rate of kinetic energy transferred from the buoyant gas. For the ladle with spherical bubbles, this value amounted to 2185 W, while the spherical capped bubble setup required a flow energy dissipation rate of 2912 W. The difference between these two values indicates that the spherical bubble setup required a 25% smaller energy dissipation rate in the flow. This is also an indication that the rate of energy input by the spherical bubbles is 25% smaller. The agreement between the 28.6% estimate in the previous paragraph and the 25% of this paragraph confirms that the DPM in FLUENT adheres to these fundamental principles bubble-liquid energy transfer.

D. Kinetic Energy Transfer Modelling by the DPM

The DPM simulates the transfer of energy from the pressure energy of the bubble to the kinetic energy of the continuous phase as a source term in the momentum equation. This source term is expressed as follows (31):

$$F = \sum \left(\frac{18 \mu C_D \, \mathrm{Re}}{\rho_p d_p^2 24} \left(u_p - u \right) + F_{other} \right) m_p \Delta t \qquad \text{Equation 89}$$

The momentum source term in Equation 89 gives the rate of change in momentum (also known as the force) caused by the DPM particles in a specific computational cell for a specific time step (Δt).

The way in which the bubble slip velocity reduces this force exerted on the continuous phase is by reducing the mass of particles over which the momentum source can be summed. The mass of all particles in the control volume is given by $M_{tot} = m_p \times t_{cross}$ where t_{cross} is the time required by the particle to cross the height (y_{CV}) of the control volume. Therefore:

$$M_{tot} = m_p \frac{y_{CV}}{\left(v_c + v_s \right)} \qquad \text{Equation 90}$$

If all particles in the control volume are of equal mass (M_p) the number of particles in the control volume is given by $N_p = M_{tot}/M_p$.

$$N_p = \frac{m_p}{M_p} \frac{y_{CV}}{\left(v_c + v_s \right)} \qquad \text{Equation 91}$$

For the special case of particles having a constant size and mass, Equation 89 can be adapted with Equation 91:

$$F = \frac{1}{(\upsilon_c + \upsilon_s)} \frac{y_{CV}}{M_p} \left(\frac{18 \mu C_D \, \mathrm{Re}}{\rho_p d_p^2 24} (u_p - u) + F_{other} \right) m_p^2 \Delta t$$ Equation 92

The rate of kinetic energy input by this force can now be calculated as force times velocity:

$$e_k = \frac{\upsilon_c}{(\upsilon_c + \upsilon_s)} \frac{y_{CV}}{M_p} \left(\frac{18 \mu C_D \, \mathrm{Re}}{\rho_p d_p^2 24} (u_p - u) + F_{other} \right) m_p^2 \Delta t$$ Equation 93

As explained in Subsection A, the ratio of $\upsilon_c/(\upsilon_c + \upsilon_s)$ represents the fraction of the bubbles' pressure energy converted to kinetic energy in the continuous phase. From an energy conservation point of view, Equation 93 shows that the DPM source terms model only the fraction of the bubbles' pressure energy converted to kinetic energy in the carrier phase, completely ignoring the energy dissipated by slip.

2.1.2. Buoyant Energy Transfer Efficiency

The equation for the specific rate of buoyant energy input to the melt (Equation 3) has been derived from the starting point of the total rate at which pressure energy is fed to the system (1):

$$\begin{aligned} e &= (\rho_l g H) \cdot \frac{dV}{dt} \\ &= (\rho_l g H) \cdot Q_V \end{aligned}$$ Equation 94

The volumetric flow rate is subsequently adapted for the logarithmic mean pressure and temperature and divided by the total mass of fluid in the bath to give Equation 3 (repeated below).

$$\varepsilon_k = \frac{336 Q_{V,N} T_l}{M_l} \ln \left(1 + 0.681 \frac{H}{P_0} \right)$$ Equation 95

The question that now arises is how much of this pressure energy actually ends up as kinetic energy in the melt. Mazumdar and Evans (5) concluded in a review of cold modelling studies that as much as 60% of the buoyant energy input to gas stirred ladles would be dissipated due to the bubbles slipping with respect to the continuous phase. The typically small value of the slip velocity in comparison with the plume velocity seems to indicate that the percentage dissipated would be much less than 60% though.

At this point it is suitable to define the kinetic energy transfer efficiency (η). Kinetic energy transfer efficiency indicates the fraction of pressure energy contained in the injected gas that is successfully

transferred to the kinetic energy of the continuous phase. The specific rate at which kinetic energy is transferred to the melt can therefore be described from the standard equation for the specific rate of buoyant energy input (Equation 95).

$$\varepsilon_k = \eta \frac{336 Q_{V,N} T_l}{M_l} \ln\left(1 + 0.681 \frac{H}{P_0}\right)$$ Equation 96

The drag coefficient is the most direct influence on the kinetic energy transfer efficiency. A low drag coefficient would result in higher slip velocities, in turn leading to higher energy losses to viscous dissipation as shown in Subsection C of the previous section. Complete energy transfer (Equation 94) would occur if the drag coefficient approaches infinity, thereby exerting its full drag force with an infinitely small amount of slippage.

There is another very important factor influencing the kinetic energy transfer efficiency, however. To investigate this effect, an experiment was conducted using the steady state simplification of the full scale model described in Chapter IV:3. By using this model, all the sources of energy dissipation can be eliminated except for viscous dissipation. This is accomplished by specifying all the boundaries as walls with perfect slip between the wall and the liquid. In this way, no energy can be lost by friction at the wall. The flat free surface also prevents any energy losses in the deformation of the free surface. Under these conditions the kinetic energy input rate would be identical to the rate of turbulent dissipation integrated over the mass of liquid in the melt.

Experimentation with this modelling setup yielded the primary influential variable on buoyant energy as the compliance of the bubble plume with overall ladle flow patterns. This concept is illustrated in Figure 68.

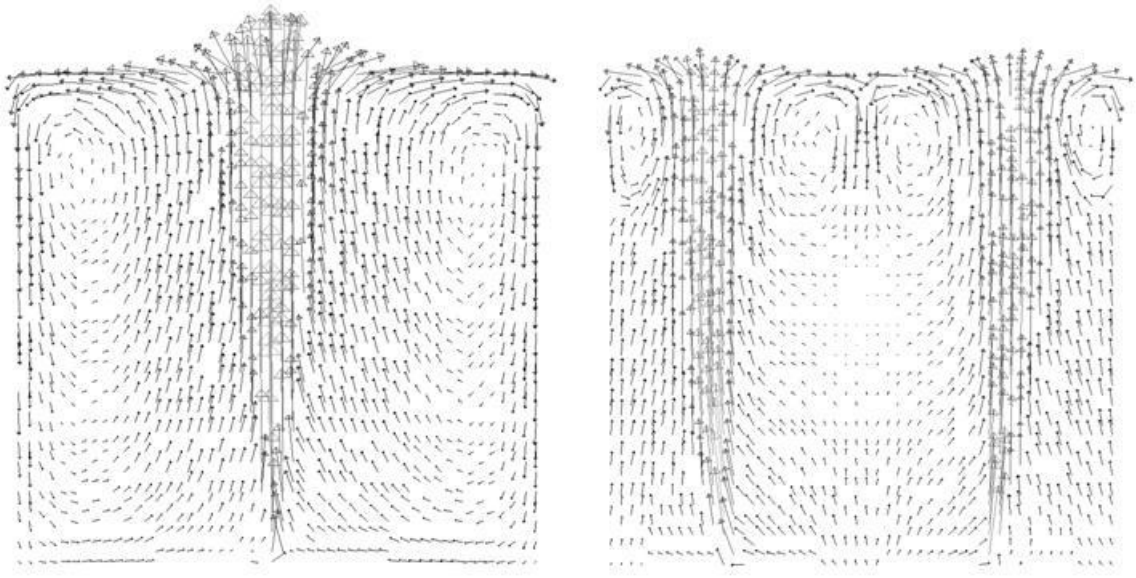

Figure 68: Smooth circulatory flow patterns (left) and disrupted flow patterns (right).

The left hand side of Figure 68 shows fully developed circulatory flow where the plume is in compliance with the flow direction. The ladle setup on the right, however, shows two tuyeres forcing

the flow in different directions – the left hand tuyere develops clockwise flow and the right hand tuyere develops counter clockwise flow. Kinetic energy transfer efficiency is calculated in Table 11.

Table 11: Efficiencies of different tuyere setups at a specific buoyant energy input rate of 0.0303 W/kg.

Tuyere Setup	Ideal Specific Energy Input Rate [W/kg] (Equation 95)	Actual Specific Energy Input Rate [W/kg] (model)	Efficiency (η) [%]
1 central tuyere (Figure 68)	0.0303	0.0232	76.6
2 tuyeres (Figure 68)	0.0303	0.0180	59.4
1 asymmetrical tuyere (Figure 69)	0.0303	0.0153	50.5

The substantial difference in the efficiency of buoyant energy input conversion lies in the directional nature of momentum. Plume velocity and the momentum it contains are directed upwards. The momentum of downwards recirculating flow patters created by additional tuyeres is in the opposite direction. These flows meet in an inelastic collision, reducing the velocity of both the upward plume and the downwards circulatory flows while conserving overall momentum in the system. The kinetic energy which is lost in the process is converted back to bubble pressure energy and subsequently dissipated by slip to viscous heat. This increased dissipation can be better understood by recognising the resulting decrease in plume velocity while the bubble slip velocity remains constant. The percentage of bubble pressure energy dissipated (expressed as v_s/v_b) therefore increases.

It is interesting to note that a single bubble plume can create conflicting flows onto itself. Figure 69 gives one such example where gas is injected though a single asymmetrical plug located on the right hand side of the ladle.

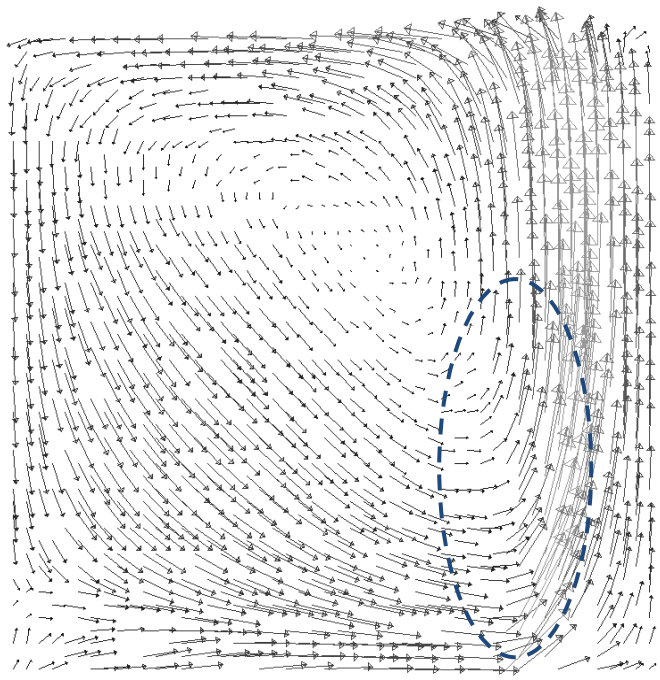

Figure 69: Circulatory flow patterns in conflict with the rising plume.

The highlighted part of Figure 69 clearly shows the downwards moving recirculating flows colliding with the plume moving upwards. Since the plume velocities are higher, the downwards recirculating flows are bent in an upwards direction by the plume, thereby reducing the magnitude of momentum in both directions. Plume velocities are therefore reduced by this interference and the kinetic energy transfer efficiency is adversely affected as shown in Table 11.

In the full scale simulation, with no-slip boundaries and a mobile free surface, the recirculating flows are likely to be significantly weakened by the energy losses at other locations. This effect will therefore be less profound real gas stirred ladles.

2.1.3. Energy Input Through Turbulence Sources

It is known that the bubbles within the plume can make substantial contributions to continuous phase turbulence properties, primarily through the turbulent wake created by the slippage between bubble and fluid. This is usually modelled as additional source terms for both k and ε.

From the information provided in Section 2.1.1.A, it is easy to assume that all the pressure energy lost by bubble slippage will be converted to continuous phase turbulence and subsequently dissipated by the turbulence kinetic energy cascade described in Section 1.2. This is not the case, however. Joshi (72) draws an important distinction between the large scale of turbulence produced by the mean velocity gradients, and the much smaller scale of bubble induced turbulence. It follows from this distinction that only a fraction of turbulent eddies resulting from the bubble slippage will be large enough to affect transport phenomena in the carrier phase. The balance will be in the form of very small eddies which are almost immediately dissipated to the internal energy of the fluid.

Working from this principle, a constant (C_B) can be defined to represent the fraction of bubble induced turbulence affecting transport phenomena in the carrier phase. Joshi (72) reviewed a number of studies giving the value of C_B as anything in the range of 0 to 0.2. The conclusion was also drawn that substantial additional work is required to further the understanding of this transport phenomenon.

2.2. Turbulence Energy Dissipation

Turbulence plays a crucial role in the kinetic energy budget within the ladle – both by dissipating kinetic energy to heat and by greatly enhancing diffusive momentum transfer. The modelling of turbulence has enjoyed more focus than any other flow modelling aspect through the years. Still, no model exists that can accurately model turbulence effects over a wide range of engineering applications. The workhorse of turbulent modelling, the standard k-ε model, is known to introduce some error when modelling complex flows (31). Complex flow phenomena in the current application include the highly strained plume region, rotating flows in the bulk recirculation zones and a possible swirling motion.

Improvements on the SKE model have been made and are evaluated fully in Chapter IX:2, but the SKE model was still left as the best alternative for the current modelling situation. This decision was based on the unavailability of generalized turbulence source terms within the plume and is discussed in Chapter IX:4.2.

Turbulence contributions by the bubbles are a very important field of modelling in buoyancy driven flows, but are ignored in the majority of engineering simulations. This simplification is justified to some extent by the small value of C_B described in the previous section. Such a relatively small error in the plume turbulence is unlikely to have a large impact on the bulk recirculating flows in the remainder of the vessel.

2.3. Dissipation at the Free Surface

Energy dissipation at the free surface is regularly ignored in mathematical modelling studies, but represents one of the primary kinetic energy sinks in the ladle. The dissipation due to surface wave formation and bubble bursting is likely to be negligible, but the effects of increased turbulence kinetic energy dissipation and surface deformation cannot be ignored.

2.3.1. Increased Turbulence Kinetic Energy Dissipation

Increased dissipation of turbulence kinetic energy seems to be the primary kinetic energy sink in the plume eye region. The actual effect of omitting this important modelling aspect is quite interesting and has been investigated by employing the small scale Wood's metal model used in the validation experiment conducted in Chapter VII:1.

This model was fitted with a strong, linearly increasing source term of ε in the top 10% of the vessel to simulate the increased turbulent dissipation in that region (the methodology of adding these source terms is described in Chapter IX:1.5). The resulting turbulence outputs are given below:

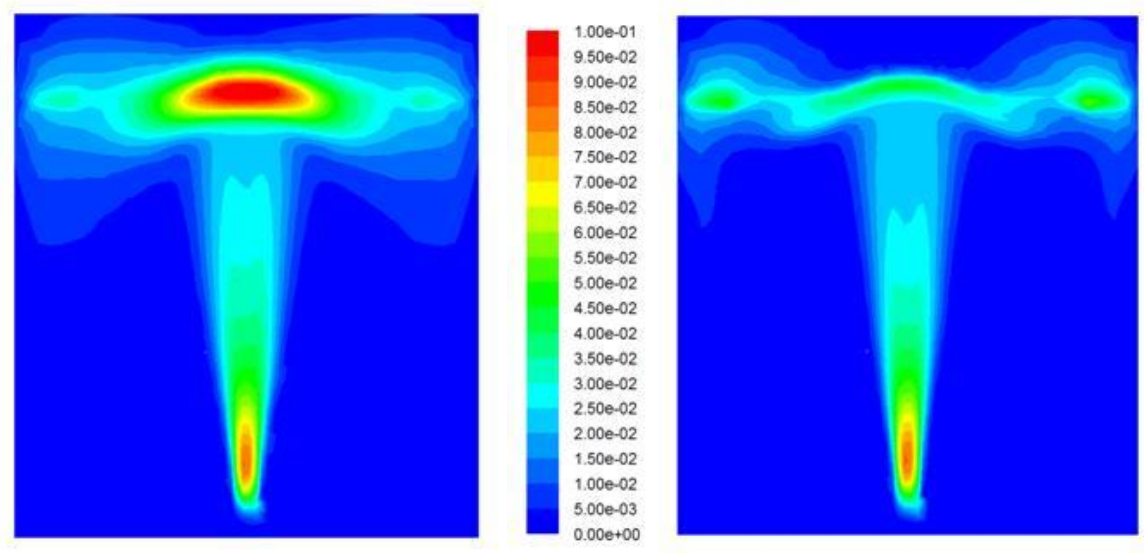

Figure 70: Contours of turbulence kinetic energy for the simulation with (right) and without (left) turbulence dissipation source terms.

Figure 70 displays a marked difference in the turbulence kinetic energy profiles of the simulation with and without added turbulence dissipation source terms. The contours of turbulence dissipation rate displayed in Figure 71, however, do not show such a distinct difference.

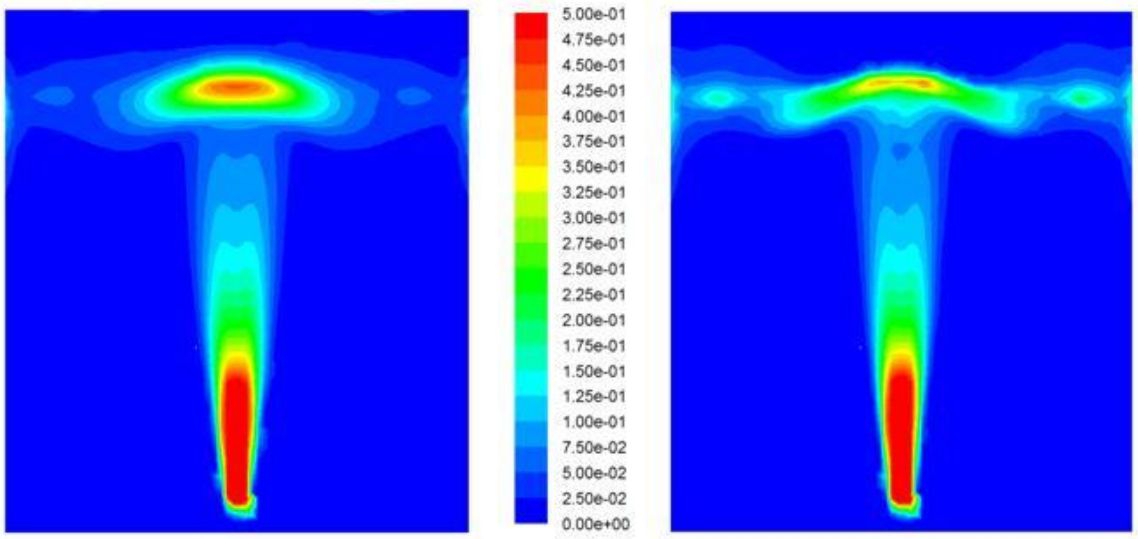

Figure 71: Contours of turbulence kinetic energy dissipation rate for the simulation with (right) and without (left) turbulence dissipation source terms.

The difference between the predictions of turbulence dissipation at the surface of the two simulations can be quantified by defining zones in the vessel as shown below:

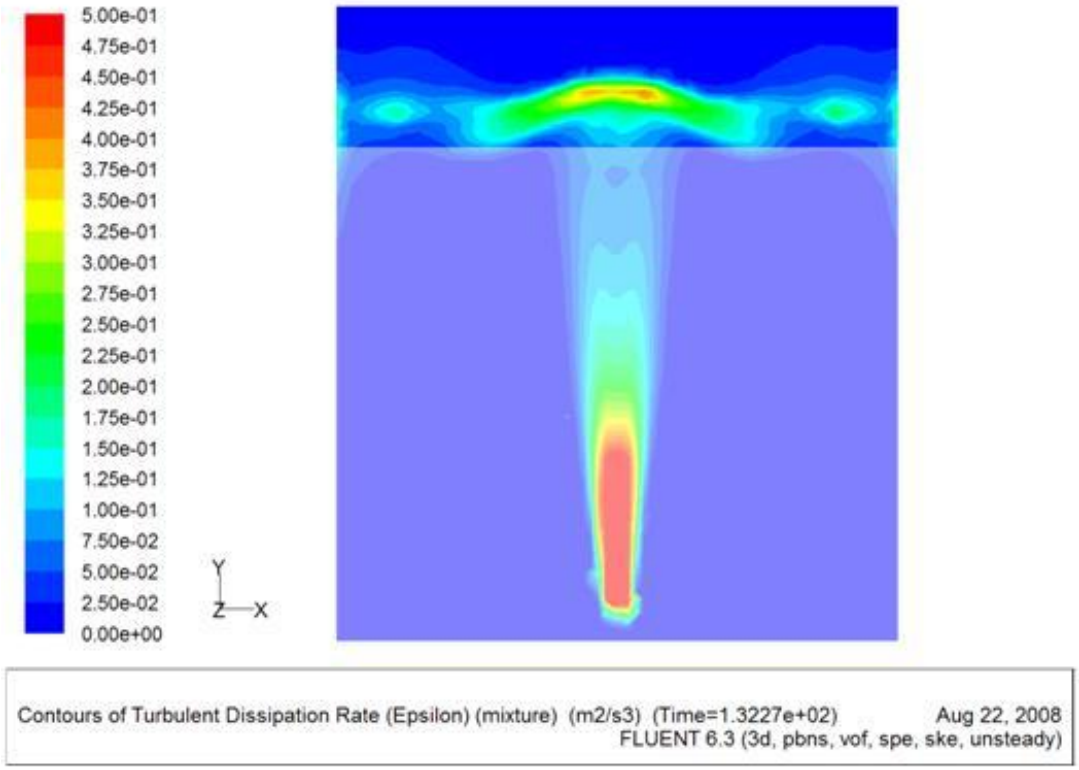

Figure 72: A representation of the two zones in which the dissipation rate is measured.

The turbulence kinetic energy dissipation rate in the two zones identified in Figure 72 was calculated in FLUENT and displayed in Table 12.

Table 12: Energy dissipation to viscous heat in the two different setups.

Zone	Dissipation in model without added ε source terms (W)	Dissipation in model with added ε source terms (W)
Top	1.686	2.125
Bottom	2.982	2.694
Total	**4.668**	**4.819**

For the purpose of accurate flow modelling it is necessary that the energy dissipation at the surface (clear zone in Figure 72) be similar between the two simulations. Such a similarity would mean that the correct amount of energy is available to facilitate flow in the bottom zone. Table 12 shows the dissipation at the surface for the model without added ε source terms to be about 20% less than predictions by the model including surface energy dissipation. Also, the rate of energy dissipation in the bottom region of the plume shows only a 10% difference. When looking at the substantial difference in the distribution of turbulence kinetic energy (Figure 70), this difference is quite small. For modelling purposes, this implies that the omission of surface energy dissipation will not influence the flow solution as much as could be expected.

The only reason for the 20% error in the prediction of the dissipation rate is that the under-predicted values of ε cannot remove the turbulence present in the plume eye quickly enough. The accumulated turbulence then simulates an excessively large fraction of the kinetic energy to be present in the form of randomly fluctuating velocities, leaving only a small amount of kinetic energy in the form of directional mean velocities. This reduction in mean velocities results in a subsequent reduction in mean velocity gradients, which reduces the rate at which mean kinetic energy is lost to turbulence kinetic energy according to Equation 79 in Section 1.2. Since all turbulence kinetic energy is cascaded down the eddy length scale and eventually dissipated as heat, the reduced rate of kinetic energy conversion from mean to turbulent also reduces the rate of viscous dissipation. Quite ironically then, the gross over-prediction of k is directly responsible for the under-prediction of ε.

The large (and incorrect) accumulation of turbulence kinetic energy in the top regions of the vessel does create a problem by influencing the amount of kinetic energy held within the ladle. This will be discussed shortly in Section 4 and in more detail in Chapter IX:3.

2.3.2. Deformation of the Free Surface

The kinetic energy lost by deformation of the free surface is automatically accounted for when the VOF model is used under a gravity field. The mechanism by which this is simulated presents an interesting application of momentum conservation and is briefly outlined below:

$$\frac{\partial}{\partial t}\left(\rho\vec{v}\right)+\nabla\cdot\left(\rho\vec{v}\vec{v}\right)=-\nabla p+\nabla\cdot\left(\bar{\bar{\tau}}\right)+\rho g+\vec{F} \qquad \text{Equation 97}$$

When a control volume is drawn in a fluid standing motionless in a container, the force of gravity acting downwards (second last term) is countered exactly by the force due to the hydrostatic pressure gradient acting upwards (first term on the right). If the fluid mass is then deformed by

some external force, the balance between gravity and hydrostatic pressure gradient is disrupted and a counter force is created to restore the system to equilibrium. In order to sustain this deformation over time, the external force has to continuously counteract the restoring force due to the imbalance between the gravitational acceleration and the hydrostatic pressure gradient.

The external force (final term in Equation 97) in the case of a gas stirred ladle is the buoyant force exerted in an upwards direction by the bubble plume. The restoring force resulting from the deformed plume eye will act downwards, thereby effectively subtracting from the upwards buoyant force. Therefore, only a part of the momentum source term is used to drive the flow and the balance is required to counteract the force acting to restore the system to equilibrium.

From an energy conservation standpoint, this means that the buoyant energy transfer efficiency is reduced in a fashion similar to the conflicting flow patterns presented in Section 2.1.2. The resulting reduction in plume velocity will cause a larger distance to be covered by slip, allowing a smaller distance over which kinetic energy is transferred.

2.3.3. Effect of Surface Deformation on Turbulence Losses

The amount of surface deformation will have a substantial effect on turbulence losses in the plume eye. When the free surface is substantially deformed by a strong and concentrated plume, flows entering the plume eye will be forced to turn very sharply as shown on the right of Figure 73.

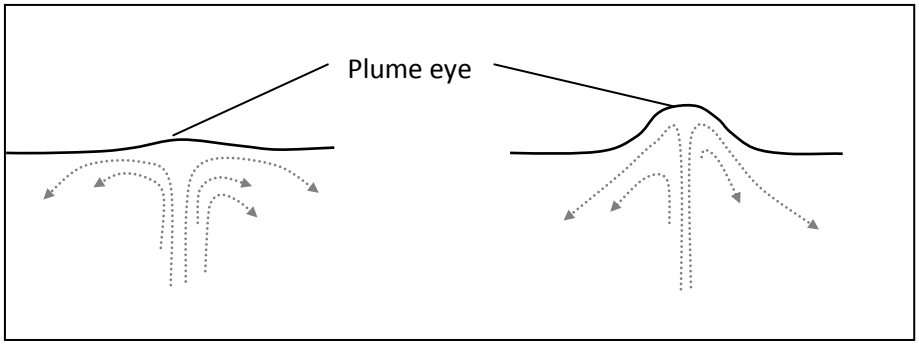

Figure 73: Flow patterns in the plume eye for a weak or dispersed plume (left) and for a strong or concentrated plume (right).

Such a situation will lead to large mean velocity gradients within the plume, generating a large amount of turbulence (Equation 79 in Section 1.2) which is subsequently cascaded down the length scale to be dissipated as heat (Equation 80).

A weaker plume, on the other hand, will cause almost no surface deformation and result in a similar situation as the modelling assumption of a flat free surface. As shown in Chapter VI:2.1, this assumption created substantial over-predictions of the circulatory flow patterns due to under-predicted turbulence losses in the plume eye.

2.4. Friction at the Wall

The wall friction due to shear is well modelled by FLUENT 6.3 and no additional work is required. The no-slip boundary condition employed at the wall should be a good representation of the real

process. Walls also influence the turbulent dissipation rate as can be seen in the top regions of Figure 71. The standard wall functions employed by FLUENT are expected to handle this accurately.

3. Relative Importance of Each Factor

Kishimoto *et al.* (71) conducted experimental measurements and used mathematical modelling by Sheng and Irons (55) to determine the energy dissipation rates in various regions of the vessel. Their results are repeated below:

- Liquid recirculation zone: 36%
- Gas-liquid plume zone : 22%
- Gas-liquid spout zone: 41%
- Surface wave zone: <1 %

Similarly, the small scale water model simulation to be reported in Chapter IX:1.4 was used to assess the quantity of turbulence kinetic energy dissipation in different zones within the ladle. Zones were defined as follows:

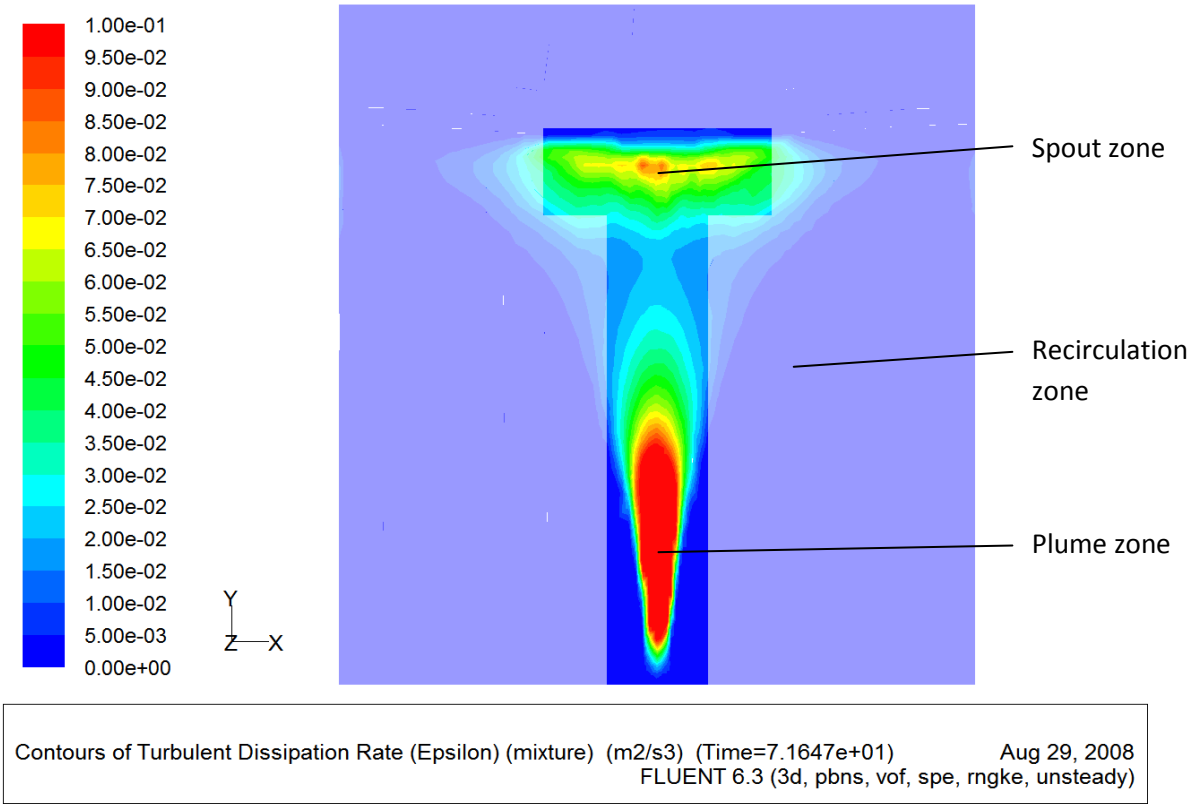

Figure 74: Different zones identified for measurement of turbulence kinetic energy dissipation rate.

The results from this numerical experiment showed the following energy dissipation distribution:

- Liquid recirculation zone: 0.0906 W (48.8%)
- Gas-liquid plume zone: 0.0450 W (24.2%)
- Gas-liquid spout zone: 0.0502 W (27.0%)

Prediction by the present model is in reasonable agreement with the work of Kishimoto *et al.* (71). The biggest reason for any differences lies in the specification of the zone sizes shown in Figure 74. The exact size and shape of the spout and even the plume region is not well defined.

Both sets of results agree, however, that substantially more than 50% of the melt kinetic energy is dissipated in the vicinity of the plume. This means that less than half of the kinetic energy transferred from the rising gas reaches the bulk flow regions on the outside of the plume. When considering that the available kinetic energy is only a fraction of the total buoyant energy input, the transfer process of buoyant energy input to bulk metal kinetic energy is indeed quite poor.

The impact of the ladle wall as a kinetic energy sink was investigated by simply employing a no-slip boundary condition in the perfect slip experiment conducted in Section 2.1.2. The total turbulence kinetic energy dissipation rate of this experiment was 3417 W. When the no-slip boundary condition was employed, the total dissipation rate fell to 3251 W. The 5% difference shows that the wall does serve as a kinetic energy sink, but only to a minor degree. Note also that the flat free surface approximation employed in this experiment produced gross over-estimations of recirculating flow velocities. It can therefore safely be concluded that wall energy losses will be substantially lower in real gas stirred ladles.

Another interesting observation is that the rate of turbulent kinetic energy dissipation integrated over the entire volume is an excellent indication of the rate at which kinetic energy is transferred to the melt by the buoyant plume. As shown in Section 2.3, the deformation of the free surface simply decreases the buoyant energy input efficiency, thereby reducing the rate of kinetic energy transfer rather than removing kinetic energy already in the system. Friction at the wall is the only true kinetic energy sink and was just proven to be negligibly small. Therefore, the rate of kinetic energy input must equal the rate of turbulent dissipation.

4. Kinetic Energy Within The Ladle

The amount of kinetic energy within the ladle at any time plays a dominant role in determining the efficiency of mixing within that ladle. An understanding of the factors influencing the so called 'kinetic energy holding capacity' of the ladle will therefore be of great use for interpreting future experimental results.

The kinetic energy within any computational cell in the melt can be defined by combining the mean and fluctuating velocity components as follows:

$$E_k = \frac{1}{2} M \left(\upsilon + \upsilon'\right)^2$$
$$= M\left(\frac{1}{2}\upsilon^2 + \upsilon\sqrt{2k} + k\right)$$

Equation 98

4.1. Maximising Kinetic Energy Holding Capacity

It was shown in the previous section that turbulence kinetic energy dissipation rate, especially in the region of the plume and plume eye, is the primary factor influencing energy dissipation within the ladle. The logical next step is to design the ladle to attain smooth circulatory flows with the minimum amount of turbulence. Flows with smaller velocity gradients will lose a smaller amount of mean kinetic energy to turbulence kinetic energy (Equation 79) which is subsequently cascaded down the eddy length scale to be dissipated as heat (Equation 80).

To illustrate the effect of this concept, two separate model setups were selected from the experimental results presented in Chapter X:3.2; one with smooth circulatory flow patterns and another with conflicting flows. Outputs illustrating the difference in kinetic energy holding capacity are presented below:

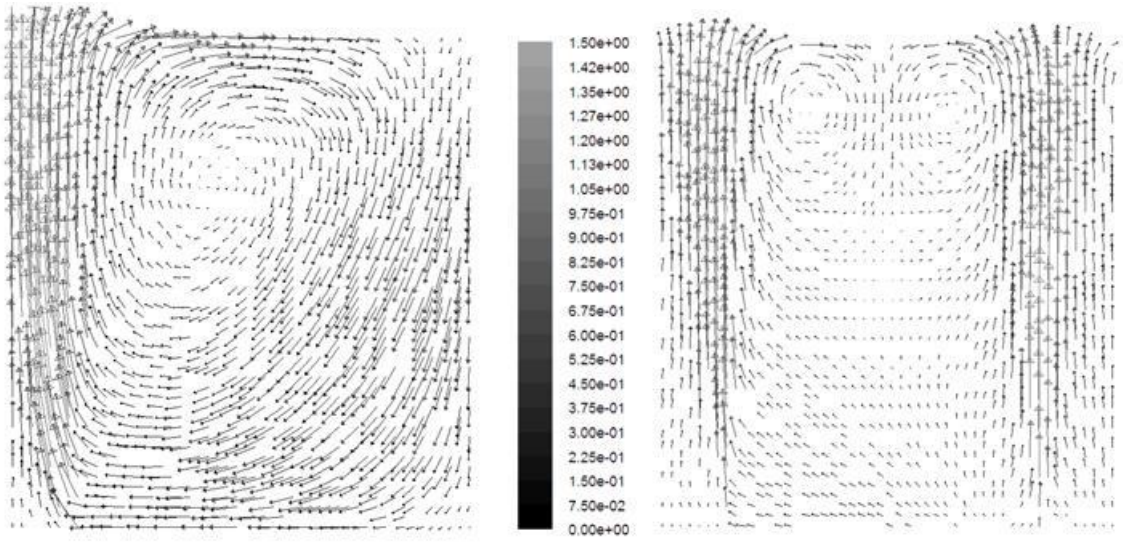

Figure 75: Flow patterns in a smooth (left) and disrupted (right) flow setup.

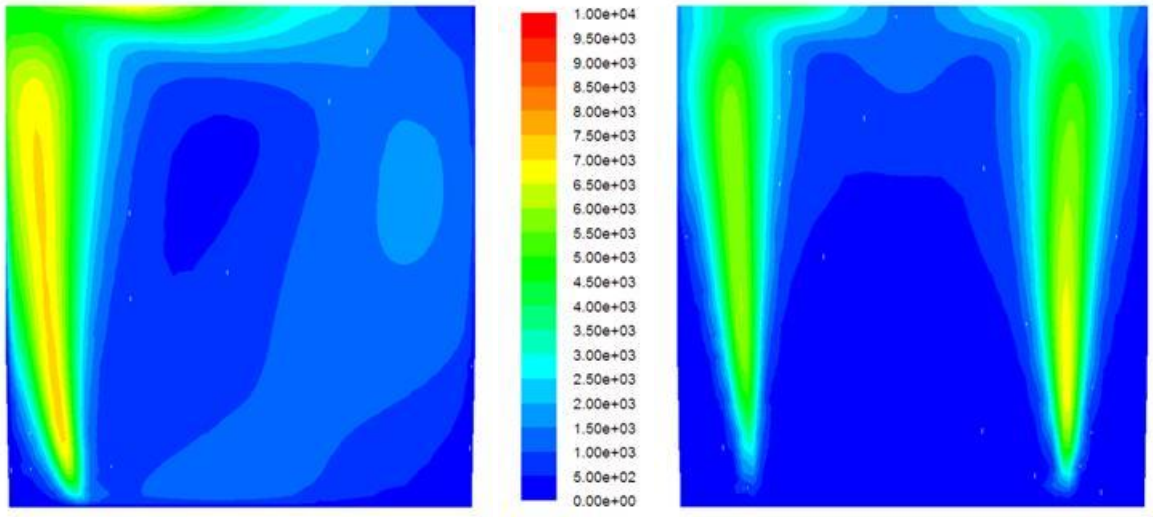

Figure 76: Contours of kinetic energy content (J/m^3) of the two setups.

Figure 76 illustrates the impact of flow pattern development (Figure 75) on kinetic energy distribution throughout the vessel. The left hand side shows some kinetic energy present in the bulk flow regions, while the right hand side contains significant amounts of kinetic energy in the plume regions only. When quantified, the kinetic energy content and the dissipation rate to viscous heat can be calculated by integrating over the volume and the mass of the ladle respectively:

Table 13: Kinetic energy content and viscous dissipation rate in two different flow setups.

Flow setup	Kinetic energy content [J]	Viscous dissipation rate [W]
Smooth	25429	2008
Disrupted	16523	1927

Table 13 shows the marked difference in kinetic energy holding capacity between the two flow setups. The smooth circulatory flow setup shows a 54% improvement in kinetic energy content on the setup with disrupted flow patterns. This is due to the smaller velocity gradients in the vessel with smooth flows, restricting the amount of mean kinetic energy lost to the turbulence kinetic energy cascade.

The similarity in energy dissipation rates confirms the small impact of wall friction as a kinetic energy sink. Kinetic energy losses at the wall will be considerably greater in the ladle setup with well developed circulatory flows, leaving less energy to be dissipated by turbulence. Yet, the disrupted flow setup dissipates less energy as viscous heat, implying that the reduced buoyant energy transfer efficiency resulting from the conflicting flows (Section 2.1.2 of this chapter) create larger kinetic energy losses than the wall friction.

It is also interesting to note the similarities in the smooth circulatory flow patterns shown on the left hand side of Figure 75 and those displayed in Figure 69 on page 113. Even though the tuyere setups are very similar, the conflict of the recirculating flow patterns with the rising plume in Figure 69 is substantially greater than that displayed in Figure 75. Figure 69 was obtained with a flat free surface, while the flows in Figure 75 featured a mobile free surface. This just emphasises the importance of developing an accurate mathematical modelling strategy to give true representations of the complex transport phenomena inside gas stirred ladles.

4.2. Turbulence Migration Over the Free Surface

When simulations were run with a slag phase included, the accumulated turbulence kinetic energy at the free surface seemed to be reduced. The amount by which the accumulated turbulence was reduced was found to be a function of the density of the slag phase. To further investigate this matter, the centric tuyere setup used in Chapter X:1 was implemented with fictitious top gas phase densities of 0.5, 2000 and 4000 kg/m^3.

A gaseous representation was selected over the more realistic inclusion a separate liquid phase on top of the steel because the gas would not exert any additional force on the melt. The weight of a liquid, on the other hand, would exert an additional force on top of the plume eye, thereby adding another variable to the investigation. When the top phase is a gas, the density is the only influential variable.

Accumulated turbulence below the free surface in the three experimental runs is given below:

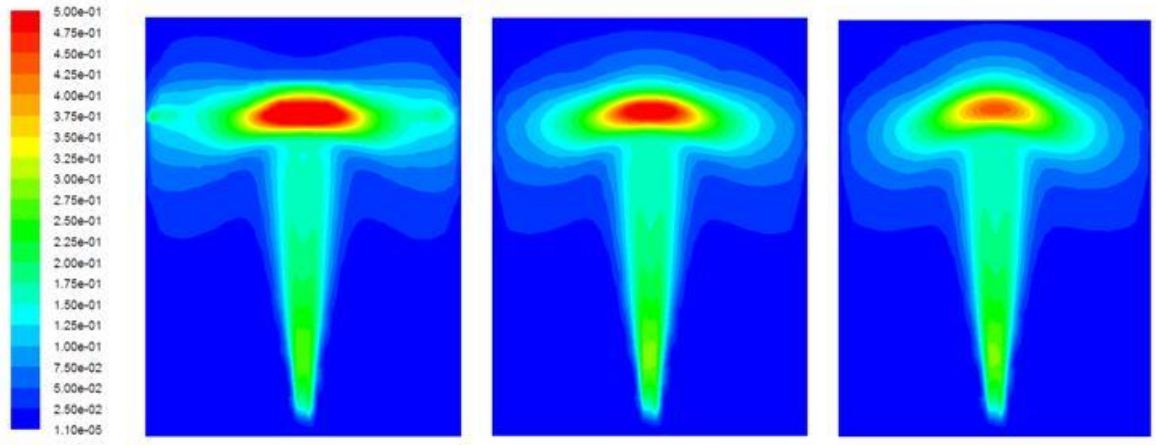

Figure 77: Turbulence kinetic energy profiles at top gas densities of 0.05, 2000 and 4000 kg/m^3.

The turbulence kinetic energy (k) only reports the specific (mass weighted) kinetic energy of the turbulent velocity fluctuations. When k is multiplied with liquid density to give the actual kinetic energy of the turbulent fluctuations per unit volume, the turbulence profiles look quite different:

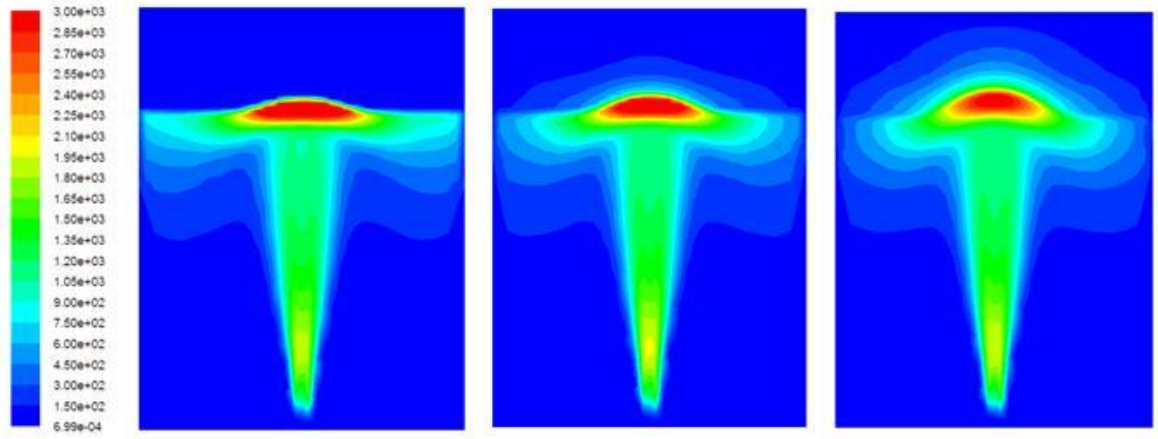

Figure 78: Turbulence kinetic energy per unit volume (J/m^3) in the three experiments.

Figure 78 shows significant migration of turbulence kinetic energy over the free surface and into the denser top gas phases. This diffusion of kinetic energy from the metal to the top gas phase is a result of the mixed fluid multiphase framework employed by the VOF model (assumption discussed in Chapter VI:1.5). Since the mixed fluid approach solves a single set of conservation equations between all the phases, the molecular and turbulent diffusion terms of the momentum equation (second and last on the right of Equation 99) disperses momentum in all directions regardless of any interfaces present in the domain.

$$\frac{\partial}{\partial t}\left(\rho\bar{u}\right)+\nabla\cdot\left(\rho\vec{v}\bar{u}\right)=-\frac{\partial\bar{p}}{\partial x}+\nabla\cdot\left(\mu\nabla\bar{u}\right)+\bar{S}_u + \left(\frac{\partial}{\partial x}\left(-\rho\overline{u'u'}\right)+\frac{\partial}{\partial y}\left(-\rho\overline{u'v'}\right)+\frac{\partial}{\partial z}\left(-\rho\overline{u'w'}\right)\right) \quad \text{Equation 99}$$

In the region just below the free surface, the turbulence (and therefore the turbulent diffusion) is especially large. In this region, the last term in Equation 99 makes a large contribution, dispersing momentum (in the form of fluctuating velocities) in all directions.

The Reynolds stresses in this term are modelled using the turbulent viscosity (Equation 31 in Chapter III:4.1.4.A) according to the Boussinesq hypothesis (Equation 26 in Chapter III:4.1.2). The turbulent viscosity, in turn, is proportional to the density in the cell, thereby stifling the momentum diffusion to light buoyant phases by making a very small contribution.

The difference between this simulated turbulence migration and the actual physical process cannot be estimated at present. The impact of the migration process on flow inside the metal can be quantified though. Table 14 shows the energy distributions between the surface region and the bulk metal phase (zones defined similarly to Figure 72).

Table 14: Energy distributions within the ladle with different top gas densities.

Region	0.5 kg/m³	2000 kg/m³	4000 kg/m³
Turbulence kinetic energy [J]			
Plume eye and top gas	1879	2313	2756
Bulk metal	3236	3106	3089
Total	5115	5419	5845
Total kinetic energy [J]			
Plume eye and top gas	4567	5046	5386
Bulk metal	9665	9317	8953
Total	14232	14363	14339
Turbulence kinetic energy dissipation rate [W]			
Plume eye and top gas	1333	1328	1345
Bulk metal	1614	1523	1473
Total	2947	2851	2818

The turbulence kinetic energy and the total kinetic energy in the plume eye and top gas seem to increase quite substantially with increased turbulence migration. Despite this increase, the dissipation rate in this region remains relatively constant. This can be attributed to the slow dissipation rate of the turbulence kinetic energy that has migrated to the gas phase. Since there is very little mean velocity in the gas, the generation term in the ε transport equation (Equation 28 Chapter III:4.1.4.A) is close to zero and the resulting values of ε are very low. This slow dissipation rate in the gas phase increases the turbulence kinetic energy holding capacity in the surface region.

Looking at the bulk metal region, it can be seen that all the energy quantities in this region decrease with increased turbulence migration. The decrease in the turbulence kinetic energy dissipation rate can only indicate that another dissipation mechanism is getting stronger as the gas density is increased. Since special care was taken to ensure a constant buoyant energy input for all the runs and wall friction has been shown to make a negligible influence on energy dissipation, energy dissipation due to the deformation of the free surface is the only alternative.

The increased surface deformation can be explained by noting the marked decrease in turbulence kinetic energy in the plume eye (Figure 77 and Figure 78) resulting from the turbulence migration to

the gas phase. The decreased values of k in this region results in much reduced values of the turbulent viscosity, thereby decreasing the turbulence and increasing the mean velocities in this region. This means that more of the momentum entering the plume eye region is directed upwards. The result is that more of the total momentum can be used to deform the free surface, thereby increasing the restoring force alluded to in Section 2.3.2 of this chapter.

Rates of turbulence kinetic energy dissipation should also be increased by the larger mean velocities present in the plume eye. Yet, Table 14 shows that the rate of turbulence kinetic energy dissipation remains constant with an increase in top gas phase density. The most probable reason for this is the increased surface deformation reducing buoyant energy transfer in the plume eye region. This would mean that the momentum in the stronger mean flow velocities which is not lost to turbulence is now lost to deform the free surface.

4.3. Size of the Plume Eye

The numerical experiment completed in the previous section also provides an interesting application of Archimedes' principle of buoyancy which states that the upwards buoyant force on the immersed body is equal to the weight of the fluid displaced by the body. This principle also applies to a liquid immersed in a gas. Therefore, the buoyant force acting on the deformed plume eye region is given as follows:

$$F_b = \rho_g g V_{eye}$$ Equation 100

It can plainly be seen that the buoyant force will be substantially stronger at the fictitious gas density of 4000 kg/m^3 than at the normal density of 0.5 kg/m^3.

The force balance over the plume eye equates the joint contributions of the buoyancy and the bubble plume to the weight of the deformed liquid in the plume eye. Thus, if the contribution from the bubble plume remains constant, the increased buoyant force resulting from a denser upper phase must be able to support the weight of a larger plume eye. This effect is well illustrated in the model.

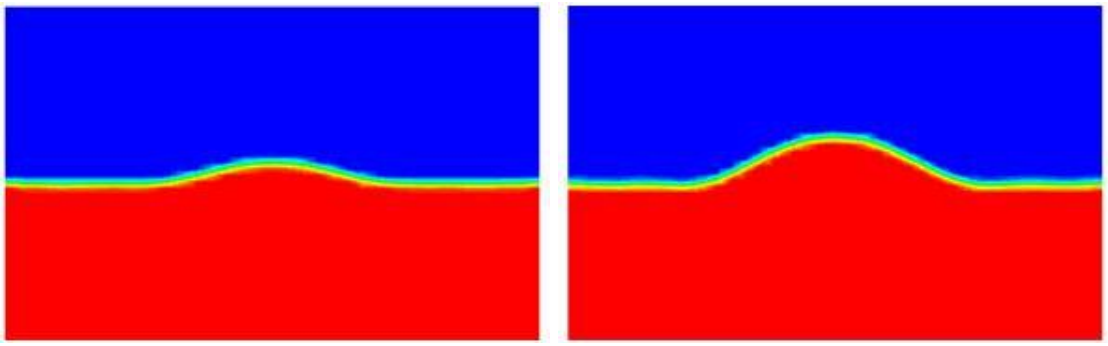

Figure 79: Difference in plume eye with a top gas phase density of 0.5 kg/m^3 (left) and 4000 kg/m^3 (right).

4.4. Turbulence Migration to a Slag Layer

The turbulence migration observed above also occurs when a liquid slag layer is present. The distribution of turbulence kinetic energy per unit volume from this case is displayed below:

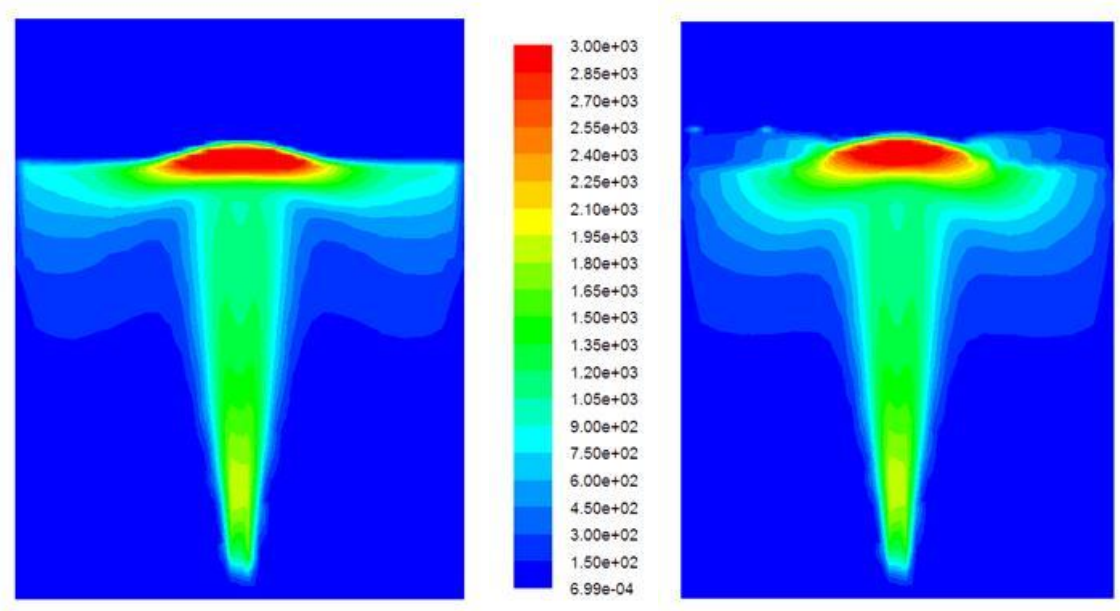

Figure 80: Contours of turbulence kinetic energy (J/m^3) with (right) and without (left) a slag layer.

The migration of turbulence kinetic energy from the plume eye region to the slag layer ($\rho = 2860\ \mathrm{kg/m^3}$) is clearly visible in Figure 80. It is interesting to note, however, that the influence of the liquid slag layer on energy distributions within the ladle is quite different from that of denser gaseous phases. Table 15 illustrates:

Table 15: Energy distributions within the ladle with and without a slag layer.

Region	No slag	Slag
Turbulence kinetic energy [J]		
Plume eye, slag and top gas	1879	2173
Bulk metal	3236	3336
Total	5115	5509
Total kinetic energy [J]		
Plume eye, slag and top gas	4567	3902
Bulk metal	9665	8944
Total	14232	12846
Turbulence kinetic energy dissipation rate [W]		
Plume eye, slag and top gas	1333	1150
Bulk metal	1614	1509
Total	2947	2659

It is immediately evident that the presence of a slag layer decreases the total kinetic energy and the turbulence kinetic energy dissipation rate both in the top and bottom regions of the ladle. This is a result of the increased work required to keep the free surface deformed in the presence of a liquid

slag layer. With no slag layer, only the restoring force of the deformed steel is present. When a slag layer is included, however, it is deformed around the plume eye and therefore exerts an additional restoring force. This means that more of the buoyant energy input is required to constantly counter this larger restoring force (Section 2.3.2 of this chapter).

When considering implications on modelling accuracy, turbulence migration to the slag layer is expected only to increase the accuracy of the model. By extracting turbulence kinetic energy from the region of the plume eye, the slag layer is simulating the increased dissipation rates in the plume eye region. The subsequent decrease in k within the plume eye is an improvement in itself and allows for greater mean velocity gradients and therefore greater (and more accurate) losses of mean kinetic energy to turbulence kinetic energy (Equation 79).

CHAPTER IX:
RESULTS & DISCUSSION PART 2: MODELLING IMPROVEMENTS

> *I have yet to see any problem, however complicated,*
> *which, when you looked at it in the right way,*
> *did not become still more complicated.*
> ***- Paul Anderson***

It is often true that closer scrutiny of an interesting subject turns up a substantially larger number of questions than answers. The current situation is no different and this chapter is dedicated to the search for answers to some of these questions.

A number of answers are investigated, but not implemented in the full scale model. The reason is simply that these new developments need to go through a thorough generalization study before they can safely be implemented in a full scale modelling exercise on a wide variety of ladle setups, gas flow rates and bubble distributions yielding a wide variety of flow situations. Time constraints on the project did not allow for these important developments and this chapter serves more as an indicator for future research.

1. The Bubble Plume

As the sole driving force for mixing, accurate modelling of the bubble plume is essential to ensure an accurate flow solution. Lagrangian particle tracking provides the basic tool with which this can be achieved, but requires a number of additional models for closure. An accurate and informed development of these models is essential for the creation of a model that can safely be generalized over a wide range of ladle setups. Additional modelling requirements include the following:

- An accurate drag law (Chapter V:2.5.2.A)
- Additional forces influencing bubble movement
- Starting size distribution (Chapter V:2.6.2)
- Bubble growth and subsequent breakup (Chapter V:2.5.2.B & Chapter V:2.5.2.C)
- Bubble interaction
    - Breakup and coalescence
    - Wake effects
- Turbulent dispersion of bubbles (Chapter V:2.5.2.D)
- Void fraction
- Bubble induced turbulence

It was established in the previous chapter that the kinetic energy transfer will be accurate as long as the buoyant force is modelled correctly. The bubble size distribution and even the drag law were of

secondary importance. The strength of the plume is not the only concern, however. The correct modelling of its shape is just as important. A very narrow and concentrated plume can underestimate the amount of kinetic energy lost by slippage by raising the bubble rise velocity. Such a plume will also distort the plume eye, thereby over-predicting turbulence in the spout area. The opposite is true for a plume that is too wide.

To ensure an accurate representation of the plume, both in strength and dimension, all of the above mentioned models have to be understood and implemented if necessary. Those that have not been implemented in the present model (Chapter V: Numerical Model Setup Part 2) will be therefore be evaluated below.

1.1. Additional Forces Influencing Bubble Movement

The additional, less influential forces acting on a rising bubble include the transversal lift force, added mass force and hydrodynamic forces. It is standard practice to omit these forces from engineering scale simulations, but no quantitative proof of their insignificance could be found in the literature. A short account of each of these forces will be given below as an indicator for future research (57).

- The transversal lift force is similar to the drag force, only perpendicular to the flow direction. This force is mainly due to velocity gradients in the carrier phase. The primary effect of the transversal lift force is to move the larger spherical capped bubbles towards regions of higher flow and the smaller spherical bubbles towards regions of lower flow velocity. In bubble driven flows, this would result in the larger bubbles migrating towards the centre and smaller bubbles towards the outside of the plume, thereby concentrating more of the stirring power towards the plume centre.
- The added mass force is exerted on a body (bubble, droplet or particle) accelerating relative to the surrounding fluid. Since the bubble travels at a constant terminal slip velocity for the majority of the plume, this force is expected to be negligible. It is known, however, that the added mass force has a greater effect on bubbles due to the low density of the gas.
- The hydrodynamic forces between bubbles are very hard to model in engineering scale simulations. These forces are dependent on the boundary layer formation in and around groups of bubbles which cannot be simulated on any usable scale. For more dense secondary phases, Eulerian-Granular models are available to account for collision and inter-particle friction effects. The Lagrangian approach, however, functions in complete ignorance of this force since the particles can pass straight through each other without experiencing any effect.

The primary purpose of accurate specification of the bubble force balance is to ensure that the kinetic energy transfer is simulated correctly, both in magnitude and location. Hydrodynamic forces can serve to decrease the drag on individual bubbles within the swarm, thereby reducing the magnitude of kinetic energy transfer (Chapter VIII:2.1.1.C). This effect is accounted for by the custom drag law employed as reviewed in Chapter III:5.2.

The transversal lift force, on the other hand, will change the location of energy input by shifting the larger bubbles towards the centre of the plume and the smaller ones towards the outside. It was

found that this effect led to a significant redistribution of the bubbles in the plume (56). The resulting shift in kinetic energy input towards the centre of the plume will lead to higher mean velocity gradients and larger turbulence generation both in the plume and plume eye. Further research is required to quantify the resulting effect on bulk mixing efficiency.

1.2. Bubble Interactions

1.2.1. Bubble Fragments

The small scale VOF model discussed in Chapter IV:4 shows that small bubble fragments are continuously breaking away from larger bubbles (see Figure 81). These bubble fragments have a much smaller terminal velocity and therefore fall away from the larger mother bubble. When they are caught in the wake of the larger bubbles, however, they are lifted quickly to join into the bottom of the bubble once more.

Figure 81: Large bubble surrounded by smaller bubble fragments continuously breaking away and rejoining.

Contributions of these small bubble fragments to overall kinetic energy transfer can safely be ignored. They typically have volumes of three orders of magnitude lower than the larger spherical capped bubbles responsible for the majority of the stirring.

The breakup and rejoining of these bubble fragments can also be viewed as a steady state process. Even though bubble fragments are constantly breaking off and rejoining, the overall situation shown in Figure 81 will remain the same through time. If optimal accuracy is desired, these bubble fragments can be simulated by specifying the starting size distribution accordingly. It was shown in Chapter VI:1.3.3, however, that improvements in the specification of the size distribution will have almost no effect on the overall flow situation.

1.2.2. Coalescence and Breakup of Larger Spherical Capped Bubbles

The larger spherical capped bubbles are primarily responsible for the kinetic energy input in the buoyant plume. Interactions among these bubbles can influence the process of buoyant energy transfer and must therefore be analysed.

The coalescence and breakup characteristics of these bubbles were investigated with the small scale VOF model (Chapter IV:4) to determine the behaviour of a number of spherical bubbles released in the continuum (see Figure 82, left). It was found that the initial spherical bubbles rapidly deformed into the spherical capped shape and collided primarily through wake effects. On collision, the bubbles joined together and grew to a critical size after which breakup occurred. Through this mechanism the typical final distribution of stable spherical capped bubbles resulted as shown on the right of Figure 82. This distribution was maintained for the remainder of the simulation.

Figure 82: Starting (left) and final (right) bubble distributions.

The fact that the distribution on the right of Figure 82 was maintained over time shows that the coalescence and breakup of the larger bubbles can also be seen as a steady state process. Even large deviations from this steady state situation (such as the left of Figure 82) will rapidly be corrected. This also proves that the final size distribution is independent of the starting conditions. For modelling purposes the implication is that no coalescence/breakup model will be necessary if the correct size distribution is specified at the inlet.

Chapter III:5.3 has reviewed models maintaining the correct size distribution when large variations in flow rate are investigated. It is known that bubble plumes resulting from larger gas purging rates also comprise of larger bubbles. When these higher gas purging rates (> 0.01 kg/s/plug) are under investigation, such a model should be considered. The current model, however, will not operate in these regions.

1.3. Void Fraction

The DPM is valid only for flows with a void fraction of 12% or lower due to the discrete particles occupying no volume. At higher volume loadings, the volume occupied by the dispersed phase cannot be ignored. Such high volume loadings do occur in the lower regions of the plume, possibly leading to over-predictions of momentum transfer.

This region has been argued to have little influence on bulk flow when the gas purging rate is kept relatively low (Chapter VI:1.3.1). When optimal accuracy is required or when the need arises to study higher gas purging rates, however, additional modelling is required to account for the volume occupied by the dispersed phase.

The appropriate strategy for void fraction calculation has been identified in Chapter III:5.5. No attempt was made to model the void fraction in the current study because the flow rates employed are relatively low ($< 0.01\ \mathrm{kg/s/plug}$). The model has also been shown to give accurate results even at higher flow rates (Chapter VII:1).

The next version of FLUENT, FLUENT 12.0, will contain a dense phase DPM which is valid for dispersed phase volume fractions of up to 30%. This model will account for the void fraction, therefore ensuring accurate momentum transfer.

1.4. Bubble Induced Turbulence

As shown in Chapter VIII:2.1.3, the slippage of the rising bubbles contribute significantly to the amount of turbulence in the continuous phase. By neglecting this additional turbulence source term, flow velocities in the plume are over-predicted (see Chapter VII:1.2) and turbulence properties are under-predicted.

Bubble induced turbulence is not well understood and is rarely implemented in mathematical modelling studies. A substantial amount of evidence indicates that the inclusion of this effect is essential for accurate flow modelling though. Therefore, a separate study into possible strategies for including this effect in the framework of a commercial CFD package was conducted.

The basic strategy was built on the modelling of additional turbulence source terms with the DPM. These sources of turbulence kinetic energy (k) and its dissipation rate (ε) were introduced by means of a user defined function (Chapter XV:4).

1.4.1. Specification of the Source Terms

A number of possible turbulence source terms were reviewed in Chapter III:5.4. Unfortunately, these source terms do not reflect the turbulence contribution of a single bubble (as required by the DPM) or contain terms that cannot be accessed by means of user defined functions.

Therefore, a theoretical approach was adopted following Joshi (72) as well as Johansen and Boysan (46). It was shown in Chapter VIII:2.1.1.A that the rate at which the bubble loses its pressure energy to turbulent dissipation is given by the product of the buoyant force and the slip velocity:

$$e_d = \left(\rho_l g \upsilon_s\right) \cdot V_B$$ Equation 101

According to Joshi (72), the rate at which this energy dissipation contributes to continuous phase turbulence is given by:

$$e_d = C_B\left(\rho_l g \upsilon_s\right)\cdot V_B$$ Equation 102

To employ this relationship in the k-ε transport equations, it must be handled as another turbulence generation term (G_B).

$$\frac{\partial}{\partial t}(\rho k)+\frac{\partial}{\partial x_j}(\rho k u_j)=\frac{\partial}{\partial x_j}\left[\left(\mu+\frac{\mu_t}{\sigma_k}\right)\frac{\partial k}{\partial x_j}\right]+G_k+G_b+G_B-\rho\varepsilon-Y_M+S_k$$ Equation 103

$$\frac{\partial}{\partial t}(\rho \varepsilon)+\frac{\partial}{\partial x_j}(\rho \varepsilon u_j)=\frac{\partial}{\partial x_j}\left[\left(\mu+\frac{\mu_t}{\sigma_\varepsilon}\right)\frac{\partial \varepsilon}{\partial x_j}\right]+ C_{1\varepsilon}\frac{\varepsilon}{k}\left(G_k+C_{3\varepsilon}G_b+C_{4\varepsilon}G_B\right)-\rho C_{2\varepsilon}\frac{\varepsilon^2}{k}+S_\varepsilon$$ Equation 104

This bubble induced turbulence generation term (G_B) must be specified as a source term (S_k or S_ε). Therefore, the source terms for k and ε are defined as follows:

$$S_k = G_B$$ Equation 105

$$S_\varepsilon = C_{4\varepsilon}\frac{\varepsilon}{k}G_B$$ Equation 106

The rate of turbulence generation (G_B) by each bubble can be described by Equation 102. To be usable as a source term, however, the contribution of the specific particle stream in a given cell for a specific time step (Δt) is required. This was accomplished by multiplying Equation 102 (W/bubble) with the strength of the particle stream (bubbles/s) and the time step size (s) to give to give the rate of turbulence kinetic energy input by a specific particle stream during the current time step (W):

$$\varepsilon_d = \left(C_B\left(\rho_l g \upsilon_s\right)\cdot V_b\right)\cdot strength\cdot \Delta t$$ Equation 107

It was found that the source term in Equation 113 had to be multiplied by a factor in the order of 30 to give a true representation of the two-way turbulence coupling. The necessity of this factor is not well understood and must lie in the method of coupling the turbulence source terms to the transport equations employed by FLUENT. The FLUENT UDF manual (31) states that the macro, DEFINE_DPM_SOURCE, "...allows access to the accumulated source terms for a particle in a given cell before they are added to the mass, momentum and energy exchange terms for coupled DPM calculations." The UDF given in Chapter XV:4 adds Equation 107 to the accumulated particle source terms as recommended in the manual, but had to be augmented with a factor of 30. The resulting best fit value of C_B was 17.5.

The constant $(C_{4\varepsilon})$ used in the source term for the turbulence kinetic energy dissipation rate (Equation 106) was determined empirically as 1.29. The empirical values of C_B and $C_{4\varepsilon}$ were obtained by tuning the model to fit experimental data from Sheng and Irons (55) as will be described shortly in Section 1.6.

Both source terms had to be damped in the bottom regions of the plume where the dispersed phase volume fraction is above the recommended value of 12%. If no damping is employed, the over-predicted turbulence properties would drastically distort the plume in these lower regions. The damping was implemented by linearly increasing both source terms from zero to their actual value over the bottom 20% of the vessel.

1.5. Turbulence at the Free Surface

The over-predicted turbulence just below the free surface (Chapter VIII:2.3.1) was dissipated by introducing a strong source term of ε just below the free surface. It was found that this source term was best described as a linearly increasing function over the top 15% of the melt:

$$S_{\varepsilon 2} = C_{\varepsilon 2}\left(y_{p,N} - 0.85\right)\cdot strength \cdot \Delta t \qquad \text{Equation 108}$$

The source term described in Equation 108 is added to Equation 106 when the normalized height of the particle in the melt $\left(y_{p,N}\right)$ is more than 0.85. The constant $(C_{\varepsilon 2})$ was empirically determined as 4.0.

1.6. Performance of the Model

The model setup employed in this investigation was identical to the specification in Chapter V: Numerical Model Setup Part 2 except for two alterations. The first was the employment of the more advanced RNG k-ε model. This model was chosen since it performs well in highly strained flows (such as the plume) and also in low-Reynolds number flows such as the recirculating flows in a small scale water model. The second was in the specification of bubbles as mono-sized 1 cm spheres. These bubbles had their diameter increased with a factor of 1.5 to account for the bubble shape as described in Chapter V:2.5.2.B. The same custom drag law was used.

The model results were compared to the results from Sheng and Irons (55) in terms of contour plots of k and graphical representations of axial and radial measures of axial flow velocity and turbulence kinetic energy. Results are based on a water model, 42 cm in height and 50 cm in diameter, purged with air through a centric plug. This setup was replicated exactly in the numerical experiment.

1.6.1. Contour Plots

The contour plots of turbulence kinetic energy were compared to experimental measurements and mathematical model outputs. Published mathematical model results are based on a modified version of the SKE model with added source terms for bubble induced turbulence (55).

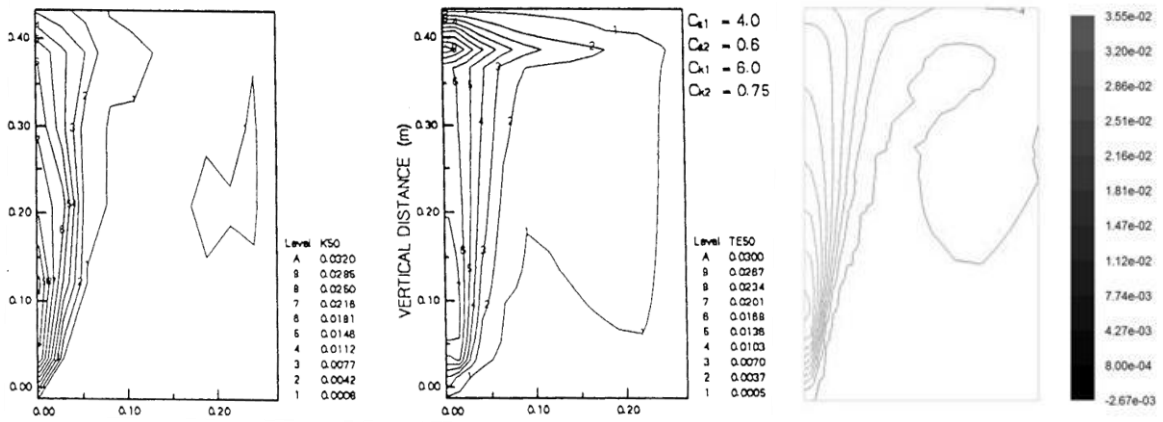

Figure 83: Turbulence contour comparison for a flow rate of 50ml/s. Measured (left), previous modelling (centre) and current modelling (right).

The figures indicate that the current model offers significant improvements in turbulence modelling. The large accumulation of turbulence kinetic energy just below the free surface is completely removed and turbulence in the bulk plume region is no longer under-predicted. Closer scrutiny of the contours also show that the current model offers a quantitative improvement in turbulence modelling on the one employed by Sheng and Irons (55).

1.6.2. Quantitative Comparison

Flow velocities and turbulence kinetic energy were measured in the axial direction along the centreline of the plume. These quantities were also recorded in the radial direction at a height of 21 cm. The experimental values (55), obtained at a gas flow rate of 50 ml/s, are reported below together with model predictions with and without bubble turbulence modulation included. The model with no turbulence modulation was based on the SKE model.

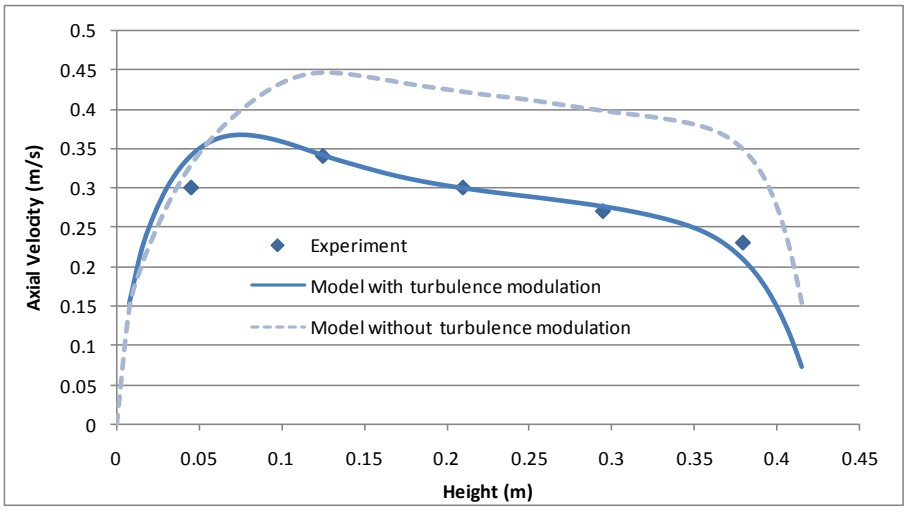

Figure 84: Axial comparisons of modelled flow velocity with and without turbulence modulation.

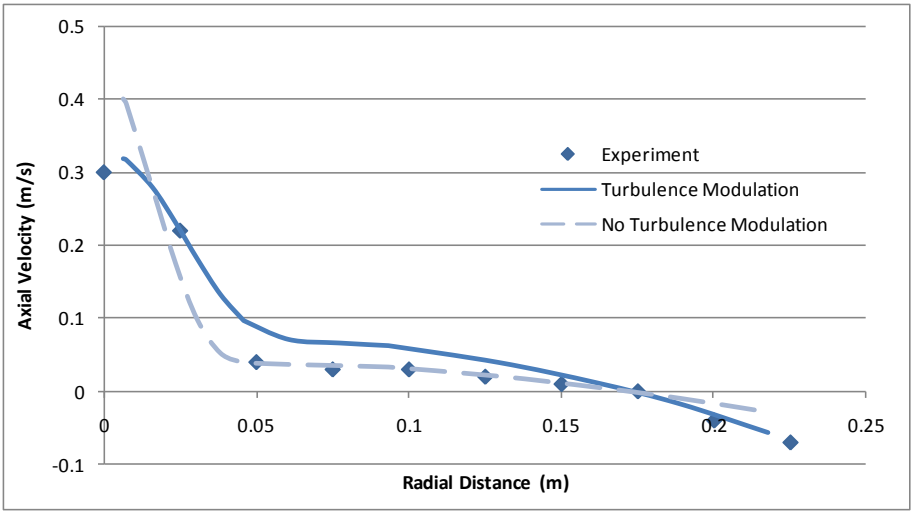

Figure 85: Radial comparisons of modelled flow velocity with and without turbulence modulation.

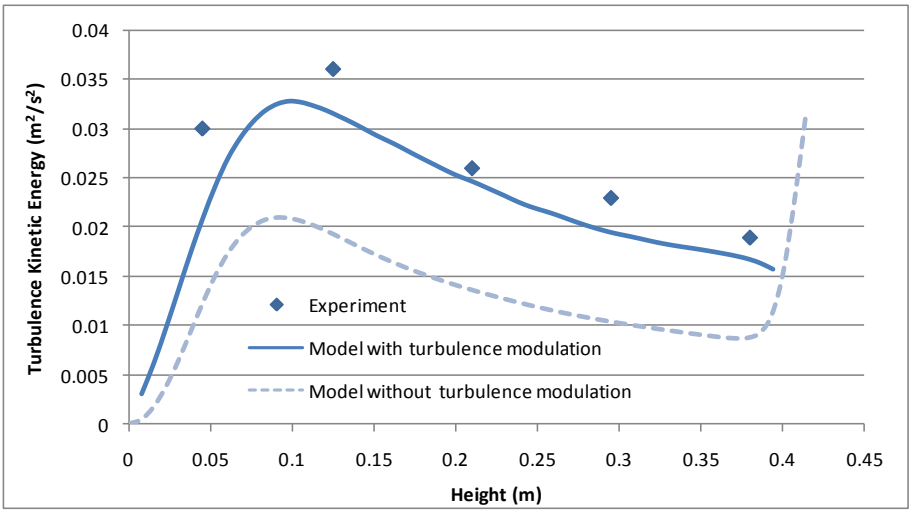

Figure 86: Axial comparisons of modelled turbulence kinetic energy with and without turbulence modulation.

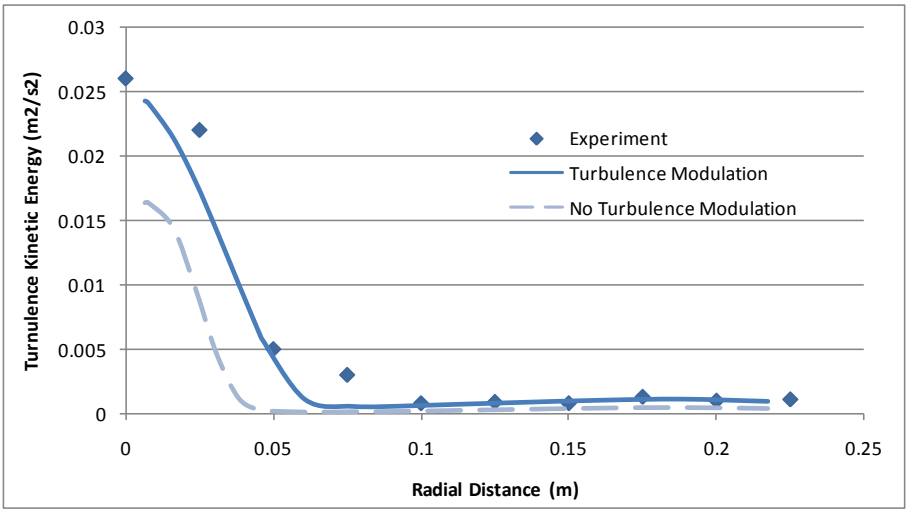

Figure 87: Radial comparisons of modelled turbulence kinetic energy with and without turbulence modulation.

The comparative results clearly show the importance of including turbulence modulation. When no turbulence modulation is employed, the plume is narrowed, velocity is over-predicted and

turbulence is under-predicted. It is also clear that the present approach to turbulence modulation works very effectively in correcting plume characteristics.

The over-prediction of flow velocity in the regions just outside the plume (Figure 85) is a source of concern however. It can be seen from Figure 87 that the turbulence kinetic energy is under-predicted in those same regions, indicating that turbulence modelling in these regions failed to convert a sufficient quantity of mean kinetic energy to turbulence kinetic energy. A possible cause is the over-specification of turbulence source terms, both k and ε, as will be discussed in the following section.

1.6.3. The Value of C_B

The total rate of buoyant energy input in this system can be calculated with Equation 109 since no significant bubble growth occurs within the small scale water model.

$$e = \left(\rho_l g H\right) \cdot Q_V$$ Equation 109

For a gas flow rate of 50 ml/s, the total energy input rate is 0.2058 W.

Chapter VIII:3 showed that the rate of turbulence kinetic energy dissipation integrated over the entire volume is an excellent indication of the total rate of kinetic energy input. For the full scale model, the kinetic energy input is only in the form of mean kinetic energy. When turbulent source terms are employed, the kinetic energy input consists of both mean- and turbulence kinetic energy.

The integrated turbulence kinetic energy dissipation rate amounted to 0.1698 W for the model with turbulence modulation and 0.1070 W for the model with no turbulence modulation. It can be estimated from these results that the bubbles transferred 0.01070 W of their pressure energy to the mean kinetic energy of the fluid while the balance (0.0988 W) is dissipated through slippage. Of the 0.0988 W lost to slip, $0.1698 - 0.1070 = 0.0628$ W was modelled to take part in continuous phase transport.

These results amount to a C_B value of $0.0628/0.0988 = 0.636$. This is much higher than the recommended range of 0 to 0.2 described in Chapter VIII:2.1.3. Extensive trial runs with the turbulence source terms could not achieve the fit shown in Figure 84 to Figure 87 with any smaller amount of turbulence added by the source terms (repeated below for easy reference).

$$S_k = G_B$$ Equation 110

$$S_\varepsilon = C_{4\varepsilon} \frac{\varepsilon}{k} G_B$$ Equation 111

If both source terms were reduced by lowering G_B, insufficient turbulence modulation was simulated resulting in over-predictions of plume velocity and under-predictions of turbulence kinetic energy. If G_B was lowered together with $C_{4\varepsilon}$ so that less of the bubble induced turbulence would be

dissipated, the plume dispersed too much. The increased turbulent dispersion resulted from an increase in the ratio of k/ε in the Lagrangian integral time (Equation 47 in Chapter III:4.2.2.A.iii) used to model turbulent dispersion in the discrete phase model.

The error could lie with the constant (0.15) in the Lagrangian integral time equation which is conceded to be not well known (31). The dense DPM concentration at the bottom of the plume and the consequent damping of turbulence source terms in that region can also contribute to this error.

Despite this large over-specification of C_B, the results in the previous section are still very favourable. The only detriment seems to be an over-prediction of flow velocity and an under-prediction of turbulence kinetic energy in the region just outside the bubble plume. This error is a direct result of the over-specification of both k and ε. These enlarged source terms will introduce a greater amount of turbulence kinetic energy, but also dissipate it much more rapidly. The large sink $(-\rho\varepsilon)$ on the right hand side of the transport equation for k (Equation 28 in Chapter III:4.1.4.A) seems to limit the concentration of k to the centre of the plume only as illustrated in Figure 87. Kinetic energy present as random turbulent fluctuations is therefore modelled to become part of the internal energy of the fluid before it can spread to the outer regions of the plume.

2. Evaluation of Turbulence Models

2.1. Models Including Turbulence Modulation

The question of turbulence modelling is raised quite often in literature regarding the modelling of buoyancy driven flows. It has already been shown that the Reynolds Stress Model gives completely misleading results (Chapter VI:1.4.1), leaving the three k-ε variants for modelling turbulence in the continuous phase. The results presented in the previous section were based on the RNG k-ε model. This section will evaluate the comparative performance of the standard and realizable k-ε models.

The comparative results are presented in similar axial and radial plots of turbulence quantities as shown previously.

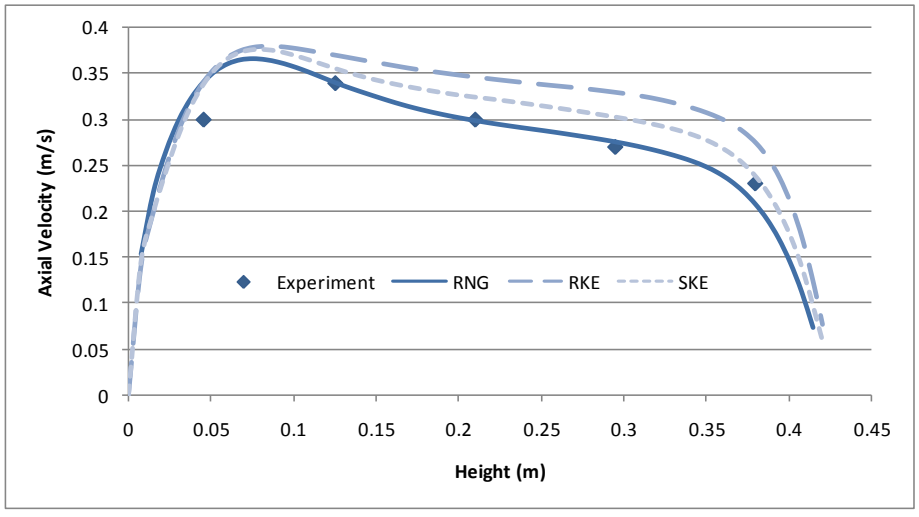

Figure 88: Axial comparisons of flow velocity modelled with different turbulence models.

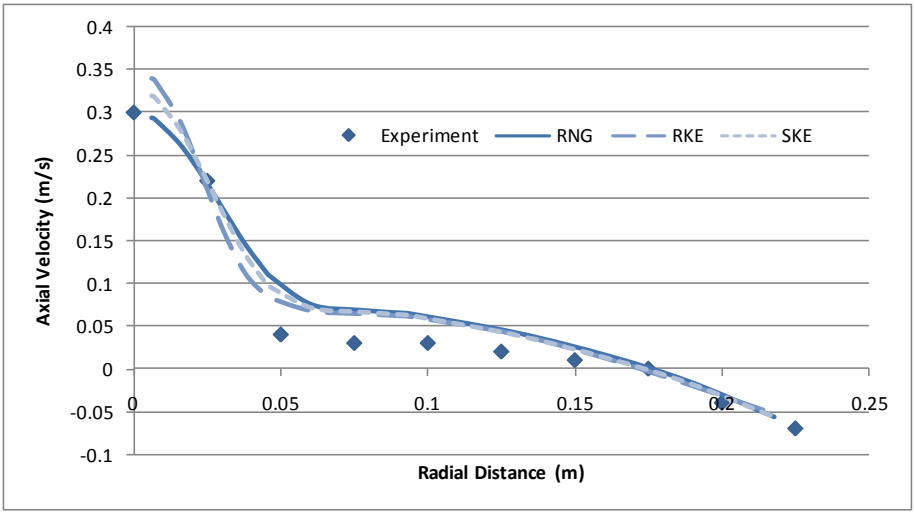

Figure 89: Radial comparisons of flow velocity modelled with different turbulence models.

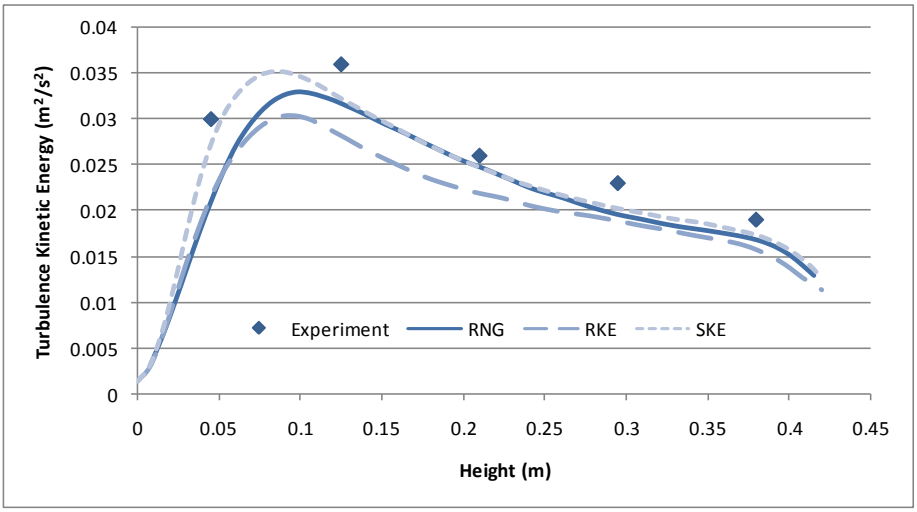

Figure 90: Axial comparisons of turbulence kinetic energy modelled with different turbulence models.

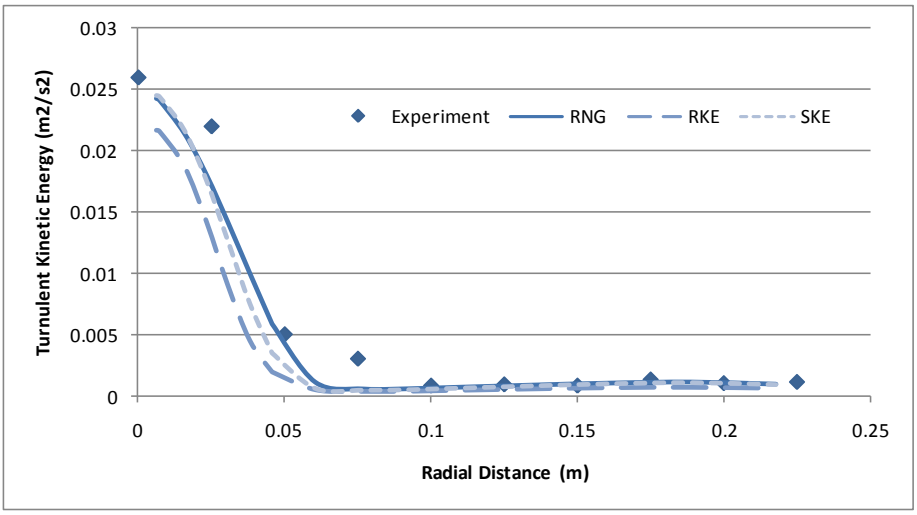

Figure 91: Radial comparisons of turbulence kinetic energy modelled with different turbulence models.

When interpreting these figures, one must take into account that the empirical constants in the model (G_B and $C_{4\varepsilon}$) were especially tuned for use with the RNG k-ε model. Similar fits might be

attainable with the other k-ε variants by changing the values of G_B and $C_{4\varepsilon}$. Theoretically, however, the RNG k-ε model should provide the best results in the current situation.

Results immediately show that the SKE model gives results which are quite close to that of the RNG k-ε model. This is an indication that the flows in the plume are not very highly strained so that the strain term (R_ε in Equation 32) does not make a large improvement in modelling ε.

The RKE model results show a more substantial deviation from those produced by the RNG k-ε model. The over-predictions of plume velocity and the under-predictions of turbulence kinetic energy show that the rate of turbulence kinetic energy dissipation is quite substantially over-predicted by the modified ε transport equation employed by the RKE model. These over-predictions of ε are visible in the recirculating flows outside the plume as well:

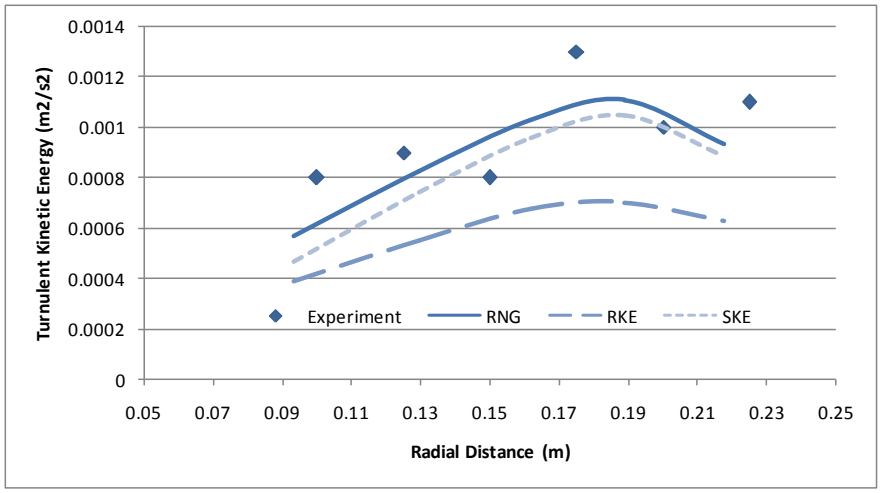

Figure 92: Radial predictions of turbulence kinetic energy outside the plume.

Figure 92 shows that predictions by the SKE and RNG k-ε models are in good agreement with the measured results (55). The RKE model, however, shows a 30-40% under-prediction of turbulence in these regions. When considering that the bulk circulatory flow regions comprise more than 80% of the vessel, this error is quite severe.

2.2. Model Without Turbulence Modulation

Turbulence modelling in the full scale model (developed in Chapter V: Numerical Model Setup Part 2) was based on the SKE model with a slightly reduced ε generation constant. This alteration was necessary for lack of a generilized model for bubble induced turbulence and will be discussed shortly in Section 4.2.

Performance of this model was also compared against the experimental results from Sheng and Irons (55):

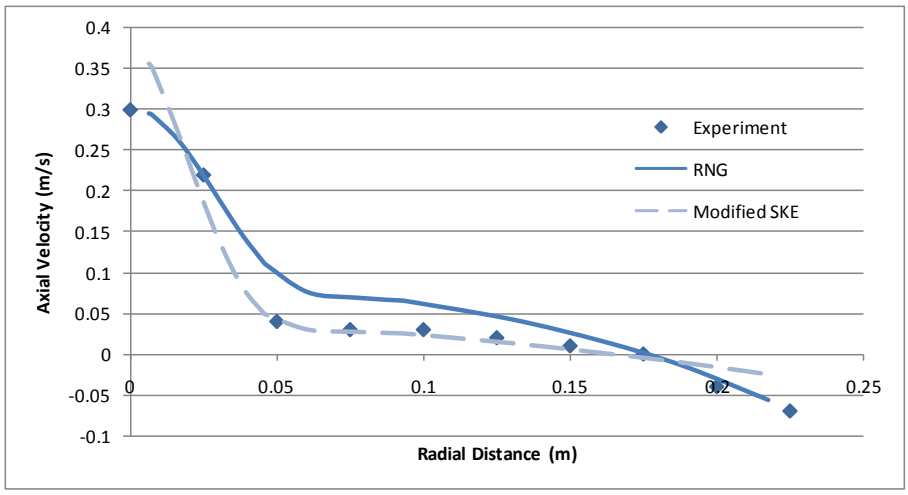

Figure 93: Radial comparisons of flow velocity modelled with turbulence source terms (RNG) and with a reduced ε generation constant (modified SKE).

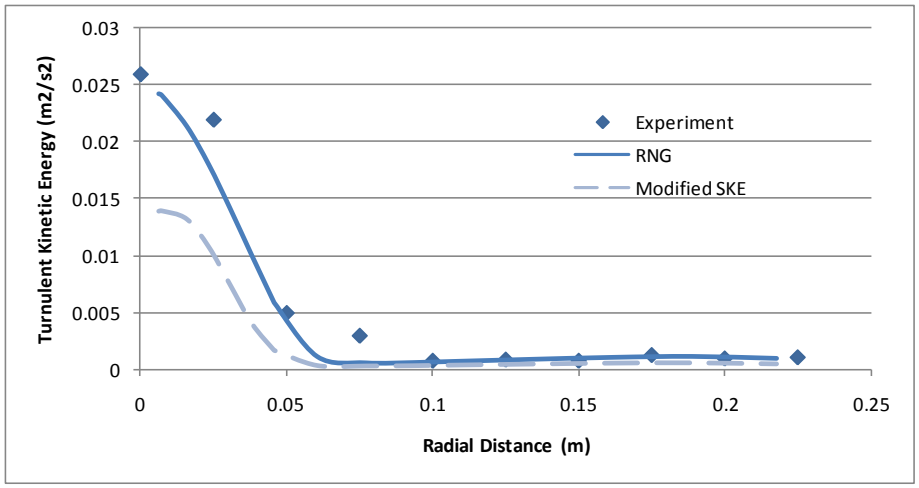

Figure 94: Radial comparisons of turbulence kinetic energy modelled with turbulence source terms (RNG) and with a reduced ε generation constant (modified SKE).

Apart from the expected over-predictions of plume centreline flow velocities, the modified SKE model gives a very good account of flow velocity within the vessel, improving even on the model with included turbulence modulation. Values of turbulence kinetic energy, however, are substantially under-predicted both inside and outside the plume. The under-predictions outside the plume are represented in Figure 95.

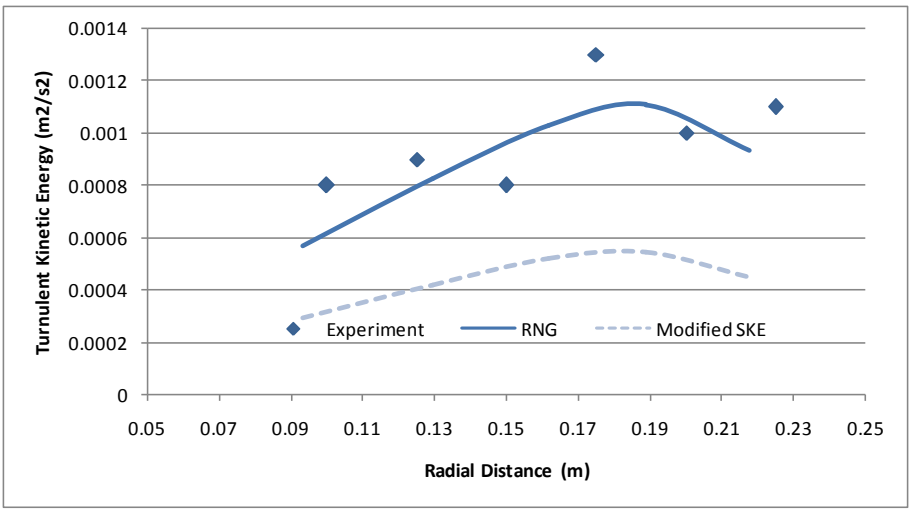

Figure 95: Radial comparisons of turbulence kinetic energy outside the plume modelled with turbulence source terms (RNG) and with a reduced ε generation constant (modified SKE).

Figure 95 shows a turbulence kinetic energy under-prediction of almost 50% in the regions outside the plume. It is therefore clear that the omission of turbulence modulation by the bubbles creates errors outside the plume as well.

These under-predicted values of k would normally lead to over-predicted values of mean flow velocity, but Figure 93 shows that the mean flow velocities outside the plume are in good agreement with the experimental data. This occurrence can be explained by the incorrectly simulated accumulation of turbulence just below the free surface (introduced in Chapter VIII:2.3.1) as outlined in the following section.

3. Turbulence Accumulation at the Free Surface

"In the vicinity of the free surface the turbulence is damped by the stagnation pressure when eddies approach and locally lift the surface. This causes a redistribution of turbulence energy in different directions and leads to increased dissipation rates." – Johansen and Boysan (46).

The quoted paragraph above is the only direct reference to the turbulence accumulation and its cause that could be found in the literature. This is most surprising since the accumulation of turbulence just below the free surface is one of the most influential factors on the mathematical modelling of flow and mixing in gas stirred ladles.

The strategy implemented by Johansen and Boysan (46) entails employing a boundary condition on the plume eye to account for the dissipation resulting from the deformation of the free surface. Yet, the current model features a mobile and deformable free surface, which is indeed deformed by the axial momentum in the plume eye region. At first glance, this gives reason to believe that the effect of increased dissipation rates should be accounted for automatically. In reality, however, the turbulence over-predictions in the current model are even greater than those in previous models featuring a flat free surface. This is largely because the plume eye deformation forces the flow to turn more sharply, creating larger mean velocity gradients.

3.1. The Effect of Accumulated Turbulence on Flow Velocity

The options for countering this error within a commercial CFD package such as FLUENT 6.3 are very limited. The turbulence dissipation source term introduced with the discrete phase model (as described in Chapter IX:1.5) is the only feasible option at present. Still, the model with the large turbulence over-predictions at the free surface performed very well in validation experiments (Chapter VII:1). To investigate this matter, the validation experiment was repeated, only this time removing the accumulated turbulence with the method of strong ε source terms as described in Chapter IX:1.5. The resulting mean flow velocities were substantially over-predicted. A comparison with the flows generated from the actual validation experiment is presented below:

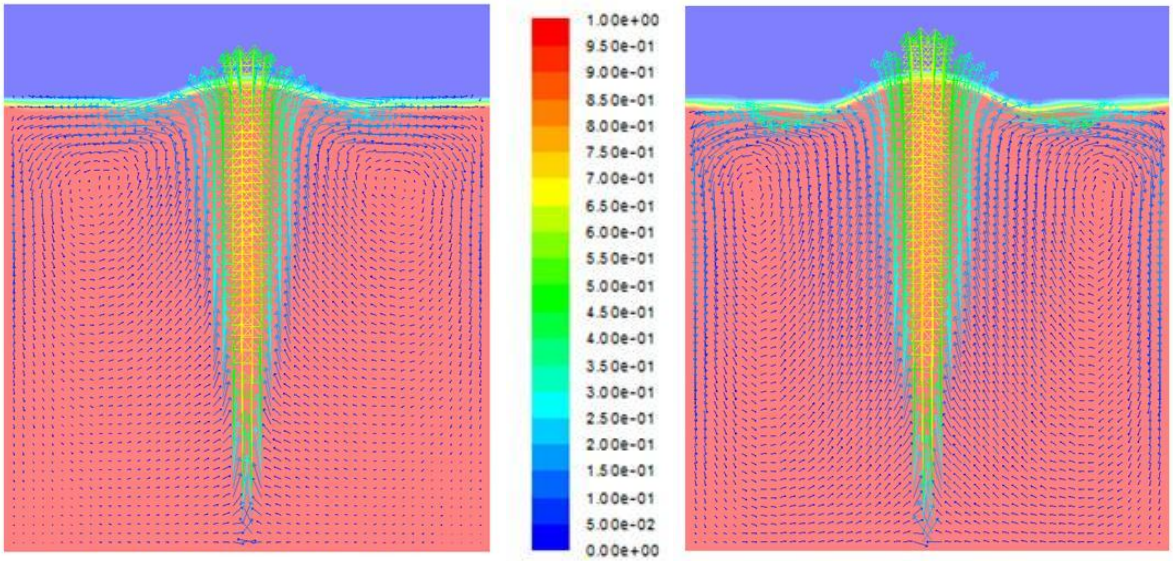

Figure 96: A comparison of flow results with (left) and without (right) the accumulated turbulence.

The difference between the experiments is clear from Figure 96. Substantial over-predictions of the recirculating flows outside the plume can be distinguished in the simulation without any accumulated turbulence at the free surface. The torus developing in the upper regions of the vessel is elongated to fill the entire vessel, leaving no dead zones at the bottom of the ladle.

Therefore, the model with correct turbulence kinetic energy dissipation modelling at the free surface actually performs worse than the model with the incorrect turbulence accumulation. The reason behind this inconsistency lies in the omission of turbulence source terms and can be explained as follows:

The over-predicted flow velocities on the outside of the plume are the direct result of under-predicted quantities of turbulence kinetic energy in these regions, simulating only a small amount of kinetic energy to be to present as fluctuating velocities (turbulence kinetic energy). Turbulence generation in these smooth, slow moving circulatory flow regions is almost non-existent due to the very low mean velocity gradients. Therefore, the majority of turbulence in the bulk recirculating flow regions is generated in the highly strained plume and carried there by convective transport with the mean flow velocities (the convection term in Equation 28, the transport equation for k). However, turbulence in the plume region is substantially under-predicted due to the omission of bubble

induced turbulence. A smaller amount of turbulence kinetic energy is therefore available to be transported to the outer regions of the plume.

The question then arises as to why the model with the incorrect accumulated turbulence at the free surface produced such admirable flow velocities in the regions outside the plume (Chapter VII:1.2). This can be answered by recognizing that the over-predicted turbulence at the free surface simulates a larger percentage of the kinetic energy to be present as random fluctuations (turbulence kinetic energy) and a much smaller percentage to be left as directional mean velocities. The resulting imbalance between mean- and turbulence kinetic energy will drastically change the way in which momentum is transported from the plume eye region. Turbulent diffusion will now be the primary method of momentum transport, causing a steady spread of momentum in all directions, while the directional convective momentum transport will be much reduced. The result of this imbalance will be a reduction of mean flow velocities on the outside of the plume.

By mere chance, it seems to unfold that the over-predictions of turbulence kinetic energy in the plume eye and the under-predictions thereof in the circulatory flows on the outside of the plume combine to give the correct amount of kinetic energy manifested as mean recirculating flows. This is well illustrated in the validation experiment in Chapter VII:1.

The resulting imbalance between convective and diffusive momentum transport, however, could cause errors in the prediction of kinetic energy distribution throughout the ladle. Such errors would impact the mixing results generated by the full scale model. The exact impact of this cannot be quantified at present though.

4. Implications on Full Scale Modelling

4.1. Developments Required in the Field of Turbulence Modulation

The previous section has shown the importance of including turbulence modulation by the bubbles into the simulation. Turbulence in the bubble plume needs to be increased so as to provide the correct amount of turbulence kinetic energy for convective transport to the bulk recirculating flows. The accumulated turbulence at the free surface also needs to be removed in order to allow the correct amount of convective transport from the region of the plume eye.

A number of developments are required before turbulence modulation can safely be included in a general full scale simulation of a gas stirred ladle. These are listed below:

4.1.1. Correct Value of C_B

As described in Section 1.6.3, the value of C_B resulting from the current turbulence source terms is substantially too high, indicating that values of both k and ε are over predicted in the plume. The result will be an incorrect value of the turbulent viscosity (Equation 31 in Chapter III:4.1.4.A) which will affect the way in which turbulent diffusion is simulated in the momentum transport equation. Further development is therefore required to predict the correct amount of mean and turbulence

kinetic energy within the plume, while maintaining a C_B value in the recommended range of 0 to 0.2 and ensuring that the plume does not become too wide.

4.1.2. Accounting for the Void Fraction

The bottom regions of the plume, where the DPM concentrations are substantially higher than the recommended 12%, required that the turbulence source terms be damped by a linear function (see Section 1.4.1). This artificial way of turbulence modulation is bound to influence results and needs to be improved upon.

4.1.3. Removal of Accumulated Turbulence at the Free Surface

The present method for accomplishing this is purely empirical and not safe for generalization. A sound theoretical basis for the increased dissipation at the surface needs to be established so that a general modelling strategy can be built.

4.2. Alternative Modelling Approach

In the absence of a generalized method for modelling turbulence modulation by gas bubbles, this effect will have to be ignored in the full scale simulation exercise. The repercussions of this omission are over-predictions of plume velocity and under-predictions of plume turbulence. Most importantly, these errors result in a narrowed and concentrated plume as shown in the comparison of axial velocities in Figure 85. This narrow plume gives rise to a tall and narrow plume eye which leads to even further over-predictions of turbulence below the free surface.

The direct reason for the reduction in plume diameter is a reduction in the Lagrangian time scale governing the amount of turbulent dispersion experienced by the particles:

$$T_L = 0.16\frac{k}{\varepsilon}$$ Equation 112

This implies that the turbulence kinetic energy (k) is more substantially under-predicted by the omission of bubble induced turbulence than its dissipation rate (ε). The reason for this occurrence is discussed below:

The narrow and concentrated plume results in over-predicted velocity gradients which are implemented in the equation for calculating the turbulence production due to mean velocity gradients (the only remaining turbulence source):

$$G_k = -\rho\overline{u'_i u'_j}\frac{\partial u_j}{\partial x_i}$$ Equation 113

The resulting over-predicted turbulence generation term is then implemented in the model equations of both k and ε. For ease of reference, the model equations for the SKE model are repeated here:

$$\frac{\partial}{\partial t}(\rho k)+\frac{\partial}{\partial x_i}(\rho k u_i)=\frac{\partial}{\partial x_j}\left[\left(\mu+\frac{\mu_t}{\sigma_k}\right)\frac{\partial k}{\partial x_j}\right]+G_k+G_b-\rho\varepsilon-Y_M+S_k \qquad \text{Equation 114}$$

$$\frac{\partial}{\partial t}(\rho \varepsilon)+\frac{\partial}{\partial x_i}(\rho \varepsilon u_i)=\frac{\partial}{\partial x_j}\left[\left(\mu+\frac{\mu_t}{\sigma_\varepsilon}\right)\frac{\partial \varepsilon}{\partial x_j}\right]+ C_{1\varepsilon}\frac{\varepsilon}{k}(G_k+C_{3\varepsilon}G_b)-\rho C_{2\varepsilon}\frac{\varepsilon^2}{k}+S_\varepsilon \qquad \text{Equation 115}$$

It can be seen G_k is implemented in the generation terms of both transport equations (second terms on the right). It has been established that ε is larger than k in the central parts of the plume:

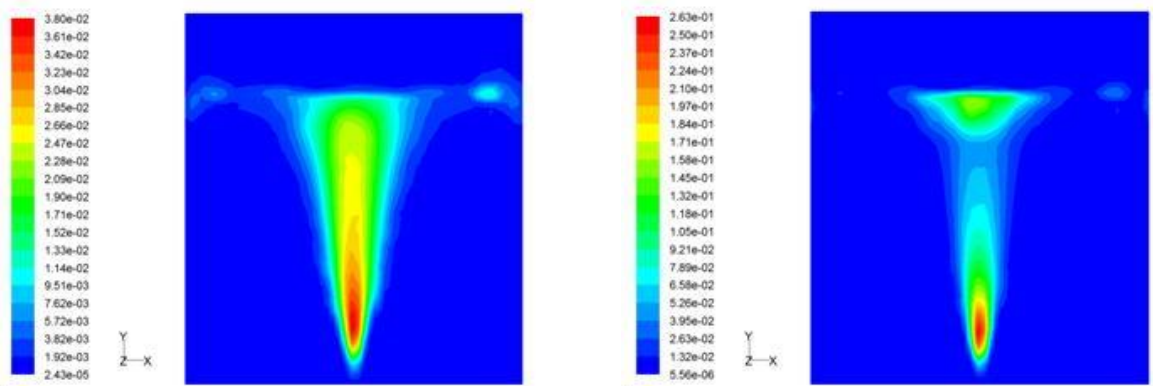

Figure 97: Contours of turbulence kinetic energy (left) and its dissipation rate (right) inside a typical gas plume.

The quantity $C_{1\varepsilon}(\varepsilon/k)$ preceding the generation term in Equation 115 will therefore be substantially greater than unity (the constant $C_{1\varepsilon}=1.44$). This implies that any over-prediction in G_k will be further augmented in the generation term of the ε transport equation, thereby causing larger over-predictions in ε than in k.

Advanced turbulence models augment this error even further. When using the RNG k-ε model for example, the transport equation for turbulence dissipation rate is modified with an extra term, R_ε:

$$\frac{\partial}{\partial t}(\rho \varepsilon)+\frac{\partial}{\partial x_j}(\rho \varepsilon u_j)=\frac{\partial}{\partial x_j}\left[\left(\mu+\frac{\mu_t}{\sigma_\varepsilon}\right)\frac{\partial \varepsilon}{\partial x_j}\right] +C_{1\varepsilon}\frac{\varepsilon}{k}(G_k+C_{3\varepsilon}G_b)-\rho C_{2\varepsilon}\frac{\varepsilon^2}{k}-R_\varepsilon+S_\varepsilon \qquad \text{Equation 116}$$

This term (second last on the right) is meant to increase model accuracy in highly strained flow by making a positive contribution, and therefore acting as another source term for ε. In the current

situation, this modification results in further over-predictions of ε, thereby reducing the plume diameter even more.

The ε transport equation used by the RKE model is more complex, but is designed to result in similar improvements than those offered by the RNG k-ε model. It can therefore be assumed that the over-prediction in ε will be manifested by the RKE model as well.

The only remedy for the current problem is to reduce the constant $(C_{1\varepsilon})$ influencing the production of ε in Equation 115. It was established through trial and error that the correct plume diameter (as shown in Chapter VII:2) could be attained with the SKE model by reducing $C_{1\varepsilon}$ from the default 1.44 to 1.38. This small alteration resulted in a decrease in ε and a subsequent increase in k, thereby increasing the Lagragian integral time and widening the plume.

The RNG and realizable k-ε models required much more drastic alterations in the model constants, however. Due to the strong interdependency of these constants, alterations of this magnitude could result in substantial modelling errors. The traditional SKE model is therefore left as the only alternative for modelling turbulence.

The reduction in the dissipation rate source term is expected to increase the accuracy of turbulence modelling both inside and outside the plume. This improvement is brought about by the formulation of the turbulent viscosity, the final expression of turbulence used to close the RANS equations.

$$\mu_t = \rho C_\mu \frac{k^2}{\varepsilon}$$ Equation 117

Inside the plume region, both k and ε are under-predicted – k more so than ε. The result is a substantial under-prediction of the turbulent viscosity. By decreasing the ε generation constant, ε is decreased and k is increased, thereby markedly increasing the turbulent viscosity. It is admitted that this correction will probably not be enough, but it is a definite improvement.

In the bulk recirculation zones outside the plume, it has been shown that the SKE model without turbulence source terms under-predicts k quite substantially (Figure 95). The slight increase in k and decrease in ε brought about by this alteration would therefore be an improvement here as well.

The only place in which this modification will have an adverse effect is in further over-predicting the accumulation of turbulence in the vicinity of the plume eye (Chapter VIII:2.3).

4.3. Developments Required for Complete Accuracy

It has been shown that the method of momentum input with the Lagrangian discrete phase model works very effectively as long as the bubble growth is accounted for, a reasonably accurate drag law is implemented and a rough estimate of the correct size distribution is provided. For complete accuracy in energy input, however, a generalized model for turbulence contribution (both k and ε) by the bubbles is required as outlined in Section 4.1 above.

In the region of the plume eye, the turbulence kinetic energy dissipation rate needs to be substantially increased. The method of introducing turbulence dissipation with the rising discrete phase particles has been shown to work very well, but needs to be generalized for successful application in full scale gas stirred ladles. Some additional investigations into the energy transfer mechanisms in the region of the plume eye are recommended. This region is one of the most influential, but also one of the most poorly understood modelling focal points in the ladle.

The new and improved dense discrete phase model and separated fluid volume of fluid model offered by FLUENT 12 should be investigated. In theory, the dense DPM will provide added accuracy in the lower regions of the plume where the gas concentration is higher by accounting for the void fraction. The new separated fluid VOF model offered by FLUENT 12 could eliminate the diffusion of momentum from the metal phase to the slag and provide the opportunity to include possible slippage between metal and slag.

The impact of additional players in the bubble force balance (such as the transverse drag force) should be quantified. It is postulated, however, that these forces will have a reasonably small impact on the ladle energy budget and therefore the flows resulting from the discrete phase momentum sources. Whether this impact is negligible is yet to be determined.

4.4. Why the Current Model Works

When looking at the recommendations for improvement in the previous section, it is quite surprising that the current model can give such accurate comparisons to measured values as shown in Chapter VII: Validation. The accuracy of the present model can be attributed to the rather fortuitous interaction between all the modelling shortcomings described above.

The omission of turbulence source terms is justified to some extent by the fact that only a small percentage of bubble slip dissipation is manifested as turbulence in the continuous phase (Chapter VIII:2.1.3). The turbulent viscosity will still be under-predicted, but the reduction in the ε generation constant should reduce this error to some extent (Section 4.2 above).

The substantial under-predictions of turbulence in the recirculating zones outside the plume combines with the over-prediction of turbulence kinetic energy in the plume eye region to still result in accurate flow velocities (Section 3.1 of this chapter). The under-prediction of turbulence kinetic energy and subsequent values of the turbulent viscosity should be corrected to some degree by the reduction in the ε generation constant.

When tracer diffusion is considered, the under-prediction of turbulence throughout the volume will result in reduced diffusive species transport (reviewed in Chapter III:3.4). Bulk mixing efficiency is more dependent on effective convective transport though. Convective transport is responsible for bringing the species to the furthest corners of the vessels while diffusive transport acts more as a local mechanism responsible for dispersing and homogenising species concentration once convection has delivered it.

It is important that diffusive species transport be sufficient to ensure that the tracer species does not simply pass through a specific location in the continuum without leaving a trace of its ever being

there. As a rough analogy it can be said that diffusive transport is responsible for marking all the places where the tracer concentration has visited through convection. Observations during the numerous experimental runs competed has proven the simulated diffusive transport to be sufficient for this purpose. Additionally, the constant turbulent Schmidt number is expected to larger than the default value of 0.7 in the bulk recirculating flow regions (a value of 1 is recommended in Chapter III:3.4.1). Keeping the default value will therefore increase the simulated diffusion of the tracer species, compensating for the reduced turbulent diffusion to some degree.

The low gas purging rates investigated in the current application only deliver void fractions in excess of the recommended 12% in the bottom regions of the plume. The standard DPM is therefore expected to handle this aspect successfully (Section 1.3 of this chapter).

The significant migration of turbulence kinetic energy over the free surface to a relatively dense buoyant upper phase has been proven to simulate the increased turbulence kinetic energy dissipation rates at the surface. It is therefore expected that this 'error' induced by the mixed fluid VOF model will only increase the accuracy of the simulation (see Chapter VIII:4.4).

Still, with so many possible sources of error, the model cannot be expected to generate results which are in perfect quantitative agreement with the actual flow situation. For comparative measures, however, the accuracy of the model should be sufficient. The designed experiments used to investigate the effects of various independent variables on mixing efficiency will quantify these effects in a comparative manner. Results from these experiments should therefore provide a good representation of the actual process.

4.5. Suitable Performance Measures

Traditionally, the mixing time is the primary performance variable when studying mixing in gas stirred ladles. From the kinetic energy considerations discussed in the previous chapter, two more equally important performance variables can be extracted.

The first of these measures is the rate of turbulence kinetic energy dissipation integrated over the mass in the ladle. As described in Chapter VIII:3, this is a good indication of the rate at which kinetic energy is being transferred from the buoyant gas to the molten steel. The following chapters will refer to this performance measure as the 'kinetic energy transfer rate' (e_k). If need be, the efficiency with which buoyant input energy is converted to melt kinetic energy can also be estimated as follows:

$$\eta = \frac{e_k}{e_b} = \frac{e_k}{M_l \varepsilon_b}$$ Equation 118

The second performance measure is the total kinetic energy (mean plus turbulent as given in Equation 98) available within the ladle. This so-called 'kinetic energy holding capacity' (E_{tot}) will give a good indication of how efficiently the power available for flow pattern development is being used by measuring the quantity of mixing achieved by any flow setup. A high value of this

performance variable will represent flows losing only a small percentage of mean kinetic energy to turbulence, thereby achieving much higher flow velocities for the amount of stirring power available.

Mixing time is a measure of the distribution of kinetic energy within the ladle. The primary function of the mixing time will be to identify ladle setups that contain dead zones. Such inefficient setups will be identified by a substantial increase in mixing time despite acceptable energy measures in the ladle. For well mixed ladle setups (setups without dead zones) the mixing time will be of secondary importance, however. Ladle operation times are typically more than ten times longer than mixing times for well mixed ladles, implying that the entire mass within the ladle will make several visits to the various reaction sites within the ladle. Under these situations, the intensity of mixing within the ladle (measured by the kinetic energy holding capacity) will be more important to ensure a high rate of reactant/product turnover at the reaction sites.

CHAPTER X:
RESULTS & DISCUSSION PART 3: OPERATING VARIABLES

However beautiful the strategy,
you should occasionally look at the results.
- Winston Churchill

It has taken nine chapters to describe the beauty of the strategy involved and the real full scale modelling results can now finally be unveiled. This chapter is the first in a series of three and presents the effects of various operating variables on the mixing performance of the ladle. The relevant variables were identified in Chapter II:4 and are summarized below:

- Operating variables
  - Gas purging
    - Total gas purge rate
    - Distribution of gas purge rate between multiple tuyeres
  - The depth of molten steel
  - Liquid temperature
  - Operating pressure
  - The slag layer

Designed experiments were used to aid in the interpretation of the results. For specifics on the design these experiments, see Chapter XVI: Design of Experiments. Factors in the various experimental designs were abbreviated for easy discussion. These abbreviations are explained at the start of each experiment as well as in the nomenclature (Chapter XIV:2).

1. Buoyant Energy Input

First of all, the operating variables of gas flow rate (Q), melt depth (H), melt temperature (T) and surface pressure (P) were investigated. The results were also used to investigate whether the equation of buoyant energy input (below) proposed by Ghosh (1) is valid for the system under consideration.

$$\varepsilon_b = \frac{336 Q_{V,N} T_l}{M_l} \ln\left(1 + 0.681 H / P_0\right) \qquad \text{Equation 119}$$

A 2^{4-1} fractional factorial design was used in the investigation. Factors were chosen so that a change in levels from low to high in each of the four independent variables would result in the same positive change in buoyant energy input (see Chapter XVI:2 for more details). Therefore, if Equation 119

holds, the resulting effects of the four factors will be identical. Results from this investigation are shown below:

Table 16: Results from the buoyant energy input experiment.

Run	Q [kg/s]	T [K]	P [atm]	H [m]	ε_b [W/kg]	e_k [W]	E_{tot} [J]	$\tau_{95\%}$ [s]	η [%]
1	0.008	1820	1.0	2.1	0.0184	1921	8180	86.5	71.0
2	0.010	1820	1.0	3.0	0.0288	2888	14253	152.0	68.1
3	0.008	2275	1.0	3.0	0.0288	2895	14248	158.0	68.3
4	0.010	2275	1.0	2.1	0.0287	3131	11031	72.5	74.0
5	0.008	1820	0.7	3.0	0.0283	2777	13868	155.5	66.7
6	0.010	1820	0.7	2.1	0.0288	3123	11022	71.5	73.6
7	0.008	2275	0.7	2.1	0.0288	3127	11024	70.5	73.7
8	0.010	2275	0.7	3.0	0.0442	4503	19205	149.5	69.2

The effects of the main factors are presented below as percentages of variance explained.

Table 17: Percentage of variance explained by Q, T, P and H.

Factor	ε_b	e_k	E_{tot}	$\tau_{95\%}$	η
Q	25.1	30.3	10.9	0.6	5.9
T	25.1	30.8	10.9	0.2	7.1
P	23.4	25.7	8.9	0.5	0.8
H	23.4	11.0	66.9	98.3	84.4
Error	3.0	2.2	2.5	0.4	1.8
Total	**100.0**	**100.0**	**100.0**	**100.0**	**100.0**

Table 17 shows a very good fit of the statistical model to experimental results with minimal error variance. All factor effects are significant ($p < 0.05$) except for the effects of Q, T and P on mixing time and the effect of P on the kinetic energy transfer efficiency.

The expected similarity exists between the effects of Q, T and P on all the dependent variables. The effects of Q and T are especially similar. The effect of H, however, deviates quite substantially from that of the other independent variables. Since the change in buoyant energy input is identical in each factor, the unexpectedly different effects of H definitely merits further investigation.

Table 17 also shows the effective change in the rate of buoyant energy input is slightly (7%) lower in P and H than in Q and T despite the efforts to keep all changes in buoyant energy input rate constant. This is due to the rather unfortunate late discovery of the printing error in the buoyant energy equation provided by Ghosh (1) as mentioned in Chapter II:4. The experiment was therefore designed on the erroneous formulation of buoyant energy input and time constraints did not allow for a rerun of the experiment. Still, the resulting error is not great and will not detract from the discussion.

1.1. The Effect of H

The effect of H on the kinetic energy transfer rate and the kinetic energy holding capacity is in accordance with Equation 119. In each of these performance measures, the taller vessel provides higher quantities of mixing energy. The effect of H on mixing time, however, is in the opposite direction, i.e. the 2.1 m vessel offers substantial improvements despite having a smaller rate of buoyant energy input. For a better understanding of this occurrence, the flow patterns have to be consulted.

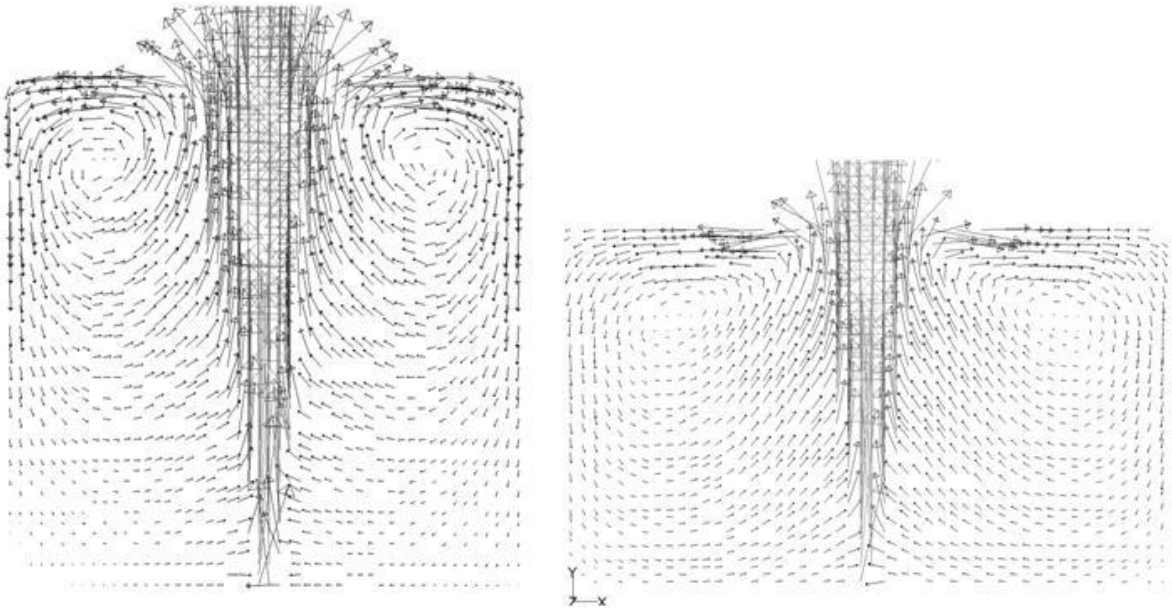

Figure 98: Flow patterns in the 3 m vessel (left) and the 2.1 m vessel (right).

The reason for the shorter mixing times in the 2.1 m vessel is immediately clear from Figure 98. Substantial dead zones are present in the lower regions of the 3 m vessel, while a smooth circulatory flow pattern fills the entirety of the 2.1 m vessel. These dead zones have a substantial elongating impact on mixing times despite the strong circulatory flows occurring in the top regions of the vessel. Marginal means show mixing times in the tall vessel to be 77 s (100%) longer than mixing times in the shorter vessel.

The large effect of H on the kinetic energy transfer efficiency also favours the shorter vessel, resulting in marginal means of 73% for the taller vessel and 68% for the shorter vessel. The right hand side of Figure 98 shows that the recirculating flow patterns in the shorter vessel do not interfere with the rising bubble plume as described in Chapter VIII:2.1.2. The circulatory flows pass down the outside of the ladle, get turned by the ladle floor and rejoins the plume without having any downwards momentum that can subtract from the upwards momentum in the plume.

In the taller vessel, however, the recirculating flow patterns are forced too close to the rising plume by the smaller aspect ratio of the ladle. The result is shown on the left hand side of Figure 98 where the flow patterns are not turned by the ladle floor as in the shorter vessel, but by the plume itself. In the process of turning the flow patterns, the downward component of momentum on the outside of the ladle has to be negated and converted to upward momentum near the centre. Since the turning process is facilitated solely by the plume, the increase in the upwards component of momentum in

the recirculating flows has to be balanced by an equal decrease in the upwards component of momentum in the plume to ensure momentum conservation. The resulting flow pattern interference is primarily responsible for the 7% decrease in kinetic energy transfer efficiency.

This flow pattern interference is also the reason for the comparatively small amount of variance (11%) explained by H in the kinetic energy transfer rate. Even though the taller vessel has a higher rate buoyant energy input, the efficiency with which the available buoyant energy is being transferred to the kinetic energy of the melt is hampered by the interference described above.

Interference of the plume with the recirculating flows is also the primary reason for the dead zones observed in the bottom regions of the vessel. The recirculating flows are simply turned by the plume before they can reach the lower regions of the ladle.

Despite this reduced buoyant energy conversion efficiency, the factor H still offers the largest improvement in kinetic energy holding capacity (51.9%) from the shorter to the taller vessel. The reason for the poor kinetic energy holding capacity of the shorter vessel can also be observed in Figure 98. Since the plume has not had time to disperse over the shorter height of the 2.1 m vessel, it hits the surface in a very narrow and concentrated form. This creates a tall and narrow plume eye leading to high mean velocity gradients. The resulting increase in turbulence generation dissipates much of the mean kinetic energy successfully transferred from the buoyant gas to the internal energy of the fluid (see Chapter VIII:2.3.3).

1.2. The Effects of Q, T and P

In accordance with Equation 119, the effects of Q, T and P on all the dependent variables are relatively similar. This is explained by the ideal gas law relationship which maintains that changes in Q, T and P all affect the volume of gas, and therefore the amount of buoyant potential energy, available to do the stirring. Improvements in mixing brought about by changing Q can thus be mirrored by equivalent changes in T and P.

The effect of P, however, is shown to be slightly different from the effects of Q and T. This is partly due to the slight error in experimental design described in the last paragraph of Section 1 above. The other contributing factor is that changes in melt surface pressure also influence the region in the plume where the majority of buoyant energy is transferred. When a strong vacuum is drawn, the rapid expansion of gas towards the surface of the melt cause the locus of energy input to by shifted upwards, thereby changing the shape flow patterns in the melt. To further investigate this effect a number of additional runs were performed at lower values of P.

1.2.1. Effect of Lower Surface Pressures

Experiments were carried out at reduced pressures by lowering both P and Q in Equation 119 so that the theoretical buoyant energy input will remain constant at 0.0288 W/kg over all the runs. Table 18 displays the experimental results.

Table 18: Results from the reduced pressure experiment.

Run	Q [kg/s]	P [atm]	e_k [W]	E_{tot} [J]	$\tau_{95\%}$ [s]
1	0.0100	1.000	2888	14253	152.0
2	0.0080	0.671	2872	14089	157.0
3	0.0060	0.374	2739	13435	157.5
4	0.0050	0.244	2649	12862	172.5
5	0.0040	0.132	2494	11992	207.5

The pressure reductions are shown to have a negative impact on the kinetic energy transfer rate and the kinetic energy holding capacity, especially when strong vacuums are drawn. This can be attributed to increased energy inputs near the surface of the vessel which result in further surface deformation and larger amounts of turbulence generation in the plume eye. Both these factors subtract from the quantity of mixing energy available as described in Chapter VIII:2.3.

Mixing time also shows a marked increase under strong vacuum (runs 4 and 5). The reason for this lowering in mixing quality can be deduced from the flow pattern development.

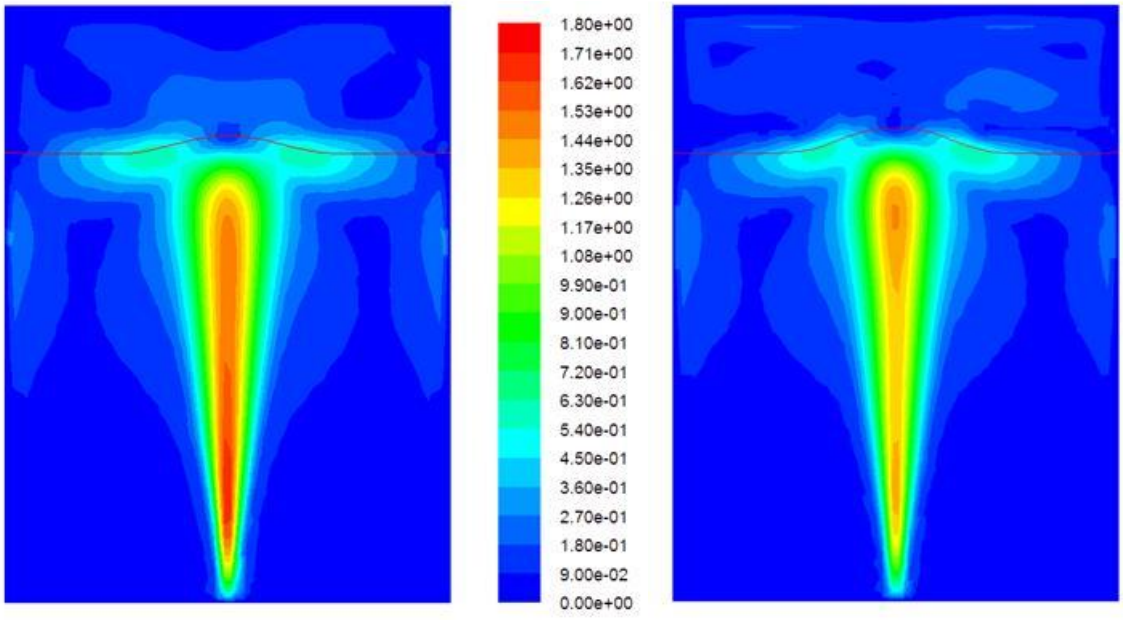

Figure 99: Flow velocity contours at pressures of 1 atm (left) and 0.132 atm (right).

As expected, the bulk of the buoyancy induced flow is shifted to the top regions of the plume at lower pressures. The free surface is also further deformed. Apart from the increased dissipation rates in the plume eye, the stronger upper regions of the buoyant plume also force the recirculating flows to turn sooner, leaving larger dead zones in the lower regions of the vessel.

1.3. Closure

The experiment draws a clear distinction between the quantity and the quality of mixing inside gas stirred ladles. Despite containing large amounts of kinetic energy, the taller vessel still left significant

dead zones in the lower regions capable of compromising the functionality of the ladle. The tall centrically purged ladle setup can therefore be classified as delivering mixing of high quantity but low quality.

It is very hard to define a specific point where mixing quality becomes more important than mixing quantity. The current high end mixing times (in the range of 150 s) still mean that all the metal in the ladle will make several visits to the reaction sites in a typical 30 minute gas purging cycle. This raises the need for a specific mixing quality criterion (measured by the mixing time) above which the quality of mixing can be labelled insufficient for acceptable process performance. Unfortunately, there is no way in which this value can be determined at present.

For the present study, the mixing quality criterion will be set at 100 s. This value is not claimed to be accurate, but is picked simply to facilitate a comprehensive discussion of results. The remaining chapters will therefore operate on the assumption that mixing quantity (kinetic energy holding capacity) is the primary performance variable only if the mixing time (indicator of mixing quality) is smaller than 100 s. Further research is required to refine this criterion.

Another insight gained from this experiment is that changes in operating variables capable of influencing the overall shape of flow pattern development (such as H) have a much greater potential effect on process performance than similar changes in variables influencing only the strength of these flow patterns (such as Q, T and P). The effect of H was the largest by some amount when measuring both the quantity (kinetic energy holding capacity) and the quality (mixing time) in the ladle.

2. The Effect of Gas Flow Rate

The gas flow rate has probably enjoyed more research focus than all of the other independent variables combined. Therefore, a separate experiment varying only the gas flow rate was completed for comparison with correlations available in the literature.

Table 19: Results from the dual plug gas flow rate experiment.

Total gas flow rate [kg/s]	e_k [W]	E_{tot} [J]	$\tau_{95\%}$ [s]
0.022	5788	33129	44.0
0.020	5289	30581	44.5
0.018	4723	28660	46.0
0.016	4168	26014	48.5
0.014	3633	23439	52.0
0.012	3078	20810	56.0
0.010	2552	18025	63.0
0.008	1990	15235	70.0
0.006	1449	12222	78.5
0.004	953	9026	93.5

The simulated geometry was the 3 by 3 m cylinder employed as the tall vessel in the previous section. It was shown, however, that a single centrically located plug does not provide mixing of an acceptable quality on the criterion of $\tau_{95\%} > 100$ s. Therefore, the ladle was fitted with two plugs, situated at mid radius positions diagrammatically opposite each other. The dual plug setup is known to provide lower mixing times than centrically stirred setups (Chapter II:4.1.1.A.ii). Numerical experiments were conducted without a slag layer since the majority of correlations available in the literature were obtained in a water model without a simulated slag layer.

As expected, Table 19 shows that increases in gas purge rate improve both mixing quality and mixing quantity. These influences will be discussed separately below.

2.1. Response of the Mixing Quality Variable

The most prominent twin plug correlation available in the literature is one by Mandal *et al.* (11):

$$\tau_{95\%} = 3.75 \frac{D^{2.0}}{Q^{0.38} H^{0.56}}$$ Equation 120

Figure 100 shows a comparison between model predictions and the correlation in Equation 120.

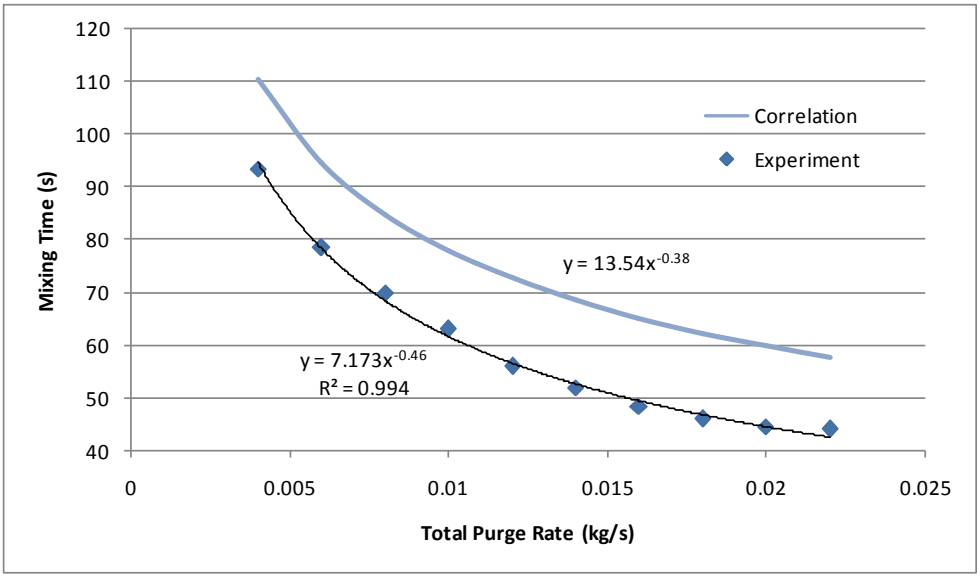

Figure 100: Response of mixing time to changes in gas flow rate from the numerical experiment and from a correlation in the literature (11).

It can be seen that the current results differ from Equation 120 both in the power (0.46 to 0.38) and the coefficient (7.173 to 13.54). Model predictions are constantly about 15 s lower than calculated values.

Predictions via Equation 120 are valid only for flow situations in the inertial- and gravitational force dominated regime (11). This regime is characterised by an invariant flow pattern filling the ladle despite further increases in flow rate. From the distinction made in Section 1.3, this regime takes

place when the gas flow rate acts purely as a flow pattern strengthening variable, having no influence on the flow pattern shape.

According to Mandal *et al.* (11), the transition to the inertial- and gravitational force dominated regime happens at a specific buoyant energy input rate of 0.007 W/kg. The lowest gas flow rate employed in the numerical experiment (0.004 kg/s) translates to a specific buoyant energy input of 0.012 W/kg, implying that the entire experiment should lie within the inertial- and gravitational force dominated regime. To validate this notion, the circulatory flow patterns of the 0.004 kg/s and the 0.022 kg/s experiments were compared on the plane identified below:

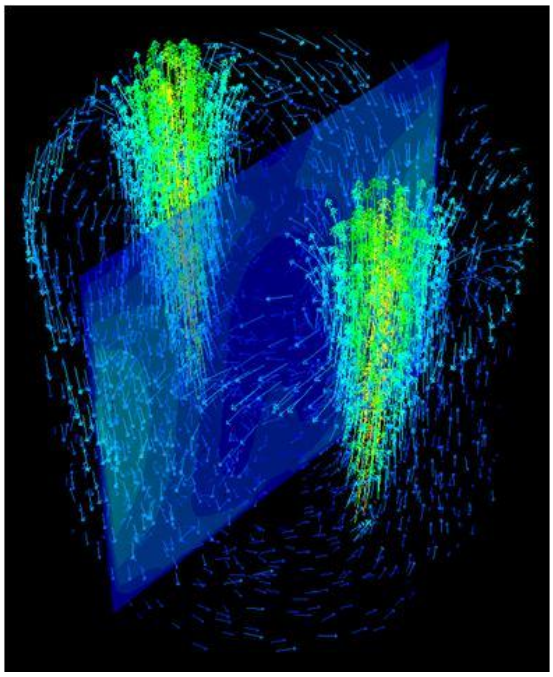

Figure 101: Plane between the plumes where the strongest circulatory flows occur.

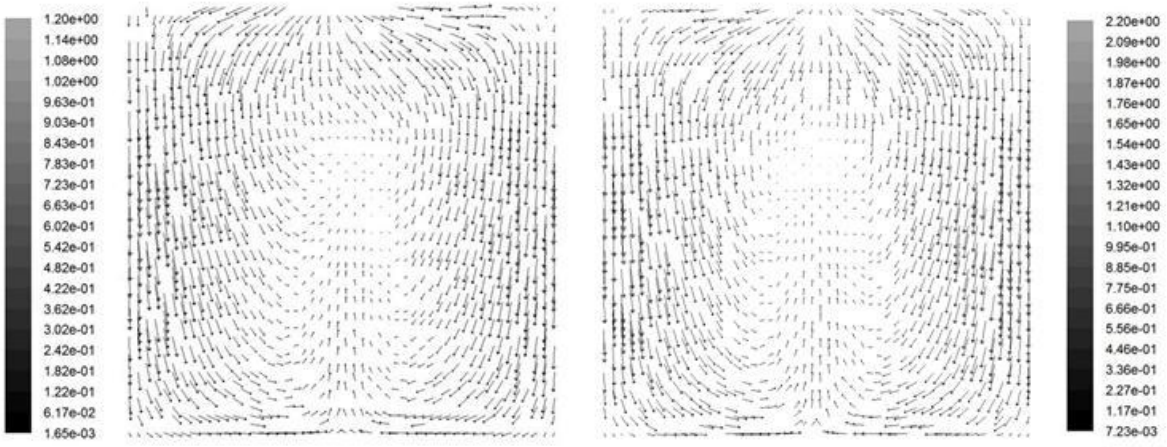

Figure 102: Flow patterns from the 0.004 kg/s (left) and 0.022 kg/s run (right) on the plane defined in Figure 101.

Figure 102 shows a very similar flow pattern shape between the two runs. The strength of the flow patterns differs substantially, however, affirming the influence of gas flow rate as a flow pattern strengthening variable only. This confirms that the experiment is in the correct range for use of Equation 120.

It is therefore clear that the numerical experiment shows the gas flow rate to have a stronger influence on mixing time than the predictions of Equation 120. This difference prompted a deeper investigation into the experimental data collected by Mandal *et al*. (11).

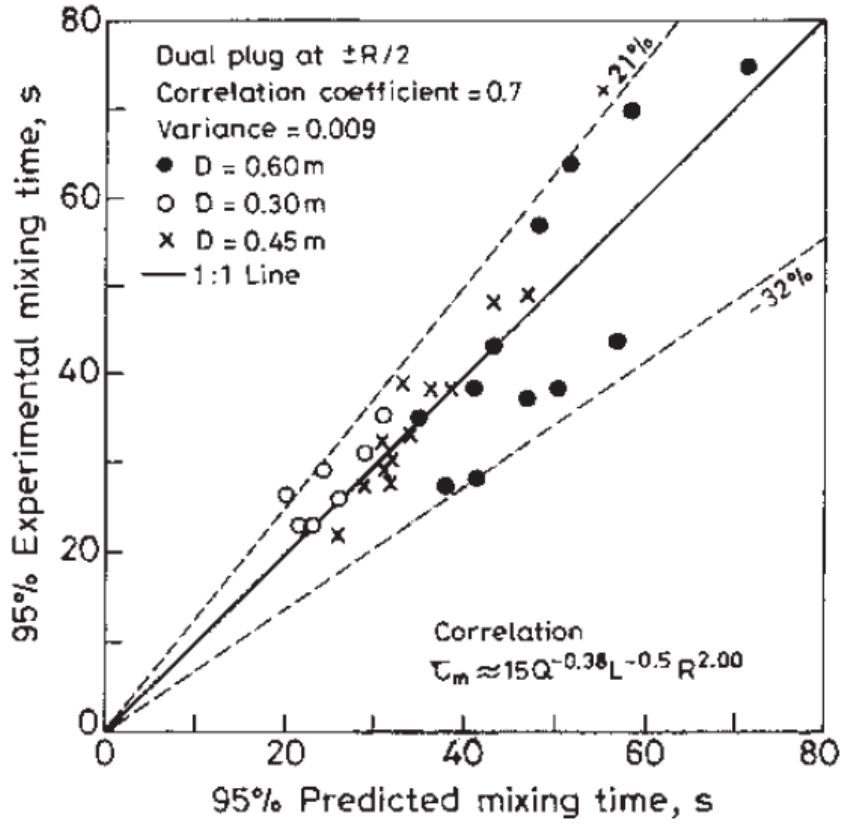

Figure 103: Experimental mixing times vs. predictions with Equation 120 (11).

Two characteristics are evident from the fit presented in Figure 103. The first is that the correlation seems to under-predict mixing times in the small vessel ($D = 0.3$ m), be reasonably accurate in predicting mixing times in the medium vessel ($D = 0.45$ m) and over-predict mixing times in the large vessel ($D = 0.6$ m). This is an indication that the correlated influence of the ladle geometry on mixing time ($\tau_{95\%} \propto D^2/H^{0.56}$) might be slightly too large.

The second characteristic is that the correlation seems to under-predict high end mixing times and over-predict low end mixing times for all three vessels. This effect is especially visible in the medium vessel ($D = 0.45$ m). The implication is that Equation 120 over-predicts mixing times at higher gas purge rates raising the possibility that the effect of gas purge rate might be greater that the proposed relation of $\tau_{95\%} \propto Q^{-0.38}$.

On these notions, the data was refitted on the correlation given in Equation 121 using the nonlinear estimate tool in Statistica 7.1.

$$\tau_m = K \frac{D^z}{Q^x H^y}$$ Equation 121

The new correlation obtained is given in Equation 122 and represented on a plot of experimental vs. predicted mixing times in Figure 104.

$$\tau_m = 1.37 \frac{D^{2.65}}{Q^{0.49} H^{-1.26}}$$

Equation 122

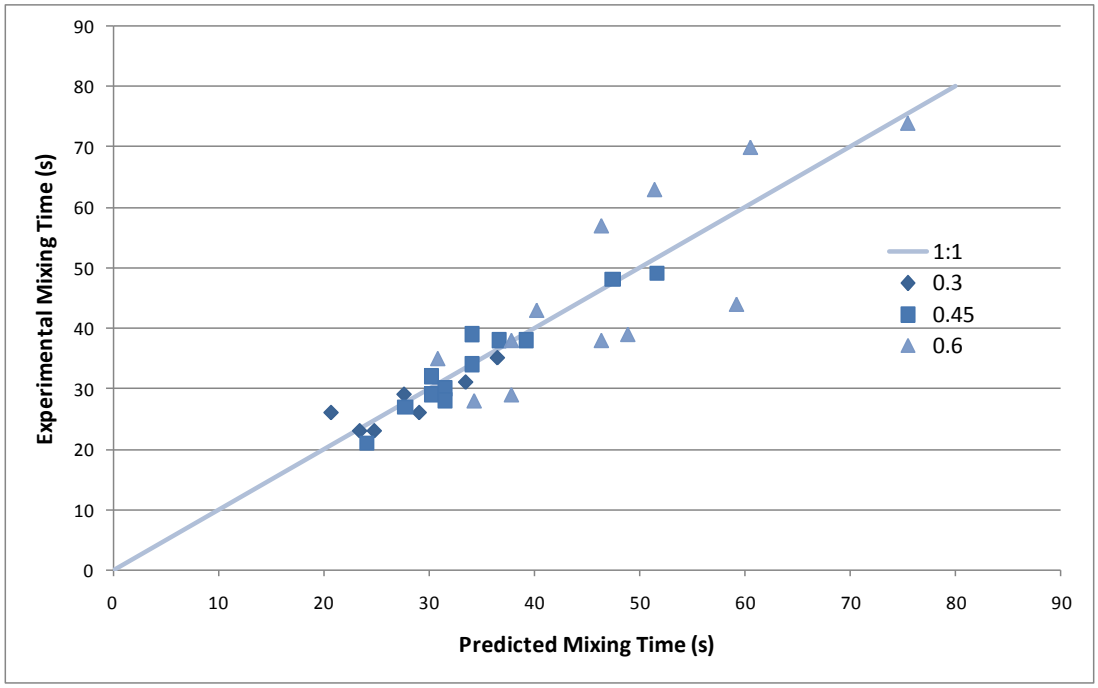

Figure 104: Experimental mixing times vs. predictions with Equation 122.

Figure 104 shows a much improved fit to data from all three vessels. The proportion of variance accounted for by the new correlation is 0.82 as opposed to the 0.7 in Figure 103. The ANOVA table confirms the quality of the fit.

Table 20: ANOVA results for the correlation given in Equation 122.

	Sum of Squares	Degrees of Freedom	Mean Squares	F-value	p-value
Regression	48081.95	4	12020.49	330.4870	0.000000
Residual	982.05	27	36.37		
Total	49064.00	31			
Corrected Total	5357.68	30			
Regression vs. Corrected Total	48081.95	4	12020.49	67.3080	0.000000

In comparison to Figure 100, the new correlation fits the simulation results very well and is provided in Figure 105.

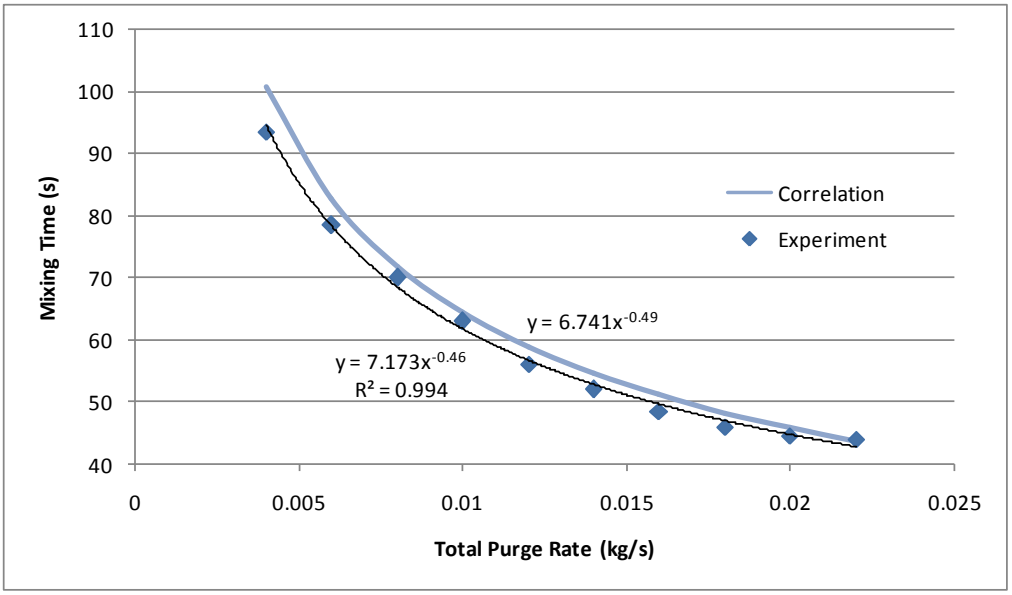

Figure 105: Response of mixing time to changes in gas flow rate from the numerical experiment and from the correlation in Equation 122.

The newly calculated proportionality of $\tau_{95\%} \propto Q^{-0.49}$ shows that the gas flow rate has a substantial influence on the mixing quality even when it serves only as a flow pattern strengthening variable.

Equation 122 is not proposed as a definite improvement on Equation 120 published by Mandal *et al.* (11) since very little was known about the experimental procedure employed. Data was simply lifted from Figure 103 and a new correlation was established. The improved fit shown in Figure 104 as well as the substantial difference in the proportionality of mixing time to gas flow rate does however indicate that a revised experiment might be in order.

2.2. Response of the Mixing Quantity Variables

Where improvements in the mixing quality became smaller as the gas flow rate was increased, mixing quantity variables kept on improving in an almost linear fashion.

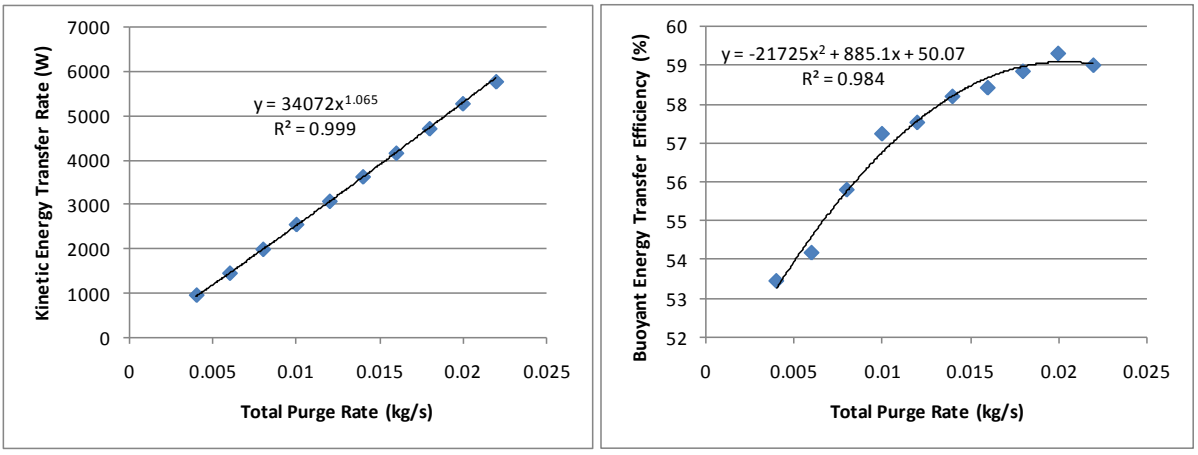

Figure 106: Correlation between kinetic energy transfer variables and total gas flow rate.

The power curve fitted to the response of kinetic energy transfer rate shows that the increase is slightly more than linear. This is the result of increased plume velocities at higher gas flow rates. Since slip velocities remain constant, an increase in plume velocity will mean that a shorter distance is covered by slip resulting in smaller losses to the internal energy of the fluid (Chapter VIII:2.1.1.C).

Higher plume velocities will also increase the size of the plume eye, creating a stronger counter force (Chapter VIII:2.3.2). The decrease in kinetic energy transfer efficiency resulting from this counter force seems to be smaller than the increase stemming from the larger plume velocity.

The kinetic energy transfer efficiency (right of Figure 106) shows a substantial initial increase in efficiency due to the increase in plume velocity. At higher gas flow rates, however, the efficiency seems to decrease again. This can be attributed to the recirculating flows becoming sufficiently strong to interfere with the rising plumes (Chapter VIII:2.1.2). It is therefore expected that the kinetic energy transfer efficiency would decrease with further increases in gas purge rate according to the second order polynomial fit.

The kinetic energy holding capacity also displayed a slight lag at higher flow rates:

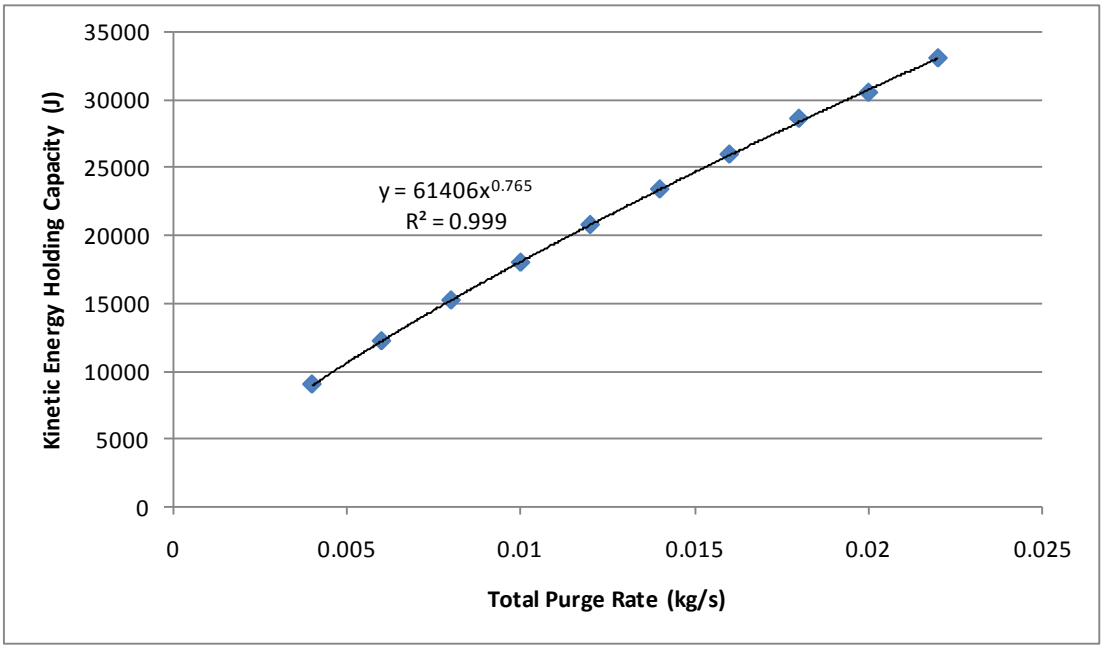

Figure 107: Correlation between kinetic energy holding capacity and total gas flow rate.

The proportionality of $E_k \propto Q^{0.765}$ shows that the increase in kinetic energy holding capacity with increased gas purging is somewhat smaller than linear. This is an indication that a larger percentage of the mean kinetic energy is being lost to turbulence kinetic energy and subsequently dissipated as heat (see Chapter VIII:4.1) at higher gas purging rates. These increased losses to turbulence are mainly due to the enlargement of the plume eye. An increased deformation of the free surface will force the flow to turn more sharply, thereby creating larger velocity gradients and subsequent turbulence losses (Chapter VIII:2.3.3).

2.3. Closure

It is clear from the mixing time results that the mixing quality achieved with two plugs is substantially better than that achieved with only one centrically located plug. The point below which single plug setups provide superior mixing to twin plug setups (reviewed in Chapter II:4.2.1.B) does not seem to exist in the operating range of industrial gas stirred ladles.

Mixing quality and quantity respond quite differently to changes in gas purging rates. When the vessel is well mixed, increases in gas flow rate have a significantly stronger influence on mixing quantity than on mixing quality. The mixing time can therefore underestimate the mixing efficiency in well mixed vessels. Values of kinetic energy holding capacity would provide a better measure of the mixing performance under these circumstances.

In physical modelling, however, the kinetic energy holding capacity of a vessel is very difficult to measure and the mixing time would still be the primary performance variable. The exact correlation between mixing time and gas flow rate was questioned in Section 2.1. Since the dual plug system is the most common setup utilized in the industry, this relationship is quite important and further research is recommended for confirmation.

3. Operating Variables in an Industrial Ladle

A set of experiments have been designed on a real industrial gas stirred ladle in operation at Mittal Steel, Saldanha. The size of the ladle in comparison to a man is shown below:

Figure 108: Ladle employed at Mittal Steel: Saldanha.

The dimensions of this ladle as well as the positioning of purge plugs are provided in Figure 109.

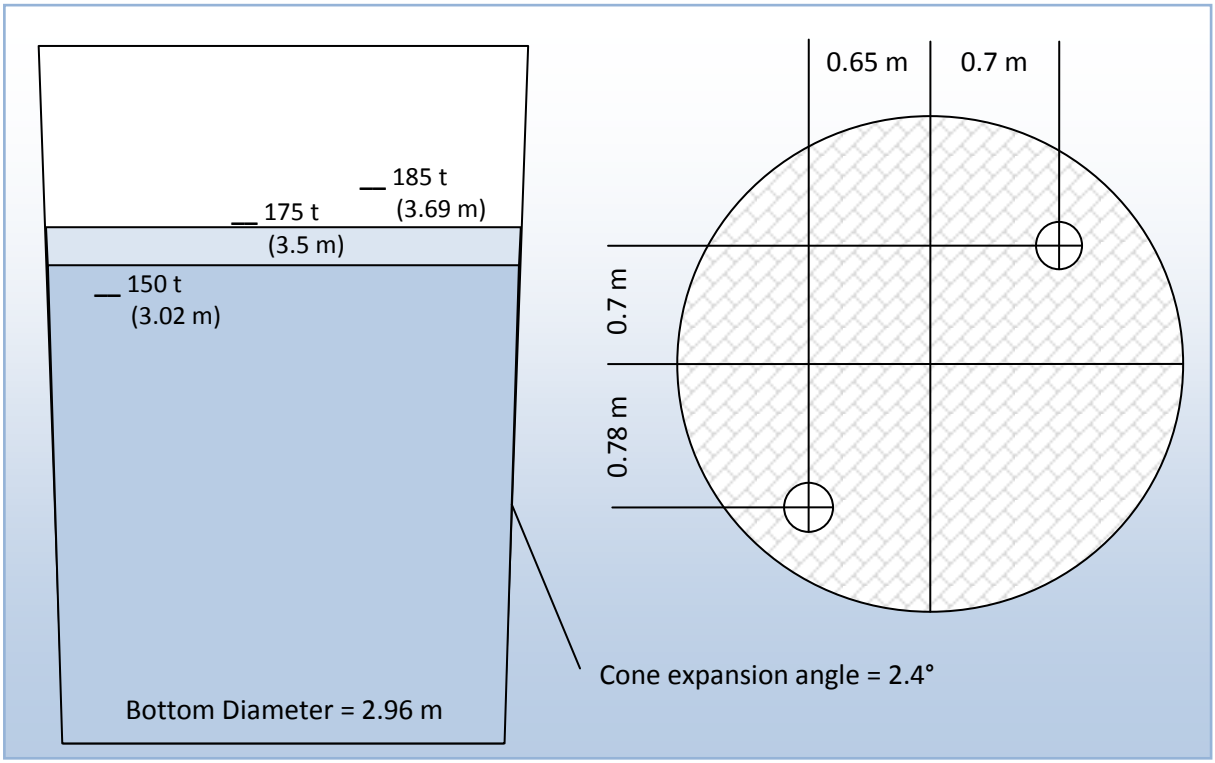

Figure 109: Layout of the industrial vessel.

The operating variables under scrutiny include the total gas purge rate, the gas distribution between tuyeres, the height of the melt and the depth of the slag layer. Additionally, slag phase physical properties can be adjusted by means of flux additions.

3.1. Gas Flow Rate and Distribution

The plant operator has the most direct control over the gas flow rate (Q_{tot}) and its distribution between the two tuyeres $(Dist)$. These two important factors were therefore investigated in a central composite design to better visualize their effects on the responses of the flow variables. A 20 cm slag layer was included in the 175 t mass loading. Experimental results are given below:

Table 21: Results from the gas flow rate and distribution experiment.

Run	Q_{tot} [kg/s]	$Dist$ [fraction]	e_k [W]	E_{tot} [J]	$\tau_{95\%}$ [s]	η [%]
1	0.0070	0.07	1700	14417	83.5	51.6
2	0.0070	0.43	1734	14184	76	52.6
3	0.0130	0.07	3559	24568	85	58.2
4	0.0130	0.43	3356	23868	60	54.9
5	0.0058	0.25	1363	12303	88	50.3
6	0.0142	0.25	3341	22633	60.5	49.9
7	0.0100	0.00	2832	21384	80	60.2
8	0.0100	0.50	2418	18799	68	51.4
9 (c)	0.0100	0.25	2600	18710	66.5	55.3
10 (c)	0.0100	0.25	2580	18722	62.5	54.8

The variance explained by the different factors in the design is reported below. L and Q denote linear and quadratic factor effects respectively.

Table 22: Percentage of variance explained by Q_{tot} and $Dist$.

Factor	e_k	E_{tot}	$\tau_{95\%}$	η
(1) Q_{tot} (L)	94.9	91.1	34.3	8.0
(1) Q_{tot} (Q)	0.8	0.7	12.7	20.0
(2) $Dist$ (L)	1.4	1.6	29.4	26.1
(2) $Dist$ (Q)	0.2	1.8	12.1	2.3
1L by 2L	0.3	0.0	7.4	4.6
Error	1.9	2.9	11.6	27.0
Total	100.0	100.0	100.0	100.0

Table 22 shows that Q_{tot} is the only influential factor on the kinetic energy transfer rate and the kinetic energy holding capacity of the vessel. Both these measures give an indication of the quantity of mixing in the ladle. Being the only source of stirring power, the gas flow rate (Q_{tot}) is the logical factor to have an effect on these variables.

The quality of mixing, on the other hand, has already been shown (Chapter X:1) not to be as dependent on the amount of buoyant energy input, but rather on the efficient conversion of the available buoyant energy into fully developed flow patterns. This case seems to be no different. $Dist$, the flow pattern altering variable, has a significant effect $(p = 0.033)$ on mixing time despite having negligible influence on overall flow velocity and turbulence kinetic energy.

No factor had a significant effect $(p < 0.05)$ on the kinetic energy transfer efficiency.

3.1.1. Response of the Mixing Quantity Variables

To observe the actual effect that increases in Q_{tot} had on the kinetic energy transfer rate and holding capacity, the appropriate response surfaces are provided in Figure 110. It is shown that, over the range of the experiment, both variables can be seen as being directly proportional to Q_{tot}. One can therefore safely assume that twice the gas flow rate will result in twice the amount of stirring in the ladle.

An interesting effect is visible at the highest levels of Q_{tot}. It seems that the both energy measures are slightly inhibited at $Q_{tot} > 0.013$ and $Dist \approx 0.25$. This might be an indication that the recirculating flow patterns are becoming sufficiently strong to interfere with the rising buoyant plumes, thereby decreasing the efficiency of buoyant energy input (Chapter VIII:2.1.2). Statistically, the evidence provided in Figure 110 is insufficient to make any further conclusions. Further discussion on this point is provided in a future experiment (Section 3.2.1 of this chapter).

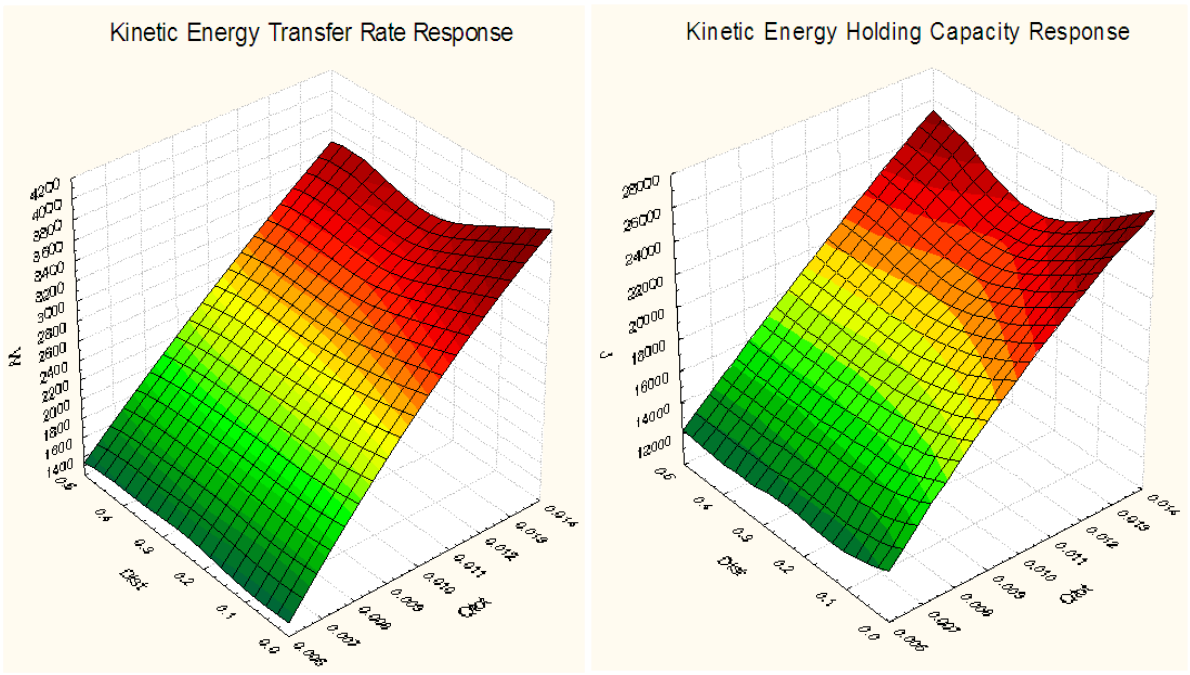

Figure 110: Spline response surface of flow quantity altering variables to changes in Q_{tot} and $Dist$ in the presence of a slag layer.

3.1.2. Response of the Mixing Quality Variable

The response of mixing time to changes in Q_{tot} and $Dist$ is shown below:

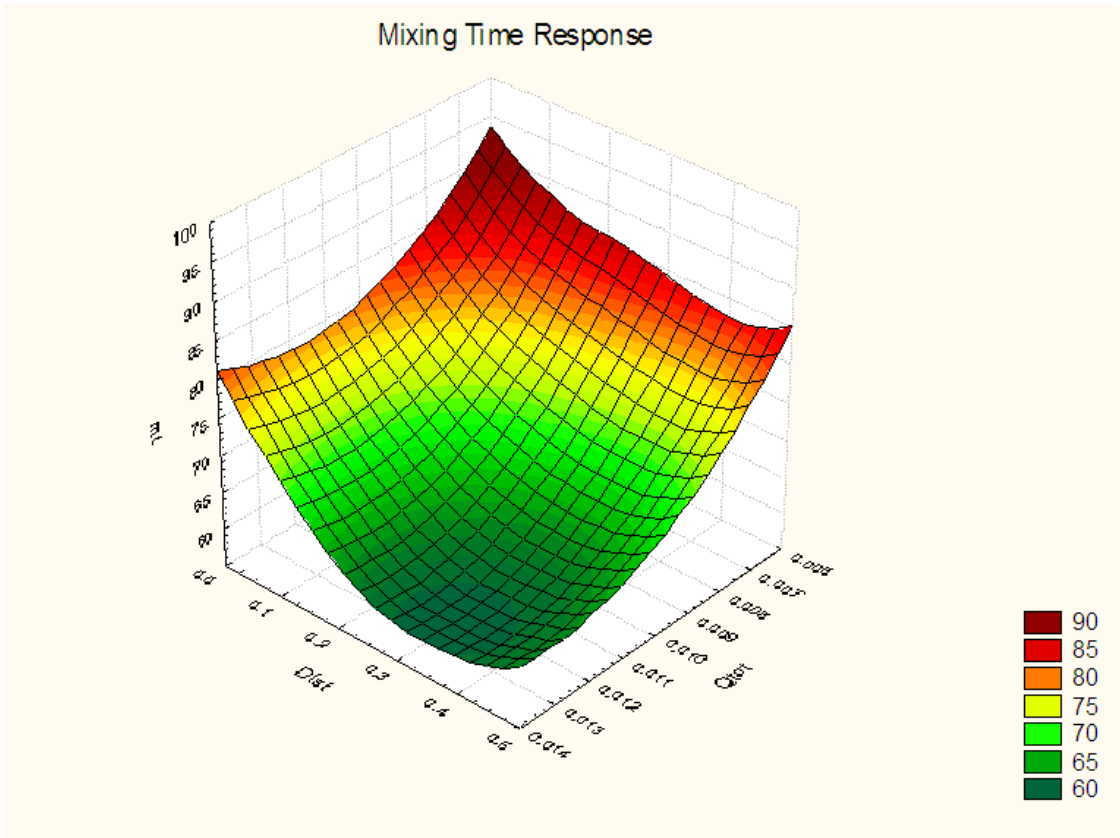

Figure 111: Spline response surface of mixing time to changes in Q_{tot} and $Dist$ in the presence of a slag layer.

The spline fit clearly shows the strong influence of both Q_{tot} and $Dist$ on mixing time. As expected, higher levels of Q_{tot} result in better quality mixing. The effect of $Dist$, however, is characterised by a local minimum between values of 0.3 and 0.5. This indicates that significant stirring is required from both tuyeres to ensure an adequate spread of the available kinetic energy through the vessel.

All the mixing times shown in Figure 111 fall below the 100 s criterion defined in Chapter X:1.3, however, indicating that no serious dead zones occur under any of the flow conditions investigated in the experiment. It can therefore be concluded that $Dist$ will only have a marginal influence on the overall process performance. Since the kinetic energy transfer rate and holding capacity depend only on Q_{tot}, the improvement offered by operating at $Dist > 0.3$ will be small.

3.2. No Slag Layer

The impact of the slag layer was investigated for two reasons: to quantify its effect on mixing and to assess the possibility of omitting it from future simulations.

The slag layer is regularly ignored in mathematical modelling studies as a simplifying assumption. In the present modelling setup, however, the slag layer can be accommodated without adding any further complexity since the VOF model automatically captures the additional interface. The extra interface will require additional refining of the grid though, thereby lengthening simulation time. Gas entrainment can also be simulated in the slag layer, decreasing solver stability and therefore requiring smaller time steps. For these reasons it will still be beneficial if the slag layer can safely be omitted.

The central composite design reported in the previous section was repeated for a simulation setup with no slag layer present. If the same conclusions can be drawn from this experimental design, the slag layer can be safely ignored in future experiments.

Experimental results are reported below:

Table 23: Results from the gas flow rate and distribution experiment with no slag layer present.

Run	Q_{tot} [kg/s]	$Dist$ [fraction]	e_k [W]	E_{tot} [J]	$\tau_{95\%}$ [s]	η [%]
1	0.0070	0.07	1722	24490	74.0	52.3
2	0.0070	0.43	1757	16792	71.5	53.3
3	0.0130	0.07	3566	40206	59.0	58.3
4	0.0130	0.43	3470	27061	54.5	56.7
5	0.0058	0.25	1129	15978	84.5	41.7
6	0.0142	0.25	3182	30886	57.5	47.5
7	0.0100	0.00	2998	36343	59.0	63.7
8	0.0100	0.50	2548	22837	61.0	54.2
9 (c)	0.0100	0.25	2038	25981	64.0	43.3
10 (c)	0.0100	0.25	2034	25956	62.0	43.2

The resulting factor effects can now be compared to the experiment including a slag layer.

Table 24: Percentage of variance explained by Q_{tot} and $Dist$ for the experiments with and without a slag layer.

Factor	e_k		E_{tot}		$\tau_{95\%}$		η	
	Slag	No slag	Slag	Slag	No slag	No slag	Slag	No slag
(1) Q_{tot} (L)	94.9	83.7	91.1	52.5	34.3	80.3	8.0	8.0
(1) Q_{tot} (Q)	0.8	0.7	0.7	1.1	12.7	8.7	20.0	2.2
(2) $Dist$ (L)	1.4	1.0	1.6	37.8	29.4	0.3	26.1	5.1
(2) $Dist$ (Q)	0.2	12.3	1.8	3.4	12.1	1.7	2.3	71.5
1L by 2L	0.3	0.1	0.0	1.4	7.4	0.1	4.6	0.4
Error	1.9	2.4	2.9	0.8	11.6	2.6	27.0	9.3
Total	100.0	100.0	100.0	100.0	100.0	100.0	100.0	100.0

It is immediately evident that the slag layer cannot be safely omitted from the simulation exercise. The differences in the ANOVA results from the two experiments indicate that the slag layer has a substantial influence on flow pattern development and mixing inside the ladle.

The absence of the slag layer seems to increase the effect of $Dist$ on the mixing quantity variables. For the kinetic energy transfer rate, the quadratic effect of $Dist$ is now significant $(p = 0.01)$. When looking at the kinetic energy holding capacity $Dist$ is significant in both the linear $(p = 0.0002)$ and quadratic $(p = 0.015)$ effects.

The complete opposite seems true when looking at the mixing time. Where $Dist$ played an important role when a slag layer was present, its effect is now insignificant. In the absence of a slag layer, the buoyant energy conversion efficiency also shows a highly significant $(p = 0.005)$ quadratic effect of $Dist$.

3.2.1. Response of the Mixing Quantity Variables

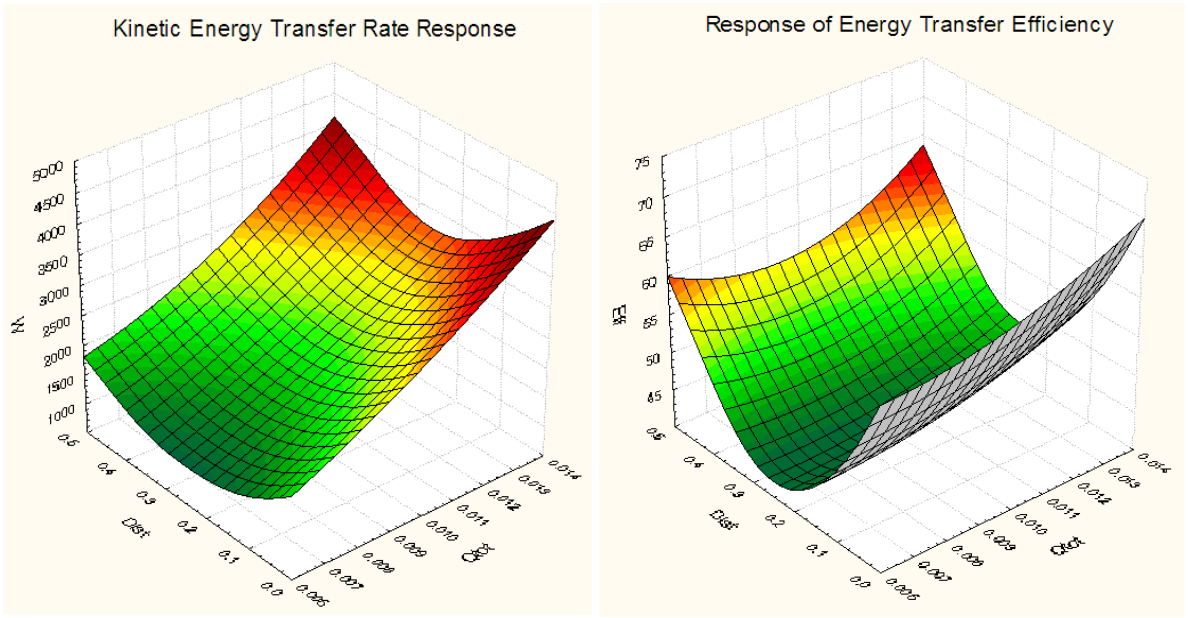

Figure 112: Spline response surfaces of flow dissipation and input efficiency of kinetic energy to changes in Q_{tot} and $Dist$ with no slag layer present.

Figure 112 shows a distinct valley around $Dist = 0.25$ in the response surface of kinetic energy transfer rate. The reason for this is clearly visible in the response of buoyant energy conversion efficiency. A clear minimum is visible at $Dist = 0.25$ implying that the buoyant energy input efficiency is seriously inhibited at around a flow distribution of 75/25%.

The reason for the reduced buoyant energy input efficiency is the conflicting flows between the plumes and the recirculating flows as discussed in Chapter VIII:2.1.2. The flow patterns from different gas flow distributions are presented below:

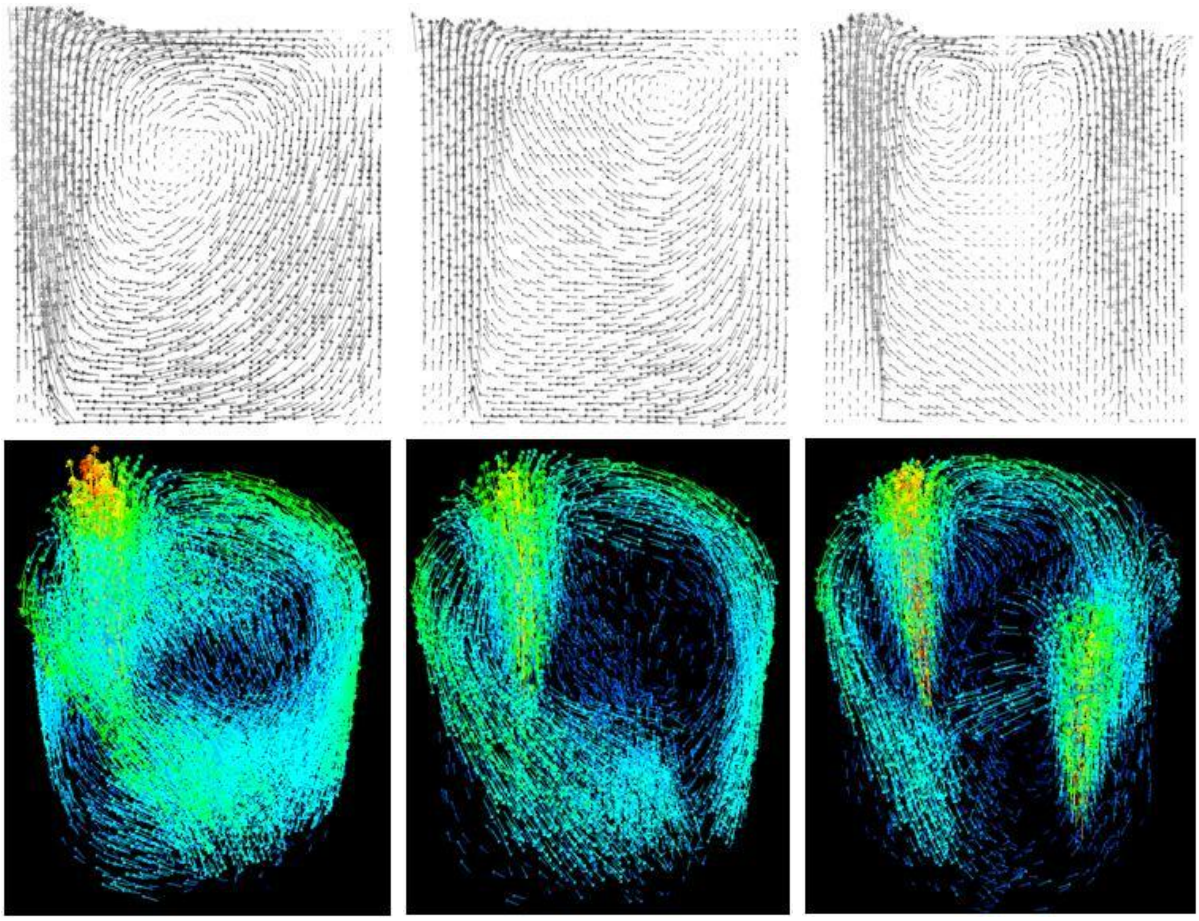

Figure 113: 2D and 3D flow patterns at $Dist = 0$ (left), $Dist = 0.25$ (centre) and $Dist = 0.5$ (right).

The left hand side of Figure 113 shows the flow patterns resulting from one tuyere when no impeding flows are present from the other tuyere. On the right hand side, the flow is split equally between the two tuyeres. Flows resulting from the second tuyere in this setup are sufficient to steer the flow patterns on a less intrusive course. The flow patterns shown in the centre, however, seems like a weakened version of the flow resulting from the single tuyere. This is an indication that these flows are not sufficiently strong to alter the flow patterns (like the setup on the right) and serve only to interfere with the downward recirculating flows.

Incidentally, the flow setup shown in the center of Figure 113 $(Dist = 0.25)$ was also the hardest to converge and never really reached a flow steady state. This is a clear indication of the instability caused by the weaker plume interfering with the recirculating flows from the stronger plume.

In the experiment with a slag layer included, the recirculating flows from the stronger plume were insufficient to cause this magnitude of interference with the weaker plume. This is the result of increased energy dissipation at the surface when a slag layer is present (Chapter VIII:4.4). It was seen in Section 3.1.1 of this chapter, however, that the inhibiting effect from the weaker tuyere is just starting to become visible at higher values of Q_{tot}. At these higher gas purging rates, the circulatory flow patterns from the stronger tuyere become strong enough to overpower the plume formed by the weaker tuyere. It is therefore expected that the unstable situation shown in the center of Figure 113 can be repeated in the presence of a slag layer by increasing the value of Q_{tot}.

Inclusion of the slag layer is therefore very important for accurate flow modelling. If the correct amount of kinetic energy is not dissipated at the free surface, the resulting recirculating flow patterns become excessively strong and completely alter the flow situation within the ladle. A further illustration of this point is given in Figure 114.

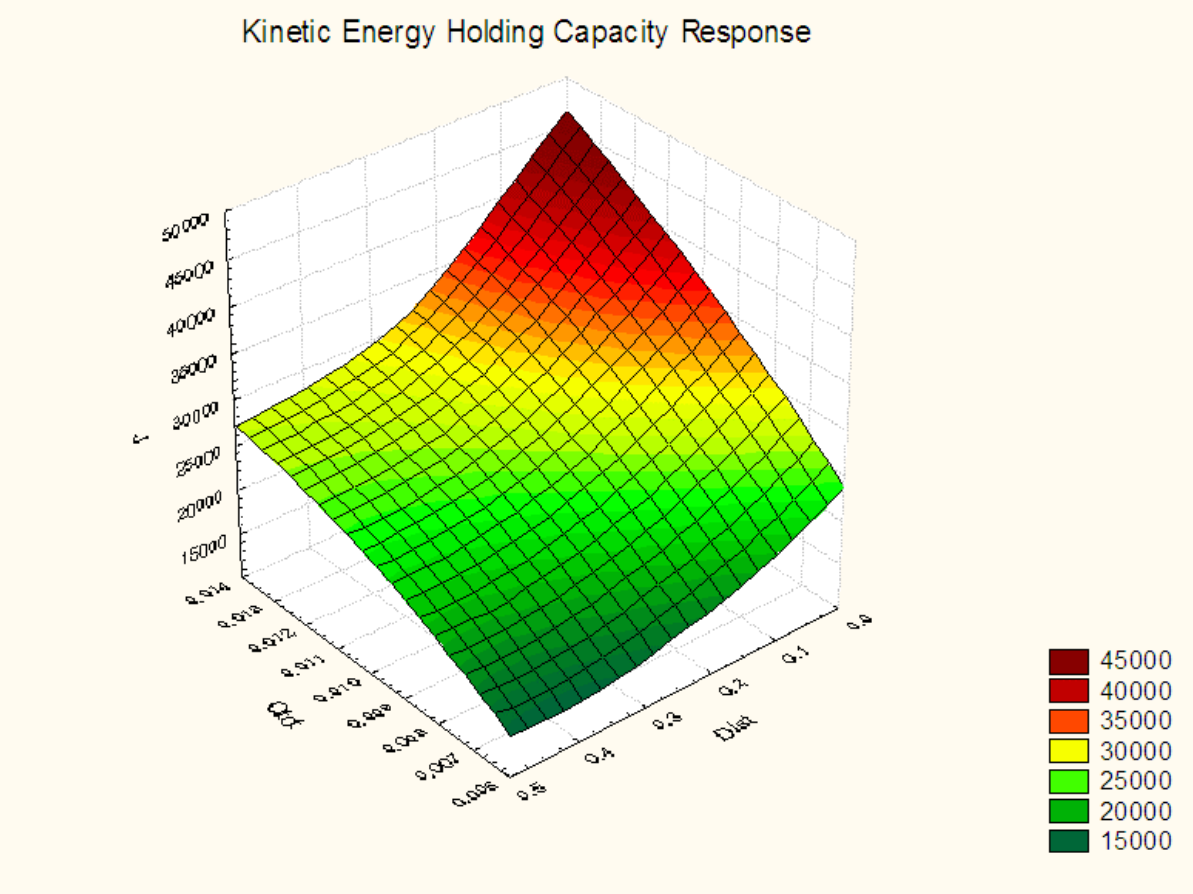

Figure 114: Spline response surface of kinetic energy holding capacity to changes in Q_{tot} and $Dist$ with no slag layer present.

Figure 114 gives a clear indication of the increased importance of recirculatory flow pattern development when no slag layer is present. The effect of $Dist$ on kinetic energy holding capactiy is no longer negligible, but shows a strong increase towards setups with a more asymmetric flow distribution.

When neglible energy dissipation occurs in the plume eye region, all the buoyant energy input is chanelled towards the formation of smooth circulatory flows through the entire volume of the ladle.

Asymmetric tuyere setups are especially conducive towards the formation of these large scale recirculating flow patterns. As discussed in Chapter VIII:4.1, smooth circulating flows concede a very small percentage of the mean kinetic energy to turbulence, thereby markedly increasing the kinetic energy holding capacity of the ladle.

3.2.2. Response of the Mixing Quality Variable

The response surface of mixing time is given below:

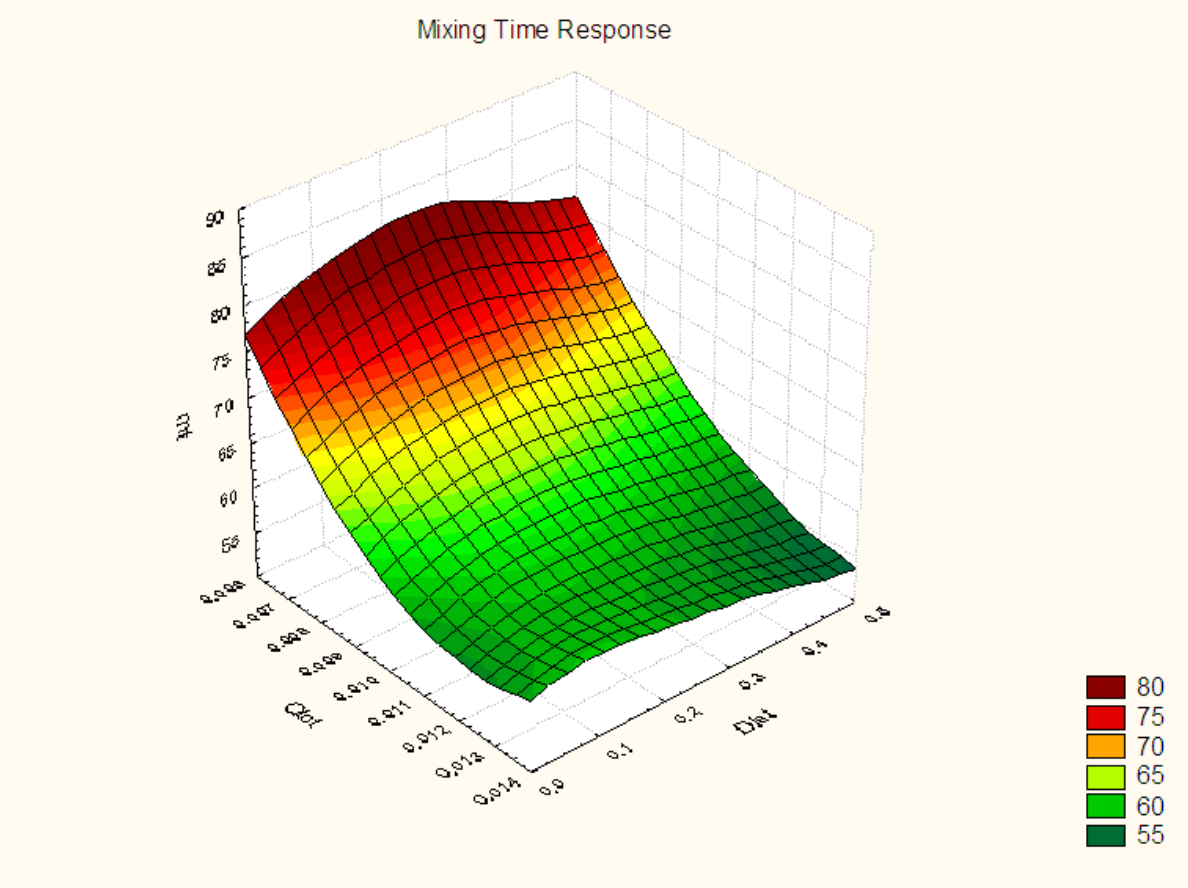

Figure 115: Spline response surface of mixing time to changes in Q_{tot} and $Dist$ with no slag layer present.

Figure 115 differs from its counterpart (case with the slag layer included) by showing a marked improvement in mixing quality at lower levels of $Dist$. This improvement can be attributed to the substantial increase in kinetic energy holding capacity affected by lower levels of $Dist$. The experimental results therefore also indicate that increases in mixing quantity can result in increased mixing quality as well.

The regions which produced the highest quality of mixing in the case with the slag layer included $(Dist > 0.3)$ now show no significant improvement. This can largely be attributed to the conflicting flow patterns developed by these flow setups.

3.3. Impact of the Slag Layer on Mixing

To quantify the impact that a slag layer has on mixing, the two central composite designs discussed in the previous two sections were compiled into one design with the slag layer as the blocking variable. The ANOVA results from this design are given below:

Table 25: Percentage of variance explained by Q_{tot}, $Dist$ and the presence of a slag layer (blocks).

Factor	e_k	E_{tot}	$\tau_{95\%}$	η
Blocks	0.5	30.0	16.0	5.0
(1) R (L)	88.4	42.1	44.4	6.7
R (Q)	0.0	0.6	9.0	0.1
(2) θ (L)	1.1	12.6	8.4	8.4
θ (Q)	4.1	1.8	1.3	32.8
1L by 2L	0.1	0.4	2.2	1.0
Error	4.9	10.8	20.1	36.3
Total	**100.0**	**100.0**	**100.0**	**100.0**

Table 25 shows that the slag layer (Blocks) has no impact on the kinetic energy transfer rate or on the efficiency of buoyant energy conversion. Even though the presence of a slag layer causes additional energy losses at the free surface, it seems that the impeding circulatory flows created with no slag layer present caused the same limiting effect.

Despite the conflicting circulatory flows, the setup with no slag layer still produced a superior quality and quantity of mixing. These improvements are quantified by calculating the means:

- Kinetic energy holding capacity: 7694 J (40.5% improvement)
- Mixing time: -8.3 s (11.4% improvement)

3.4. Mass Loading and Slag Parameters

The industrial ladle under scrutiny can accommodate different mass loadings, altering the depth of the molten steel (M) as an operating variable. It is also possible to alter the slag in terms of density (ρ_s), viscosity (μ_s) and depth (H_s). The effects of these four variables were investigated in the 2^{4-1} fractional factorial designed in Chapter XVI:3.2.

The runs were completed at a constant total flow rate of $Q_{tot} = 0.01$ kg/s. The value of $Dist$ was specified as 0.375 following the marginal improvements achieved by this flow distribution in Section 3.1.2. A marginally asymmetrical flow distribution is also implemented as a practical measure in the actual ladle to allow flux addition to the stronger plume where the slag cannot solidify and cause an obstruction.

Table 26 reports the results gathered from the experiment. The mixing time results are scaled to the time required to mix a mass loading of 175 tons for easy comparison to the previous experimental designs.

Table 26: Results from the mass loading and slag parameters experiment.

Run	M [ton]	ρ_s [kg/m³]	μ_s [Pa.s]	H_s [m]	e_k [W]	E_{tot} [J]	$\tau_{95\%}$ [s]	η [%]
1	150	2000	0.02	0.1	2516	17345	85.8	56.3
2	185	4000	0.02	0.1	2693	21758	61.0	53.5
3	150	4000	0.02	0.4	2205	15691	86.9	49.3
4	185	2000	0.02	0.4	2483	21536	60.1	49.3
5	150	4000	0.06	0.1	2436	16854	86.9	54.5
6	185	2000	0.06	0.1	2674	22195	58.2	53.1
7	150	2000	0.06	0.4	2334	16790	82.8	52.2
8	185	4000	0.06	0.4	2377	20321	63.9	47.2

A subsequent ANOVA yielded the following:

Table 27: Percentage of variance explained by M, ρ_s, μ_s and H_s.

Factor	e_k	E_{tot}	$\tau_{95\%}$	η
M	35.3	93.1	97.8	15.9
H_s	55.1	3.7	0.0	71.6
μ_s	0.4	0.0	0.0	0.4
ρ_s	5.7	2.7	1.4	7.9
Error	3.5	0.5	0.7	4.3
Total	100.0	100.0	100.0	100.0

The first indication from the data that μ_s has no influence on mixing efficiency. This seems to indicate that the slag layer will reduce the buoyant energy transfer efficiency (see Chapter VIII:4.4) as long as it is sufficiently fluid. Crusty, almost solid slags sometimes form in gas stirred ladles though. These might actually lessen the surface deformation, thereby increasing the buoyant energy transfer efficiency. Further research is indicated.

M is the most important factor in the design and is at least moderately significant ($p < 0.05$) in all the dependent variables. The second most influential variable, H_s, is significant ($p < 0.02$) in all dependent variables save for the mixing time. ρ_s is only moderately significant ($p = 0.03$) in determining the kinetic energy holding capacity of the ladle.

3.4.1. Analysis of the Mixing Quantity Variables

A. Kinetic Energy Transfer Rate and Efficiency

An increase in M from 150 to 185 t caused a moderate increase of 180 W (7.7%) in the kinetic energy transfer rate despite a 2.2% drop in the kinetic energy transfer efficiency. This scenario provides a good example of how the height of the ladle influences the energy transfer and can be analysed as follows:

A taller ladle will achieve a higher rate of buoyant energy input since every bubble entering the melt will have a larger amount of pressure energy (Equation 81 in Chapter VIII:2.1.1.A). Concurrently, the taller plume will disperse further, thereby reducing the plume velocity in the upper regions of the

ladle (Figure 116). This reduction in continuous phase flow velocity will increase the ratio of v_s/v_b, thereby allowing a larger percentage of the pressure energy in the bubble to be lost to slip (Chapter VIII:2.1.1.C). A taller melt therefore acquires a larger amount of buoyant energy from a fixed gas flow rate, but is less efficient in converting it to kinetic energy. In this case, the increase in buoyant energy input seems to outweigh the decrease in kinetic energy transfer efficiency to sum to an overall increase in the kinetic energy transfer rate.

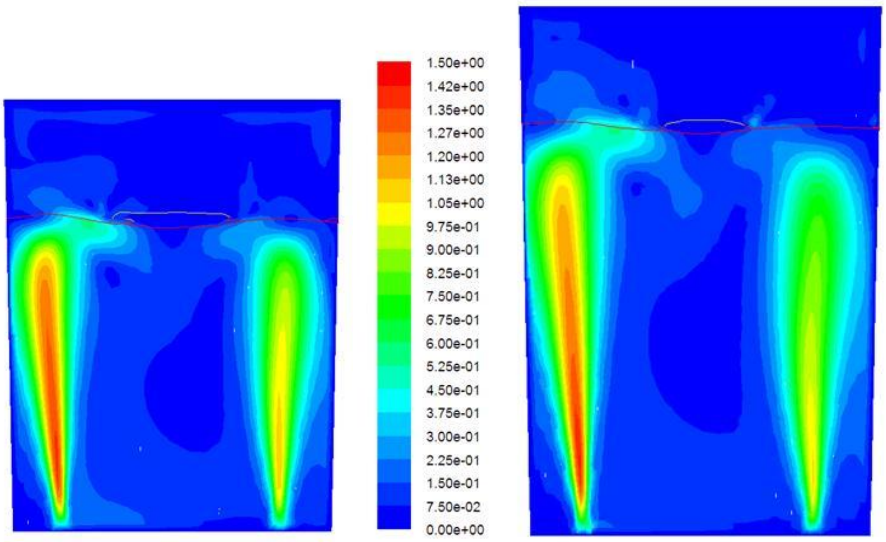

Figure 116: Comparison of plume flow velocities in the 150 t (left) and 185 t (right) mass loading.

The energy transfer rate dropped by 230 W (9.8%) when H_s was increased. This is the direct result of a 4.7% (9.5%) drop in the kinetic energy transfer efficiency. The reduction in kinetic energy transfer efficiency can be explained by the slag layer not completely covering the plume eye at the low level of H_s. When the top of the plume eye is not completely covered with slag, a part thereof is in contact with the top gas which does not apply any additional downwards force. The completely covered plume eye, however, deforms a substantially larger volume of slag, thereby invoking a larger counter force (Chapter VIII:4.4). An illustration of this effect is shown in Figure 117.

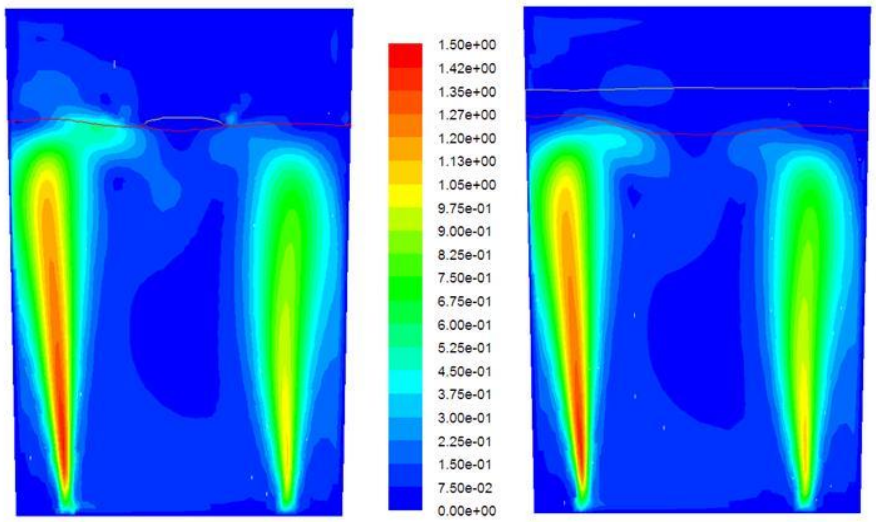

Figure 117: Position of the slag/gas interface (yellow line) relative to the plume eyes (red line) for the low (left) and high (right) levels of H_s.

It is also interesting to note that the slag density has no effect on the kinetic energy transfer rate. This confirms that a slag layer of higher density does not result in a stronger counter force on the plume eye.

B. Kinetic Energy Holding Capacity

The effects of factors H_s and ρ_s were only marginally significant $(0.01 < p < 0.05)$ and did not result in a change of more than 5% in the kinetic energy holding capacity of the vessel. An increase in the mass loading (M), however, resulted in a 28% improvement in kinetic energy holding capacity.

Changes in the mass loading (M) also change the height of the melt. This allows the plumes more distance to disperse, thereby reducing the kinetic energy transfer efficiency slightly as alluded to in the previous subsection. More importantly though, this reduction in plume concentration creates a wider and flatter plume eye, thereby allowing the flow to turn more freely at the interface. The result is a reduction in turbulence generation in the plume eye and a subsequent development of stronger flow patterns in the bulk metal. This effect is shown in Figure 118.

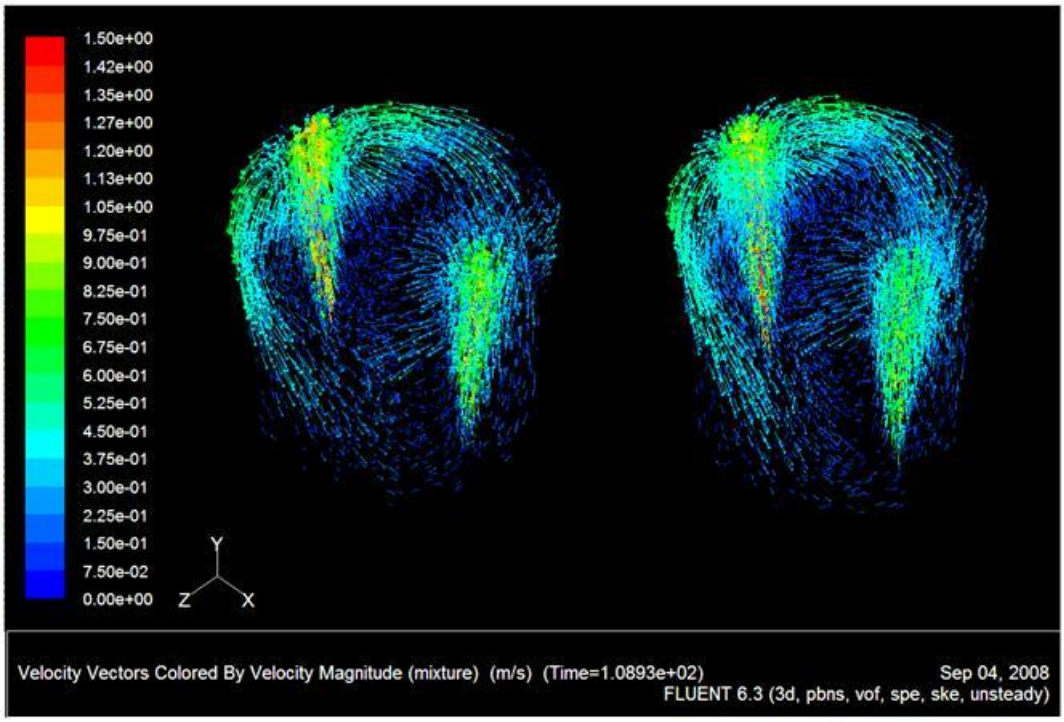

Figure 118: The slight increase in recirculating flows in the 185 t ladle (right) compared to the 150 t ladle (left).

When interpreting Figure 118, it should be kept in mind that the 185 t ladle setup is required to agitate 35 tons of steel more than the 150 t setup by utilizing the same rate of gas input. Despite its smaller specific energy input, the 185 t setup still creates stronger circulatory flows than the 150 t setup.

The 4.8% decrease in kinetic energy holding capacity resulting from a thicker slag layer (H_s) is the direct result of the 9% decrease in kinetic energy transfer rate described in the previous subsection. It is also possible that these values are deceivingly low due to the flow distribution $(Dist = 0.375)$ employed in the experiment. Chapter X:3.2.1 showed that the kinetic energy transfer efficiency is substantially reduced around $Dist = 0.25$. The stronger plume was shown to cause significant

interference with the rise of the weaker plume when no energy is required to deform a slag layer at the surface. In the present experiment, the thin slag layer allows for much stronger flows, leading also to stronger flow pattern interference.

The 4.3% reduction in kinetic energy holding capacity caused by the larger slag density (ρ_s) is somewhat surprising seeing that ρ_s had no effect on the rate of kinetic energy transfer. It is postulated that this effect is caused by the increased plume eye deformation resulting from a denser slag phase (Chapter VIII:4.3). A greater deformation in the plume eye will require the flow patterns to turn more sharply at the free surface, thereby increasing the mean velocity gradients and the turbulence generation.

The combined effect of H_s and ρ_s on flow pattern development is displayed below.

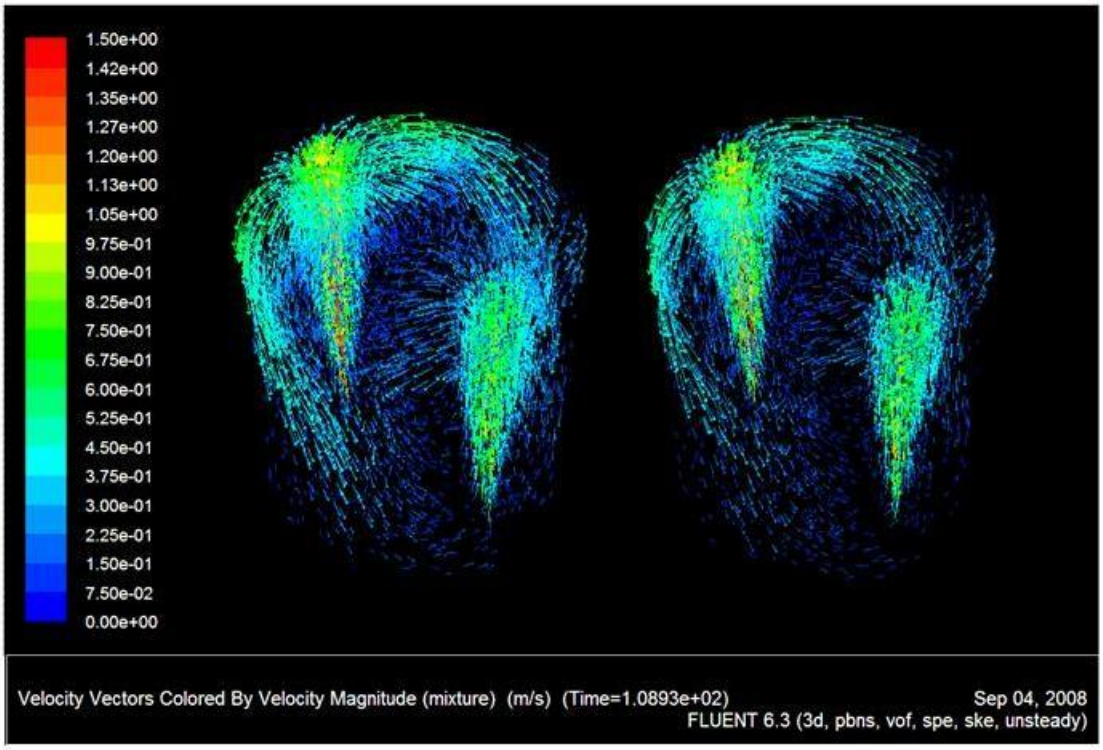

Figure 119: Flow patterns with both H_s and ρ_s at their low (left) and high (right) levels.

Figure 119 shows a clear decrease in the circulatory flows outside the plumes when H_s and ρ_s are set to their high levels.

3.4.2. Analysis of the Mixing Quality Variable

Changes in the mass loading had a strong effect on the mixing quality, causing a 20 s decrease in mixing time when M is increased from 150 to 185 t. This is a further illustration of the potential power of flow pattern altering variables on mixing quality. Contrary to the experiment completed in Section 1 of this chapter, however, the taller vessel now results in a better quality of mixing.

Figure 118 in the previous section shows that the circulatory flow patterns resulting from the taller ladle setup penetrate further downwards, towards the quiescent lower regions of the vessel. Even

though the qualitative comparison is subtle, the quantitative result is a 40% increase in mixing quality.

3.5. CLOSURE

The total gas flow rate was re-established as the most influential operating variable in Section 3.1. Being a flow pattern strengthening variable, its effect on mixing quantity is greater than its effect on mixing quality. Section 3.2 showed, however, that specific ladle setups can result in serious interference between one rising plume and the recirculating flows originating from another. The distribution of gas flow between different tuyeres can therefore become an important operating variable, especially at higher gas flow rates where the recirculating flows become stronger.

It was found that the presence of a slag layer had a substantial dampening influence on circulatory flow pattern development. This was the result of the work required to keep the slag layer deformed and is in agreement with the literature reviewed in Chapter II:4.1.5. The effect of the slag layer was far from constant over different operating procedures, however. It was shown that the same experiment with and without a slag layer resulted in completely different responses of both quantity and quality of mixing due to the increased interaction between the plumes.

The mass loading was also established as an important operating variable. Larger mass loadings increased the buoyant energy input to the ladle and decreased the turbulence generation at the free surface, thereby allowing the mean velocities in the plume to turn much easier and form strong circulatory flows in the bulk of the vessel. Results revealed that a 35 t increase in mass loading yielded improvements in mixing quantity similar to a gas purging rate increase from 0.01 kg/s to 0.014 kg/s. The mixing quality was also substantially improved.

These results are in accordance with the literature reviewed in Chapter II:4.2.5.B predicting that the ladle aspect ratio will have a significant effect on the mixing efficiency. Section 3.4.2 showed that a 23% increase in aspect ratio yielded a 40% improvement in mixing time. Care must be taken, however, to avoid the dead zone formation displayed by the taller single tuyere setup investigated in Section 1 of this chapter.

CHAPTER XI:
RESULTS & DISCUSSION PART 4:
DESIGN VARIABLES

> *Results! Why, man, I have gotten a lot of results.*
> *I know several thousand things that won't work.*
> ***- Thomas Edison***

A trial and error approach to searching for the ideal ladle design is like looking for the proverbial needle in a haystack. Such an approach might require an amount of experimentation similar to that completed by Thomas Edison on his search for the correct filament for the electric light bulb.

This chapter adopts another approach, however. By completing designed experiments, the effects of various design variables can be determined and interpreted with the aid of kinetic energy considerations. Such a fundamental understanding of the effects of all design variables will reduce the size of the haystack considerably and give clear direction towards finding the ideal ladle design.

The relevant variables were identified in Chapter II:4 and are summarized below:

- Design variables
  - Tuyere setup
    - Number of tuyeres
    - Positioning of tuyeres on the ladle floor
  - Flow pattern manipulation
  - Ladle geometry
    - Ladle shape
    - Ladle dimensions
    - Ladle size

1. TUYERE SETUP

The effect of tuyere setup was investigated in two 2-factor central composite designs; one employing two tuyeres and the other employing three tuyeres.

1.1. TWO TUYERES

The first central composite design investigated the impact of the positioning of two tuyeres on the ladle floor. The two factors under consideration were the normalized distance from the centre (R) and separation angle (θ) as illustrated in Figure 120.

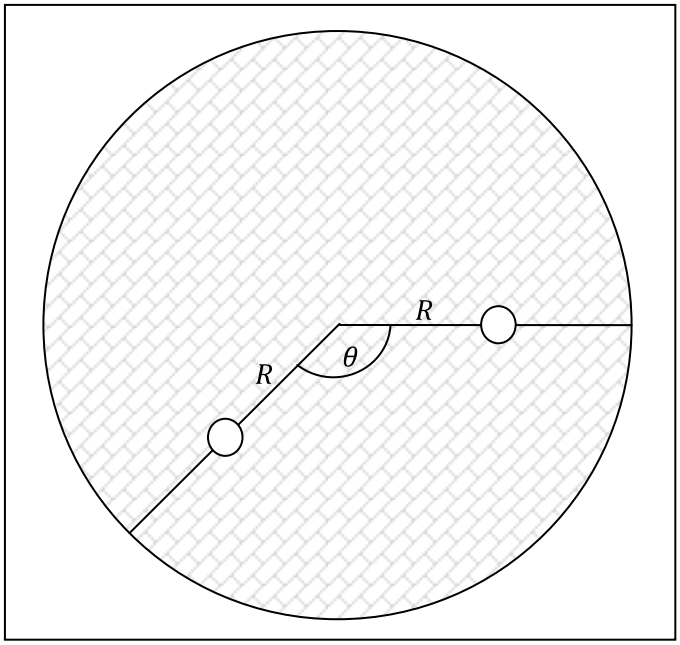

Figure 120: The specification of R and θ in the designed experiment.

The experiment was carried out in a ladle, 3 m in diameter and melt height (including a 20 cm slag layer). The total flow rate of 0.01 kg/s was split equally between the two tuyeres. Results from the experiment are given below:

Table 28: Results from the two tuyere positioning experiment.

Run	R [fraction]	θ [degrees]	e_k [W]	E_{tot} [J]	$\tau_{95\%}$ [s]
1	0.300	60.5	2560	12918	177.0
2	0.300	159.5	2378	13459	123.0
3	0.700	60.5	2331	15255	70.5
4	0.700	159.5	2393	15794	72.5
5	0.217	110.0	2419	13494	196.0
6	0.783	110.0	2384	14288	84.2
7	0.500	40.0	2332	19962	61.5
8	0.500	180.0	2444	12726	70.0
9 (c)	0.500	110.0	2409	12657	73.5
10 (c)	0.500	110.0	2406	12527	71.5

Table 29: Percentage of variance explained by R and θ.

Factor	e_k	E_{tot}	$\tau_{95\%}$
(1) R (L)	22.9	9.0	57.9
(1) R (Q)	0.1	2.1	27.3
(2) θ (L)	0.5	22.4	0.9
(2) θ (Q)	0.3	27.8	0.0
1L by 2L	39.3	0.0	3.7
Error	36.8	40.1	3.0
Total	100.0	100.0	100.0

The large error terms in Table 29 shows that no model fit could be attained in the dependent variables measuring mixing quantity. The most likely reason for the unpredictability of these results is that the range of experimentation was excessively large.

In contrast, the model fit to the response of mixing time is very good. It can clearly be seen that R is the only variable of importance when determining mixing quality. Both the linear $(p = 0.0009)$ and the quadratic $(p = 0.0037)$ effects are highly significant.

1.1.1. Response of the Mixing Quality Variable

The mixing time response surface is given below:

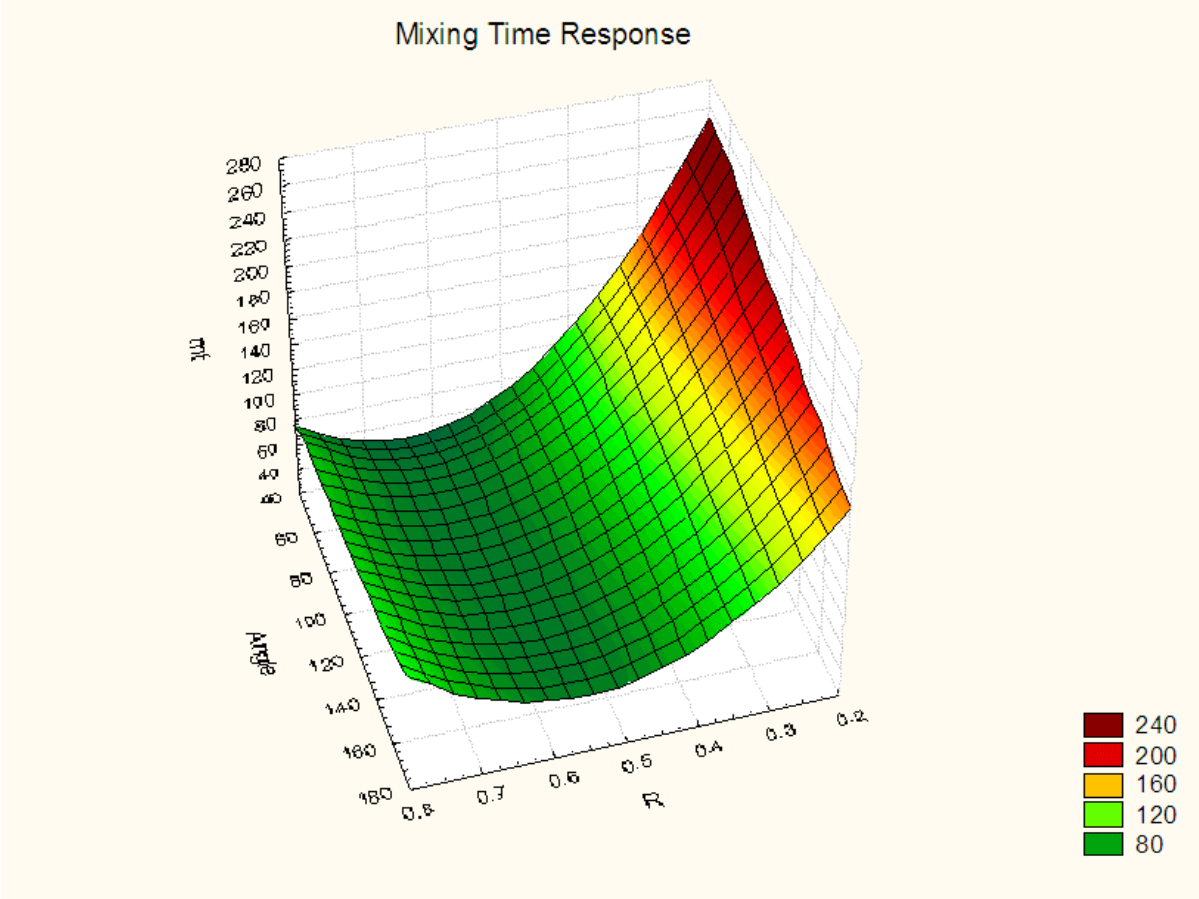

Figure 121: Spline response surface of mixing time to changes in R and θ for the two tuyere experiment.

Figure 121 shows a clear minimum in the mixing time at $R = 0.6$. This is in accordance with literature sources stating that tuyeres placed at a mid-radius position provide the best mixing (Chapter II:4.2.1).

The excessively long mixing times achieved by lower levels of R confirm the poor performance of centric tuyere setups. This was expected since the centric tuyere setup evaluated in Chapter X:1 yielded dead zones even without the presence of a slag layer. The slag layer included in the current model will weaken the recirculating flows further.

The mixing time response also indicates that the quality of mixing is not at all influenced by the level of asymmetry included in the design. The completely symmetric design ($\theta = 180°$) is shown to result in identical mixing times to the highly asymmetrical flow setup with $\theta = 40°$.

1.2. Three Tuyeres

The experiment in the previous section was repeated with an additional tuyere positioned in an equiangular fashion between the two existing tuyeres. The total flow rate between all the tuyeres was kept constant, thereby splitting the 0.01 kg/s gas feed rate equally between the three tuyeres. Results are given below:

Table 30: Results from the three tuyere positioning experiment.

Run	R [normalized]	θ [degrees]	e_k [W]	E_{tot} [J]	$\tau_{95\%}$ [s]
1	0.300	60.5	2570	12851	113.5
2	0.300	159.5	2292	14200	101.0
3	0.700	60.5	2329	24565	51.0
4	0.700	159.5	1699	20445	39.5
5	0.217	110.0	2532	13192	197.0
6	0.783	110.0	2275	18198	53.5
7	0.500	40.0	2085	22864	54.5
8	0.500	180.0	1196	16833	47.0
9 (c)	0.500	110.0	1467	24114	43.5
10 (c)	0.500	110.0	1467	24099	46.5

The ANOVA results are displayed below:

Table 31: Percentage of variance explained by R and θ for three tuyeres.

Factor	e_k	E_{tot}	$\tau_{95\%}$
(1) R (L)	8.2	39.2	59.8
(1) R (Q)	56.1	39.3	28.3
(2) θ (L)	26.8	8.0	0.7
(2) θ (Q)	3.9	9.8	0.0
1L by 2L	1.4	3.7	0.0
Error	5.6	9.5	4.8
Total	100.0	100.0	100.0

The third tuyere provided a degree of similarity between the experimental runs. Therefore, the experimental range was not too wide anymore and suitable fits were attained for all the dependent variables.

R is confirmed as the most dominant factor in the design, again explaining all the variance present in the response of mixing time. When looking at the mixing quantity variables, however, θ becomes more prominent. The linear effect of θ is statistically significant $(p = 0.012)$ on the kinetic energy transfer rate. θ also explains some of the variance present in the kinetic energy holding capacity of the ladle. These effects are not statistically significant though.

1.2.1. Response of Mixing Quantity Variables

The response surfaces of energy dissipation in the flow and kinetic energy holding capacity are given below:

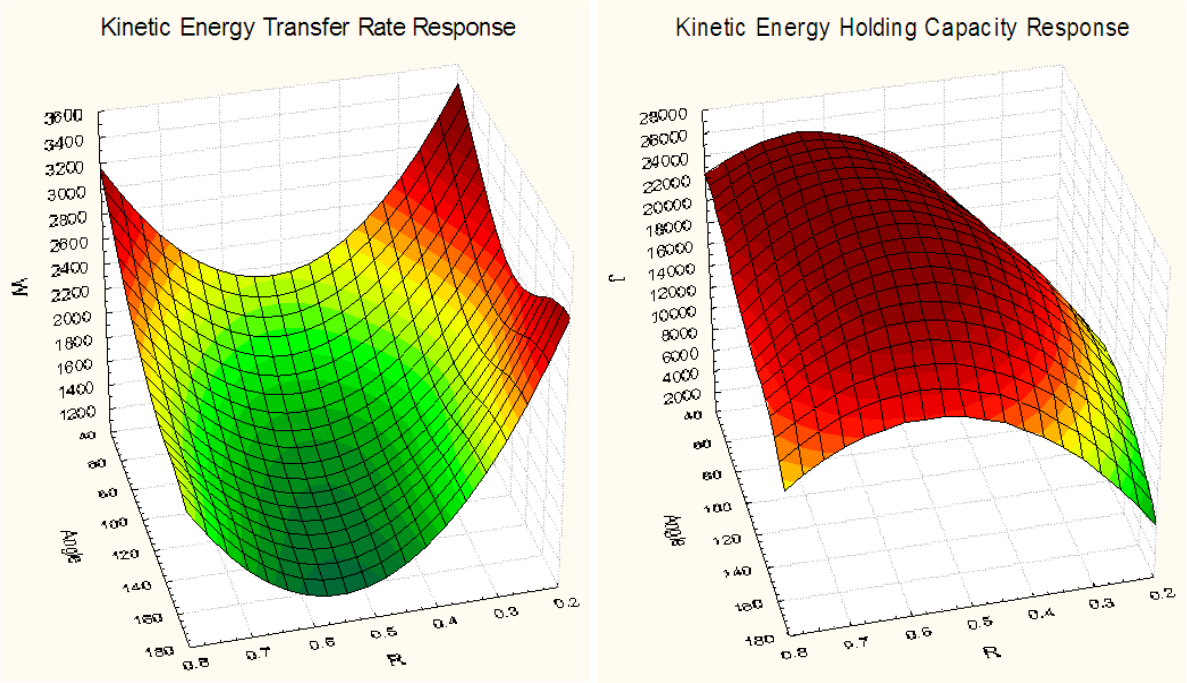

Figure 122: Spline response surface of energy dissipation in the flow to changes in R and θ for the three tuyere experiment.

The curves shown in Figure 121 show completely opposite responses to changes in tuyere positioning. This proves a rather unexpected point that the efficiency of buoyant energy transfer to the kinetic energy of the fluid is not even close to being the primary factor in determining the kinetic energy holding capacity of the ladle. It seems that sufficiently smooth flow patterns can hold on to large amounts of kinetic energy even under conditions where the buoyant energy input efficiency is very poor.

To further an investigation into the reasons behind the low values of kinetic energy transfer rate, the interaction between the recirculating flows and the rising bubbles is displayed in Figure 123.

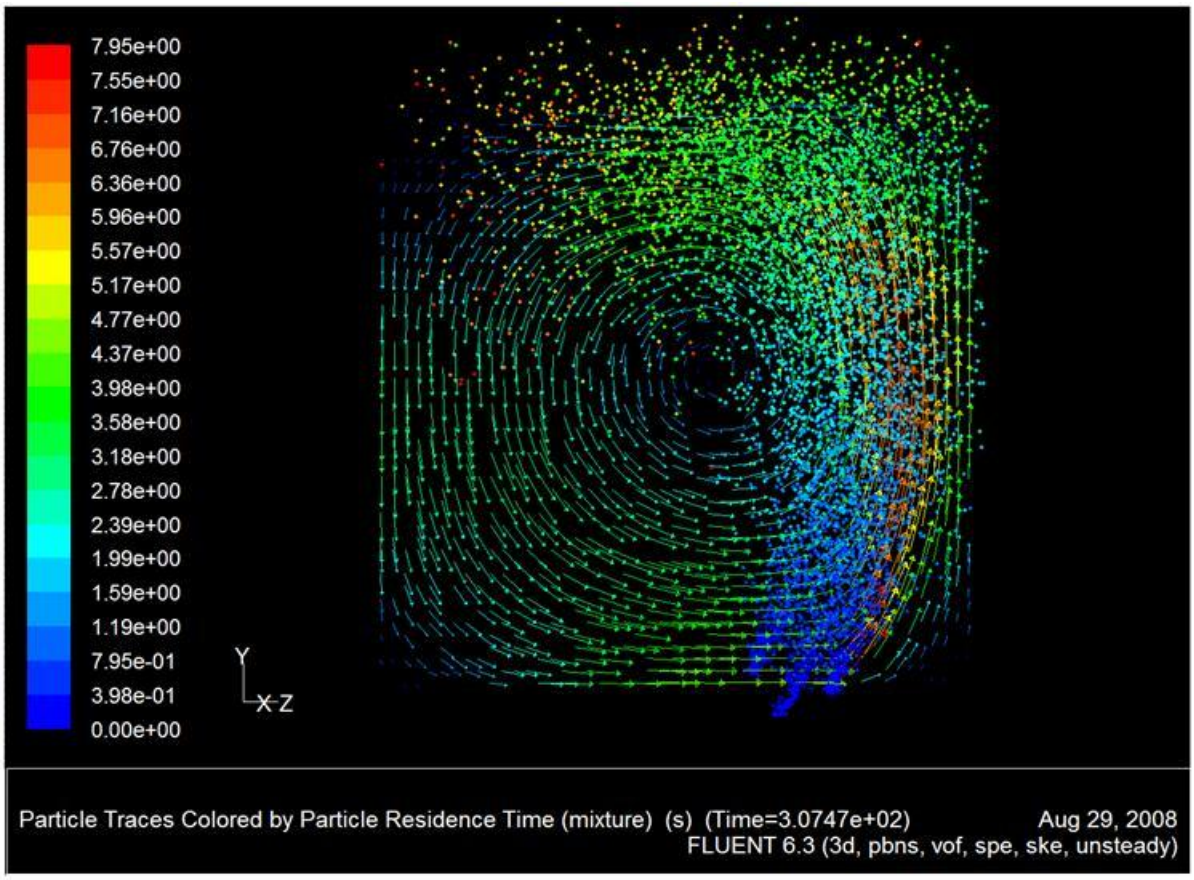

Figure 123: Particle traces along the flow patterns developed in the experiment with $R = 0.5$ and $\theta = 110°$.

The reason behind the poor kinetic energy transfer efficiency is clear from Figure 123. The circulatory flow patterns present in this ladle setup are sufficiently strong to entrain some of the bubbles to the downward flowing regions shown on the left of Figure 123. A large amount of kinetic energy is therefore being lost back to buoyant potential energy in this region (final paragraph of Chapter VIII:2.1.1.A).

This entrainment phenomenon will act as a limiting mechanism to the strength of circulatory flow patterns that can develop in gas stirred ladles. Recirculating flows moving downward at velocities greater than the terminal rising velocity of a bubble ($\approx 0.3\ \mathrm{m/s}$) will always entrain a percentage of the gas input, thereby losing substantial amounts of kinetic energy. Figure 123 indeed confirms that the downwards flows are moving at a rate in close proximity to the bubble terminal velocity. If not for the bubble entrainment phenomenon, the circulatory flows achieved by this ladle setup would be substantially greater.

1.2.2. Response of Mixing Quality Variable

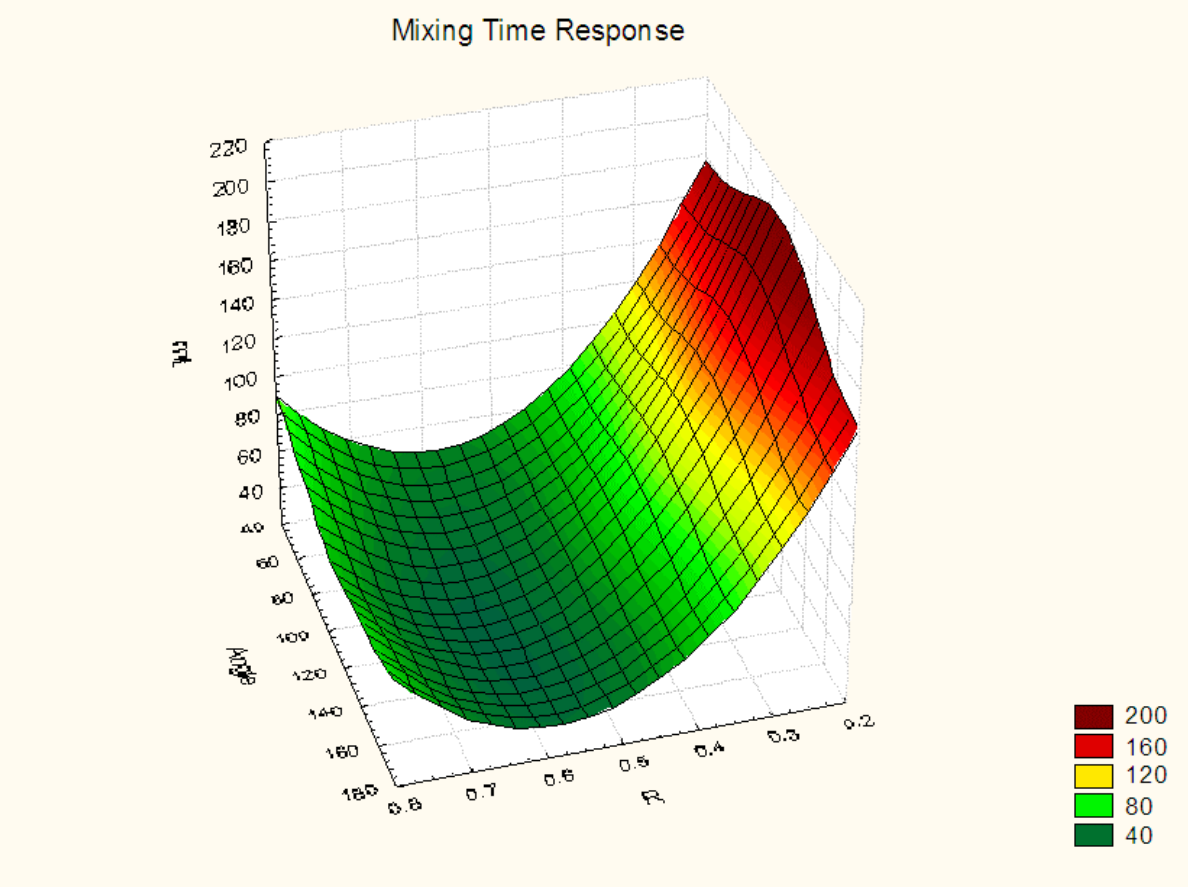

Figure 124: Spline response surface of mixing time to changes in R and θ for the three tuyere experiment.

The mixing quality response shown in Figure 124 is almost identical to that observed in the two tuyere experiment. This is confirmation that the highest quality mixing is achieved at $R = 0.6$ regardless of the measure of asymmetry present in the ladle.

It is also important to note that the quality and quantity of mixing is synonymous in this flow experiment. Both of these performance measures are attained at $R = 0.6$.

1.3. Effect of Increasing the Number of Tuyeres

To investigate the effect that the change from two to three tuyeres had, the results from the previous two sections were put into a single design with the number of tuyeres as a blocking variable. The ANOVA results from this combination are presented in Table 32.

The number of tuyeres (Blocks) was found to be significant $(p < 0.05)$ in all of the factors. The difference in means achieved by an increase in the number of tuyeres is given below:

- Kinetic energy transfer rate: -414 W (17.2% decline)
- Kinetic energy holding capacity: 4828 J (33.7% improvement)
- Mixing time: -25.3 s (25.3% improvement)

Table 32: Percentage of variance explained by R, θ and the number of tuyeres (Blocks).

Factor	e_k	E_{tot}	$\tau_{95\%}$
Blocks	27.8	32.1	6.8
(1) R (L)	4.3	16.4	54.8
R (Q)	20.1	8.5	25.9
(2) θ (L)	9.2	7.2	0.7
θ (Q)	1.3	0.1	0.0
1L by 2L	0.0	1.0	0.9
Error	37.8	33.7	4.5
Total	100.0	100.0	100.0

A marked improvement in mixing can therefore be attained by using more tuyeres. The negative influence that an increase in the number of tuyeres seems to have on the kinetic energy transfer rate can be attributed to the bubble entrainment discussed in Section 1.2.1.

1.4. Closure

Findings from this experiment are in reasonable accordance with the literature (Chapter II:4.2.1) confirming that small scale water models give a reasonable indication of flow phenomena in full sized ladles. The best mixing was attained with tuyeres positioned close to mid-way between the ladle wall and centre point $(R = 0.6)$. It was shown that ladle setups with tuyeres positioned close to the centre performed especially poorly. More tuyeres caused better mixing.

The angle between the tuyeres was found to have almost no influence on the quality or quantity of mixing inside the ladle. Angular positioning of tuyeres in a new ladle design can therefore be guided purely by practical considerations as long as the radial positioning is close to $R = 0.6$.

2. Flow Pattern Manipulation

The possible improvements offered by flow pattern manipulation were investigated by lowering a cylinder, 1 m in diameter, from the vessel roof onto the plume eye. A simple axis-symmetric tuyere setup had to be employed in the experiment since the locations of plume eyes are very hard to predict in multiple- and/or unsymmetrical tuyere setups. The flow pattern altering cylinder had to be specified at a fixed position with the creation of the geometry and could not be relocated according to the motion of the plumes.

Yamashita and Iguchi (22) concluded from water modelling that the depth of a plate immersed in the bath is the only important variable if the diameter of the plate is greater than that of the plume. Therefore, the experiment could be simplified to contain only one variable – the cylinder depth.

Experiments were completed in a ladle, 3 m in melt height and diameter, stirred centrically at a gas flow rate of 0.01 kg/s. A 40 cm slag layer was included. Results are reported below:

Table 33: Results from the flow pattern manipulation experiment.

Depth of immersion relative to the slag/metal interface [m]	e_k	E_{tot}	$\tau_{95\%}$
None	2709	13066	258.5
- 0.2	2748	12496	291.0
- 0.1	2787	13348	197.5
0	2841	14574	110.0
0.1	2669	12717	77.5
0.2	2469	11514	77.0

The experimental results will be categorized into immersions depths above the slag/metal interface and immersions on and below the interface.

2.1. Immersions Above the Metal/Slag Interface

Flow patterns resulting from the three experimental runs with immersions above the free surface are presented below:

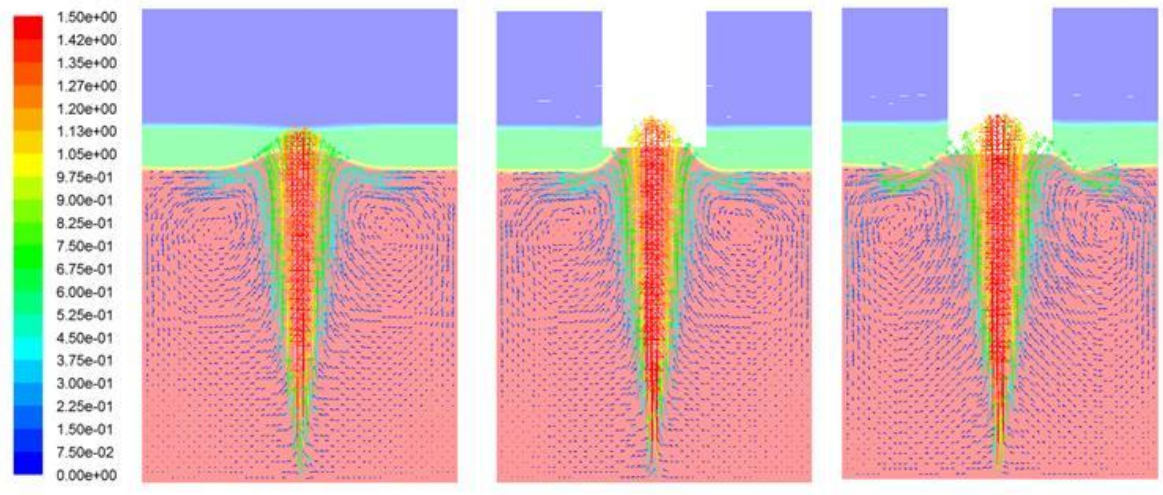

Figure 125: Flow patterns for experimental runs with no flow pattern manipulation (left) and immersions of 0.2 m (centre) and 0.1 m (right) above the metal/slag interface.

Table 33 shows a small increase in the kinetic energy transfer rate as the cylinder is moved downward. This is due to the cylinder restricting the amount of surface deformation. Since the cylinder redirects the upwards momentum near the metal/slag interface, a smaller amount of momentum is used to keep the interface deformed and can be used to drive the flow instead. It is clear that this effect is quite small, causing an improvement of only 5% from the case with no flow pattern manipulation to the case where the cylinder is located at the interface.

The kinetic energy holding capacity shows an interesting response to flow pattern manipulation. At an immersion of -0.2 m, the kinetic energy is reduced from the base case. Figure 125 shows that this very shallow immersion causes the plume eye to become tall and narrow, thereby increasing the velocity gradients and turbulence losses. This problem is rectified by further increasing the

immersion to flatten out the plume eye which allows the plume velocities to turn much easier, hence the improvement offered by the -0.1 m immersion.

All three runs yielded mixing times in excess of 197 s, affirming the poor quality of mixing obtained in tall, centrically stirred vessels (Chapter X:1). Figure 125 shows large dead zones in the bottom regions of the ladle. It is interesting to note that the small improvement in plume eye shape from the -0.2 to the -0.1 m immersion resulted in a 100 s improvement in the mixing time.

2.2. Immersions On and Below the Slag/Metal Interface

Flow patterns resulting from the three experimental runs with immersions on and below the free surface are presented below:

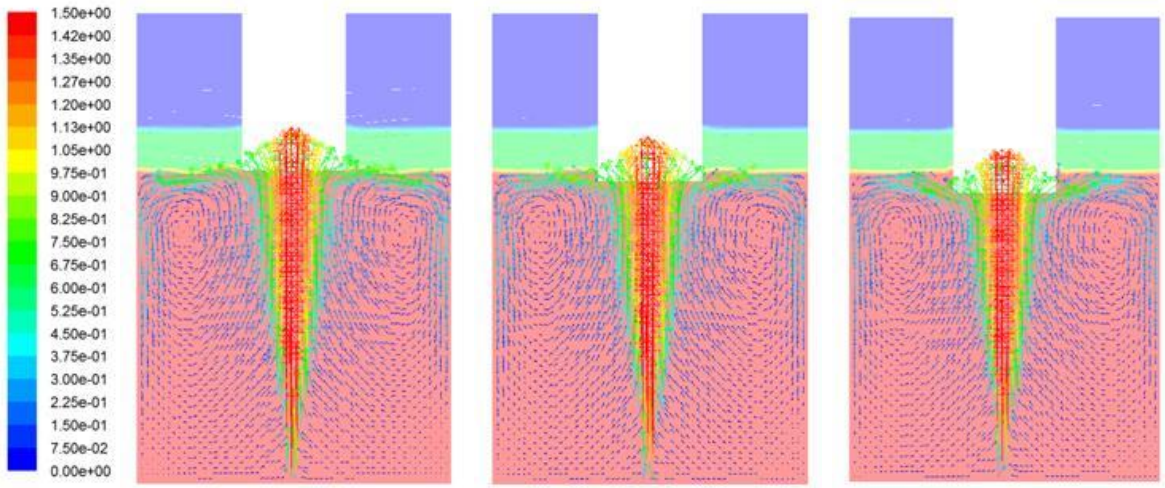

Figure 126: Flow patterns for experimental runs with immersions of 0 (left), 0.1 (centre) and 0.2 m (right) below the metal/slag interface.

Table 33 shows a marked decrease in kinetic energy transfer rate as the immersion depth is increased below the metal/slag interface. This is largely due to the immersed cylinder shortening the plume and therefore the distance over which kinetic energy is transferred. The stronger recirculating flow patterns also cause a larger amount of interference with the rising plume (Chapter VIII:2.1.2).

The substantial decrease in the kinetic energy holding capacity with increased levels of immersion can be attributed to the cylinder effectively removing a portion of the plume containing and contributing a large amount of kinetic energy. Figure 126 shows that this decrease in kinetic energy holding capacity does not have a large influence on the bulk recirculating flows.

Mixing times achieved with immersions below the metal/slag interface are substantially better than those with immersions above the slag/metal interface. By comparing Figure 126 to Figure 125 it can be seen that the circulatory flows become much stronger when the cylinder is moved below the slag/metal interface. This improvement results partly from the momentum saved by not deforming the slag layer. The primary cause, however, is the ease with which the flows can turn against the flat surface of the cylinder.

Chapter VI:2.1 has discussed the error involved in assuming the melt free surface to be flat. It was concluded that a flat and frictionless free surface will grossly overestimate the recirculating flow velocities due to the under-predicted turbulence losses in the plume eye. By implementing flow pattern manipulation at the plume eye, these advantages can be attained in a model with a mobile free surface.

2.3. Closure

The experiment has shown that significant improvements can be attained by submerging a cylinder onto the plume eye. Experimental results are in accordance with the literature reviewed in Chapter II:4.2.4 concluding that the mixing is most improved by submersions below the slag/metal interface. A submergence on or just below the slag/metal interface seems to attain the highest mixing efficiency, offering improvements of 11.5% in kinetic energy holding capacity and 57.4% in mixing time.

The implementation of this type of flow pattern manipulation effectively removes the detrimental effects that a slag layer has on mixing inside the melt. Implementation of flow pattern manipulation in the industrial ladle investigated in Chapter X:3 will therefore yield improvements similar, or even slightly better than those achieved by simply removing the slag layer. These improvements were quantified in Chapter X:3.3 as 40.5% for the kinetic energy holding capacity and 11.4% for the mixing time.

Further research is required to determine whether these improvements are sufficient to verify the running costs and operational difficulties of implementing such a device in the hostile environment of an industrial gas-stirred ladle.

3. Ladle Geometry

Three possible alterations to the vessel geometry were considered: changes in the overall ladle capacity (M_L), changes in aspect ratio (AR) and changes in the angle at which the ladle walls expand upwards (θ_L). These factors were investigated in a three-factor, five-level, rotatable central composite design.

Two tuyeres were used, positioned at $R = 0.6$ diagrammatically opposite each other on the ladle floor as recommended in Section 1.4 of this chapter. The total gas purge rate was scaled according to the mass loading to mirror a gas flow rate of 0.01 kg/s in a 150 ton ladle. Further detail on the experimental design can be viewed in Chapter XVI:5.

Experimental results were scaled so that the kinetic energy transfer rate and holding capacity would reflect the quantity of kinetic energy transferred and maintained from a gas purge rate of 0.01 kg/s. No scaling was required for the mixing time since the ratio of gas flow rate and mass loading was kept constant. Scaled results are presented in Table 34.

Table 34: Results for the ladle geometry experiment.

Run	M_L [t]	AR	θ_L [degrees]	e_k [W]	E_{tot} [J]	$\tau_{95\%}$ [s]	η [%]
1	100.0	0.703	0.00	2166	8306	98.5	61.2
2	100.0	0.703	10.00	2163	8663	117.5	61.2
3	100.0	1.297	0.00	2268	16845	49.0	49.5
4	100.0	1.297	10.00	2313	15272	69.5	50.7
5	200.0	0.703	0.00	2565	10898	132.5	62.4
6	200.0	0.703	10.00	2589	11172	117.0	63.1
7	200.0	1.297	0.00	2607	21805	51.0	49.8
8	200.0	1.297	10.00	2691	19709	78.5	51.6
9	65.9	1.000	5.00	2035	10517	79.5	54.0
10	234.1	1.000	5.00	2773	16986	72.0	56.8
11	150.0	0.501	5.00	2175	7089	175.5	65.3
12	150.0	1.499	5.00	2386	19896	49.0	45.6
13	150.0	1.000	-3.41	2494	16445	65.5	55.7
14	150.0	1.000	13.41	2512	14266	108.0	56.3
15	150.0	1.000	5.00	2520	14437	63.0	56.3
16	150.0	1.000	5.00	2520	14509	64.0	56.3

An analysis of variance yielded the following results:

Table 35: Percentage of variance explained by M_L, AR and θ_L.

Factor	e_k	E_{tot}	$\tau_{95\%}$	η
(1) M_L (L)	82.1	16.2	0.4	1.3
(1) M_L (Q)	1.5	0.2	0.6	0.1
(2) AR (L)	6.0	79.2	72.4	97.6
(2) AR (Q)	8.0	0.4	13.1	0.1
(3) θ_L (L)	0.3	1.1	5.9	0.3
(1) θ_L (Q)	0.0	0.3	2.6	0.0
1L by 2L	0.2	0.8	0.3	0.1
1L by 3L	0.1	0.0	0.5	0.0
2L by 3L	0.2	0.8	1.3	0.1
Error	1.0	0.4	5.1	0.3
Total	100.0	100.0	100.0	100.0

The ANOVA results identify θ_L as the least influential factor in the design, being mildly significant $(p = 0.039)$ in the mixing time only. The primary effects of M_L and AR explain the majority of variance in all the dependent variables. An insignificant amount of interaction and error variance is present in the model.

3.1. Effect of θ_L on Mixing Time

The response of mixing time to changes in θ_L and AR is given below:

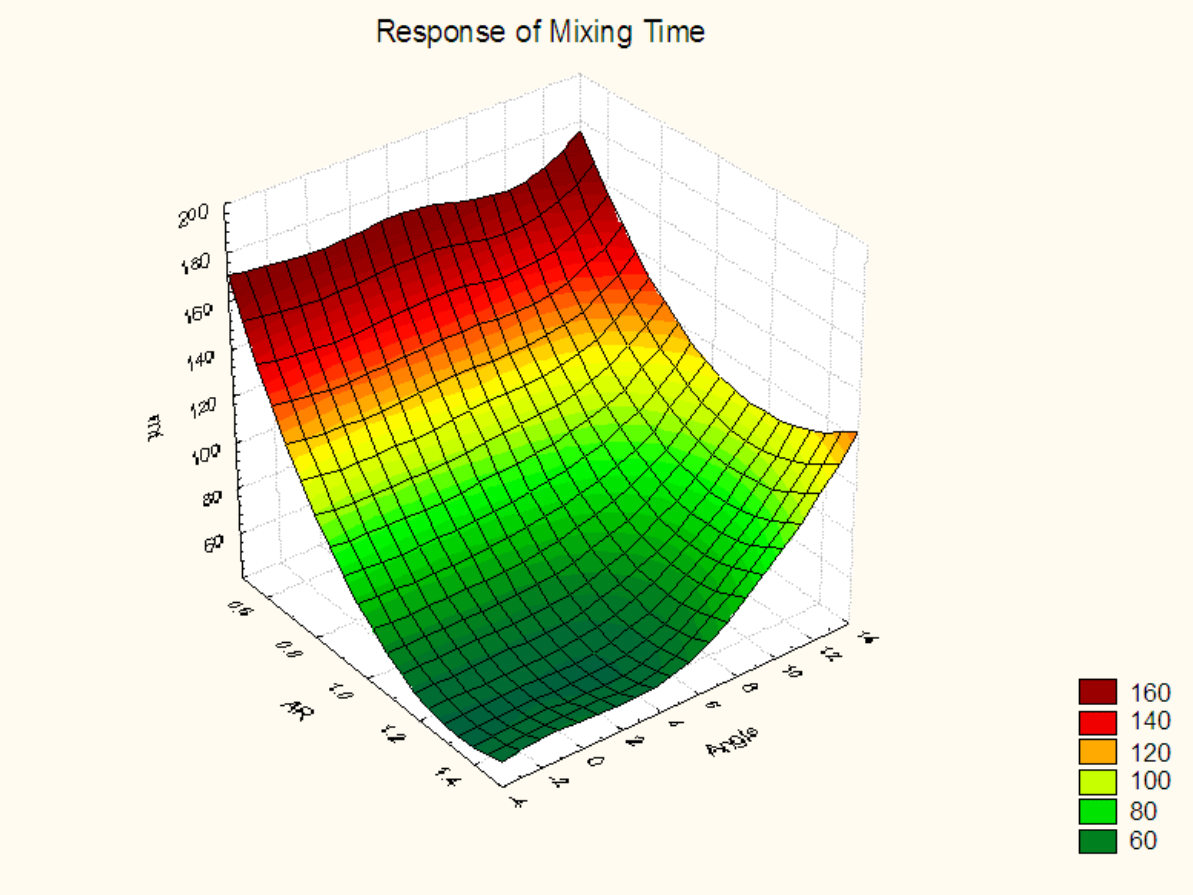

Figure 127: Spline response surface of mixing time to changes in θ_L and AR.

It can plainly be seen that the only effect of θ_L is to cause a decrease in mixing quality when both AR and θ_L are set to their high levels. A ladle with large values for both θ_L and AR will have a top diameter which is substantially larger than the bottom diameter. Since the tuyere spacing of $R = 0.6$ is based on the bottom diameter, the plumes in such a ladle setup will be quite close together when seen relative to the top diameter. Chapter XI:1.1.1 has shown that the mixing quality is significantly worsened when the tuyeres are moved closer together.

Figure 127 also shows that the mixing time is at a minimum around $\theta_L = 0$, indicating that a ladle shaped as a simple cylinder will provide the highest quality mixing.

3.2. Effect of M_L and AR on Mixing Quantity Variables

3.2.1. Kinetic Energy Transfer Rate and Efficiency

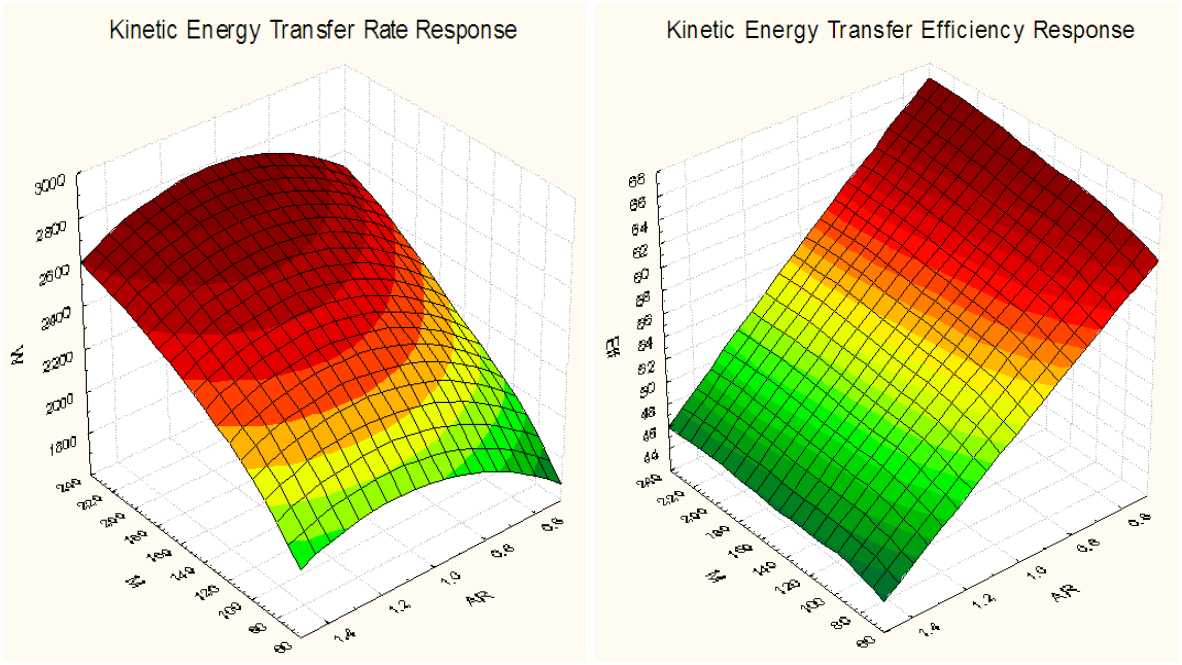

Figure 128: Spline response surface of kinetic energy transfer rate and efficiency to changes in M_L and AR.

Figure 128 displays a distinctly different response between the kinetic energy transfer rate and efficiency. These responses provide some meaningful insights into the factors influencing kinetic energy transfer from the buoyant gas to the bulk metal and are analysed below.

When considering the aspect ratio (AR) of the ladle, it is clear higher levels of this factor have a substantial detrimental effect on the kinetic energy transfer efficiency. This is simply because higher levels of AR would result in taller vessels, giving the plume more time to disperse and slow down, thereby increasing the ratio υ_s/υ_b (Chapter VIII:2.1.1.C). The smaller diameters of ladles with a high aspect ratio will also force the downwards recirculating flows closer to the upwards flowing plumes, leading to larger conflicts between the plume and the bulk circulatory flows (Chapter VIII:2.1.2).

As discussed in Chapter X:3.4.1.A, the larger quantity of pressure energy contained in the gas entering taller vessels will compensate for this reduction in kinetic energy transfer efficiency. When considering the left hand side of Figure 128, however, it can be seen that a maximum in kinetic energy transfer rate is reached around $AR = 1.1$. This is a clear indication that the kinetic energy transfer efficiency decreases faster towards higher levels of AR than the buoyant energy input can increase.

When looking at the equation for buoyant energy input (Equation 3 in Chapter II:4) it can be seen that the rate of buoyant energy input is proportional to the natural logarithm of melt height. From the right hand side of Figure 128, a linear decrease of kinetic energy transfer efficiency with increases in melt height can be observed. Therefore, increases in buoyant energy input with melt

height will be dampened by the logarithmic relationship while the kinetic energy transfer efficiency will simply continue to decrease in a linear fashion.

The capacity of the ladle (M_L) is shown to have a definite influence on the kinetic energy transfer rate. This effect once again lies with the increase in melt height achieved by the taller ladle setups. Since the experiment was designed and scaled to reflect the performance delivered by 0.01 kg/s of gas purging, the gas purging rate can be assumed to be constant between all runs. Vessels with a larger capacity, however, will have a larger melt height and therefore also a higher rate of buoyant energy input for the same gas purging rate. Since the kinetic energy transfer efficiency is not influenced by M_L, this increase in the rate of buoyant energy input will be mirrored by the kinetic energy transfer rate. The logarithmic relationship alluded to in the previous paragraph is also observed in the response of kinetic energy transfer rate to changes in M_L (left of Figure 128).

The very small effect of M on the kinetic energy transfer rate is somewhat surprising since the increased ladle height should cause similar reductions in efficiency as those observed with the factor AR. Figure 129 shows that the expected reduction in kinetic energy transfer efficiency at higher ladle capacities is countered by the increase in plume velocity.

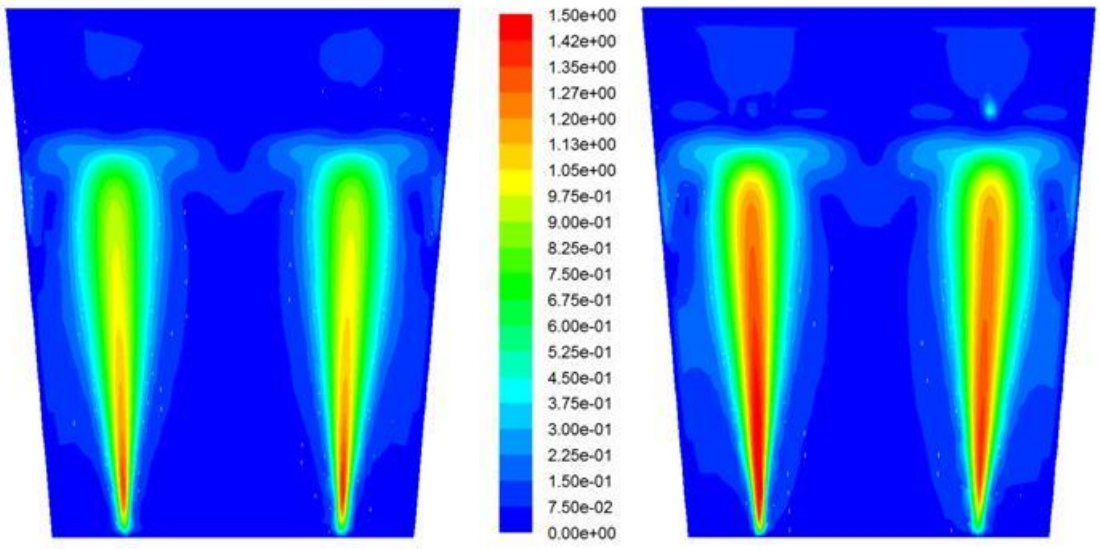

Figure 129: Plume velocities in the 65.9 t (left) and the 234.1 t (right) ladle setups.

According to the experimental setup, the larger vessel in Figure 129 was purged with a higher gas flow rate which resulted stronger plumes. Since bubble pressure energy losses are governed only by the ratio of v_s/v_b and the slip velocity (v_s) remains constant across all mass loadings, the higher plume flow rate will decrease the amount of bubble pressure energy lost to slip.

Quantitatively, it seems that the increased transfer efficiency created by the stronger plumes is balanced almost exactly by the larger height of the ladle allowing the plumes to disperse further. The linear effect of M on kinetic energy transfer efficiency was significant though $(p = 0.003)$. Effect estimates from the experimental design revealed that a change in ladle capacity from 65.9 to 234.1 t would result in a 2.2% increase in kinetic energy transfer efficiency.

3.2.2. Kinetic Energy Holding Capacity

The response of kinetic energy holding capacity to changes in M_L and AR is presented below:

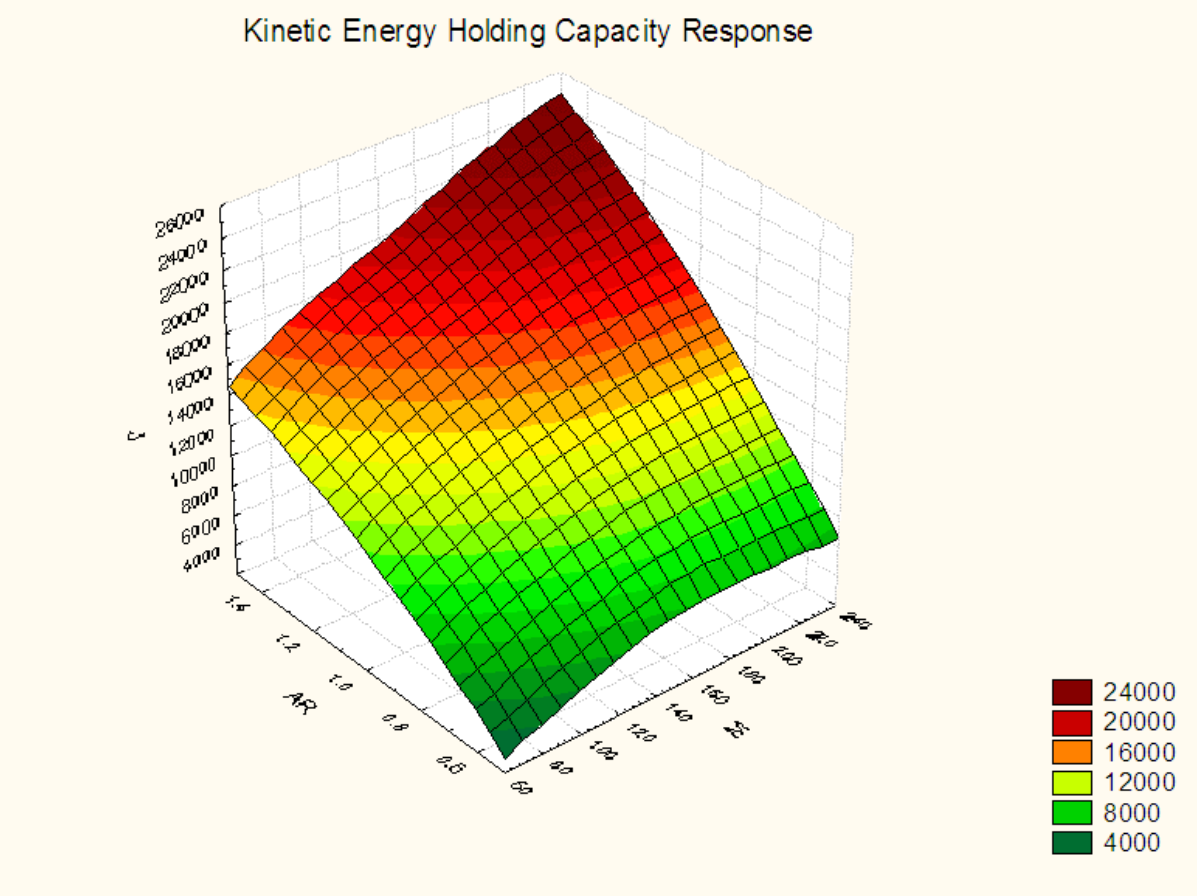

Figure 130: Spline response surface of kinetic energy holding capacity to changes in M_L and AR.

The strong effects of M_L and AR on kinetic energy holding capacity are clearly displayed in Figure 130. It is shown that higher levels of both these factors will greatly increase the quantity of mixing energy in the ladle.

Once again, these effects are the result of the increase in ladle height brought about by higher levels of both M_L and AR. An increase in ladle height has two important positive effects on mixing: An increase in the rate of buoyant energy input and the creation of a flatter plume eye as described in Chapter X:3.4.1.B.

It was shown in the previous section, however, that higher levels of AR resulted in a reduced kinetic energy transfer rate due to the large decrease in kinetic energy transfer efficiency. Despite this decrease, Figure 130 shows that the kinetic energy holding capacity keeps on increasing with higher levels of AR. The explanation can be found in Figure 131.

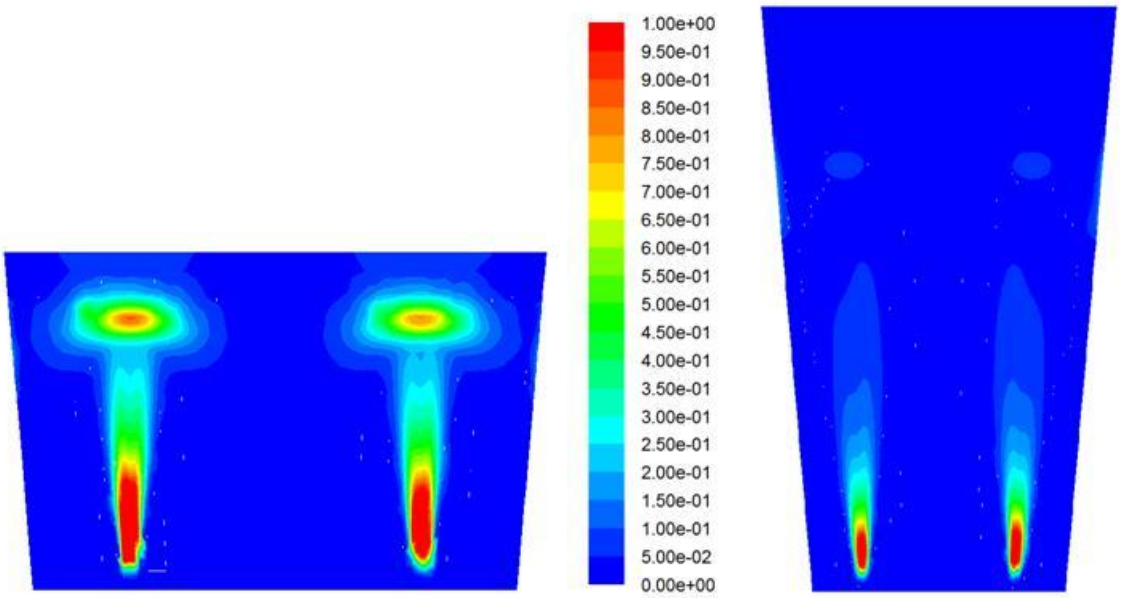

Figure 131: Contours of turbulence kinetic energy dissipation rate at $AR = 0.5$ (left) and $AR = 1.5$ (right).

Figure 131 clearly shows the large amount of turbulence kinetic energy dissipation in the plume eye regions of the shorter vessel. This is the result of a concentrated plume hitting the free surface, creating a tall plume eye and large velocity gradients and therefore losing a substantial amount of kinetic energy to viscous dissipation. The taller vessel, on the other hand, shows almost no turbulence kinetic energy dissipation in the region of the plume eye because the plume has been allowed to disperse before hitting the free surface. The mean velocities in the plume are now allowed to turn with minimal energy losses, implying that more kinetic energy is available for the development of strong circulatory flow patterns on the outside of the plume.

The magnitude of this effect certainly becomes clear from the response surface in Figure 130. When quantified, the linear effect estimate of AR shows that an increase in AR from 0.5 to 1.5 (effectively doubling the melt height) affects an improvement in kinetic energy holding capacity of 13800 J. This is more than a 200% improvement in mixing quantity.

The effect of M_L is less profound since the 234.1 ton ladle had a height of only 1.5 times that of the 65.9 ton ladle. Nonetheless, a change in M from 65.9 to 234.1 t resulted in a 6550 J increase in the scaled kinetic energy holding capacity.

3.3. Effect of M_L and AR on the Mixing Quality Variable

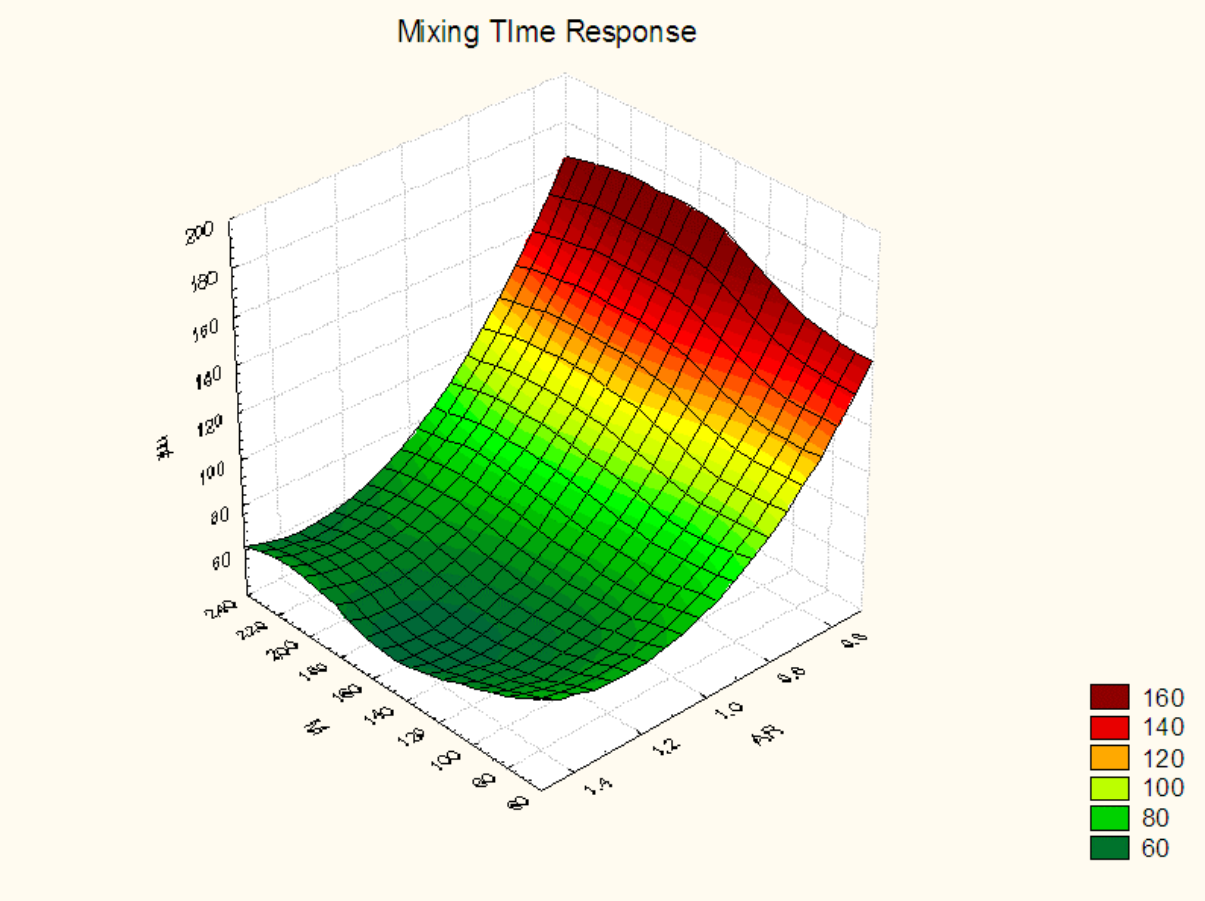

Figure 132: Spline response surface of mixing time to changes in M_L and AR.

AR is the dominant factor in the response of mixing time and is highly significant in both the linear and quadratic effect. The result is the characteristic flattening out of the mixing time as the ladle becomes well mixed (Chapter X:2.3). It can therefore be concluded that the increased mixing quantity brought about by increases in AR will result in similar improvements in mixing quality.

Theoretically speaking, dead zones should eventually occur if the aspect ratio is increased further due to the downward recirculating flows conflicting with the rising plumes and losing all of their downward momentum before reaching the lower regions of the ladle. The trend in Figure 132 shows a possible minimum in the mixing time around $AR = 1.5$. Further runs are required for verification, but it can be said with a reasonable amount of certainty that mixing time will increase at aspect ratios greater than 1.5.

The factor of M_L shows no influence on the mixing time despite offering substantial improvements in the kinetic energy holding capacity. This is an indication that the even distribution of kinetic energy throughout the ladle is slightly compromised at larger capacities. Nonetheless, the results show that the quality of mixing is not reduced when the process is scaled up.

3.4. Closure

Results from the ladle geometry experiment clearly show the positive impact that ladle height can have on the efficiency of mixing within the ladle. These results are in accordance with the literature reviewed in Chapter II:4.2.5.B. No maximum in kinetic energy holding capacity was reached in the experiment featuring ladle heights of up to 5 m, implying that the mixing quantity will continue to increase with further increases in ladle height.

The ladle height can be increased either by increasing the aspect ratio (AR) or by process scale-up (M_L). Where larger aspect ratios can lead to conflicting flows by forcing the downwards recirculating flows closer to the rising plumes, a simple scale-up will not pose this problem. In fact, higher levels of M_L were shown to increase the kinetic energy transfer efficiency as a result of the larger gas purging rates creating a larger plume velocity. The mixing quality was not influenced by changes in M_L, but the substantial positive effect that scale-up had on the mixing quantity resulted in an overall increase in mixing efficiency.

4. Theoretical Guidelines for Ladle Design

Turbulence characteristics in the plume eye is the most influential factor in ladle design. If the plume is allowed to disperse, upward plume momentum will impinge gently on the free surface, cause a minimum amount of surface deformation and allow flows to turn with minimal turbulence losses. Two separate design considerations offer improvement is this area: The ladle height and the number of tuyeres.

4.1. Ladle Height

The profound influence of ladle height on mixing efficiency was described in Section 3 of this chapter. Taller vessels simply allow the plume more distance to disperse.

It has been shown, however, that an increase in plume length also reduces the efficiency of kinetic energy transfer due to increases in the ratio v_s/v_B. These reductions in efficiency can eventually cause a decreased rate of kinetic energy transfer from the buoyant gas to the melt. The effect of decreased kinetic energy transfer efficiency has been proven to be of secondary importance though. Over the range of experimentation presented in Section 3.2, the kinetic energy holding capacity continued to increase despite reductions in the kinetic energy transfer rate.

An increase in the aspect ratio is the easiest way to increase ladle height. Care must be taken to ensure that the downwards recirculating flow patterns are not forced too close the rising plumes by reductions in the ladle diameter. The trend displayed in Section 3.3 shows that the mixing quality might be adversely affected by this phenomenon at aspect ratios greater than 1.5.

Scale-up is another way in which ladle height can be increased. Conversely to increases in aspect ratio, scaled-up ladles cause an increase in kinetic energy transfer efficiency. Results in Sections 3.2 and 3.3 show that the mixing quantity is significantly improved by process scale-up while the mixing

quality remains unaffected. It is therefore recommended that ladles be designed to be as large as practically possible at an aspect ratio close to 1.5.

Industrial ladles are normally designed on an aspect ratio of 1 or less, mostly for practical reasons. In this case, flow pattern manipulation (Section 2) by means of a circular disk submerged on the plume eye can simulate the flat plume eye created by a well dispersed plume. Such a modification can allow even a concentrated plume to turn with minimal turbulence losses to create strong circulatory flow patterns on the outside of the vessel.

4.2. Number of Tuyeres

The impact of increasing the number of tuyeres from 2 to 3 was also shown to be significant in Section 1.3. When the flow is divided between multiple tuyeres, the plumes are weakened considerably and the amount of turbulence losses at the free surface is reduced accordingly. An increase in the number of tuyeres can therefore reduce the aspect ratio required for minimal turbulence losses at the surface.

This implies that a more practical aspect ratio of 1 will also provide improved mixing efficiency when more than two tuyeres are employed. The question then arises on where to place these additional tuyeres. Incorrect tuyere placement can result in serious conflicts between the various plumes and the recirculating flow patterns.

Tuyeres should therefore be positioned in a manner which allows sufficient space between the downwards recirculating flows and the rising plumes. From this standpoint, asymmetrical systems are the only alternative for multiple tuyere setups. These setups will result in upwards flow on one side of the ladle and downwards flow on the other, causing a minimal amount of flow pattern interference.

The experimental results from the three tuyere experiment in Section 1.2 can be used as a guide for the amount of eccentricity required. The angle within which the tuyeres were positioned had a very small amount of impact on the mixing efficiency achieved, but did show that the mixing quantity is reduced slightly when the angle approaches 180°. The tuyeres should therefore be equally spaced within an angle of 150° or less.

The distance from the ladle centre at which these tuyeres are positioned is highly influential. Tuyere placements near the centre of the ladle tend to join together to form one strong plume which creates larger turbulence losses at the surface. Additionally, these setups convert the axial momentum in the plume to radial momentum in all directions at the plume eye. The large area over which the momentum is distributed creates very weak circulatory flows. These weakened downward flows are also forced to pass quite close to the rising plumes, thereby losing all of their momentum to flow impediment before they can reach the lower regions of the ladle. These effects are illustrated in the experiment with $R = 0.217$ and $\theta = 110$ reported in Section 1.2.

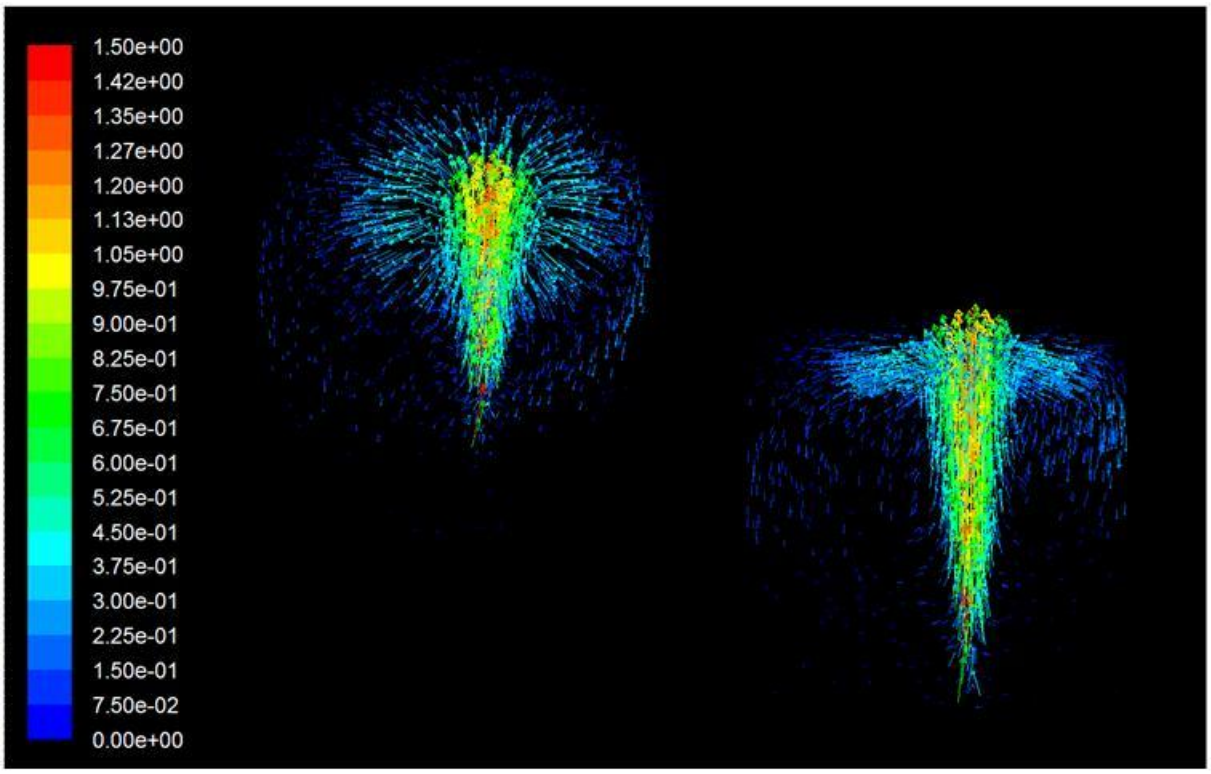

Figure 133: Flow velocities resulting from three tuyeres positioned close to the ladle centre.

In contrast to the poor flows displayed in Figure 133, tuyeres positioned closer towards the wall create strong circulatory flow patterns throughout the ladle. These flows are illustrated with the $R = 0.783$ and $\theta = 110$ experimental run reported in Section 1.2.

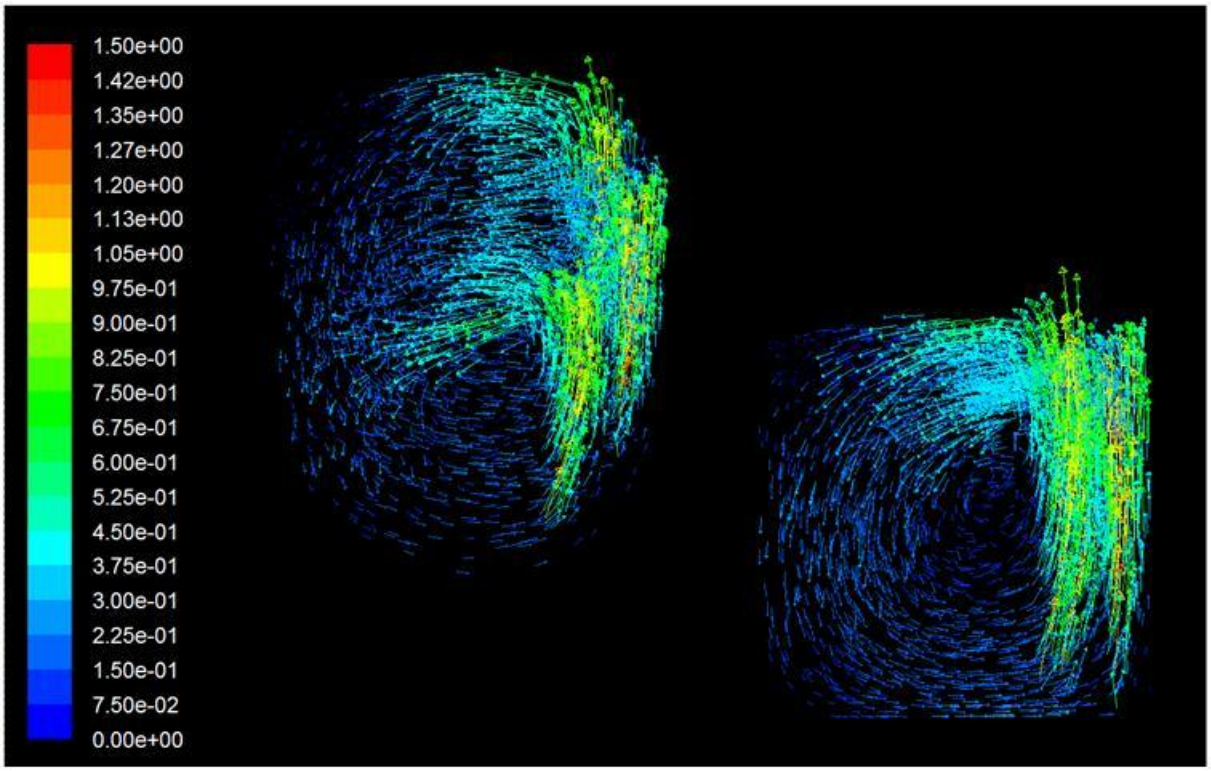

Figure 134: Flow velocities resulting from three tuyeres positioned close to the ladle wall.

Figure 134 shows that the three plumes stay separate, channel radial momentum only to the left hand side and causes downward recirculating flow patterns which are far removed from the rising plumes. These three improvements amount to a substantial increase on the flow patterns displayed in Figure 133.

Chapter XI:1 showed that the highest quantity and quality of mixing can be attained when tuyeres are positioned at a normalized radius of 0.6 around the centre point of the ladle floor. It is therefore recommended that multiple tuyeres be positioned within an angle of 150° on a normalized radius of 0.6. The ideal number of these tuyeres will depend on the aspect ratio employed. Further experimentation is required in this regard.

4.3. Modelling Improvements

The design guidelines provided above were largely derived from knowledge of the turbulence characteristics within the plume eye. Chapter IX:4.1 has concluded, however, that substantial improvements are still required in turbulence modelling within the plume and especially the plume eye. The present model does not give an accurate account of turbulence in this very important region and can therefore only provide general directions for ladle design. Further development of generalized models for turbulence modulation by the bubbles and increased turbulence kinetic energy dissipation rates in the plume eye is required before the model can safely be used to direct the ladle design process.

CHAPTER XII:
RESULTS & DISCUSSION PART 5:
SURFACE WAVE FORMS

> *You can't stop the waves, but you can learn to surf.*
> ***- Jon Kabat-Zinn***

Surface wave formation is currently avoided in gas stirred ladle operation for fear of melt spillage and vessel vibration. Various studies have indicated, however, that these swirling motions constitute an additional mixing mechanism and can be highly beneficial to mixing.

This knowledge has been within the scientific community for quite some time, and the fact that the steelmaking industry has not learnt to surf yet indicates that the cons still outweigh the pros. Drawbacks of accommodating swirl include:

- Safety hazard
- New design
    - Some mechanism for initiating the wave
    - Central tuyere
    - New operating procedure
- Increased vessel vibration
- Increased refractory wear
- Increased heat losses

When these drawbacks are considered, the benefit of surface wave formation would have to be quite dramatic for it to become feasible on a large scale. This chapter aims to firstly understand why surface wave formation occurs and also why it is beneficial for mixing. After this has been accomplished, some experimental results will evaluate the feasibility of designing a gas stirred ladle that functions with the aid of surface wave formation.

1. Surface Wave Formation

Wave formation sometimes spontaneously occurs on the surface of gas agitated baths. This spontaneous wave formation is the result of surface oscillations caused by the quasi periodical arrival of bubbles to the surface (17). Two types of wave forms exist: a side-to-side motion referred to as sloshing and a circulatory motion called swirling.

1.1. SLOSHING

Schwarz (73) completed an insightful study into the mechanism of side-to-side sloshing in gas stirred baths. The wave motion was described as a result of the resonance between the natural motion of the plume and the natural sloshing motion of the bath.

This interaction between the plume and the surface wave was studied in a numerical experiment on the 2.1 m ladle employed in Chapter X:1. The outputs from this experiment will be used to explain the sloshing mechanism according to Schwarz (73).

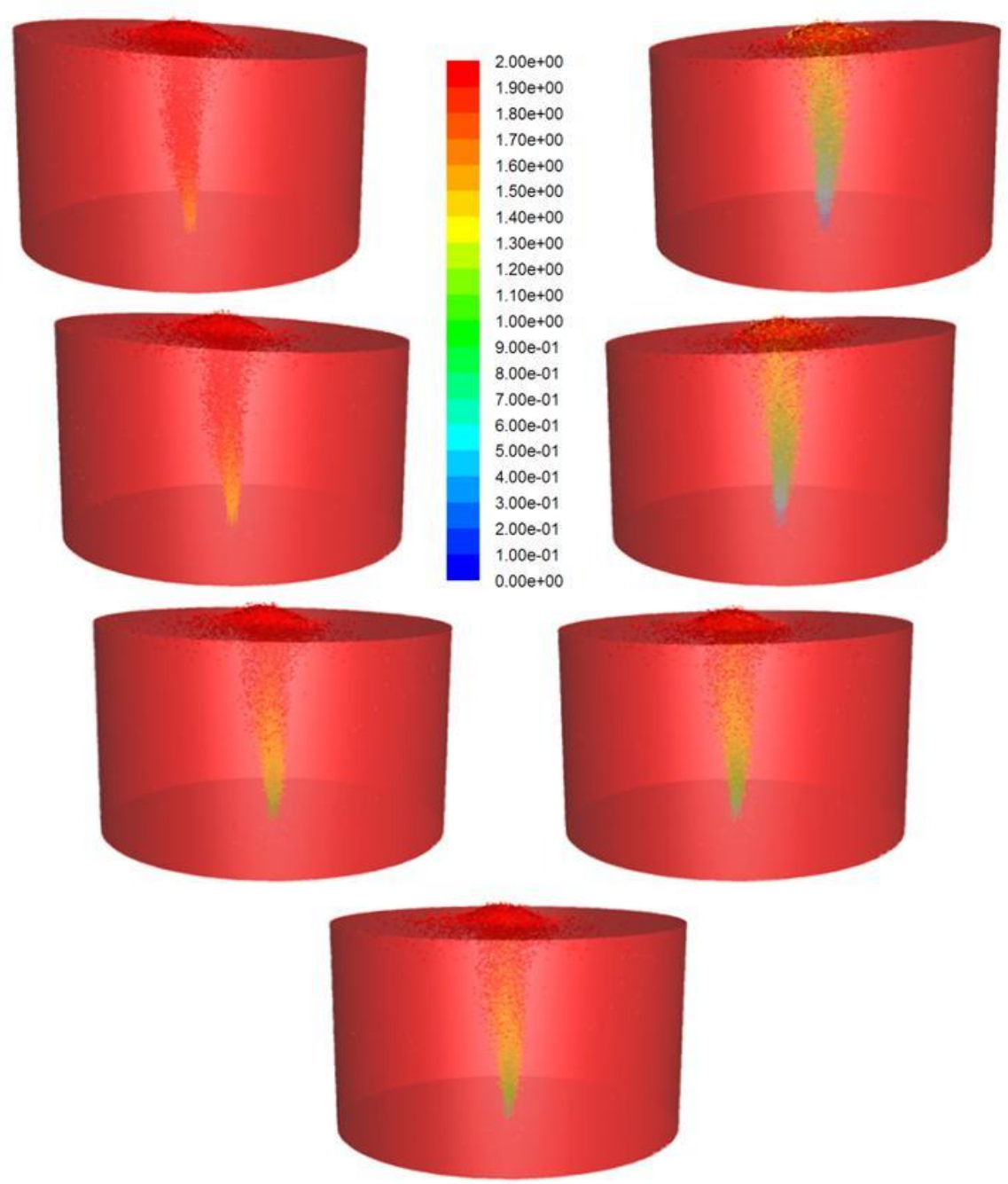

Figure 135: Interaction between the rising bubble plume and the surface wave form. The plume is coloured by the particle residence time.

Figure 135 is meant to be viewed from the top left to the bottom and finally to the top right. It starts with the surface wave at its maximum amplitude to the left. The plume can be seen to supply momentum to the left hand side of the ladle, thereby reinforcing the sloshing motion. As the wave sloshes back towards the right, the bulk liquid within the melt also moves from the left to the right, especially near the bottom of the vessel. The bottom of the plume is then moved to the right (the yellow particles in Figure 135) and starts to supply momentum to the right hand side of the ladle. The kinetic energy transferred from the plume then combines with the kinetic energy converted from the potential energy of the left hand surface deformation to deform the right hand side of the melt even further.

The resonance between the plume and the free surface wave form is dependent on the rise time of the bubbles and on the period of the swirl motion. Figure 135 shows that the yellow particles are injected when the maximum amplitude is reached on the left and just start to exit when the maximum amplitude is reached on the right. These two points are exactly one half of a period apart.

The fact that the yellow particles have not exited the melt by the time the right hand maximum is reached presents a problem in that they still exert a force which now works against the restoring force of the natural surface wave. The yellow particles now start to damp the surface wave formation.

For this reason, Schwarz (73) proposes that a sloshing motion will be sustained if the bubble rise time is on or just below one half of the surface wave period. This will ensure that the bubble will reinforce the natural wave formation for the majority of its rise and exit the melt before it can start to inhibit the sloshing motion.

Schwarz (73) identifies the optimal bubble rising time over which resonance between the plume and the wave will occur as being between one quarter and one half of the wave period. This criterion immediately creates a problem for application to full scale gas stirred ladles. Since the period of surface waves in melts is typically around 2 s and the rise velocity of bubbles is typically around 1.5 m/s, the melt height required for a resonating surface wave is between 0.75 and 1.5 m. Industrial ladles are typically in the range of 2.5 to 4 m high, implying that the side-to-side surface wave will not be maintained.

1.2. SWIRLING

The circulatory swirl motion can be seen as the sum of two non-rotating waves at right angles and 90° out of phase (73). Such waves are only possible in centrically stirred vessels where the plume is allowed to move in all directions, thereby creating waves on any mode. A row of tuyeres or an eccentric tuyere will always favour a single mode.

When a surface wave forms spontaneously in a centrically stirred bath it is always of the rotating kind. Schwarz (73) explains that no particular two dimensional wave is preferred to any other when centric stirring is employed. Since all possible resonating wave forms in such a system have the same frequency, energy can easily be transferred from one mode to another by means of non-linear coupling.

Since the swirling wave essentially comprises of two sloshing waves, the same limitation on ladle height is expected to hold. It is therefore expected that large scale ladles will not be able to sustain a swirling wave form.

2. Kinetic Energy Considerations

A sloshing or swirling wave formation is said to introduce another mixing mechanism to the melt. This implies that more kinetic energy is available do the mixing in a swirling vessel despite having a buoyant energy input identical to that of a non-swirling vessel.

Figure 136 displays this increase in kinetic energy holding capacity as a vessel is made to slosh at $t = 30$ s and swirls at $t = 85$ s. The sloshing was induced artificially by altering the direction of gravity in FLUENT 6.3 so as to simulate a 5° tilt of the vessel. This tilt was maintained for one quarter of the wave period, i.e. the time it takes for the wave to slosh from the centre to the side of the vessel. The gravity was subsequently restored, allowing the wave to slosh back. Swirl was initiated by repeating this procedure for another wave perpendicular to the first one and 90° out of phase.

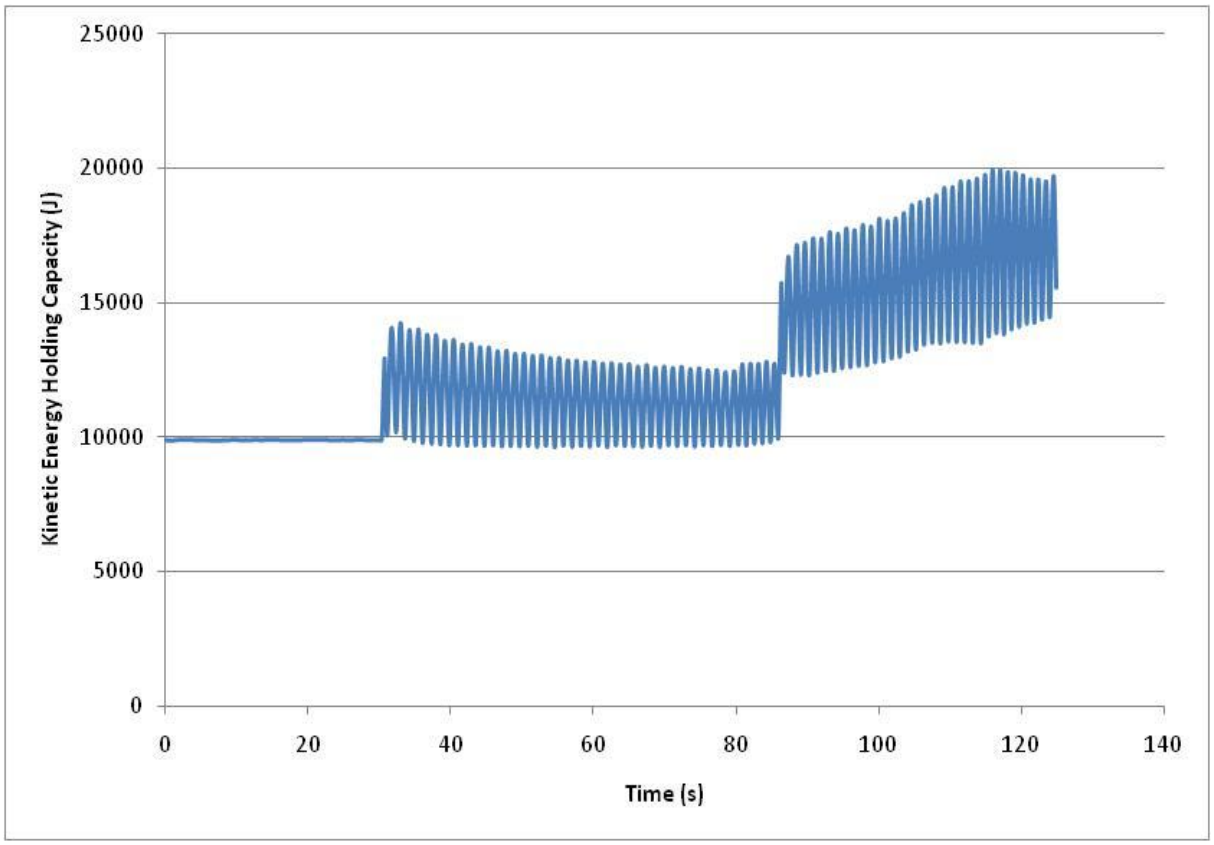

Figure 136: Kinetic energy holding capacity in a 2.1 m ladle (slosh at 30 s and swirl at 85 s).

Figure 136 shows only a marginal increase in kinetic energy holding capacity when the sloshing motion is present, but a substantial increase when swirling occurs. The reason for these improvements lies in the high conversion efficiency of potential energy in the deformed surface to kinetic energy in the melt.

Chapter VIII:3 revealed that the bubble plume actually is a very inefficient method of energy input. Only about 60% of the buoyant energy input is converted to melt kinetic energy, half of which is dissipated in the plume itself. On the other hand, the conversion efficiency of potential energy in the surface deformation to kinetic energy in the melt can be assumed to be 100%.

It was shown in Chapter VIII:4.1 that the ladle kinetic energy holding capacity can be improved if energy inputs result in smooth flow patterns losing a small percentage of mean kinetic energy to turbulence. The bubble plume is an example of an energy input mechanism resulting in large velocity gradients and high losses to turbulence, hence the large amount of dissipation within the plume itself. Kinetic energy received from the potential energy of the wave, however, is transferred over a large volume, keeping velocity gradients and turbulence losses to a bare minimum.

The amount of potential energy stored in a single sloshing wave is not sufficient to make a large improvement in kinetic energy holdup. Additionally, the bulk side-to-side motion induced by sloshing is not highly conducive to mixing since it simply translates the fluid from one side of the melt to the other and then back again.

Swirling, being the product of two sloshing waves, can store twice the amount of potential energy. The angular momentum induced throughout the melt also causes a substantial increase in kinetic energy holding capacity. This slow rotational flow causes motion in all areas of the melt at almost no additional losses to turbulence. Swirling motion also offers an improvement in mixing quality by translating the fluid around the perimeter of the vessel instead of just from side to side.

These effects can clearly be distinguished in Figure 136. When the sloshing is initiated, additional potential energy is introduced to the system by tilting the vessel. This additional energy is then converted to kinetic energy and back to potential energy again as the self-sustaining sloshing motion continues. The initiation of swirl is marked by a doubling in the amount of kinetic energy in the ladle as additional potential energy is introduced through tilting. A gradual rise in kinetic energy holding capacity then indicates the steady development of angular momentum in the ladle.

3. Feasibility of Swirl in Full Scale Ladles

Iguchi and co-workers (17; 26; 28) have conducted several studies on the swirl motion arising from the resonance between the surface wave and the bubble jet motion at centric gas injection. Contrary to the fundamental approach followed by Schwarz (73) where the bubble rising time must be just under one half of the wave period, these studies predict the occurrence of swirl by the aspect ratio of the vessel. It is shown that the swirling wave will be sustained at an aspect ratio between 0.3 and 1 (17).

The link between these two approaches arises from the wave period increasing with ladle diameter. When a vessel is enlarged while keeping the aspect ratio constant, the bubble rising time will increase with the increased height of the ladle and the wave period will increase with the ladle diameter. It is therefore possible that the swirl motion will persist in larger vessels with the correct aspect ratio.

The approach by Schwarz (73) is still preferred since it is derived from the fundamental interaction between the surface wave and the bubble plume. The aspect ratio criterion (17) is based on empirical observation.

Therefore, the possibility of attaining swirl in full scale ladles is a simple matter of estimating the period of the swirling wave form (T_s) and the average rising time of the bubbles (T_b). The feasibility of swirl can then be assessed by evaluating the ratio T_s/T_b. A ratio falling between 2 and 4 will indicate a situation where the swirling motion will be sustained.

3.1. Calculation of Parameters

3.1.1. The Wave Period

The wave period was initially described by Iguchi *et al*. (17):

$$\frac{(D/g)^{0.5}}{T_s} = 0.23 \qquad \text{Equation 123}$$

This simple relation tended to over-estimate the wave period in larger vessels and was later refined by Hiratsuka *et al.* (30),

$$\frac{(D/g)^{0.5}}{T_s} = \frac{0.918}{2\pi}\left(\frac{D}{D_{app}}\right)^{0.5} \times \left(3.68\tanh\left(3.68\frac{H}{D}\frac{D}{D_{app}}\right)\right)^{0.5} \qquad \text{Equation 124}$$

where

$$\frac{D}{D_{app}} = 1.25 - 0.25\frac{H}{D} \qquad \text{Equation 125}$$

This relationship was tested against the model in the validation exercise presented in Chapter VII:5 and showed a very satisfactory agreement. It can therefore be safely implemented to calculate the swirl period over a wide range of full scale gas stirred ladles.

3.1.2. The Bubble Rising Time

No generalized expressions could be found for the bubble rising time. Hence, an expression was derived from two expressions for the plume radius (r_p) and the volumetric flow capacity of the plume $(\dot{V}_p)$ (13).

$$r_p = 0.38 \cdot Q_1^{0.15} \cdot x_1^{0.62}$$ Equation 126

$$\dot{V}_p = 1.52 \cdot Q_1^{0.55} \cdot x_1^{1.13}$$ Equation 127

where

$$Q_1 = \frac{Q}{\rho_N} \cdot \frac{T}{T_N} \cdot \left(\frac{1.43}{1.43 + H} \right)$$ Equation 128

$$x_1 = (1.43 + H) \ln \left(\left(1 - \frac{x}{1.43 + H} \right)^{-1} \right)$$ Equation 129

The area of the plume can be estimated from Equation 126 under the assumption that the plume has a circular cross section. By dividing the volumetric flow capacity of the plume (m^3/s) with the plume cross sectional area (m^2), the average plume velocity (v_p) can be calculated at any height (x) within the plume.

The small scale VOF simulation in Chapter IV:4 showed that the bubble slip velocity is 0.35 m/s. Hence, the bubble velocity at any point in the plume can be estimated as the sum of the average plume velocity and the bubble slip velocity $(v_b = v_p + v_s)$.

To find the average rising time of the bubble, the height of plume was divided into 10 cm sections and the bubble velocity was computed at each of these sections. From the local bubble velocity, the time required for the bubble to traverse each of these 10 cm sections was calculated. The total bubble rising time could then simply be summed over all the sections.

The method was tested against the centric tuyere results in Chapter X:1 for melt heights of 3 m and 2.1 m. A bubble rising time of 2.1 and 1.4 s was predicted for the 3 and 2.1 m ladles respectively. These predictions are compared to model outputs below:

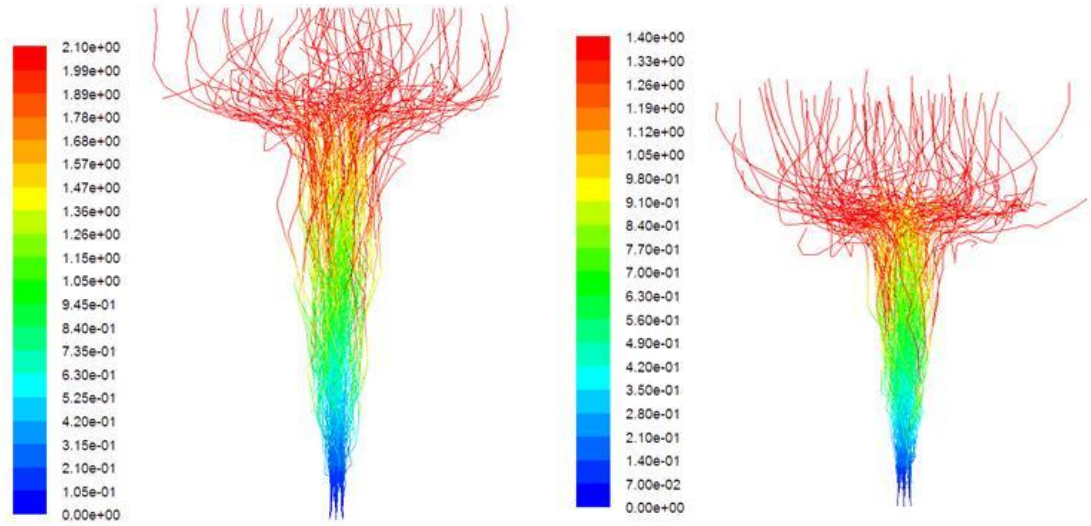

Figure 137: Particles tracks coloured by particle residence time for the 3 m (left) and the 2.1 m (right) ladle.

Figure 137 shows that the method for estimating bubble rise times agrees very well with model predictions. Closer scrutiny reveals, however, that the majority of the particles exit the melt slightly earlier than predicted. This is due to the omission of bubble induced turbulence in the full scale model. As described in Chapter III:5.4, this modelling assumption creates over-predictions of plume velocity, thereby shortening the bubble rise time.

3.2. Designed Experiment

Having obtained suitable expressions for T_s and T_b, an experiment was designed to quantify the effect of ladle height and diameter on the ratio of T_s/T_b which governs the resonance between the wave and the plume. The experiment was competed for a gas purging rate of 0.01 kg/s.

A central composite design was employed to yield the results shown below:

Table 36: Results from the surface wave feasibility experiment.

Run	H [m]	D [m]	T_s/T_b
1	1.50	1.50	1.51
2	1.50	3.50	2.22
3	3.50	1.50	0.67
4	3.50	3.50	0.84
5	1.09	2.50	2.70
6	3.91	2.50	0.67
7	2.50	1.09	0.86
8	2.50	3.91	1.28
9 (c)	2.50	2.50	1.07
10 (c)	2.50	2.50	1.07

Already it can be seen that the ratio T_s/T_b is rarely in the range of 2 to 4 required for resonance between the surface wave and the bubble plume. The response of T_s/T_b to changes in ladle height and diameter is better visualised in the contour plot displayed in Figure 138.

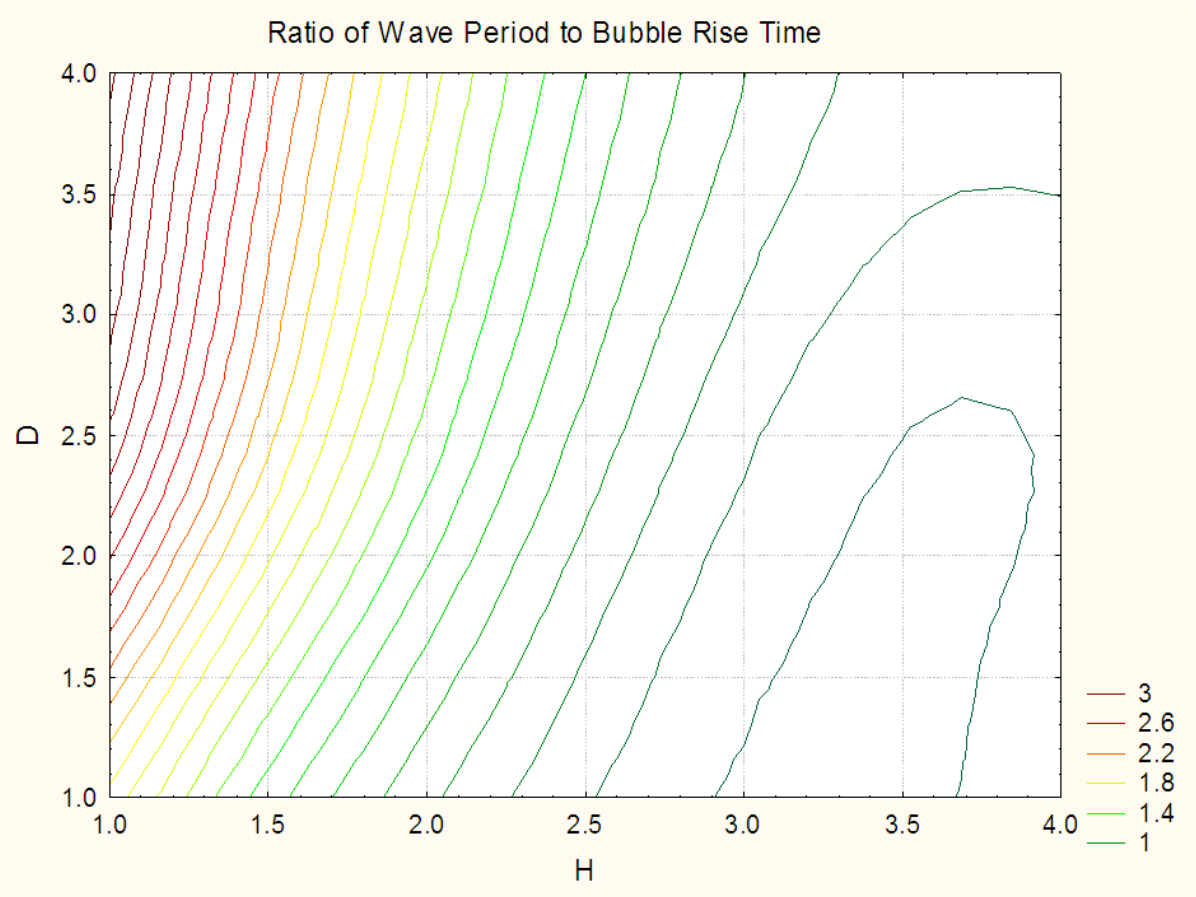

Figure 138: Spline contours of the response of T_s/T_b to changes in ladle height and diameter.

Figure 138 shows that the surface wave will not be sustained at any ladle height above 1.8 m even if the diameter is as large as 4 m. At a standard ladle diameter of 3 m, the melt height will have to be smaller than 1.6 m to sustain the surface wave. Even at this height, the wave will only just be sustained and the amplitude will be quite small. For a stronger wave form, T_s/T_b should approach a value of 3. In a standard 3 m ladle, this would mean a melt height of 1 m which is about one third of the normal capacity of the ladle.

It is therefore clear that resonating surface wave formation is not feasible in full scale gas stirred ladles unless some very low aspect ratios are employed.

4. Mixing Enhancements due to Swirl

Even though the aspect ratio required for a sustained swirling motion in full scale gas stirred ladles is very low, it is still possible to obtain. Therefore, the 2.1 m ladle ($D = 3.54$) used in Chapter X:1 was employed as a borderline case for resonating wave formation to investigate the mixing effects and general flow behaviour in the presence of swirl.

No slag layer was included in the simulation to save some computational time. The constant movement of the free surface required smaller time steps and more regular grid adaption. Additionally, the spread of tracer could not be solved on the frozen flow patters (Chapter VI:1.6) since the swirling motion is inherently transient.

The characteristic surface wave form could only be maintained for a limited time period of roughly 50 s, but the angular momentum created by the wave motion remained in the ladle for the remainder of the simulation.

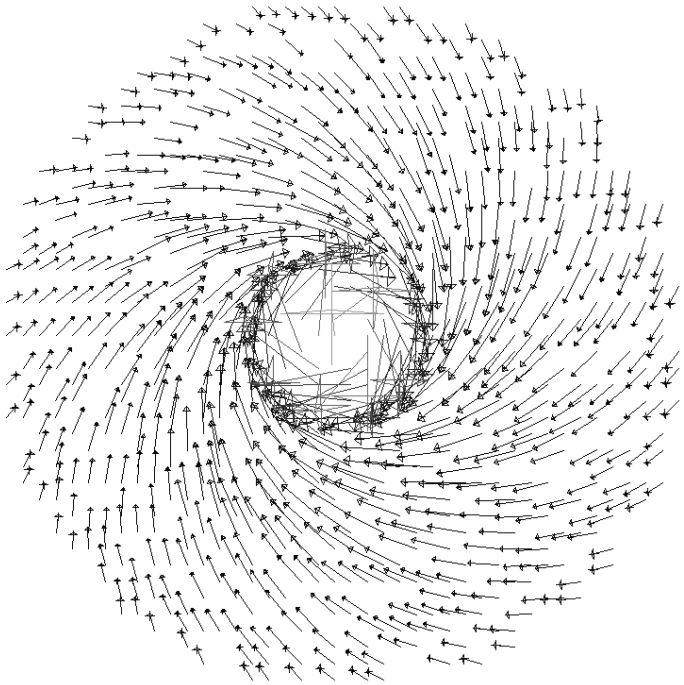

Figure 139: Angular velocities at a height of 1 m.

A gas flow rate of 0.01 kg/s gave the following results:

Table 37: Performance of the 2.1 m ladle with and without swirl.

Performance Variable	No swirl	Swirl
ε_{tot} [W]	2505	1895
E_{tot} [J]	9965	15586
$\tau_{95\%}$ [s]	81.5	62.0

The improvements offered by swirl in Table 37 are significant, but can easily be replicated and improved upon by a simple twin tuyere setup at a higher aspect ratio. Taller twin tuyere setups examined in Chapter XI:3 achieved kinetic energy holding capacities in access of 20 000 J and similar values of mixing time even in the presence of a slag layer. It can therefore be safely concluded that swirling is not a viable option in full scale gas stirred ladles and that taller, multiple tuyere systems will still provide the highest degree of mixing.

5. Sloshing in Taller Vessels

As shown in Chapter XI:3, larger aspect ratios can be highly beneficial towards mixing in gas stirred ladles. Therefore, a final test was performed to see whether sloshing can be maintained in a standard 3 by 3 m ladle. The resulting kinetic energy plot is reported below:

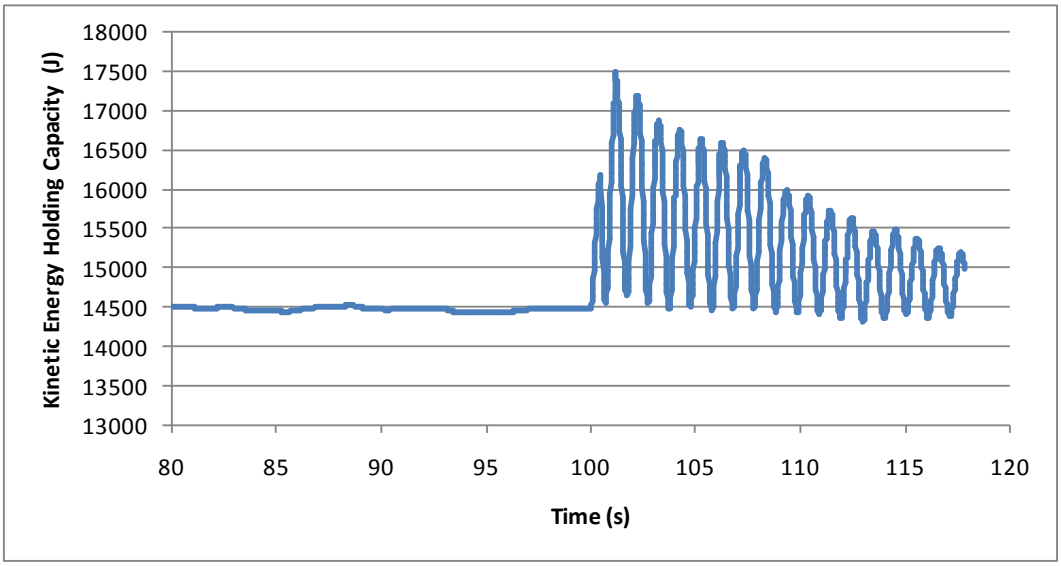

Figure 140: Kinetic energy within the taller ladles after the initiation of swirl at $t = 100$ s.

It is clear from Figure 140 that the sloshing wave is rapidly damped out. At this ladle setup, the ratio of T_s/T_b is approximately 1, meaning that the rising bubble plume will only impede the motion of the surface wave. Model predictions therefore agree with the theory in that resonating surface wave formation is not possible in ladles with a normal aspect ratio.

CHAPTER XIII:
GENERAL CONCLUSIONS

He did not arrive at this conclusion by the decent process of quiet, logical deduction, nor yet by the blinding flash of glorious intuition, but by the shoddy, untidy process halfway between the two by which one usually gets to know things.
- Margery Allingham

1. The Model

The broad study presented in this thesis has demonstrated the ability of mathematical modelling as a tool for conducting in-depth investigations into fluid flow and mixing phenomena in gas stirred ladles. Such a research tool can be of great value in process development of secondary steelmaking- and various other equally hostile processes where gas injection is utilized as the only feasible method of agitation.

The model described in Chapter V: Numerical Model Setup Part 2 has the capability of determining the mixing efficiency of a full scale gas stirred ladle with a high degree of numerical accuracy at very reasonable computational costs. The average simulation time of 2 days on a single 3 GHz processing core is very low when the size and complexity of the flow problem is considered.

At the present stage of development, however, the model is recommended for investigation on a comparative basis only. Chapter IX:4.3 lists the future developments required to attain complete quantitative agreement between modelled results and the physical process. Two aspects are of particular importance: the inclusion of bubble induced turbulence and the increased dissipation rate of turbulence kinetic energy at the free surface. A firm theoretical basis has been established for the former, but the latter is not well understood as of yet.

2. Kinetic Energy Budget

Kinetic energy budget considerations provide a new approach for evaluating fluid flow and mixing in gas stirred ladles. Mathematical modelling also provides the ideal platform for tracking and measuring the input and distribution of kinetic energy, something which is very hard to measure in physical experiments.

Factors governing the efficiency of kinetic energy input from the buoyant gas have been identified (Chapter VIII:2.1.2 and 2.3.2) and offer a useful fundamental understanding of how gas agitation affects motion in the bulk liquid. Chapter VIII:3 showed that the dissipation of turbulence kinetic energy to heat was the primary mechanism through which continuous phase kinetic energy was lost.

Gas injection is a fairly inefficient way of affecting motion in a liquid bath. Rising bubbles transfer only about 60% of their pressure energy to kinetic energy within the bulk liquid, dissipating the balance to the internal energy of the fluid. Due to high velocity gradients in the plume and the plume eye, more than half of the kinetic energy transferred from the bubbles is immediately lost to turbulence and subsequently dissipated to heat at the Kolmogorov microscale. Only about 25% of the total buoyant energy input is therefore available to drive the bulk liquid on the outside of the plume.

3. Performance Measures

In addition to the mixing time, three additional dependent variables were identified from kinetic energy considerations to describe the mixing efficiency: The kinetic energy transfer rate and efficiency as well as the kinetic energy holding capacity of the ladle. These variables give an indication of the quantity of mixing energy provided to, and utilized, by any specific ladle setup.

The mixing time is a measure of the quality of mixing achieved by a specific ladle setup and has been argued to control process performance only when dead zones are present in the ladle (Chapter IX:4.5). When the vessel is well mixed, however, the quantity of mixing will control process performance. Further research is required to identify a mixing time criterion below which the vessel can be considered to be well mixed.

4. Experimental Procedure

Designed experiments were implemented as a highly effective tool for quantifying and visualising the effects of various operating and design variables on mixing efficiency. Mathematical modelling produces high quality data since human, measurement or any other environmental errors are minimized. The high degree of repeatability in the numerically generated results requires no repetitions of the experiment, thereby keeping simulation time to a bare minimum.

5. Experimental Results

5.1. Operating Variables

The majority of operating variables (such as flow rate, melt temperature and surface pressure) influence only the strength of the flow patterns. These variables have a significant influence on mixing quantity, but only a limited effect on mixing quality. Their influence is limited to strengthening existing flow patterns, leaving any dead zones intact.

Flow pattern altering variables such as melt depth and the presence of a slag layer have the potential to affect much greater changes in both the quantity and quality of mixing. These variables influence the shape of flow pattern development and can therefore have a great effect on kinetic energy transfer efficiency and dissipation rates. Alterations in flow pattern shape can also create or remove dead zones in the ladle.

5.2. Design Variables

Design variables offer the largest scope for experimentation and present the opportunity to design the ladle for optimal energy efficiency. It was found that the largest improvements in kinetic energy holding capacity could be achieved by controlling the rate of dissipation in the plume and especially the plume eye. Factors that improve the efficiency of kinetic energy transfer from the buoyant gas mostly resulted in greater increases in turbulence kinetic energy dissipation than kinetic energy input.

Turbulence generation in the plume eye proved to hold the largest potential for reducing the rate of kinetic energy dissipation. Ladle design should therefore aim to reduce the intensity with which the plume impinges on the free surface, thereby reducing mean velocity gradients and subsequent turbulence generation in the plume eye.

This can be accomplished in two ways: Increasing the ladle height or increasing the number of tuyeres. A taller ladle will allow more distance over which the plume can disperse so that it meets the surface of the melt in a less concentrated manner. Multiple tuyeres will divide the total gas purge rate into a number of weaker plumes as opposed to a single stronger one. These weaker plumes will reduce turbulence losses both in the plume eye and within the plume itself.

Both these strategies must be implemented with care so as to avoid serious flow pattern interference. General guidelines are provided in Chapter XI:4.

5.3. Surface Wave Forms

Swirling motion is only achievable in a full scale ladle with a very small aspect ratio (less than 0.5). The performance improvements of such a ladle with added swirl was tested and found to be smaller than the benefits provided by other, much more practical design changes. The possibility of employing swirl as an extra mixing mechanism is therefore dismissed as an interesting, but impractical idea.

6. Future Work

Further developments are required to correctly account for the turbulence characteristics within the plume and plume eye. Sufficiently generalized models towards this end will enable the model to be safely implemented as a fast, efficient and cost effective design tool for optimising the performance of gas stirred ladles. Results from this study have given clear direction towards the optimal operating and design strategy and can be used to guide experimentation with the improved model.

The model setup can also be augmented to accommodate reacting species and thermal transport. These effects have been omitted from the present model based on literature recommendation, but can aid in facilitating the holistic understanding which is still lacking in many pyrometallurgical process operations. A model that can successfully simulate and visualize the complex interactions between the various physical processes involved can therefore be invaluable in the development of future metallurgical processes.

CHAPTER XIV:
APPENDICES PART 1:
NOMENCLATURE

The nomenclature is divided into three sections:

- List of symbols used in equations
- List of abbreviations used as factor names in designed experiments
- List of acronyms used in the text

1. SYMBOLS USED IN EQUATIONS

The section is split into an explanation of base symbols and subscripts. In each case, the Greek symbols will be presented first, followed by symbols from the modern alphabet.

Symbols with an over-bar (such as $\bar{u}$) refer to an averaged quantity, while symbols with an accent (u') refer to the fluctuating component. An arrow over-bar indicates a vector ($\vec{v}$).

1.1. ALPHABETICAL LISTING OF BASE SYMBOLS

α	Volume fraction
β	Thermal expansion coefficient [K^{-1}]
Γ^{ϕ}	Diffusion constant
δ	Delta function
ε	Specific rate of energy transfer [W/kg]
ε	Turbulence kinetic energy dissipation rate [m^2/s^3]
η	Efficiency
κ	Von Kármán constant
μ	Dynamic viscosity [Pa.s]
ν	Kinematic viscosity [m^2/s]
ρ	Density [kg/m^3]
σ	Prandtl number
σ	Surface tension (N/m)
τ	Mixing time [s]
τ	Shear stress [N/m^2]
τ	Time scale [s]
$\bar{\bar{\tau}}$	Stress tensor
υ	Velocity [m/s]
ω	Specific dissipation rate [s^{-1}]
ϕ	Flow variable
Ω	Mean rate of rotation tensor
A	Area [m^2]
AR	Aspect ratio
C	Concentration [ppm]
C	Constant or coefficient

D	Ladle diameter [m]
D	Mass diffusion coefficient [m^2/s]
d	Diameter [m]
E	Energy [J]
e	Rate of change in energy [W]
E_0	Eotvos number
F	Force [N]
G	Generation term
g	Gravitational acceleration [m/s^2]
H	Ladle or melt height [m]
h	Enthalpy [J/kg]
J	Diffusive flux [kg/m^2s]
k	Coefficient
k	Turbulence kinetic energy [m^2/s^2]
L	Length scale [m]
M	Mass [kg]
m	Mass flow rate [kg/s]
M_r	Molar mass [kg/mol]
N	Ensemble size
N	Number of
n	Spread parameter
P	Pressure [Pa]
P	Production term
p	Pressure [Pa]
Q	Flow Rate [kg/s, m^3/s if volumetric]
R	Ideal gas constant
R	Reaction source term
r	Radius [m]
Re	Reynolds number
$\bar{R}_{ij}$	Reynolds stress
S	Mean rate of strain tensor
S	Source term
s	Fluctuating rate of strain tensor
Sc	Schmidt number
SI	Solution instability
T	Integral time [s]
T	Period [s]
T	Temperature [K]
t	Time [s]
u	Velocity in x-direction [m/s]
V	Volume [m^3]
v	Velocity in y-direction [m/s]
w	Velocity in z-direction [m/s]
X	Fraction conversion or mixing
x	Distance in x-direction [m]
Y	Species or particle class mass fraction
Y_M	Dilation dissipation term
y	Distance in y-direction [m]
z	Distance in z-direction [m]

1.2. Alphabetical Listing of Subscripts

ε	Turbulence kinetic energy dissipation rate
μ	Viscosity
0	Surface
app	Apparent
ave	Average
B	Bubble
b	Buoyant
c	Continuous phase
c	Convergence
CV	Control volume
D	Drag
d	Diameter
d	Dissipation
E	Energy
e	Eddy
eff	Effective
emp	Empirical
exp	Expansion
f	Friction
g	Gas
i	Inert
i	The i'th species
j	The j'th species
k	kinetic energy (mean or turbulent)
L	Ladle
L	Lagrangian
l	Liquid
m	Mass or mass transfer
m	Molecular
min	Minimum
mod	Modified
N	Normal conditions or Normalized
q	The q'th phase
R	Residence
p	Particle
p	Plume
p	The p'th phase
s	Slip
s	Swirl
t	Turbulent
tot	Total
u	Velocity in x-direction
V	Volumetric
v	Velocity in y-direction
w	Velocity in z-direction
w	Wall
x	x-direction
y	y-direction
z	z-direction

2. Abbreviations used in Designed Experiments

θ	Separation angle between tuyeres
θ_L	Ladle wall expansion angle
μ_s	Slag layer viscosity
ρ_s	Slag layer density
AR	Ladle aspect ratio
$Discrete$	Discretization scheme
$Dist$	Gas flow rate distribution between tuyeres
$Grid$	Grid size
H	Melt height
H_s	Height of slag layer
M	Mass loading
M_L	Ladle mass when scaled
NOT	Discrete phase number of tries
$Refine$	Level of grid refinement
P	Surface pressure
Q	Gas flow rate
Q_{tot}	Total gas flow rate
R	Normalized distance from the floor centre point
T	Melt temperature

3. Acronyms Used in the Text

CBD	Computational bubble dynamics
CCD	Central composite design
CFD	Computational fluid dynamics
DNS	Direct numerical simulation
DPM	Discrete phase model
LES	Large eddy simulation
$RANS$	Reynolds-Averaged Navier-Stokes
RKE	Realizable k-ε
RSM	Reynolds stress model
SKE	Standard k-ε
VOF	Volume of fluid

CHAPTER XV:
APPENDICES PART 2:
USER DEFINED FUNCTIONS

Various user defined functions were implemented to complement the standard CFD code offered by FLUENT 6.3. The source codes and implementation of these UDF's are given below:

1. Pressure Reduction

UDF's were used to reduce the pressure in the small scale VOF simulation of a single bubble to simulate the bubble's rise along the hydrostatic pressure gradient. The source code affecting the pressure reduction at the outlet boundary is given below:

```
/************************************************************************
   unsteady1.c
   UDF for specifying a transient pressure profile boundary condition
************************************************************************/

#include "udf.h"

DEFINE_PROFILE(unsteady_pressure1, thread, position)
{
  face_t f;
  real t = CURRENT_TIME;

  begin_f_loop(f, thread)
    {
      F_PROFILE(f, thread, position) = 373764. - 108976*(t-2);
    }
  end_f_loop(f, thread)
}

/************************************************************************/
```

The UDF is compiled and then selected in the inlet/outlet boundary condition panel.

2. Drag Law

A custom drag law was used to simulate the drag force exerted by the rising bubbles on the continuous phase. The code specified below was used in the simulation of a small scale water model experiment.

```
/************************************************************************
   drag_law.c
   UDF for specifying the drag force acting on DPM particles
************************************************************************/
```

```
#include "udf.h"

DEFINE_DPM_DRAG(particle_drag_force,Re,p)
{
  real drag_force;
  real Eo;
  real Cd;
  real rho = 999;
  real ST = 0.072;

  Eo = 9.81*rho*pow(P_DIAM(p),2)/ST;
  Cd = 2./3.*pow((Eo/3),0.5);
  drag_force=18.*Re*Cd/24.;
  return (drag_force);
}

/************************************************************************/
```

The UDF is compiled and selected as the drag law in the discrete phase model panel.

3. Particle Shape, Growth and Breakup

The variable scalar properties of each particle (density, volume and diameter) were updated according to the specified growth and breakup laws. The source code is presented below:

```
/************************************************************************
   unsteady_1908.c
   UDF for specifying particle scalars with steady particle tracking
************************************************************************/

#include "udf.h"
#define BREAKUP_SMALL 1e-8
void assign_init_mass_to_tp_and_p(Tracked_Particle *tp, real mass_factor)
{
#if RP_NODE
Injection *I = tp->injection;
Particle *p = NULL;
#endif
P_INIT_MASS(tp) *= mass_factor;
#if RP_NODE
if (dpm_par.unsteady_tracking)
return;
loop(p, I->p)
if (p->part_id == tp->part_id)
P_INIT_MASS(p) *= mass_factor;
#endif
}

DEFINE_DPM_SCALAR_UPDATE(diameter_update,c,t,initialize,p)
{

real P;
real m = P_MASS(p);
real V;
real x;
real mass_factor = 0.5; /* drop breaks in half */

if (C_P(c,t) > 0)
```

```
{
      P = C_P(c,t)+RP_Get_Real("operating-pressure");
}

else
{
      P = RP_Get_Real("operating-pressure");
}

P_RHO(p) = 0.000002518*P;

V = m/P_RHO(p);

P_DIAM(p) = 8./5.*1.241*pow(V,0.33333);


if (dpm_par.unsteady_tracking)
return;
if (initialize)
{
p->user[0] = 0.;
}
else
{
if ((p->user[0] < BREAKUP_SMALL) && (P_DIAM(p) > 0.04))
{
P_DIAM(p) /= pow( 1/mass_factor, 0.33333 ); /* assume droplets break in
half */
P_MASS(p) *= mass_factor;
P_MASS0(p) *= mass_factor; /* necessary if 'interaction with continuous
phase' is enabled */

assign_init_mass_to_tp_and_p(p,mass_factor);
}
}
}

/************************************************************************/
```

The preceeding UDF was used for simulations employing steady particle tracking. For unsteady particle tracking, the breakup model had to be removed. Additionally, the particles were automatically transported directly to the escape boundary once they exited the melt. This UDF is presented below:

```
/************************************************************************
   unsteady_1908.c
   UDF for specifying particle scalars with unsteady particle tracking
************************************************************************/

#include "udf.h"

DEFINE_DPM_SCALAR_UPDATE(diameter_update,c,t,initialize,p)
{

real P;
real m = P_MASS(p);
real V;
real x;
real mass_factor = 0.5; /* drop breaks in half */
```

```
if (C_P(c,t) > 0)
{
      P = C_P(c,t)+RP_Get_Real("operating-pressure");
}

else
{
      P = RP_Get_Real("operating-pressure");
}

P_RHO(p) = 0.000002522*P;

V = m/P_RHO(p);

P_DIAM(p) = 8./5.*1.241*pow(V,0.33333);

if (C_R(c,t) < 1)
{
      P_POS(p)[1] = 5;
}
}

/************************************************************************/
```

Both UDF's in this section are compiled and activated as a user defined scalar in the UDF section of the discrete phase model panel.

4. Particle Source Terms

The turbulence source terms were supplied with the discrete phase particles according to the following UDF:

```
/************************************************************************
 plume-turb.c
 UDF for specifying turbulence source terms with the DPM
************************************************************************/

#include "udf.h"
#define C_DPMS_K(c,t)C_STORAGE_R(c,t,SV_K)
#define C_DPMS_D(c,t)C_STORAGE_R(c,t,SV_D)

real C1 = 17.5;                 /* main constant */
real height = 0.42;             /* vessel height */
real bottom_fraction = 0.2;     /* fraction below which k is damped */
real top_fraction = 0.85;       /* fraction above which e is augmented */
real bottom;
real top;
real Ce = 1.29;                 /* epsilon constant */
real Ct1 = 4;                   /* top epsilon constant */
real rho_U = 980;               /* upper density limit */
real rho_L = 3;                 /* lower density limit */
real Vslip;                     /* slip velocity */

DEFINE_DPM_SOURCE(dpm_source,c,t,S,strength,p)
{
      bottom = bottom_fraction*height;
    top = top_fraction*height;
    Vslip = P_VEL(p)[1]-C_V(c,t);
```

```
   if (C_R(c,t) >= rho_L)
   {

         if (P_POS(p)[1] < bottom)
         {
       C_DPMS_K(c,t) +=
P_POS(p)[1]/bottom*C1*9.81*C_R(c,t)*P_MASS(p)/P_RHO(p)*Vslip*strength*CURRE
NT_TIMESTEP;
       C_DPMS_D(c,t) +=
P_POS(p)[1]/bottom*Ce*C1*9.81*C_R(c,t)*P_MASS(p)/P_RHO(p)*Vslip*strength*CU
RRENT_TIMESTEP*C_D(c,t)/C_K(c,t);
       }
         if (P_POS(p)[1] > bottom)
       {
         C_DPMS_K(c,t) +=
C1*9.81*C_R(c,t)*P_MASS(p)/P_RHO(p)*Vslip*strength*CURRENT_TIMESTEP;
       C_DPMS_D(c,t) +=
Ce*C1*9.81*C_R(c,t)*P_MASS(p)/P_RHO(p)*Vslip*strength*CURRENT_TIMESTEP*C_D(
c,t)/C_K(c,t);
       }
   if (P_POS(p)[1] >=  top)
   {
       C_DPMS_D(c,t) += Ct1*strength*(P_POS(p)[1]/height-
top_fraction)*CURRENT_TIMESTEP;

   }
   }
}

/************************************************************************/
```

The UDF is compiled and activated as a source term in the UDF section of the discrete phase model panel.

CHAPTER XVI:
APPENDICES PART 3:
DESIGN OF EXPERIMENTS

If you need a statistician then you should design a better experiment.
- Ernest Rutherford

The physical design process behind each of the statistical experiments completed in the study is presented in this chapter. The statistical software package, Statistica 7.1, was used to design and analyze the designed experiments. No statisticians were employed.

1. Numerical Accuracy vs. Computational Time

Three sets of statistical experiments were designed and completed: two 2^3 full factorial designs and one three-factor rotatable central composite design.

1.1. Factorial Designs

The purpose of the factorial designs was to investigate the effect of the discretization scheme $(Discrete)$. Since this factor is represented by three distinct levels (first, second and third order) it cannot be included into a central composite design, and the best alternative is two successive two level factorials.

The factors of grid independence $(Grid)$ and location specific refinement $(Refine)$ were also included to obtain some initial effect estimates and to form an idea of the best location for the centre-point of the central composite design. The discrete phase number of tries (NOT) was held constant at a very high value of 1000.

The first full factorial will investigate the effect of changing Discrete from first to second order. The high and low levels for the factorial are presented in Table 38.

Table 38: Factor specifications for the first 2^3 full factorial design.

Factor	Low level	High level
$Discrete$	First order upwind	Second order upwind
$Grid$ (unrefined size)	25.2	20 cm
$Refine$ (velocity cut-off point)	0.35	0.2

In the case of Grid and Refine, the levels were chosen so that a change from low to high would cause the number of cells in the domain to double. The levels of Grid were chosen to result in refined cell sizes of 5cm and 6.3cm, which are higher than the expected 4cm for grid independence. This was

done to ensure that changes in Grid will also explain some variance against which to compare the variance explained by Discrete.

The second full factorial investigated a change in $Discrete$ from second to third order. $Grid$ and $Refine$ were represented at the same high and low levels as shown in Table 38, but $Discrete$ had the second order upwind scheme as the low level and the third order MUSCLE scheme as the high level.

1.2. Central Composite Design

From the results of the full factorial designs, the appropriate discretization scheme was selected for use in the central composite design. The calculated effects of $Grid$ and $Refine$ were also incorporated to specify the centre point of the CCD at $Grid = 16$ cm and $Refine = 0.3$ m/s. The NOT centre point was set to 500.

Table 39: Factor specifications for the rotatable central composite design.

Factor	StarLow (-1.6818)	Low (-1)	Centre (0)	High (1)	StarHigh (1.6818)
$Grid$ [cm]	23.60	20.16	16	12.70	10.85
$Refine$ [m/s]	0.51	0.4	0.3	0.2	0.15
NOT	78	168	500	1500	3172

The levels were specified according to the following formula:

$$V = V_c \times a^c \qquad \text{Equation 130}$$

Here, V is the parameter being varied (the number of cells in the domain for $Grid$ and $Refine$ and the number of tries for NOT). V_c is the value of that parameter chosen for the centre point, a is a appropriate constant for each factor (2 for $Grid$, 1.5 for $Refine$ and 3 for NOT) and c is the coded variable for the levels (-1.6818, -1, 0, 1, 1.6818). Equation 130 ensures an increase in accuracy and computational time as the levels are changed from low to high.

2. Buoyant Energy Input

A 2^{4-1} fractional factorial design was used to estimate the primary effects of gas flow rate (Q), melt depth H, melt temperature T and surface pressure P.

Factors were chosen so that the difference in buoyant energy input (Equation 119) brought about by changing each factor from low to high would be close to identical. This criterion led to the level specifications shown in Table 40.

Table 40: Factor specifications for the 2^{4-1} fractional factorial design.

Factor	Low level	High level
Q [kg/s]	0.008	0.01
H [m]	2.1	3
T [K]	1820	2275
P [atm]	1	0.7

The 3 m high vessel had a diameter of 3 m, while the 2.1 m vessel had its diameter raised to 3.58 m to keep the mass of steel constant.

3. Industrial Ladle

3.1. Gas Flow Rate and Distribution

The CCD was designed for rotatability in the two factors of total flow rate (Q_{tot}) and gas flow rate distribution between the two tuyeres $(Dist)$.

Values of Q_{tot} were chosen to be scattered around the normal operating point of 200 Nl/min. A value of $Q_{tot} = 0.01$ kg/s (187.5 Nl/min) was chosen for the centre point. The spread of the levels was estimated so that the Q_{tot} would explain a significant amount of variance, but not overwhelm any variance explained by $Dist$.

Values of $Dist$ were specified so that the tuyere receiving the lower flow rate would receive a maximum of 50% and a minimum of 0% of the flow. These criteria resulted in the experimental design shown below:

Table 41: Factor specifications for the rotatable central composite design.

Factor	StarLow (-1.4142)	Low (-1)	Centre (0)	High (1)	StarHigh (1.4142)
Q_{tot} [kg/s]	0.0058	0.007	0.01	0.13	0.0142
$Dist$ [fraction]	0	0.07	0.25	0.43	0.5

3.2. Mass Loading and Slag Parameters

A 2^{4-1} fractional factorial design was completed to evaluate the operating variables of mass loading (M) together with slag density (ρ_s), viscosity (μ_s) and depth (H_s).

Factor levels were chosen at estimated maximum and minimum values around the normal operating conditions of $M = 175$ ton, $\mu_s = 0.04$ Pa.s $\rho_s = 2600$ kg/m^3 and $H_s = 0.2$ m. The factor level settings are specified in Table 42.

Table 42: Factor specifications for the 2^{4-1} fractional factorial design.

Factor	Low level	High level
M [ton]	150	185
ρ_s [kg/m^3]	2000	4000
μ_s [Pa.s]	0.02	0.06
H_s [m]	0.1	0.4

4. Tuyere Setup

The two central composite designs investigating tuyere setup varied tuyere positioning according to normalized distance from the floor centre (R) and angle between tuyeres (θ). In the design investigating the effects of three tuyeres, the third tuyere was placed in an equiangular fashion between the initial two tuyeres. Factors levels were specified as follows:

Table 43: Factor specifications for the rotatable central composite design.

Factor	StarLow (-1.4142)	Low (-1)	Centre (0)	High (1)	StarHigh (1.4142)
R [fraction]	0.217	0.3	0.5	0.7	0.783
θ [degrees]	40	60.5	110	159.5	180

The level specifications for R were set so that the effect could be studied over the widest possible range without being so low as to simulate a single tuyere at the centre of the vessel or so high that the entire plume rise is against the ladle wall. The levels for θ were specified so that the high level would be set at 180^o and the low level would be high enough to maintain two separate tuyeres.

5. Ladle Geometry

The factors of ladle capacity (M_L), aspect ratio (AR) and wall angle (θ_L) were investigated in a central composite design. The centre point of the design was chosen to mirror a fairly common ladle design with $M_L = 150$ t, $AR = 1$ and $\theta_L = 5^0$. Levels were specified to cover the maximum range that would be believable in ladle design as shown below:

Table 44: Factor specifications for the rotatable central composite design.

Factor	StarLow (-1.6818)	Low (-1)	Centre (0)	High (1)	StarHigh (1.4142)
M_L [t]	65.9	100	150	200	234.1
AR	0.5	0.703	1	1.297	1.5
θ_L [degrees]	-3.41	0	5	10	13.41

Geometries were created from the knowledge of the ladle height (H) as well as the top R_T and bottom R_B radii. These three parameters were obtained through the simultaneous solution of three equations describing the geometry.

The volume of a frustum of a cone is given by Equation 131:

$$V = \frac{\pi H}{3}\left(R_T^2 + R_T R_B + R_B^2\right)$$ Equation 131

The top radius was related to the bottom radius as follows:

$$R_T = R_B + H\tan\left(\theta_L\right)$$ Equation 132

The aspect ratio was approximated as the ratio of the height to the vessel centre diameter.

$$AR = \frac{H}{\left(R_T + R_B\right)}$$ Equation 133

CHAPTER XVII:
APPENDICES PART 4:
ANOVA TABLES

Statistics are like bikinis.
What they reveal is suggestive, but what they conceal is vital.
- Aaron Levenstein

To ensure that all is bared, the ANOVA results from all experiments are given below as generated by Statistica 7.1.

1. Numerical Accuracy vs. Computational Time

1.1. Factorial Designs

1.1.1. First vs. Second Order Discretization

Table 45: ANOVA table listing primary factor and two-way interaction effects on the average velocity.

ANOVA; Var.:v; R-sqr=.99738; Adj:.98166 (1st-2nd.sta) 2**(3-0) design; MS Residual=.0000031 DV: v

	SS	df	MS	F	p
(1)Size	0.000028	1	0.000028	9.0000	0.204833
(2)Refine	0.000015	1	0.000015	4.8400	0.271599
(3)Discrete	0.001128	1	0.001128	361.0000	0.033475
1 by 2	0.000003	1	0.000003	1.0000	0.500000
1 by 3	0.000015	1	0.000015	4.8400	0.271599
2 by 3	0.000000	1	0.000000	0.0400	0.874334
Error	0.000003	1	0.000003		
Total SS	0.001193	7			

Table 46: ANOVA table listing primary factor and two-way interaction effects on the average turbulence kinetic energy.

ANOVA; Var.:k; R-sqr=.99961; Adj:.99726 (1st-2nd.sta) 2**(3-0) design; MS Residual=0 DV: k					
	SS	**df**	**MS**	**F**	**p**
(1)Size	0.000001	1	0.000001	18.778	0.144385
(2)Refine	0.000001	1	0.000001	32.111	0.111200
(3)Discrete	0.000111	1	0.000111	2466.778	0.012816
1 by 2	0.000000	1	0.000000	1.000	0.500000
1 by 3	0.000001	1	0.000001	13.444	0.169501
2 by 3	0.000001	1	0.000001	18.778	0.144385
Error	0.000000	1	0.000000		
Total SS	0.000115	7			

1.1.2. Second vs. Third Order Discretization

Table 47: ANOVA table listing primary factor effects on the average velocity.

ANOVA; Var.:v; R-sqr=.94477; Adj:.90334 (2nd-3rd.sta) 2**(3-0) design; MS Residual=.0000024 DV: v					
	SS	**df**	**MS**	**F**	**p**
(1)Size	0.000113	1	0.000113	47.36842	0.002336
(2)Refine	0.000018	1	0.000018	7.57895	0.051217
(3)Discrete	0.000032	1	0.000032	13.47368	0.021379
Error	0.000009	4	0.000002		
Total SS	0.000172	7			

Table 48: ANOVA table listing primary factor effects on the average turbulence kinetic energy.

ANOVA; Var.:k; R-sqr=.94674; Adj:.90679 (2nd-3rd.sta) 2**(3-0) design; MS Residual=.0000001 DV: k					
	SS	**df**	**MS**	**F**	**p**
(1)Size	0.000003	1	0.000003	63.43902	0.001346
(2)Refine	0.000000	1	0.000000	7.04878	0.056688
(3)Discrete	0.000000	1	0.000000	0.60976	0.478509
Error	0.000000	4	0.000000		
Total SS	0.000004	7			

1.2. Central Composite Design

Table 49:ANOVA table listing factor effects on simulation time.

ANOVA; Var.:Time; R-sqr=.92606; Adj:.81514 (CCD.sta) 3 factors, 1 Blocks, 16 Runs; MS Residual=3083983. DV: Time					
	SS	**df**	**MS**	**F**	**p**
(1)Grid (L)	95121947	1	95121947	30.84386	0.001441
Grid (Q)	10794942	1	10794942	3.50032	0.110538
(2)Refine (L)	86104399	1	86104399	27.91987	0.001858
Refine (Q)	15492690	1	15492690	5.02360	0.066225
(3)NOT (L)	80016	1	80016	0.02595	0.877320
NOT (Q)	2435342	1	2435342	0.78967	0.408409
1L by 2L	31193151	1	31193151	10.11457	0.019068
1L by 3L	19900	1	19900	0.00645	0.938588
2L by 3L	54946	1	54946	0.01782	0.898179
Error	18503898	6	3083983		
Total SS	250240893	15			

Table 50: ANOVA table listing factor effects on the average velocity.

ANOVA; Var.:v; R-sqr=.91938; Adj:.79846 (CCD.sta) 3 factors, 1 Blocks, 16 Runs; MS Residual=.0000053 DV: v					
	SS	**df**	**MS**	**F**	**p**
(1)Grid (L)	0.000263	1	0.000263	49.64307	0.000409
Grid (Q)	0.000015	1	0.000015	2.75781	0.147847
(2)Refine (L)	0.000027	1	0.000027	5.16194	0.063494
Refine (Q)	0.000011	1	0.000011	2.03580	0.203535
(3)NOT (L)	0.000000	1	0.000000	0.02404	0.881879
NOT (Q)	0.000000	1	0.000000	0.00056	0.981862
1L by 2L	0.000045	1	0.000045	8.52407	0.026645
1L by 3L	0.000000	1	0.000000	0.02361	0.882913
2L by 3L	0.000003	1	0.000003	0.59031	0.471447
Error	0.000032	6	0.000005		
Total SS	0.000394	15			

Table 51: ANOVA table listing factor effects on the average turbulence kinetic energy.

ANOVA; Var.:k; R-sqr=.94306; Adj:.85764 (CCD.sta) 3 factors, 1 Blocks, 16 Runs; MS Residual=.0000001 DV: k					
	SS	**df**	**MS**	**F**	**p**
(1)Grid (L)	0.000005	1	0.000005	66.87939	0.000180
Grid (Q)	0.000001	1	0.000001	15.07075	0.008151
(2)Refine (L)	0.000001	1	0.000001	11.09737	0.015782
Refine (Q)	0.000000	1	0.000000	0.05601	0.820785
(3)NOT (L)	0.000000	1	0.000000	0.31410	0.595468
NOT (Q)	0.000000	1	0.000000	0.88383	0.383444
1L by 2L	0.000000	1	0.000000	1.66094	0.244935
1L by 3L	0.000000	1	0.000000	0.00000	1.000000
2L by 3L	0.000000	1	0.000000	0.06644	0.805209
Error	0.000000	6	0.000000		
Total SS	0.000008	15			

Table 52: ANOVA table listing factor effects on the amplitude of oscillation.

ANOVA; Var.:Amplitude; R-sqr=.86107; Adj:.65267 (CCD.sta) 3 factors, 1 Blocks, 16 Runs; MS Residual=.036576 DV: Amplitude					
	SS	**df**	**MS**	**F**	**p**
(1)Grid (L)	0.594558	1	0.594558	16.25542	0.006866
Grid (Q)	0.006017	1	0.006017	0.16450	0.699115
(2)Refine (L)	0.240126	1	0.240126	6.56513	0.042779
Refine (Q)	0.020459	1	0.020459	0.55936	0.482791
(3)NOT (L)	0.244361	1	0.244361	6.68092	0.041504
NOT (Q)	0.034291	1	0.034291	0.93753	0.370307
1L by 2L	0.135200	1	0.135200	3.69642	0.102894
1L by 3L	0.012800	1	0.012800	0.34996	0.575732
2L by 3L	0.033800	1	0.033800	0.92410	0.373523
Error	0.219456	6	0.036576		
Total SS	1.579594	15			

2. Buoyant Energy Input

Table 53: ANOVA table listing primary factor effects on the kinetic energy transfer rate.

ANOVA; Var.:W; R-sqr=.97797; Adj:.94859 (THE_1.sta) 4 factors at two levels; MS Residual=25913.79
DV: W

	SS	df	MS	F	p
(1)Q	1069453	1	1069453	41.26965	0.007645
(2)T	1085601	1	1085601	41.89279	0.007484
(3)P	907878	1	907878	35.03455	0.009634
(4)H	387640	1	387640	14.95883	0.030575
Error	77741	3	25914		
Total SS	3528314	7			

Table 54: ANOVA table listing primary factor effects on the kinetic energy holding capacity.

ANOVA; Var.:J; R-sqr=.97508; Adj:.94186 (THE_1.sta) 4 factors at two levels; MS Residual=640735.8
DV: J

	SS	df	MS	F	p
(1)Q	8386560	1	8386560	13.08895	0.036302
(2)T	8374278	1	8374278	13.06978	0.036370
(3)P	6857956	1	6857956	10.70325	0.046721
(4)H	51597561	1	51597561	80.52861	0.002921
Error	1922207	3	640736		
Total SS	77138563	7			

Table 55: ANOVA table listing primary factor effects on the mixing time.

ANOVA; Var.:mt; R-sqr=.99631; Adj:.99139 (THE_1.sta) 4 factors at two levels; MS Residual=15.41667 DV: mt

	SS	df	MS	F	p
(1)Q	78.13	1	78.13	5.0676	0.109824
(2)T	28.12	1	28.12	1.8243	0.269647
(3)P	60.50	1	60.50	3.9243	0.141921
(4)H	12324.50	1	12324.50	799.4270	0.000097
Error	46.25	3	15.42		
Total SS	12537.50	7			

Table 56: ANOVA table listing primary factor effects on the specific rate of buoyant energy input.

ANOVA; Var.:be; R-sqr=.97049; Adj:.93114 (THE_1.sta) 4 factors at two levels; MS Residual=.0000034 DV: be

	SS	df	MS	F	p
(1)Q	0.000086	1	0.000086	25.52273	0.014962
(2)T	0.000086	1	0.000086	25.52273	0.014962
(3)P	0.000080	1	0.000080	23.80762	0.016456
(4)H	0.000080	1	0.000080	23.80762	0.016456
Error	0.000010	3	0.000003		
Total SS	0.000343	7			

Table 57: ANOVA table listing primary factor effects on the kinetic energy transfer efficiency.

ANOVA; Var.:Eff; R-sqr=.98191; Adj:.95779 (THE_1.sta) 4 factors at two levels; MS Residual=.360578 DV: Eff

	SS	df	MS	F	p
(1)Q	3.53916	1	3.53916	9.8152	0.051947
(2)T	4.26292	1	4.26292	11.8225	0.041285
(3)P	0.46879	1	0.46879	1.3001	0.336980
(4)H	50.44319	1	50.44319	139.8954	0.001299
Error	1.08173	3	0.36058		
Total SS	59.79579	7			

3. Industrial Ladle

3.1. Slag Layer Included

Table 58: ANOVA table listing factor effects on the kinetic energy transfer rate.

ANOVA; Var.:W; R-sqr=.98077; Adj:.95674 (real2.sta) 2 factors, 1 Blocks, 10 Runs; MS Residual=24953.44 DV: W

	SS	df	MS	F	p
(1)Flow (L)	4927154	1	4927154	197.4539	0.000149
Flow (Q)	40662	1	40662	1.6295	0.270845
(2)Dist (L)	71156	1	71156	2.8515	0.166556
Dist (Q)	8136	1	8136	0.3261	0.598543
1L by 2L	14042	1	14042	0.5627	0.494874
Error	99814	4	24953		
Total SS	5191042	9			

Table 59: ANOVA table listing factor effects on the kinetic energy holding capacity.

ANOVA; Var.:J; R-sqr=.97051; Adj:.93366 (real2.sta) 2 factors, 1 Blocks, 10 Runs; MS Residual=1200172. DV: J

	SS	df	MS	F	p
(1)Flow (L)	148297145	1	148297145	123.5632	0.000373
Flow (Q)	1161792	1	1161792	0.9680	0.380877
(2)Dist (L)	2632069	1	2632069	2.1931	0.212747
Dist (Q)	2981752	1	2981752	2.4844	0.190105
1L by 2L	54522	1	54522	0.0454	0.841640
Error	4800690	4	1200172		
Total SS	162814558	9			

Table 60: ANOVA table listing factor effects on the mixing time.

ANOVA; Var.:mt; R-sqr=.97137; Adj:.93558 (real2.sta) 2 factors, 1 Blocks, 10 Runs; MS Residual=6.119386 DV: mt

	SS	df	MS	F	p
(1)Flow (L)	542.7009	1	542.7009	88.68551	0.000709
Flow (Q)	81.3616	1	81.3616	13.29571	0.021842
(2)Dist (L)	170.8528	1	170.8528	27.91993	0.006154
Dist (Q)	76.6116	1	76.6116	12.51949	0.024050
1L by 2L	6.2500	1	6.2500	1.02134	0.369368
Error	24.4775	4	6.1194		
Total SS	854.9000	9			

Table 61: ANOVA table listing factor effects on the kinetic energy transfer efficiency.

ANOVA; Var.:Eff; R-sqr=.7305; Adj:.39362 (real2.sta) 2 factors, 1 Blocks, 10 Runs; MS Residual=3.153658 DV: Eff

	SS	df	MS	F	p
(1)Flow (L)	3.73115	1	3.73115	1.183117	0.337875
Flow (Q)	9.37024	1	9.37024	2.971229	0.159852
(2)Dist (L)	12.22268	1	12.22268	3.875716	0.120351
Dist (Q)	1.06695	1	1.06695	0.338321	0.592004
1L by 2L	2.13299	1	2.13299	0.676355	0.457043
Error	12.61463	4	3.15366		
Total SS	46.80700	9			

3.2. Slag Layer Excluded

Table 62: ANOVA table listing factor effects on the kinetic energy transfer rate.

ANOVA; Var.:W; R-sqr=.97609; Adj:.94621 (THE_2.sta) 2 factors, 1 Blocks, 10 Runs; MS Residual=37228.97 DV: W					
	SS	**df**	**MS**	**F**	**p**
(1)Flow (L)	5217064	1	5217064	140.1345	0.000292
Flow (Q)	46518	1	46518	1.2495	0.326248
(2)Dist (L)	60795	1	60795	1.6330	0.270409
Dist (Q)	767052	1	767052	20.6036	0.010504
1L by 2L	4290	1	4290	0.1152	0.751331
Error	148916	4	37229		
Total SS	6229348	9			

Table 63: ANOVA table listing factor effects on the kinetic energy holding capacity.

ANOVA; Var.:J; R-sqr=.99209; Adj:.98221 (THE_2.sta) 2 factors, 1 Blocks, 10 Runs; MS Residual=1041967. DV: J					
	SS	**df**	**MS**	**F**	**p**
(1)Flow (L)	276925705	1	276925705	265.7720	0.000083
Flow (Q)	5649596	1	5649596	5.4220	0.080382
(2)Dist (L)	199434085	1	199434085	191.4015	0.000158
Dist (Q)	17692884	1	17692884	16.9803	0.014604
1L by 2L	7417452	1	7417452	7.1187	0.055917
Error	4167869	4	1041967		
Total SS	527037426	9			

Table 64: ANOVA table listing factor effects on the mixing time.

ANOVA; Var.:mt; R-sqr=.97395; Adj:.9414 (THE_2.sta) 2 factors, 1 Blocks, 10 Runs; MS Residual=4.994904 DV: mt					
	SS	**df**	**MS**	**F**	**p**
(1)Flow (L)	615.7201	1	615.7201	123.2697	0.000374
Flow (Q)	66.4464	1	66.4464	13.3028	0.021823
(2)Dist (L)	2.1753	1	2.1753	0.4355	0.545368
Dist (Q)	13.0179	1	13.0179	2.6062	0.181745
1L by 2L	1.0000	1	1.0000	0.2002	0.677717
Error	19.9796	4	4.9949		
Total SS	767.1000	9			

Table 65: ANOVA table listing factor effects on the kinetic energy transfer efficiency.

ANOVA; Var.:Eff; R-sqr=.90749; Adj:.79185 (THE_2.sta) 2 factors, 1 Blocks, 10 Runs; MS Residual=5.022733 DV: Eff					
	SS	**df**	**MS**	**F**	**p**
(1)Flow (L)	17.4716	1	17.4716	3.47850	0.135602
Flow (Q)	4.6715	1	4.6715	0.93007	0.389458
(2)Dist (L)	11.0923	1	11.0923	2.20843	0.211450
Dist (Q)	155.3468	1	155.3468	30.92873	0.005119
1L by 2L	0.7806	1	0.7806	0.15541	0.713535
Error	20.0909	4	5.0227		
Total SS	217.1720	9			

3.3. Blocking Experiment

Table 66: ANOVA table listing factor effects on the kinetic energy transfer rate.

ANOVA; Var.:W; R-sqr=.95076; Adj:.92804 (THE_2a.sta) 2 factors, 2 Blocks, 20 Runs; MS Residual=43460.56 DV: W					
	SS	**df**	**MS**	**F**	**p**
Blocks	53976	1	53976	1.2420	0.285274
(1)Flow (L)	10142147	1	10142147	233.3644	0.000000
Flow (Q)	98	1	98	0.0023	0.962765
(2)Dist (L)	131747	1	131747	3.0314	0.105264
Dist (Q)	466593	1	466593	10.7360	0.006013
1L by 2L	16928	1	16928	0.3895	0.543358
Error	564987	13	43461		
Total SS	11474367	19			

Table 67: ANOVA table listing factor effects on the kinetic energy holding capacity.

ANOVA; Var.:J; R-sqr=.89183; Adj:.8419 (THE_2a.sta) 2 factors, 2 Blocks, 20 Runs; MS Residual=8203188. DV: J

	SS	df	MS	F	p
Blocks	296003568	1	296003568	36.08397	0.000044
(1)Flow (L)	415262088	1	415262088	50.62204	0.000008
Flow (Q)	5967657	1	5967657	0.72748	0.409141
(2)Dist (L)	123944304	1	123944304	15.10929	0.001871
Dist (Q)	17600636	1	17600636	2.14558	0.166743
1L by 2L	4371924	1	4371924	0.53295	0.478317
Error	106641440	13	8203188		
Total SS	985855552	19			

Table 68: ANOVA table listing factor effects on the mixing time.

ANOVA; Var.:mt; R-sqr=.79923; Adj:.70656 (THE_2a.sta) 2 factors, 2 Blocks, 20 Runs; MS Residual=33.22899 DV: mt

	SS	df	MS	F	p
Blocks	344.450	1	344.4500	10.36595	0.006709
(1)Flow (L)	954.418	1	954.4182	28.72246	0.000130
Flow (Q)	192.937	1	192.9375	5.80630	0.031512
(2)Dist (L)	179.842	1	179.8424	5.41221	0.036807
Dist (Q)	29.009	1	29.0089	0.87300	0.367157
1L by 2L	47.531	1	47.5313	1.43042	0.253056
Error	431.977	13	33.2290		
Total SS	2151.550	19			

Table 69: ANOVA table listing factor effects on the kinetic energy transfer efficiency.

ANOVA; Var.:Eff; R-sqr=.63734; Adj:.46997 (THE_2a.sta) 2 factors, 2 Blocks, 20 Runs; MS Residual=7.754599 DV: Eff

	SS	df	MS	F	p
Blocks	13.9977	1	13.99773	1.80509	0.202081
(1)Flow (L)	18.6753	1	18.67535	2.40829	0.144691
Flow (Q)	0.4048	1	0.40475	0.05220	0.822841
(2)Dist (L)	23.3013	1	23.30131	3.00484	0.106652
Dist (Q)	91.0811	1	91.08114	11.74543	0.004501
1L by 2L	2.7471	1	2.74711	0.35426	0.561932
Error	100.8098	13	7.75460		
Total SS	277.9768	19			

3.4. Mass Loading and Slag Parameters

Table 70: ANOVA table listing primary factor effects on the kinetic energy transfer rate.

ANOVA; Var.:W; R-sqr=.96483; Adj:.91795 (THE_3.sta) 2**(4-1) design; MS Residual=2249.833 DV: W

	SS	df	MS	F	p
(1)M	67712.0	1	67712.0	30.09645	0.011914
(2)SH	105800.0	1	105800.0	47.02571	0.006349
(3)Smu	722.0	1	722.0	0.32091	0.610671
(4)Srho	10952.0	1	10952.0	4.86792	0.114492
Error	6749.5	3	2249.8		
Total SS	191935.5	7			

Table 71: ANOVA table listing primary factor effects on the kinetic energy holding capacity.

ANOVA; Var.:J; R-sqr=.99474; Adj:.98773 (THE_3.sta) 2**(4-1) design; MS Residual=86155.17 DV: J

	SS	df	MS	F	p
(1)M	45744613	1	45744613	530.9561	0.000179
(2)SH	1818325	1	1818325	21.1052	0.019380
(3)Smu	3612	1	3612	0.0419	0.850859
(4)Srho	1313821	1	1313821	15.2495	0.029820
Error	258466	3	86155		
Total SS	49138836	7			

Table 72: ANOVA table listing primary factor effects on the mixing time.

ANOVA; Var.:mt; R-sqr=.99254; Adj:.98259 (THE_3.sta) 2**(4-1) design; MS Residual=3.136187 DV: mt

	SS	df	MS	F	p
(1)M	1232.774	1	1232.774	393.0804	0.000280
(2)SH	0.411	1	0.411	0.1310	0.741372
(3)Smu	0.485	1	0.485	0.1548	0.720288
(4)Srho	17.617	1	17.617	5.6173	0.098496
Error	9.409	3	3.136		
Total SS	1260.696	7			

Table 73: ANOVA table listing primary factor effects on the kinetic energy transfer efficiency.

ANOVA; Var.:Eff; R-sqr=.95737; Adj:.90053 (THE_3.sta) 2**(4-1) design; MS Residual=.925025 DV: Eff					
	SS	**df**	**MS**	**F**	**p**
(1)M	10.32250	1	10.32250	11.15916	0.044370
(2)SH	46.63312	1	46.63312	50.41283	0.005748
(3)Smu	0.24078	1	0.24078	0.26030	0.645081
(4)Srho	5.12728	1	5.12728	5.54286	0.099913
Error	2.77507	3	0.92502		
Total SS	65.09876	7			

4. Tuyere Setup

4.1. Two Tuyeres

Table 74: ANOVA table listing factor effects on the kinetic energy transfer rate.

ANOVA; Var.:W; R-sqr=.63205; Adj:.1721 (real4.sta) 2 factors, 1 Blocks, 10 Runs; MS Residual=3484.006 DV: W					
	SS	**df**	**MS**	**F**	**p**
(1)Dist (L)	8678.86	1	8678.86	2.491058	0.189635
Dist (Q)	21.87	1	21.87	0.006279	0.940650
(2)Angle (L)	184.24	1	184.24	0.052883	0.829403
Angle (Q)	95.16	1	95.16	0.027314	0.876749
1L by 2L	14884.00	1	14884.00	4.272094	0.107607
Error	13936.02	4	3484.01		
Total SS	37874.40	9			

Table 75: ANOVA table listing factor effects on the kinetic energy holding capacity.

ANOVA; Var.:J; R-sqr=.59948; Adj:.09883 (real4.sta) 2 factors, 1 Blocks, 10 Runs; MS Residual=4684978. DV: J					
	SS	**df**	**MS**	**F**	**p**
(1)Dist (L)	4197585	1	4197585	0.895967	0.397463
Dist (Q)	964167	1	964167	0.205800	0.673602
(2)Angle (L)	10472752	1	10472752	2.235390	0.209202
Angle (Q)	12990878	1	12990878	2.772879	0.171204
1L by 2L	1	1	1	0.000000	0.999653
Error	18739910	4	4684978		
Total SS	46789104	9			

Table 76: ANOVA table listing factor effects on the mixing time.

ANOVA; Var.:mt; R-sqr=.9703; Adj:.93318 (real4.sta) 2 factors, 1 Blocks, 10 Runs; MS Residual=159.2376 DV: mt					
	SS	**df**	**MS**	**F**	**p**
(1)Dist (L)	12411.72	1	12411.72	77.94463	0.000908
Dist (Q)	5844.61	1	5844.61	36.70371	0.003747
(2)Angle (L)	199.79	1	199.79	1.25468	0.325371
Angle (Q)	9.20	1	9.20	0.05778	0.821850
1L by 2L	784.00	1	784.00	4.92346	0.090724
Error	636.95	4	159.24		
Total SS	21446.88	9			

4.2. THREE TUYERES

Table 77: ANOVA table listing factor effects on the kinetic energy transfer rate.

ANOVA; Var.:W; R-sqr=.94365; Adj:.87322 (THE_4.sta) 2 factors, 1 Blocks, 10 Runs; MS Residual=30831. DV: W

	SS	df	MS	F	p
(1)Dist (L)	179237	1	179237	5.81352	0.073465
Dist (Q)	1228400	1	1228400	39.84300	0.003222
(2)Angle (L)	586031	1	586031	19.00784	0.012064
Angle (Q)	85645	1	85645	2.77788	0.170903
1L by 2L	30976	1	30976	1.00470	0.372894
Error	123324	4	30831		
Total SS	2188700	9			

Table 78: ANOVA table listing factor effects on the kinetic energy holding capacity.

ANOVA; Var.:J; R-sqr=.90465; Adj:.78546 (THE_4.sta) 2 factors, 1 Blocks, 10 Runs; MS Residual=4764628. DV: J

	SS	df	MS	F	p
(1)Dist (L)	78366108	1	78366108	16.44748	0.015405
Dist (Q)	78537103	1	78537103	16.48337	0.015349
(2)Angle (L)	15961598	1	15961598	3.35002	0.141177
Angle (Q)	19552679	1	19552679	4.10372	0.112755
1L by 2L	7477490	1	7477490	1.56938	0.278538
Error	19058510	4	4764628		
Total SS	199877469	9			

Table 79: ANOVA table listing factor effects on the mixing time.

ANOVA; Var.:mt; R-sqr=.95159; Adj:.89107 (THE_4.sta) 2 factors, 1 Blocks, 10 Runs; MS Residual=270.4936 DV: mt

	SS	df	MS	F	p
(1)Dist (L)	13361.19	1	13361.19	49.39560	0.002159
Dist (Q)	6321.88	1	6321.88	23.37163	0.008434
(2)Angle (L)	149.70	1	149.70	0.55344	0.498241
Angle (Q)	0.02	1	0.02	0.00007	0.993909
1L by 2L	0.25	1	0.25	0.00092	0.977203
Error	1081.97	4	270.49		
Total SS	22348.60	9			

4.3. Blocking Experiment

Table 80: ANOVA table listing factor effects on the kinetic energy transfer rate.

ANOVA; Var.:W; R-sqr=.6219; Adj:.44739 (THE_4a.sta) 2 factors, 2 Blocks, 20 Runs; MS Residual=89732.98 DV: W					
	SS	**df**	**MS**	**F**	**p**
Blocks	858637	1	858636.8	9.568798	0.008556
(1)Dist (L)	133398	1	133398.4	1.486615	0.244404
Dist (Q)	619394	1	619394.4	6.902639	0.020895
(2)Angle (L)	282717	1	282716.6	3.150643	0.099300
Angle (Q)	40015	1	40015.1	0.445936	0.515952
1L by 2L	1458	1	1458.0	0.016248	0.900520
Error	1166529	13	89733.0		
Total SS	3085211	19			

Table 81: ANOVA table listing factor effects on the kinetic energy holding capacity.

ANOVA; Var.:J; R-sqr=.66329; Adj:.50789 (THE_4a.sta) 2 factors, 2 Blocks, 20 Runs; MS Residual=9407555. DV: J					
	SS	**df**	**MS**	**F**	**p**
Blocks	116552748	1	116552748	12.38927	0.003768
(1)Dist (L)	59418780	1	59418780	6.31607	0.025936
Dist (Q)	31048745	1	31048745	3.30041	0.092381
(2)Angle (L)	26146284	1	26146284	2.77929	0.119387
Angle (Q)	334198	1	334198	0.03552	0.853411
1L by 2L	3741480	1	3741480	0.39771	0.539203
Error	122298216	13	9407555		
Total SS	363219321	19			

Table 82: ANOVA table listing factor effects on the mixing time.

ANOVA; Var.:mt; R-sqr=.95501; Adj:.93425 (THE_4a.sta) 2 factors, 2 Blocks, 20 Runs; MS Residual=162.6023 DV: mt					
	SS	**df**	**MS**	**F**	**p**
Blocks	3192.86	1	3192.86	19.6360	0.000678
(1)Dist (L)	25764.16	1	25764.16	158.4490	0.000000
Dist (Q)	12161.81	1	12161.81	74.7948	0.000001
(2)Angle (L)	347.69	1	347.69	2.1383	0.167414
Angle (Q)	5.01	1	5.01	0.0308	0.863302
1L by 2L	406.12	1	406.12	2.4977	0.138031
Error	2113.83	13	162.60		
Total SS	46988.35	19			

5. Ladle Geometry

Table 83: ANOVA table listing factor effects on the kinetic energy transfer rate.

ANOVA; Var.:e; R-sqr=.99012; Adj:.9753 (Spreadsheet7) 3 factors, 1 Blocks, 16 Runs; MS Residual=1137.749 DV: e					
	SS	**df**	**MS**	**F**	**p**
(1)M (L)	567238.4	1	567238.4	498.5619	0.000001
M (Q)	10504.6	1	10504.6	9.2328	0.022845
(2)AR (L)	41282.4	1	41282.4	36.2843	0.000945
AR (Q)	55216.2	1	55216.2	48.5311	0.000435
(3)Angle (L)	2379.6	1	2379.6	2.0915	0.198259
Angle (Q)	19.8	1	19.8	0.0174	0.899274
1L by 2L	1458.0	1	1458.0	1.2815	0.300828
1L by 3L	544.5	1	544.5	0.4786	0.514932
2L by 3L	1458.0	1	1458.0	1.2815	0.300828
Error	6826.5	6	1137.7		
Total SS	690950.8	15			

Table 84: ANOVA table listing factor effects on the kinetic energy holding capacity.

ANOVA; Var.:E; R-sqr=.99581; Adj:.98952 (Spreadsheet7) 3 factors, 1 Blocks, 16 Runs; MS Residual=203443.6 DV: E					
	SS	**df**	**MS**	**F**	**p**
(1)M (L)	47162400	1	47162400	231.820	0.000005
M (Q)	718109	1	718109	3.530	0.109342
(2)AR (L)	230697467	1	230697467	1133.963	0.000000
AR (Q)	1267381	1	1267381	6.230	0.046785
(3)Angle (L)	3290553	1	3290553	16.174	0.006945
Angle (Q)	772670	1	772670	3.798	0.099219
1L by 2L	2305341	1	2305341	11.332	0.015112
1L by 3L	45904	1	45904	0.226	0.651575
2L by 3L	2311788	1	2311788	11.363	0.015025
Error	1220662	6	203444		
Total SS	291325125	15			

Table 85: ANOVA table listing factor effects on the mixing time.

ANOVA; Var.:mt; R-sqr=.94884; Adj:.87209 (Spreadsheet7) 3 factors, 1 Blocks, 16 Runs; MS Residual=159.6016 DV: mt					
	SS	**df**	**MS**	**F**	**p**
(1)M (L)	74.45	1	74.45	0.46647	0.520100
M (Q)	105.59	1	105.59	0.66161	0.447061
(2)AR (L)	13554.53	1	13554.53	84.92731	0.000092
AR (Q)	2455.60	1	2455.60	15.38578	0.007780
(3)Angle (L)	1107.37	1	1107.37	6.93832	0.038847
Angle (Q)	488.99	1	488.99	3.06381	0.130623
1L by 2L	63.28	1	63.28	0.39650	0.552113
1L by 3L	94.53	1	94.53	0.59230	0.470736
2L by 3L	247.53	1	247.53	1.55093	0.259427
Error	957.61	6	159.60		
Total SS	18716.75	15			

Table 86: ANOVA table listing factor effects on the kinetic energy transfer efficiency.

ANOVA; Var.:eff; R-sqr=.99652; Adj:.99131 (Spreadsheet7) 3 factors, 1 Blocks, 16 Runs; MS Residual=.2733021 DV: eff					
	SS	**df**	**MS**	**F**	**p**
(1)M (L)	6.0251	1	6.0251	22.045	0.003343
M (Q)	0.3621	1	0.3621	1.325	0.293514
(2)AR (L)	460.5023	1	460.5023	1684.957	0.000000
AR (Q)	0.2550	1	0.2550	0.933	0.371374
(3)Angle (L)	1.5321	1	1.5321	5.606	0.055699
Angle (Q)	0.0100	1	0.0100	0.037	0.854752
1L by 2L	0.4728	1	0.4728	1.730	0.236449
1L by 3L	0.2052	1	0.2052	0.751	0.419479
2L by 3L	0.6567	1	0.6567	2.403	0.172098
Error	1.6398	6	0.2733		
Total SS	471.7169	15			

CHAPTER XVIII:
APENDICES PART 5:
REFERENCES

1. **Ghosh, A.** *Secondary Steelmaking, Principles and Application.* Florida : CRC Press LLC, 2001.

2. **Ding, R., et al.** Modeling of the Vacuum Oxygen Decarburization Refining Process. *Metallurgical and Materials Transactions.* 2000, Vol. 31B, pp. 197-206.

3. **Schauwinhold, D., et al.** Steel. *Ullman's Encyclopedia of Industrial Chemistry.* 2008.

4. **Mazumdar, D. and Guthrie, R.** Mixing Models for Gas Stirred Metallurgical Reactors. *Metallurgical and Materials Transactions.* 1986, Vol. 17B, pp. 725-733.

5. **Mazumdar, D. and Evans, J.** Macroscopic Models for Gas Stirred Ladles. *ISIJ International.* 2004, Vol. 44, 3, pp. 447-461.

6. **Mazumdar, D. and Guthrie, R.** The Physical and Mathematical Modelling of Gas Stirred Ladle Systems. *ISIJ International.* 1995, Vol. 35, 1, pp. 1-20.

7. **Iguchi, M., Nakamura, K. and Tsujino, R.** Mixing Time and Fluid Flow Phenomena in Liquids of Varying Kinematic Viscosities Agitated by Bottom Gas Injection. *Metallurgical and Materials Transactions.* 1998, Vol. 29B, pp. 569-575.

8. **Mazumdar, D. and Guthrie, R.** Discussion of: "Mixing Time and Fluid Flow Phenomena in Liquids of Varying Kinematic Viscosities Agitated by Bottom Gas Injection". *Metallurgical and Materials Transactions.* 1999, Vol. 30B, pp. 349-351.

9. —. Mixing time and Correlations for Gas Stirred Ladle Systems. *Iron and Steelmaker.* 1999, Vol. 26, 9, pp. 89-95.

10. **Madan, M., Satish, D. and Mazumdar, D.** Modeling of Mixing in Ladles Fitted with Dual Plugs. *ISIJ International.* 2005, Vol. 45, 5, pp. 677-685.

11. **Mandal, J., et al.** Mixing Time and Correlation for Ladles Stirred with Dual Porous Plugs. *Metallurgical and Materials Transactions.* 2005, Vol. 36B, pp. 479-487.

12. **Mietz, J. and Oeters, F.** Mixing Theories for Gas Stirred Melts. *Steel Research.* 1987, Vol. 58, 10, pp. 446-453.

13. **Oeters, F., et al.** Fluid Flow and Mixing in Secondary Metallurgy. *Steel Research.* 1988, Vol. 59, 5, pp. 192-201.

14. **Mietz, J. and Oeters, F.** Flow Field and Mixing with Eccentric Gas Stirring. *Steel Research.* 1989, Vol. 60, 9, pp. 387-394.

15. **Xie, Y. and Oeters, F.** Experimental Studies on the Flow Velocity of Molten Metals in a Ladle Model at Centric Gas Blowing. *Steel Research.* 1992, Vol. 63, 3, pp. 93-104.

16. —. Measurements of Bubble Plume Behaviour and Flow Velocity in Gas Stirred Liquid Wood's Metal with an Eccentric Nozzle Position. *Steel Research.* 1994, Vol. 65, 8, pp. 315-319.

17. **Iguchi, M., et al.** Swirl Motions in a Cylindrical Bath Induced by Gas Injection under Reduced Pressure on Surface. *ISIJ International.* 1999, Vol. 39, 8, pp. 767-771.

18. **Tatsuoka, T., Kamata, C. and Ito, K.** Expansion of Injected Gas Bubble and Its Effects on Bath Mixing under Reduced Pressure. *ISIJ International.* 1997, Vol. 37, 6, pp. 557-561.

19. **Mazumdar, D., Nakajima, H. and Guthrie, R.** Possible Roles of Upper Slag Phase on the Fluid Dynamics of Gas Stirred Ladles. *Metallurgical and Materials Transactions.* 1988, Vol. 19B, 3, pp. 507-511.

20. **Iguchi, M., et al.** Water Model Experiment on the Liquid Flow Behaviour in a Bottom Blown Bath with Top Layer. *Metallurgical and Materials Transactions.* 1996, Vol. 27B, pp. 35-41.

21. **Ilegbusi, O., et al.** Modeling Mean Flow and Turbulence Characteristics in Gas Agitated Bath with Top Layer. *Metallurgical and Materials Transactions.* 1998, Vol. 29B, pp. 211-222.

22. **Yamashita, S. and Iguchi, M.** Control of Reverse Emulsification and Mixing Time in a Bottom Blown Bath Covered with Top Slag. *ISIJ International.* 2003, Vol. 43, 9, pp. 1326-1331.

23. **Roth, C., Peter, M., Schindler, M. and Koch, K.** Cold Model Investigation into the Effects of Bottom Blowing in Metallurgical Reactors. *Steel Research.* 1995, Vol. 66, 8, pp. 325-330.

24. **Joo, S. and Guthrie, R.** Modelling Flows and Mixing in Steelmaking Ladles Designed for Single- and Dual-Plug Bubbling Operations. *Metallurgical and Materials Transactions.* 1992, Vol. 23B, pp. 765-777.

25. **Kneis, L., Trummer, B. and Knabl, B.** The Hybrid Plug - An Innovative Purging Plug for Steel Ladles.

26. **Iguchi, M., et al.** Effects of Surface Flow Control on Fluid Flow Phenomena and Mixing Time in a Bottom Blown Bath. *Metallurgical and Materials Transactions.* 1999, Vol. 30B, pp. 631-637.

27. **Mazumdar, N., et al.** Impact of Ladle Design on Bath Mixing. *ISIJ International.* 2005, Vol. 45, 12, pp. 1940-1942.

28. **Iguchi, M., et al.** Effects of the Swirl Motion of Bubbling Jet on the Transport Phenomena in a Bottom Blown Bath. *ISIJ International.* 1994, Vol. 34, 4, pp. 330-337.

29. **Takatsuka, Y. and Iguchi, M.** Effect of Swirl Motion on Mixing Time in Water Bath Agitated by Upward Gas Injection. *ISIJ International.* 2001, Vol. 41, 2, pp. 124-127.

30. **Hiratsuka, A., et al.** Prediction of the Period of Swirl Motion Appearing in Gas Injection Processes at High Temperatures. *Koon Gakkaishi.* 2007, Vol. 33, 4, pp. 169-172.

31. **Anon.** *Fluent 6.2 Documentation.* s.l. : Fluent Inc, 2006.

32. **Patankar, S.V.** *Numerical Heat Transfer and Fluid Flow.* New York : Hemisphere, 1980.

33. **Thiart, G.D.** *Numerical Fluid Dynamics 814, Part II: Viscous Flow.* Stellenbosch : University of Stellenbosch, 2007.

34. **Anderson, J.D.** *Computational Fluid Dynamics: the Basics with Applications.* Ney York : McGraw-Hill, 1995.

35. **Koeltzsch, K.** The Height Dependence of the Turbulent Schmidt Number within the Boundary Layer. *Atmospheric Environment.* 2000, Vol. 34, pp. 1147-1151.

36. **Crowe, C.T.** *Multiphase Flow Handbook.* s.l. : CRC Press, 2006.

37. **Hinze, J.O.** *Turbulence.* New York : McGraw-Hill Publishing Company, 1975.

38. **Sheng, Y. and Irons, G.** Measurements of the Internal Structure of Gas-Liquid Plumes. *Metallurgical and Materials Transactions.* 1992, Vol. 23B, pp. 779-788.

39. **Johansen, S., et al.** Fluid Dynamics in Bubble Stirred Ladles: Part I. Experiments. *Metallurgical and Materials Transactions.* 1988, Vol. 19B, pp. 745-754.

40. **Launder, B.E. and Spalding, D.B.** *Lectures in Mathematical Models of Turbulence.* London : Academic Press, 1972.

41. **Yakhot, V. and Orszag, S.** Renormalization Group Analysis of Turbulence: I. Basic Theory. *Journal of Scientific Computing.* 1986, Vol. 1, 1, pp. 1-51.

42. **Shih, T., et al.** A New k-e Eddy-Viscosity Model for High Reynolds Number Turbulent Flows - Model Development and Validation. *Computers Fluids.* 1995, Vol. 24, 3, pp. 227-238.

43. **Castillejos, A., Salcudean, M. and Brimacombe, J.** Fluid Flow and Bath Temperature Destratification in Gas-Stirred Ladles. *Metallurgical and Materials Transactions.* 1989, Vol. 20B, pp. 603-611.

44. **Ganguly, S. and Chakraborty, S.** Numerical Investigation on Role of Bottom Gas Stirring in Controlling Thermal Stratification in Steel Ladles. *ISIJ International.* 2004, Vol. 44, 3, pp. 537-546.

45. **Mukhopadhyay, A.** Role of CFD as a Process Monitoring and Prediction Tool for Secondary Steelmaking. *The Iron & Steel Cociety and The Minerals, Metals & Materials Society.* 2003, pp. 227-239.

46. **Johansen, S. and Boysan, F.** Fluid Dynamics in Bubble Stirred Ladles: Part II. Mathematical Modelling. *Metallurgical and Materials Transactions.* 1988, Vol. 19B, pp. 755-764.

47. **Mazumdar, D. and Guthrie, R.** An Assessment of a Two Phase Calculation Procedure for Hydrodynamic Modelling of Submerged Gas Injection in Ladles. *ISIJ International.* 1994, Vol. 34, 5, pp. 384-392.

48. **Xia, J. and Ahokainen, T.** Homogenization of Temperature Field in a Steelmaking Ladle with Gas Injection. *Scandinavian Journal of Metallurgy.* 2003, Vol. 32, pp. 211-217.

49. —. Transient Flow and Heat Transfer in a Steelmaking Ladle during the Holding Period. *Metallurgical and Materials Transactions.* 2001, Vol. 32B, pp. 733-741.

50. **Xia, J., Ahokainen, T. and Holappa, L.** Analysis of Flows in a Ladle with Gas-Stirred Melt. *Scandinavian Journal of Metallurgy.* 2001, Vol. 30, pp. 69-76.

51. **Guo, D., Gu, L. and Irons, G.** Developments in Modelling of Gas Injections and Slag Foaming. *Applied Mathematical Modelling.* 2002, Vol. 26, pp. 263-280.

52. **Han, J., et al.** Transient Fluid Flow Phenomena in a Gas Stirred Liquid Bath with Top Oil Layer-Approach by Numerical Simulation and Water Model Experiments. *ISIJ International.* 2001, Vol. 41, 10, pp. 1165-1173.

53. **Clift, R., et al.** *Bubbles, Drops, and Particles.* London : Academic Press Inc., 1978.

54. **Harmathy, T.** Velocity of Large Drops and Bubbles in Media of Infinite or Restricted Extent. *AIChE Journal.* 1960, Vol. 6, pp. 281-288.

55. **Sheng, Y. and Irons, G.** Measurement and Modelling of Turbulence in the Gas/Liquid Two-Phase Zone during Gas Injection. *Metallurgical and Materials Transactions.* 1993, Vol. 24B, pp. 695-705.

56. —. The Impact of Bubble Dynamics on the Flow in Plumes of Ladle Water Models. *Metallurgical and Materials Transactions.* 1995, Vol. 26B, pp. 625-635.

57. **Laux, H., et al.** CFD modelling fo Bubble-Driven Flows. *International Journal of Applied Mechanics and Engineering.* 2002, Vol. 7, 1, pp. 329-359.

58. **Tomiyama, A. and Shimada, N.** A numerical method for bubbly flow simulation based on a multi-fluid model. *Computational Technologies for Fluid/Thermal/Structural/Chemical Systems with Industrial Applications.* 1998, Vol. 2, pp. 255-262.

59. **Lo, S.** Modeling of bubble breakup and coalescence with the MUSIG model. *AEA Technology.* 1998, pp. 1-17.

60. **A., Alexiadis., Gardin, P. and Domgin, J.** Spot Turbulence, Breakup, and Coalescence of Bubbles Released from a Porous Plug Injector into a Gas-Stirred Ladle. *Metallurgical and Materials Transactions.* 2004, Vol. 35B, pp. 949-956.

61. **Davidson, J. F. and Schuler, B. O. G.** Bubble formation at an orifice in a viscous liquid. *Transactions of the Institution of Chemical Engineers.* 1960, Vol. 38, 3, pp. 144-154.

62. **Gale, W. and Totemeier, T.** *Smithells Metal Reference.* s.l. : Elsevier Butterworth-Heinemann, 2004.

63. **Macrossan, M. and Lilley, C.** Viscosity of argon at temperatures >2000 K from measured shock thickness. *Physics of Fluids.* 2003, Vol. 15, 11, pp. 3452-3457.

64. **Camac, M. and Feinberg, R.** Thermal conductivity of argon at high temperatures. *Journal of Fluid Mechanics.* 1965, Vol. 21, pp. 673-688 .

65. **Lide, D.** *CRC Handbook of Chemistry and Physics.* s.l. : CRC Press, 2006.

66. **Ekambara, K., Dhotre, M. and Joshi, J.** CFD Simulations of Bubble Column Reactors: 1D, 2D and 3D approach. *Chemical Engineering Science.* 2005, Vol. 60, pp. 6733-6746.

67. **Allibert, M., et al.** *Slag Atlas.* D-Dusseldorf : Verlag Stahleisen GmbH, 1995.

68. **Haider, A. and Levenspiel, O.** Grag Coefficient and Terminal Velocity of Spherical and Nonspherical Particles. *Powder Technology.* 1989, Vol. 58, pp. 63-70.

69. **Shen, H., et al.** *Environmental Fluid Mechanics.* s.l. : American Society of Civil Engineers , 2002.

70. **Garcia-Briones, M., Brodkey, R. and Chalmers, J.** Computer Simulations of the Rupture of a Gas Bubble at a Gas-Liquid Interface and its Implications in Animal Cell Damage. *Chemical Engineering Science.* 1994, Vol. 49, 14, pp. 2301-2320 .

71. **Kishimoto, Y., et al.** Energy Dissipation Distribution in Gas Stirred Liquids. *ISIJ International.* 1999, Vol. 39, 2, pp. 113-122.

72. **Joshi, J.** Computational Flow Modelling and Design of Bubble Column Reactors. *Chemical Engineering Science.* 2001, Vol. 56, pp. 5893-5933.

73. **Schwarz, M.** Sloshing Waves Formed in Gas Agitated Baths. *Chemical Engineering Science.* 1990, Vol. 45, 7, pp. 1765-1777.